

STAR FORMATION AND NUCLEAR ACTIVITY IN LOCAL STARBURST  
GALAXIES: A NEAR-INFRARED PERSPECTIVE

Henry Jacob Borish  
Strabane, Pennsylvania

B.S. Physics and Astronomy, University of Pittsburgh, 2010

M.S. Astronomy, University of Virginia, 2012

A Dissertation Presented to the Graduate  
Faculty of the University of Virginia  
in Candidacy for the Degree of  
Doctor of Philosophy

Department of Astronomy

University of Virginia  
May 2017

Committee Members:

Aaron S. Evans  
Robert W. O'Connell  
Rémy Indebetouw  
Robert E. Johnson

© Copyright by  
Henry Jacob Borish  
All rights reserved  
May 20, 2017

## Abstract

Near-Infrared spectroscopy provides a useful probe for viewing embedded nuclear activity in intrinsically dusty sources such as Luminous Infrared Galaxies (LIRGs). In addition, near-infrared spectroscopy is an essential tool for examining the late time evolution of type II supernovae as their ejected material cools through temperatures of a few thousand Kelvins. In this dissertation, I present observations and analysis of two distinct star-formation driven extragalactic phenomena: a luminous type II supernova and the nuclear activity of luminous galaxy mergers.

Near-infrared ( $1 - 2.4 \mu\text{m}$ ) spectroscopy of a sample of 42 LIRGs from the Great Observatories All-Sky LIRG Survey (GOALS) were obtained in order to probe the excitation mechanisms as traced by near-infrared lines in the embedded nuclear regions of these energetic systems. The spectra are characterized by strong hydrogen recombination and forbidden line emission, as well as emission from ro-vibrational lines of  $\text{H}_2$  and strong stellar CO absorption. No evidence of broad recombination lines or  $[\text{Si VI}]$  emission indicative of AGN are detected in LIRGs without previously identified optical AGN, likely indicating that luminous AGN are not present or that they are obscured by more than 10 magnitudes of visual extinction. The  $[\text{Fe II}]/\text{Pa}\beta$  of the sample is well-correlated with the optical emission line classification, with LINERs and Seyferts having  $[\text{Fe II}]/\text{Pa}\beta \geq 0.3$  and HII-region like objects having  $[\text{Fe II}]/\text{Pa}\beta \leq 0.3$ . Further, the optical classification of the comparison sample of nearby, normal star-forming galaxies, low luminosity LINERs and supernova remnants (SNRs) show a similar segregation, and is likely an indication that AGN and supernovae in LINERs and Seyferts are associated with shocks that liberate iron from grains into the gas phase. Comparison of these data with models of fast radiative shocks show an approximate agreement. The observed line ratios are not well fit

by starburst photoionization models computed with MAPPINGS III. The discrepancy between the models and data are likely largely a function of the Fe abundances adopted for the models.

We fit non-linear least squares to the profiles from each detection of Paschen  $\beta$ , Brackett  $\gamma$ , and  $\text{H}_2$  S(1) 1-0 in our sample of near-IR spectra. Of the detected Pa $\beta$  lines, 27(22) of 49 are fit by a single(double) Gaussian component. These fractions are 36(19) of 55 for Br $\gamma$  and 41(14) of 55 for  $\text{H}_2$ . Faint broad components with velocity dispersions of  $\sim 650$ ,  $750$ , and  $875 \text{ km s}^{-1}$  are found in the Seyfert galaxies NGC 1275, NGC 7469, and NGC 7674 suggesting the presence of a broad line region. Five of the LIRGs show evidence of outflows in Pa-beta emission, with velocity offsets from the systemic velocity of  $> 100 \text{ km/s}$ . The range in outflow velocities are significantly less than what is seen OH 119 micron - this difference may be a result of the ability of the far-infrared line to probe regions closer to the obscured starburst and/or AGN where the acceleration may be the strongest.

Temporal near-infrared ( $1 - 2.4 \mu\text{m}$ ) observations of the Type IIn supernova SN 2010jl, which occurred in the tidally disrupted host galaxy UGC 5189A, were obtained to study the evolution of its near-infrared (NIR) emission. The data span the age range of  $36 - 565$  days from the earliest detection of the supernova. On day 36, the H lines show an unresolved narrow emission component along with a symmetric broad component. Over the next hundreds of days, the broad components of the H lines shift to the blue by  $700 \text{ km s}^{-1}$ , as is also observed in optical lines. The narrow lines do not show a shift, indicating they originate in a different region. We show the broad H emission is consistent with electron scattering in the circumstellar medium. In contrast to the optical He lines, the near-infrared He lines are strong with well-defined profiles. The He I  $\lambda 10830$  feature has a narrow P Cygni line, with

absorption extending to  $\sim 100 \text{ km s}^{-1}$  and strengthening over the first 200 days, and an emission component which weakens with time. He I  $\lambda 10830$  and  $\lambda 20587$  lines both show an asymmetric broad emission component, with a shoulder on the blue side that varies in prominence and velocity from  $-5500 \text{ km s}^{-1}$  on day 108 to  $-4000 \text{ km s}^{-1}$  on day 219. The absence of the feature in the H lines suggests that this is from a He rich ejecta flow. This component may be associated with the higher velocity flow indicated by X-ray observations of the supernova. At day 403, the continuum emission becomes dominated by a blackbody spectrum with a temperature of  $\sim 1900 \text{ K}$ , suggestive of dust emission.

## Acknowledgements

In my preparation of this thesis, I have benefited greatly from interactions with many of the people around me. The community within the University of Virginia Department of Astronomy have been instrumental in maintaining the exchange of information that led to the completion of this work. Furthermore, I was lucky enough to be welcomed into the scientific community of the National Radio Astronomy Observatory, where I benefited from the additional expertise of the scientists there. I would especially like to thank Aaron Evans for certainly being one of the most patient and supportive mentors anyone has ever had. In my studies of LIRGs I have benefited greatly from scientific discussions with other members of the GOALS collaboration, particularly Lee Armus, Andreea Petric, Joe Mazzarella, Dong-Chan Kim, Jeff Rich, Sabrina Stierwalt, Tanio Díaz-Santos, Vivian U, George Privon, Loreto Barcos, Sean Linden, Jason Surace, and Eric Murphy. Important perspectives on this work were also provided by Tobias Fritz, Kristen Jones, John Hibbard, Jim Condon, Mark Whittle, Bob O’Connell, Rémy Indebetouw, and Scott Schnee. My supernova work would not have been possible without the help of Roger Chevalier, Chenliang Huang, Mike Skrutskie, and Ori Fox. I am eternally grateful to C. David Rigby for resurrecting my computer once, and making sure I knew how to do it myself when it was inevitably again necessary a month before my thesis defense.

Before I began grad school, my interests in science and math were guided and encouraged by many of my teachers, namely Linda Richardson, Adele Dellapiazza, Ray Rota, Joe Politan, Steve Kropinak, Michael Wood-Vasey, Gurudev Dutt, Jim Mueller, Vladimir Savinov, Paul Shepard, Eugene Engels, Piotr Hajlasz, and Dave Watson. Sergeant Anthony Wright deserves commendation for too many things to list here, but in particular for being the other half of the Iceoplex at Southpointe

Public Skate General Relativity and Star Wars Discussion Group. Thanks to Andrew Martin, Art Cornell, and Bill Dirienzo for continuously being good friends despite our physical separation.

A special thanks is owed to all the graduate students in the department, past and present, for always being as Bardeen as possible. Last but not least I thank my family: Mom, Dad, Niko, Jorma, Mimi, Pappy, McMaw, Pappap, and Uncle Rick, for providing the support and love necessary for a person to complete such an academic endeavor as this. Jessica Schiermeister: thanks for your unconditional support and for sharing all the highs and lows that have accompanied this part of my life. It wouldn't have been nearly as easy or as much fun without you. Also, thanks Jess for introducing me to the work of Lin-Manuel Miranda, who I must in turn thank for writing the soundtrack to the last year of my graduate career.

# Table of contents

<b>Abstract</b>	<b>ii</b>
<b>Acknowledgements</b>	<b>v</b>
<b>1 Introduction</b>	<b>1</b>
1.1 Luminous Infrared Galaxies . . . . .	1
1.2 Near-Infrared Spectroscopy as a Tool for Galaxy Evolution . . . . .	4
1.3 Supernovae . . . . .	5
1.4 Overview . . . . .	7
<b>2 Near-Infrared Spectroscopy of the GOALS Sample: AGN Search and Emission Line Diagnostics</b>	<b>9</b>
2.1 INTRODUCTION . . . . .	9
2.2 SAMPLE . . . . .	11
2.3 OBSERVATIONS AND RESULTS . . . . .	15
2.4 DISCUSSION . . . . .	102
2.4.1 AGN . . . . .	102
2.4.2 The Near-IR Diagnostic Diagram: [Fe II], H <sub>2</sub> , Shocks v. Photoionization . . . . .	108
2.4.3 Comparison to Computational Models . . . . .	122
2.5 CONCLUSIONS . . . . .	127
<b>3 Near-Infrared Spectroscopy of the GOALS Sample: Emission Line Fits and Kinematic Analysis</b>	<b>129</b>
3.1 INTRODUCTION . . . . .	129
3.2 RESULTS . . . . .	130
3.3 DISCUSSION . . . . .	149
3.4 CONCLUSIONS . . . . .	161
<b>4 Evidence for High Velocity Ejecta in the Near Infrared Emission Lines of SN 2010jl</b>	<b>165</b>
4.1 INTRODUCTION . . . . .	165
4.2 OBSERVATIONS . . . . .	168



4.3	SPECTRAL COMPONENTS . . . . .	172
4.3.1	Continuum Emission . . . . .	172
4.3.2	Hydrogen Lines . . . . .	175
4.3.3	He lines . . . . .	182
4.3.4	Other Lines . . . . .	192
4.4	PHYSICAL PICTURE . . . . .	195
4.5	DISCUSSION AND CONCLUSIONS . . . . .	202
<b>5</b>	<b>Summary</b>	<b>204</b>
5.1	A Near-IR Spectroscopic Survey of the Embedded Nuclear Regions of Luminous Infrared Galaxies . . . . .	204
5.2	A Time Domain Study of the Type IIIn SN 2010jl's NIR Spectrum . .	205
5.3	Future Research – Resolved Spectroscopy of Star Formation and Feed- back in the Hearts of Galaxies . . . . .	206

# Chapter 1

## Introduction

### 1.1 Luminous Infrared Galaxies

In 1983, NASA and European partners launched the Infrared Astronomical Satellite (IRAS) for the purpose of mapping the entire sky in the mid- and far-infrared for the first time (Neugebauer et al. 1984). While mapping the sky, IRAS discovered a large population of sources with no known counterpart in pre-existing optical catalogs. Most of these newly found objects were later optically identified as spiral galaxies undergoing major mergers and interactions (Soifer et al. 1987); these dynamical events trigger extreme bursts of star formation (see Sanders & Mirabel 1996, for a review). In contrast to our Galaxy, up to 90% of the light from these galaxies is manifested in the far-infrared ( $\lambda \approx 40 - 500\mu m$ ). Galaxies of this class, which have an *infrared* luminosity ( $L_{IR}$  [ $8 - 1000\mu m$ ]) greater than  $10^{11}$  Solar Luminosities ( $10^{11} L_{\odot}$ ), are called Luminous Infrared Galaxies (LIRGs). These LIRGs populate the bright end of the Infrared Galaxy Luminosity Function.

Understanding LIRGS is key to forming a picture of how massive galaxies came to be. LIRGs can provide insight on galaxy evolution in several ways.

- **LIRGs constitute giant stellar nurseries.** The star formation rates of LIRGs are elevated over those of normal galaxies by several factors of 10, and the observed activity occurs in very compact ( $< 200$  pc) regions of these galaxies. This makes them ideal targets for the study of extreme star formation environments and their relationship to massive galaxy mergers.
- **Many of these systems are believed to contain active galactic nuclei (Alonso-Herrero et al. 2012).** Almost all nearby massive galaxies are thought to contain quiescent black holes in their central regions. In order to understand the mass buildup of supermassive black holes and the interplay between their growth and the star systems directly surrounding them, we must understand the relationship between star formation and AGN. It seems likely that this relationship holds the key to unlocking the correspondence between the stellar bulge mass and the SMBH mass of nearby “normal” galaxies. Since LIRGs are systems where both processes are actively occurring, they provide an ideal sample for these investigations.
- **About half the energy in the Universe generated since the Big Bang is observed at infrared/sub-millimeter wavelengths, and likely emanates from cosmologically distant LIRGs (Lagache et al. 2005).** The total energy of the cosmic infrared background matches that of its optical counterpart. This infrared energy is from dust-enshrouded star formation, AGN activity, or a combination of both. The study of low-redshift LIRGs will lead to a better understanding of these phenomena in their early Universe counterparts.

The extreme amount of infrared light emitted by LIRGs is radiation that has been reprocessed by dust. The dust is a byproduct of star formation. As a result, it enshrouds active star forming regions, is heated by ultraviolet and optical light from newly formed massive stars and possibly an AGN, and re-emits the absorbed energy in the infrared. Due to this process, the same dust that makes LIRGs so infrared luminous tends to obscure newly formed stars as well as any AGN. This generally limits the effectiveness of visible light studies of activity within LIRGs. Another hurdle involved in studying LIRGs are the long timescales associated with their evolution; massive mergers can last in excess of a gigayear between initial encounter and final coalescence (Privon et al. 2013). The solutions to these problems lie in observing many LIRGs within every possible wavelength band. To wit, a large sample size is needed to statistically sample each stage in the process of galaxy collisions – from the initial encounter to the final coalescence into a single galaxy. Further, a survey with broad wavelength coverage will better circumvent dust extinction (Figure 1.1) and probe the relative importance of activity at various optical depths.

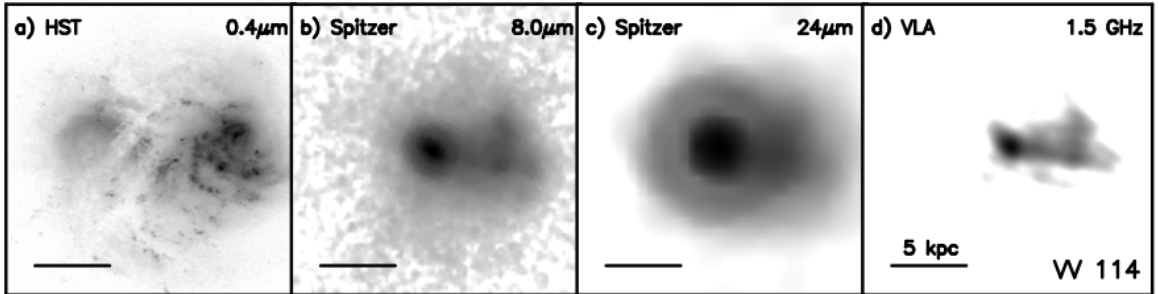


Fig. 1.1.— *Hubble Space Telescope*, *Spitzer Space Telescope*, and Very Large Array images of the GOALS LIRG VV 114. The source of the bulk of the energy, plainly visible at the longer wavelengths, is obscured by dust at  $0.4\mu\text{m}$  and is thus not visible in the *Hubble Space Telescope* image (from Evans (2008)).

In order to begin unraveling the mystery of embedded energy sources in LIRGs, we have undertaken a multi-wavelength survey of a complete flux-limited sample of 201 LIRGs from the IRAS Revised Bright Galaxy Sample (Sanders et al. 2003), known as The **G**reat **O**bservatories **A**ll-sky **L**IRG **S**urvey (GOALS, Armus et al. (2009)). GOALS includes data from the *Hubble Space Telescope*, *Spitzer Space Telescope*, *Chandra X-ray Observatory*, *Galaxy Evolution Explorer*, and the Jansky Very Large Array. Both the large sample size and exhaustive wavelength coverage of GOALS make it an excellent starting point for answering more specific questions about LIRG properties. Despite the extensive amount of data available for the GOALS LIRGs, one crucial piece is still missing: near-infrared spectroscopy. The near-infrared represents the longest wavelength regime in which current technology allows the study of diagnostics of star formation, AGN activity, and their associated phenomena, at sufficiently high spectral and spatial resolution.

## 1.2 Near-Infrared Spectroscopy as a Tool for Galaxy Evolution

The bulk of this thesis is focused on a near infrared study of the energetics occurring in the nuclear regions of LIRGs. This study builds upon prior studies (e.g. Goldader et al. 1995, 1997a; Veilleux et al. 1997b, 1999b; Murphy et al. 2001; Dannerbauer et al. 2005; Matsuoka et al. 2012) through its broad near- infrared wavelength coverage and its high spectral resolution. The study makes use of TripleSpec, which are a pair of  $0.9 - 2.4 \mu\text{m}$ , spectral resolution  $R \approx 3000$  cross-dispersed spectrographs, on the ARC 3.5-meter Telescope and the Palomar 200-inch Hale Telescope (Wilson et al. 2004; Herter et al. 2008). TripleSpec is capable of observing, in a single pointing, a

wavelength range that is 3 times broader than instruments used in previous studies were able to cover while probing motions on the order of 100 km/s. The width of the TripleSpec slit is one arcsecond, sufficiently narrow to study individual regions of each galaxy. The present study contains spectra of 42 LIRGs from the two TripleSpec spectrographs. These observations have allowed us to study:

- **Gas Excitation:** Multiple species of emission lines are visible in the near-infrared. These lines can be used to diagnose both photoionization and shock processes within the nuclear regions of galaxies.
- **Hidden Active Galactic Nuclei:** Black holes which are actively accreting matter cause the hot gas around them to be accelerated to very high velocities, leading to broadened emission lines. Recombination lines that are broadened to velocities of  $\Delta v \geq 2000 \text{ km s}^{-1}$  indicate the presence of an AGN. Emission from high ionization lines such as [Si VI]  $1.967 \mu\text{m}$  likewise signifies the presence of an AGN (Marconi et al. 1994).
- **Gas Kinematics:** In addition to assessing the nature of the ionizing sources through near-infrared emission lines, the line profiles can also be used to search for evidence of nuclear outflows induced by star formation and AGN processes.

### 1.3 Supernovae

A central theme of near-infrared spectral studies of LIRGs is the investigation of [Fe II] emission and its connection to interstellar shocks. Nucleosynthesis of Fe and the production of interstellar shocks are primarily due to supernovae. Enhanced rates of star formation naturally lead to an increase in supernova activity, ultimately culminating in the shock-driven ionization of Fe. More important in enhancing [Fe

II] emission than the production of highly ionized iron species is the liberation of Fe from the solid phase into the gas phase. This thesis concludes with a TripleSpec study of the ejecta of Supernova 2010jl, a relatively nearby and luminous type II<sub>n</sub> supernova observed in the tidally disrupted galaxy UGC 5189A. This proved to be a unique dataset as it followed the spectral evolution of the supernova at very high time resolution.

Our TripleSpec investigation of this supernova is focused on:

- **The He I Profile:** The near-infrared contains two strong Helium emission lines, allowing us to study the shape of the He I profile. A kinematic comparison of the He I profile with the Hydrogen recombination profile has the potential to reveal distinct ejecta flows that are overabundant in Helium.
- **The Temperature of The Dust:** Type II<sub>n</sub> Supernovae are notable for the production of dense cocoons of gas and dust produced by their progenitors. The cocoon is heated by the resultant supernova to temperatures of  $T \approx 2000$  K (Andrews et al. 2011; Borish et al. 2015). Long after the emission from the supernova photosphere has ceased, near-infrared spectral observations allow us to monitor the spectrum of this warm dust.
- **Electron Scattering in the Circumstellar Medium:** The shape of the broad H emission profile can be gauged to provide feedback on models of  $e^-$  scattering in the circumstellar cocoon created by the type II<sub>n</sub> progenitor. The optically thin nature of the near-infrared recombination lines allows a comparison between the quantities of scattered and unscattered photons.

## 1.4 Overview

This thesis is divided into five chapters. This chapter, the introduction, provides an overview of the scientific motivations for undertaking the work presented in chapters 2, 3 and 4. Chapter 2 presents our near-infrared spectra of 42 LIRGs from GOALS including a search for AGN signatures, a diagnostic analysis of emission line ratios, and a comparison to models of emission line strengths from the latest computational models (MAPPINGS III). Chapter 3 describes fits to emission lines from the near-infrared LIRG study, and provides an analysis of the kinematics traced therein. Chapter 4 presents our near-infrared spectroscopy of SN 2010jl along with a kinematic analysis of the line profiles, a comparison of the H line profile to models of electron scattering, and a determination of the blackbody temperatures of the continuum emission. Chapter 5 provides a summary of the entire thesis.

Many observations went into this work. SN 2010jl was observed from late 2010 to early 2012. Over a period of 219 days, we observed the supernova once every 30 days on average. After this period, the rate of spectral evolution slowed dramatically, and we observed the supernova roughly once every 4 months for 346 additional days. Early observations were performed by Ori Fox and George Privon, while I personally gathered the last several spectra with some guidance from Mike Skrutskie and occasional help from Ben Breslauer and Aaron Kingery. A campaign to gather near-infrared spectra of GOALS LIRGs was started in 2008 by Andreea Petric and Lee Armus, who gathered roughly 70% of the LIRG observations presented here (i.e. the Palomar observed sample). I observed the rest in 2012 and 2013 with TripleSpec at APO with occasional help from Kristen Jones. The data reduction was performed mainly by me, with some hands on guidance from Ori Fox and Andreea Petric. I performed the overwhelming majority of the data analysis presented here. Dongchan



Kim provided the measurements of  $H\alpha$  emission line widths in the LIRGs. Chenliang Huang is responsible for the modeling of electron scattering in the supernova wind. Chenliang and I simultaneously measured the velocity drift of the blue “shoulder” feature within the emission line profile of He I  $\lambda 10830$  in SN 2010jl.

## Chapter 2

# Near-Infrared Spectroscopy of the GOALS Sample: AGN Search and Emission Line Diagnostics

### 2.1 INTRODUCTION

It has been over thirty-years since the *Infrared Astronomical Satellite (IRAS)* discovered luminous and ultraluminous infrared galaxies (LIRGs:  $L_{\text{IR}} = 10^{11.0-11.99} L_{\odot}$ ; ULIRGs:  $L_{\text{IR}} \geq 10^{12.0} L_{\odot}$ ) as a significant population of local extragalactic sources (Neugebauer et al. 1984). These often irregular, typically interacting systems, which are host to extreme starbursts and sometimes AGN activity, have far-infrared luminosities which exceed those of normal, star-forming galaxies by factors of 10 – 100. At high redshift, the energy generated by star formation and AGN processes within U/LIRGs make up a large fraction of the infrared energy density of the Universe. A central issue is the origin of the immense amount of power produced by U/LIRGs. One approach that has been to used is to make use of optical spectroscopic obser-

vations to examine well-understood optical emission line diagnostics (Baldwin et al. 1981; Veilleux & Osterbrock 1987; Kewley et al. 2006). Optical line-ratio diagrams generally indicate AGN activity in U/LIRGs is weak or absent in lieu of strong starbursts (Veilleux et al. 1995; Kim et al. 1995, 1998; Veilleux et al. 1999a; Yuan et al. 2010). Furthermore, Rich et al. (2014) showed that U/LIRGs originally classified as starburst/AGN composites could be better explained by invoking a combination of starburst photoionization and merger driven shocks.

The primary criticism of optical studies of U/LIRGs is the fact that the targets are intrinsically dusty systems. Indeed, the prototypical ULIRG, Arp 220 has an estimated  $A_V$  in the range of 50 - 1000 towards its nuclear region (Sturm et al. 1996; Downes & Solomon 1998). Mid-IR observations of LIRGs with the *IR Space Observatory (ISO)* and the *Spitzer Space Telescope* provided better probes (albeit at coarser spatial and spectral resolutions) of the embedded energetics of LIRGs and in many cases showed evidence of AGN in systems optically identified as LINERs via their  $6.2\mu\text{m}$  PAH equivalent widths and [Ne V] emission (Petric et al. 2011; Stierwalt et al. 2013, 2014).

In this chapter, we build upon prior near-IR spectroscopic surveys of LIRGs (e.g., Goldader et al. 1995; Veilleux et al. 1997b, 1999b; Murphy et al. 2001; Dannerbauer et al. 2005; Matsuoka et al. 2012) by obtaining  $0.9\text{--}2.4\mu\text{m}$  spectroscopy of a sample of 42 LIRGs (52 individual nuclei) obtained with the TripleSpec instruments on the ARC 3.5 m telescope at Apache Point Observatory and the Hale 300 inch telescope at Palomar Observatory. With these observations, we make use of diagnostic emission line ratios in relation to empirical comparison of lower-luminosity star-formation and AGN hosts and to photoionization and shock models, as well as the width of hydrogen recombination lines, to assess to dominant sources of ionization at near-IR

wavelengths within LIRGs.

In the following chapter, we re-examine the line profiles in detail to assess the presences of BLRs and outflows. The near-IR has a 10 magnitudes of visual extinction advantage over optical spectroscopy, thus providing a better probe of the ionization processes occurring in the active regions of LIRGs. Further, the spatial and spectral resolution of the observed diagnostic lines is superior to that achieved by the aforementioned mid-IR space telescopes. Finally, follow-up high-resolution narrow-band imaging observations of select diagnostic emission lines are possible with both ground-based facilities and with the *Hubble Space Telescope*.

This chapter is organized into seven sections. In §2.2 the sample selection is summarized. §2.3 gives a summary of the observations and data reduction as well as a description of the fully reduced spectra and measurements thereof. In §2.4, the search for embedded AGN, and the analysis of the emission line ratios with respect to empirical and computational model comparisons is summarized. §2.5 contains a summary of the entire chapter.

Throughout this paper, we adopt a WMAP Cosmology of  $H_0 = 70 \text{ km s}^{-1} \text{ Mpc}^{-1}$ ,  $\Omega_{\text{matter}} = 0.28$ , and  $\Omega_{\Lambda} = 0.72$  (e.g., see Armus et al. 2009).

## 2.2 SAMPLE

The sample of 42 LIRGs here studied is drawn from the **Great Observatories All-Sky LIRG Survey** (Armus et al. 2009, GOALS). The GOALS survey as a whole consists of the complete sample of 180 LIRGs and 22 ULIRGs in the *IRAS* Revised Bright Galaxy Sample (Sanders et al. 2003, RBGS), which contains all galaxies having  $60 \mu\text{m}$  flux densities,  $f_{60\mu\text{m}} > 5.24 \text{ Jy}$  and galactic latitudes,  $b > 5^\circ$ . The selection of GOALS LIRGs observed in the sample was determined by their observability from

Apache Point and Palomar. In total 42 of the 149 GOALS U/LIRGs visible from these sites were observed. Source parameters are shown in Table ??

Of the 42 systems observed, 30 are confirmed mergers. According to the tabulation of merger state in Stierwalt et al. (2013), of these 30, two are premergers, 10 are early stage mergers, eight are middle stage mergers, and 10 are late stage mergers. Of the 42 systems in this sample, 21 have been observed with the Advanced CCD Imaging Spectrometer aboard *Chandra*. Of those 21, Iwasawa et al. (2011) finds that six show X-ray evidence for AGN in the form of the slope of the continuum and/or emission from the 6.4 keV Fe K $\alpha$  line.

Table 2.1. Source Parameters

Name ( <i>Common</i> )	Name ( <i>IRAS</i> )	R.A.	J2000.0 Decl.	$\log(L_{IR})^*$	$m_H^a$	Other Names
MCG-02-01-051/2	F00163-1039	00 18 51.4	-10 22 33	11.41	11.780 $\pm$ 0.033	Arp 256, VV 352
UGC 02369	F02512+1446	02 54 01.9	+14 58 17	11.60	...	
NGC 1275	F03164+4119	03 19 46.7	+41 30 37	11.20	8.488 $\pm$ 0.035	Mrk <sup>1</sup> b 1505, UGC 02669, Perseus A
UGC 4881	F09126+4432	09 15 54.8	+44 19 58	11.69	11.466 $\pm$ 0.043	Grasshopper
UGC 5101	F09320+6134	09 35 48.8	+61 21 22	11.95	11.528 $\pm$ 0.030	
NGC 4922	F12590+2934	13 01 25.9	+29 18 46	11.32	...	VV 609
CGCG 043-099	F12592+0436	13 01 49.9	+04 20 01	11.62	...	VV 283
MCG-02-33-098/9	F12596-1529	13 02 20.5	-15 46 05	11.11	10.804 $\pm$ 0.012	
VV 250 A	F13136+6223	13 15 34.9	+62 07 26	11.74	11.984 $\pm$ 0.042	UGC 08335 NED02, Arp 238 NED02
UGC 08387	F13182+3424	13 20 34.9	+34 08 24	11.67	11.227 $\pm$ 0.025	Arp 193, VV 821, I Zw 056
NGC 5104	F13188+0036	13 21 24.2	+00 20 27	11.20	10.148 $\pm$ 0.036	
NGC 5256	F13362+4831	13 38 18.2	+48 16 28	11.49	...	Mrk 0266, I Zw 067
UGC 08696	F13428+5608	13 44 41.8	+55 53 14	12.14	11.417 $\pm$ 0.031	Mrk 0273, I Zw 071
UGC 08739	F13470+3530	13 49 15.0	+35 15 17	11.08	10.294 $\pm$ 0.022	
NGC 5331	F13497+0220	13 52 16.6	+02 06 08	11.59	...	VV 253
CGCG 247-020	F14179+4927	14 19 43.5	+49 14 09	11.32	11.722 $\pm$ 0.037	Mrk 1490
NGC 5653	F14280+3126	14 30 09.5	+31 12 57	11.06	9.498 $\pm$ 0.015	
IRAS F14348-1447	F14348-1447	14 37 37.3	-15 00 20	12.30	12.998 $\pm$ 0.103	
VV 340	F14547+2449	14 57 00.3	+24 37 01	11.67	10.759 $\pm$ 0.026	Arp 302 NED02
CGCG 049-057	F15107+0724	15 13 12.7	+07 13 30	11.27	11.379 $\pm$ 0.031	
VV 705	F15163+4255	15 18 06.7	+42 44 41	11.89	...	Mrk 0848, I Zw 107
IRAS F15250+3608	F15250+3608	15 26 59.9	+35 58 34	12.02	13.123 $\pm$ 0.058	
NGC 5936	F15276+1309	15 30 00.9	+12 59 21	11.07	9.770 $\pm$ 0.021	
NGC 6090	F16104+5235	16 11 40.8	+52 27 27	11.51	11.323 $\pm$ 0.063	Mrk 0496, VV 626, I Zw 135
IRAS F17132+5313	F17132+5313	17 14 20.5	+53 10 34	11.89	try again later	
IRAS 18090+0130	18090+0130	18 11 37.3	+01 31 40	11.58:	12.055 $\pm$ 0.076	
NGC 6670A/B	F18329+5950	18 33 35.6	+59 53 20	11.60	...	VII Zw 812
NGC 6701	F18425+6036	18 43 12.1	+60 39 13	11.05	9.605 $\pm$ 0.016	
NGC 6786	F19120+7320	19 11 01.4	+73 25 10	11.43	10.690 $\pm$ 0.032	UGC 11414, VV 414 W

Table 2.1—Continued

Name ( <i>Common</i> )	Name ( <i>IRAS</i> )	R.A.	J2000.0 Decl.	$\log(L_{IR})^*$	$m_H^a$	Other Names
ESO 593-IG008	F19115-2124	19 14 30.7	-21 19 08	11.87	11.521 $\pm$ 0.038	
IRAS F19297-0406	F19297-0406	19 32 22.1	-04 00 02	12.37	...	
IRAS 19542+1110	19542+1110	19 56 35.4	+11 19 03	12.04	...	
IRAS 20351+2521	20351+2521	20 37 18.6	+25 31 42	11.54	11.081 $\pm$ 0.052	
II Zw 096	F20550+1655	20 57 23.3	+17 07 34	11.87	...	II Zw 096
IRAS 21101+5810	21101+5810	21 11 29.3	+58 23 04	11.75	13.991 $\pm$ 0.254	
UGC 12150	F22389+3359	22 41 12.3	+34 14 59	11.29	10.507 $\pm$ 0.016	
IRAS F22491-1808	F22491-1808	22 51 49.0	-17 52 27	12.11	13.549 $\pm$ 0.108	
NGC 7469	F23007+0836	23 03 15.5	+08 52 25	11.59	9.245 $\pm$ 0.026	Arp 0298 NED01, Mrk 1514
IC 5298	F23135+2517	23 16 01.7	+25 33 33	11.54	10.888 $\pm$ 0.032	
NGC 7674	F23254+0830	23 27 56.9	+08 46 46	11.50	10.215 $\pm$ 0.048	Arp 182 NED01, VV 343a, Mrk 0533, HCG 096A
IRAS F23365+3604	F23365+3604	23 39 01.7	+36 21 14	12.13	12.543 $\pm$ 0.098	
IRAS 23436+5257	23436+5257	23 46 05.8	+53 14 00	11.51	11.552 $\pm$ 0.039	

<sup>a</sup>“Total” photometry from 2MASS Extended Source Image Server v3.0 - <https://irsa.ipac.caltech.edu/applications/2MASS/PubGalPS/>. “The total” aperture consists of the isophotal aperture plus the integration of the surface brightness profile that extends from the isophotal aperture out to 4 disk scale lengths (i.e., well below the 1-sigma RMS noise level). With this curve of growth technique, an additional 10-20% of the galaxy flux is recovered (depending on the type of galaxy).” “The isophotal measurements are set at the 20 mag per arcsec2 isophote at Ks (corresponding to roughly 1-sigma of the background RMS), using both circular and elliptically shape-fit apertures.”

<sup>b</sup>Markarian galaxies, despite being selected for their blue optical colors, sometimes possess large infrared luminosities due to warm dust. This effect is explained in Arnus et al. (2009, §4.4) after investigations by Mazzarella & Balzano (1986); Izotov & Izotova (1989a,b); Xu & de Zotti (1989); and Mazzarella et al. (1991).

## 2.3 OBSERVATIONS AND RESULTS

The data presented in this paper were taken with the TripleSpec spectrographs at the Apache Pointe Observatory (APO) ARC 3.5m telescope and the Palomar Hale 200-inch telescope (Herter et al. 2008; Wilson et al. 2004). The APO and Palomar TripleSpec instruments have spectral resolutions of  $R \approx 3000$  and  $R \approx 2700$  respectively. Both instruments are sensitive over the wavelength range 0.9–2.4  $\mu\text{m}$ . We used a  $1 \times 40''$  slit for all observations.

These data represent a broad improvement over previous near-infrared spectral observations of interacting galaxies via a combination of greater spectral resolution ( $R \approx 3000$ ), broader bandwidth (0.9–2.4  $\mu\text{m}$  in one pointing; earlier instruments had to choose at best between  $J$ ,  $H$ , or  $K$  band for each pointing), and improved sensitivity (upper limits typically below  $1 \times 10^{-16}$  erg s $^{-1}$  cm $^{-2}$ ). By comparison, Larkin et al. (1998) observed with a resolution of  $R \approx 1000$ , bandwidths covering either 1.231–1.298  $\mu\text{m}$  or 2.07–2.24  $\mu\text{m}$ , and a noise floor giving upper limits of about  $1 \times 10^{-15}$  erg s $^{-1}$  cm $^{-2}$ .

For the majority of the galaxies, observations were obtained by nodding the galaxy nucleus (or pair of nuclei) along the slit in an ABBA pattern for up to 5 minutes per position. Subsequent sky subtraction was achieved by differencing each pair of A and B exposures. In some instances, when the extent of the host galaxy was too large, the slit was nodded to blank sky to obtain sky exposures. For each galaxy, spectral and photometric standards were observed for the purpose of telluric correction and photometric calibration – A0V and G/K standards (G/K standards: Oja 1991; Abt 2009; van Leeuwen 2007) were used for the APO and Palomar observations, respectively. An effort was made to choose standards which were close in airmass to each target. A summary of the observations is shown in Table 2.2.



Table 2.2. Observing Log

Date	Name	Exposure (minutes)	Aperture Width (arcseconds)	Observers
2008 August 20	NGC 6670	25	6	A.O. Petric
	NGC 6786 (S)	25	5	A.O. Petric
	II Zw 096 (N)	15	5	A.O. Petric
	IRAS 23436+5257	20	3	A.O. Petric
	UGC 02369 (N)	15	N/A	A.O. Petric
	UGC 02369 (S)	25	2.4	A.O. Petric
2008 August 21	IRAS 18090+0130 (E)	20	3	A.O. Petric
	IRAS 18090+0130 (bright)	20	5	A.O. Petric
	IRAS 19542+1110	10	3.4	A.O. Petric
	IRAS F19297-0406	20	4.2	A.O. Petric
	IRAS 21101+5810	20	3.6	A.O. Petric
	IC 5298	20	3.6	A.O. Petric
	IRAS F23365+3604	20	3.6	A.O. Petric
	NGC 7674	20	3	A.O. Petric
	UGC 04881	10	4.4	A.O. Petric
2009 May 24	NGC 5331 (N)	20	5	A.O. Petric
	NGC 5331 (S)	25	3	A.O. Petric
	UGC 08739	30	3.6	A.O. Petric
	VV 340 N	35	6	A.O. Petric
	NGC 6701	50	5.2	A.O. Petric
	NGC 3221	15	6	A.O. Petric
2009 May 25	NGC 5936	20	4	A.O. Petric
	VV 705	20	3	A.O. Petric
	IRAS 20351+2521	10	4	A.O. Petric
	CGCG 247-020	35	6.6	A.O. Petric
2010 July 23	Mrk 273	30	7.5	A.O. Petric
	NGC 6090	35	4	A.O. Petric
	IRAS F17132+5313	20	4	A.O. Petric
	IRAS 21101+5810 (B)	20	5	A.O. Petric
	NGC 5104	25	8	A.O. Petric
2010 July 24	UGC 12150	25	3.4	A.O. Petric
	IRAS F22491-1808	20	7.4	A.O. Petric
	MCG -02-01-051	15	3.2	A.O. Petric
	IRAS F14348-1447	25	3	A.O. Petric
2010 July 25	NGC 5256	35	4	A.O. Petric
	IRAS F15250+3608	25	5	A.O. Petric
	NGC 7469	3	6	A.O. Petric
	VV 250a	40	8	H.J. Borish
2012 February 10	VV 250b	20	6	H.J. Borish
2012 May 28	MCG-02-33-098	30	7	H.J. Borish
	NGC 5653	20	6	H.J. Borish
	CGCG 049-057	35	6	H.J. Borish

Table 2.2—Continued

Date	Name	Exposure (minutes)	Aperture Width (arcseconds)	Observers
2012 October 2	NGC 1275	40	2.6	H.J. Borish, K.M. Jones
2013 January 25	VV 340 S	80	3.6	H.J. Borish
	UGC 05101	80	4	H.J. Borish
	CGCG 043-099	80	4	H.J. Borish
	IC 0883	40	3	H.J. Borish
2013 February 24	NGC 4922	30	3	H.J. Borish
	IC 0883	50	6	H.J. Borish

Note. — The value listed in the “exposure” column refers to the total exposure time for each object.

The galaxies VV 705 and IC 883 were each observed twice. The second observation of VV 705 suffered from very poor telluric correction due to a poor choice of a standard star. Therefore, the second observation of VV 705 is excluded here. For IC 883, each observations was of high quality – both are included here to illustrate the systematic uncertainty inherent in observations with the TripleSpec systems.

All spectra were extracted with a modified version of the IDL utility *SpexTool* (Cushing et al. 2004). Extraction apertures are based on the extent of the nuclear light along the slit and range from  $3 - 8''$ . At the range of distances occupied by the galaxies in our sample, these aperture sizes correspond to a physical scales of  $1.3 - 12$  kpc. Sources for which multiple apertures were extracted are shown in imaging from the 2MASS survey (Skrutskie et al. 2006) in Figure 2.1. These images give a schematic representation of the sky locations of each aperture within each LIRG. Triplespec has a nominal spatial resolution of  $1''$ . Although the 2MASS images are few times worse than this, the author believes the lower spatial resolution mimics the level of certainty an observer on a turbulent night might expect when observing with TripleSpec in boresight guiding mode. Data from APO TripleSpec were telluric corrected and calibrated using the *SpexTool* utility. Data taken with Palomar TripleSpec were telluric corrected and calibrated using the author’s own IDL code.

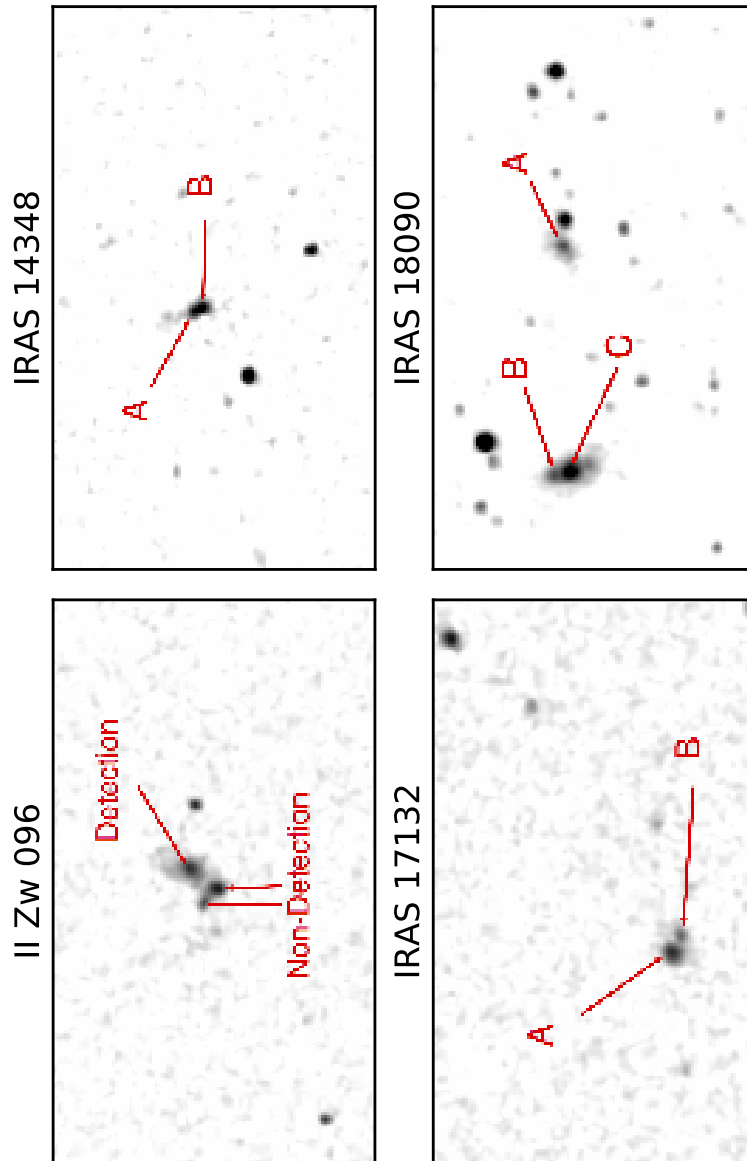


Fig. 2.1.— Extraction aperture locations for sources with multiple apertures. North is up and East is to the left. Images are roughly  $1.77' \times 3.14'$ .

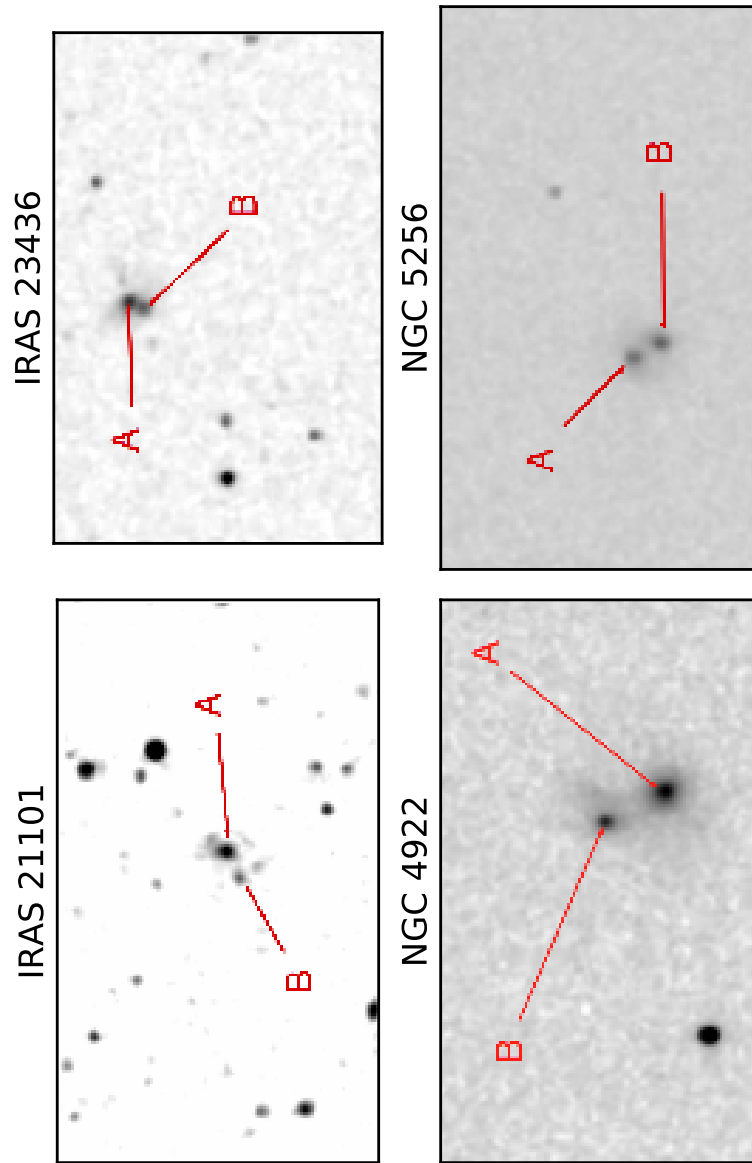


Fig. 2.1.— Extraction aperture locations for sources with multiple apertures. North is up and East is to the left. Images are roughly  $1.77' \times 3.14'$ .

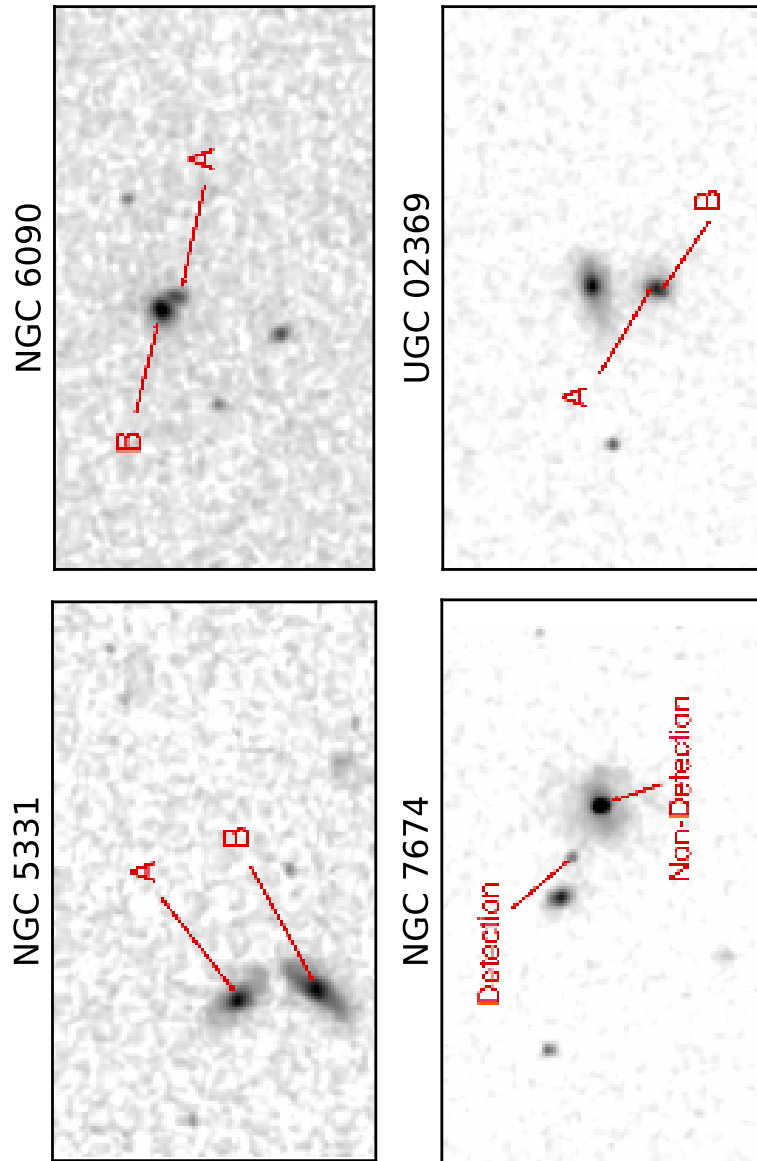


Fig. 2.1.— Extraction aperture locations for sources with multiple apertures. North is up and East is to the left. Images are roughly  $1.77' \times 3.14'$ .

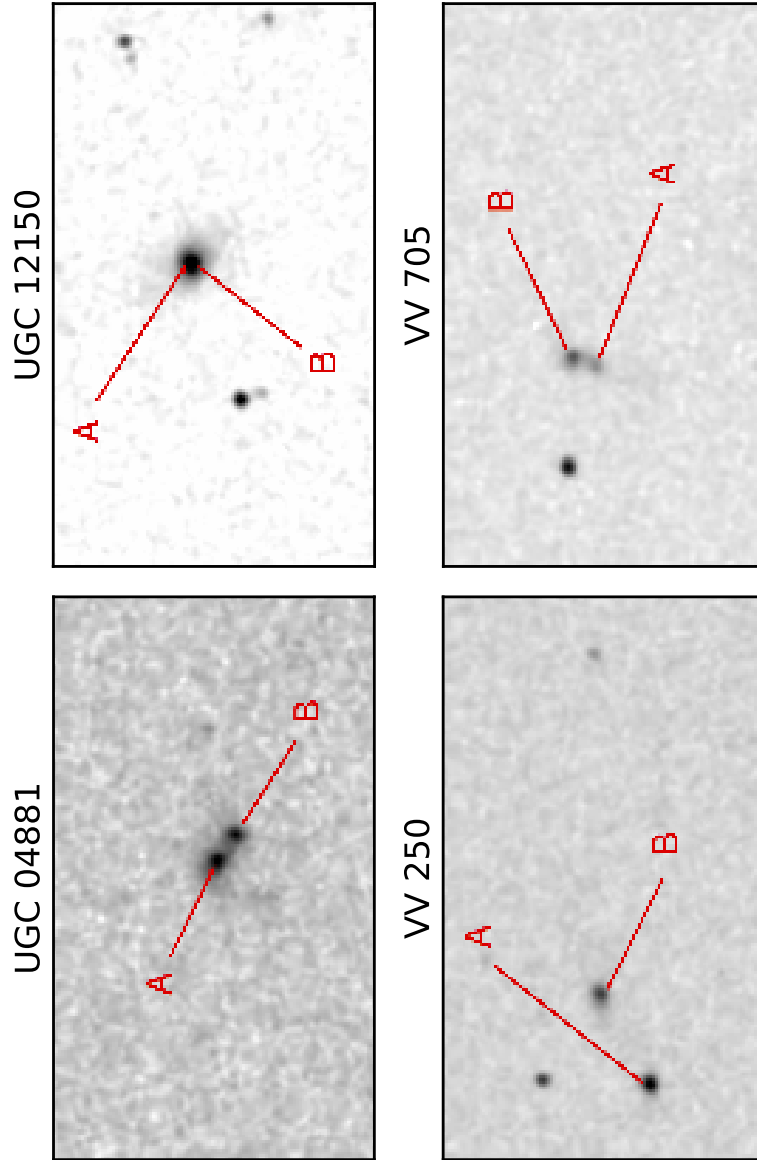


Fig. 2.1.— Extraction aperture locations for sources with multiple apertures. North is up and East is to the left. Images are roughly  $1.77' \times 3.14'$ .

Table 2.3. Features of Interest

Rest $\lambda$ $\mu\text{m}$	Name	Emission/Absorption
0.9532	[S III]	emission
0.9852	C I	emission
1.0049	Pa $\delta$	emission
1.0831	He I	emission
1.0938	Pa $\gamma$	emission
1.2570	[Fe II]	emission
1.2818	Pa $\beta$	emission
1.5557	Br 12	absorption
1.5582	CO 3-0	absorption
1.5702	Br 11	absorption
1.5780	CO 4-1	absorption
1.5881	Br 10	absorption
1.5982	CO 5-2	absorption
1.6110	Br 9	absorption
1.6187	CO 6-3	absorption
1.6397	CO 7-4	absorption
1.6408	Br 8	absorption
1.6440	[Fe II]	emission
1.6610	CO 8-5	absorption
1.6807	Br 7	absorption
1.8751	Pa $\alpha$	emission
1.9450	Br $\delta$	emission
1.9570	H <sub>2</sub> S(3)1-0	emission
2.0338	H <sub>2</sub> S(2)1-0	emission
2.0580	He I	emission
2.0735	H <sub>2</sub> S(3)2-1	emission
2.1213	H <sub>2</sub> S(1)1-0	emission
2.1655	Br $\gamma$	emission
2.2235	H <sub>2</sub> S(0)1-0	emission
2.2477	H <sub>2</sub> S(1)2-1	emission
2.2935	CO 2-0	absorption
2.3227	CO 3-1	absorption
2.3535	CO 4-2	absorption
2.3829	CO 5-3	absorption



The fully reduced spectra, uncorrected for redshift or extinction, are displayed in Figure 2.2. In this figure, both line detections and upper limits are labeled. Tables 2.5, 2.6, 2.7, and 2.8 are summaries of the values/uncertainties of line strength uncorrected for extinction and full line width at half peak of all detected non-molecular emission lines as well as the strongest ro-vibrational  $\text{H}_2$  line, S(1) 1-0 at wavelength  $\lambda 2.1213 \mu\text{m}$ . In these tables, a missing line strength implies that the corresponding value of uncertainty may be interpreted as an upper limit. The uncertainties/upper limits were estimated by finding the RMS of the flux density about a linear baseline fit to the continuum from  $1000 \text{ km s}^{-1}$  to  $3000 \text{ km s}^{-1}$  away from the line center and multiplying by the width of the line divided by the square root of the number of channels within the line. The coronal line [Si VI]  $\lambda 1.962 \mu\text{m}$ , which is of some importance in signifying AGN activity is not detected in any of the spectra presented here. It lies  $0.004 \mu\text{m}$  to the red of the  $\text{H}_2$  S(3) 1-0 line at  $1.958 \mu\text{m}$ . Due to the general absence of the coronal line and its proximity to the  $\text{H}_2$  we have omitted its label in these plots. The spectra of MCG -02-33-098, VV 250W, NGC 5653, CGCG 049-057, IRAS 18090+0130 C, and II Zw 096 suffer from particularly bad night sky line contamination due to poor background subtraction. For the most part, the sky lines are narrow and do not affect the determination of line strength. The spectrum of NGC 5104 is affected by a less than perfect telluric correction, a fact manifested in the curved shape of the continuum in the first and last orders. Due to the relatively narrow line widths, this should not have much of an effect on the calculation of line strengths.

Upon close inspection, several spectra give the appearance of faint emission lines at wavelengths having no clear line-identification. A tabulation of these features appears in Table 2.4.

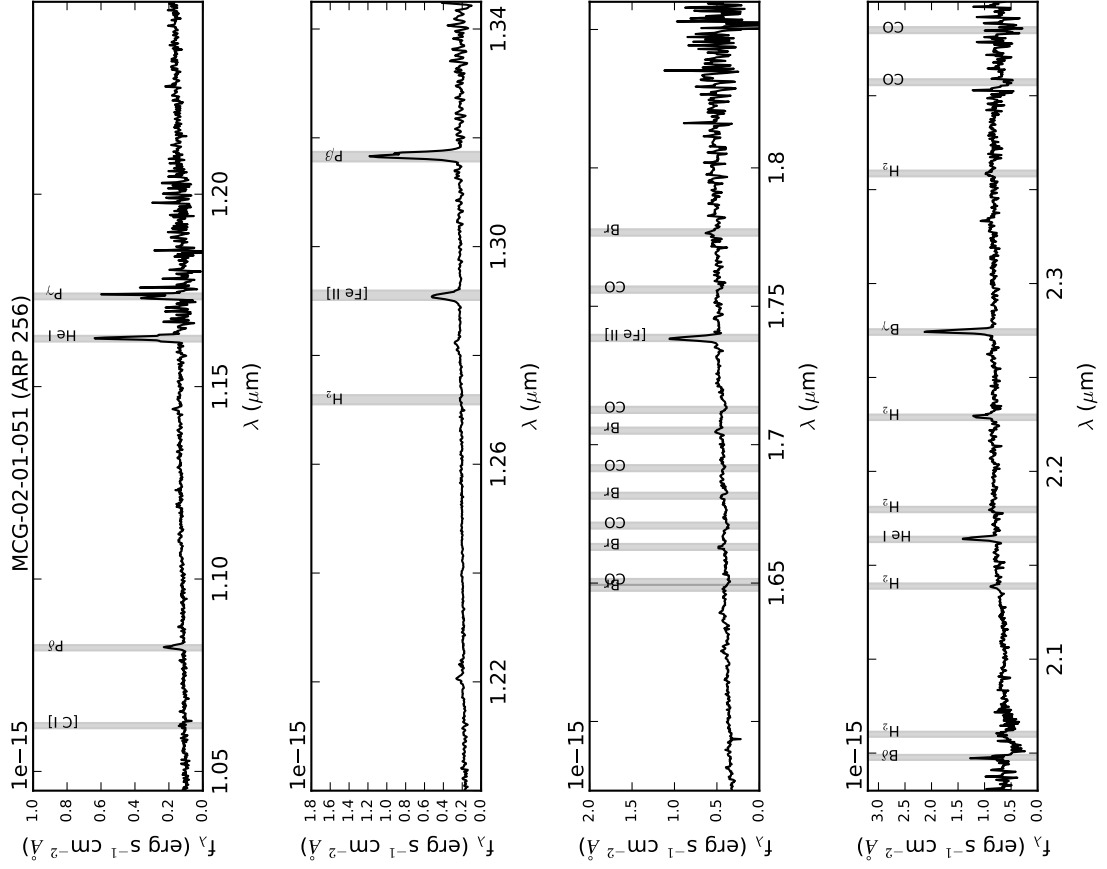


Fig. 2.2.— [Si VI] line would appear at 1.962  $\mu\text{m}$  rest frame, this is 0.004  $\mu\text{m}$  to the red of the H<sub>2</sub> S(3) 1-0 line at 1.958  $\mu\text{m}$ . Due to the general absence of the coronal line and its proximity to the H<sub>2</sub> line we have omitted its label in these plots.

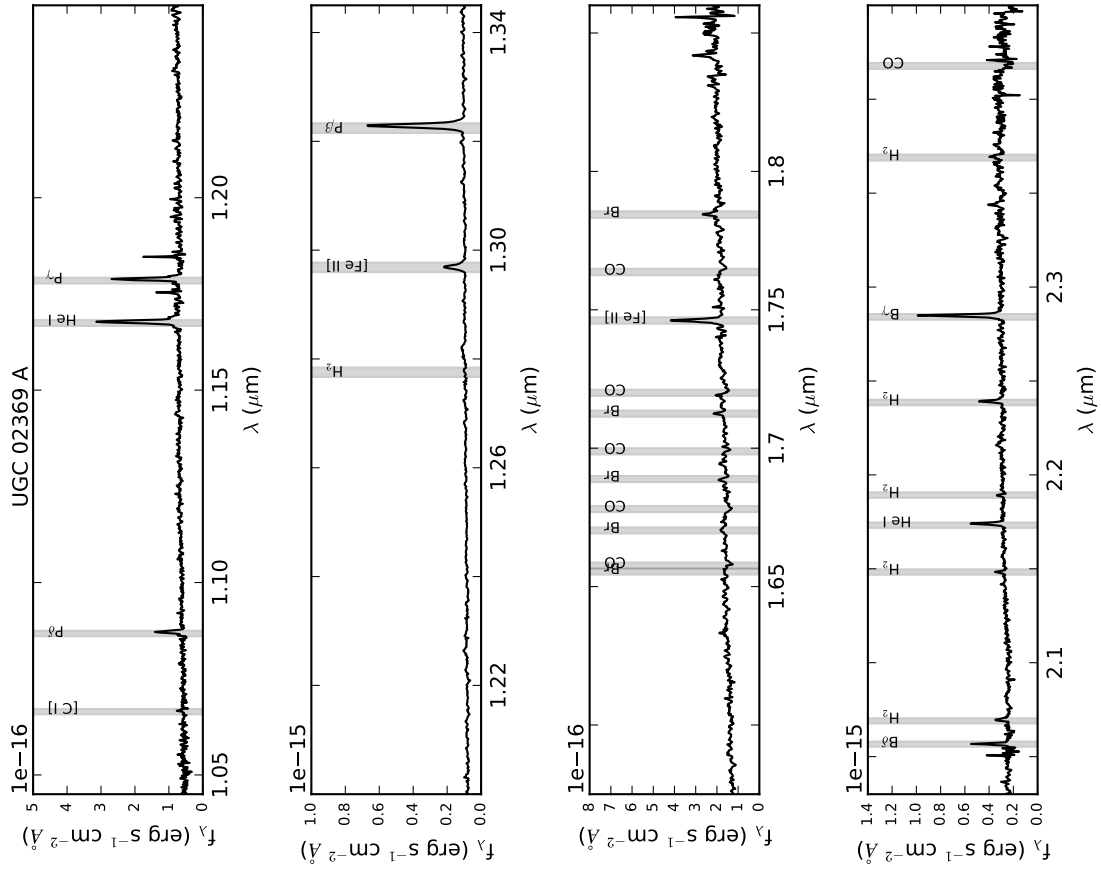


Fig. 2.2.—

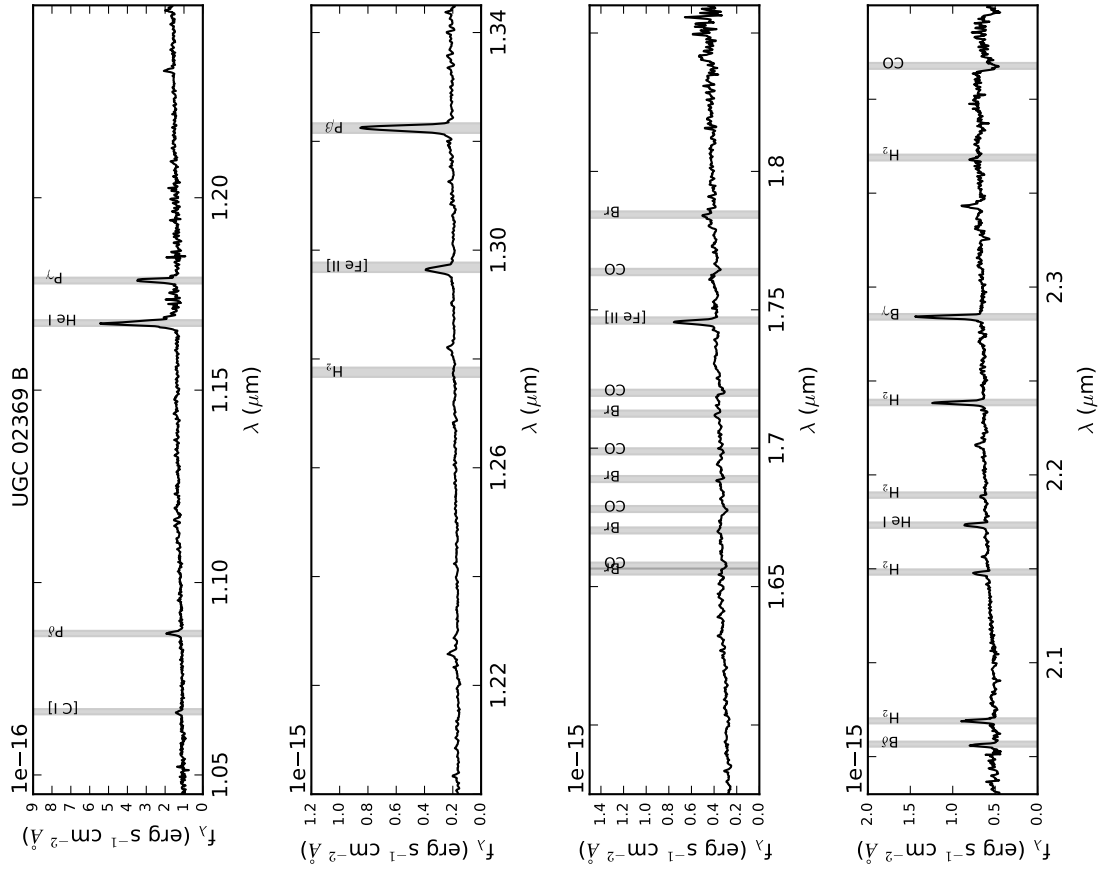


Fig. 2.2.—

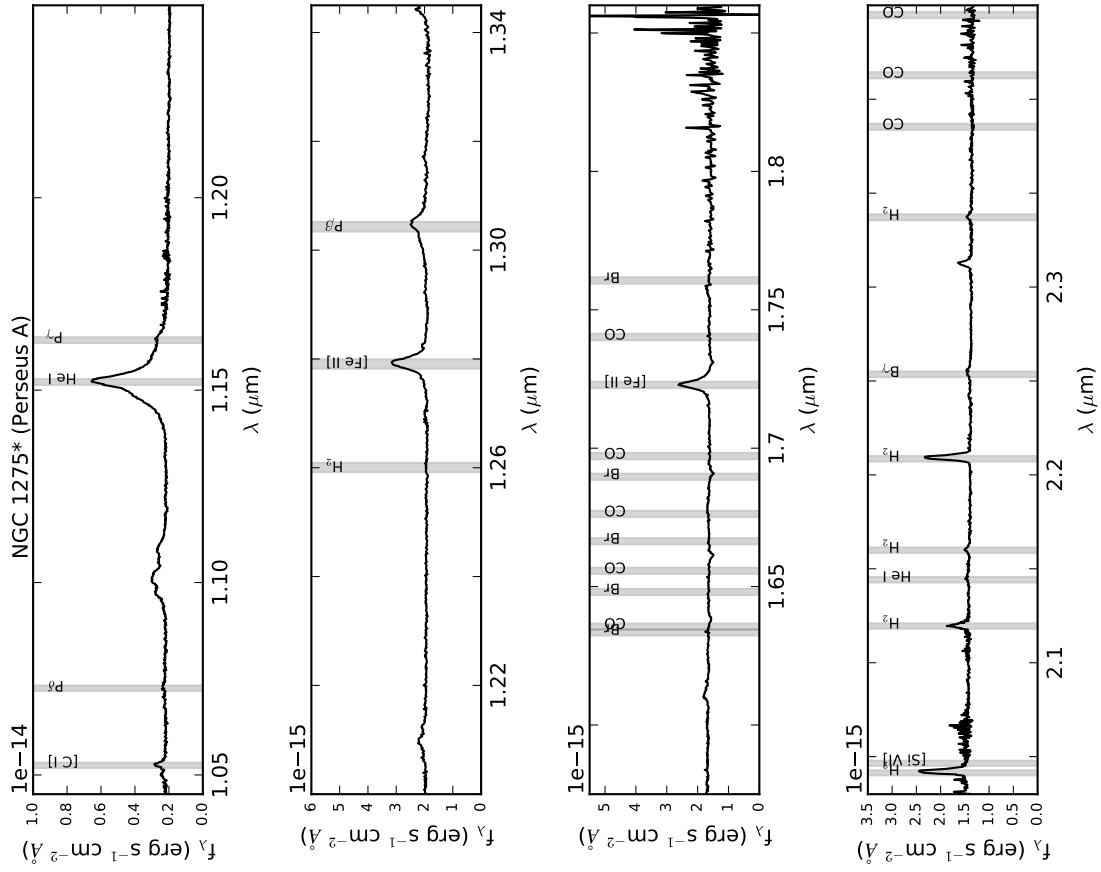


Fig. 2.2.—

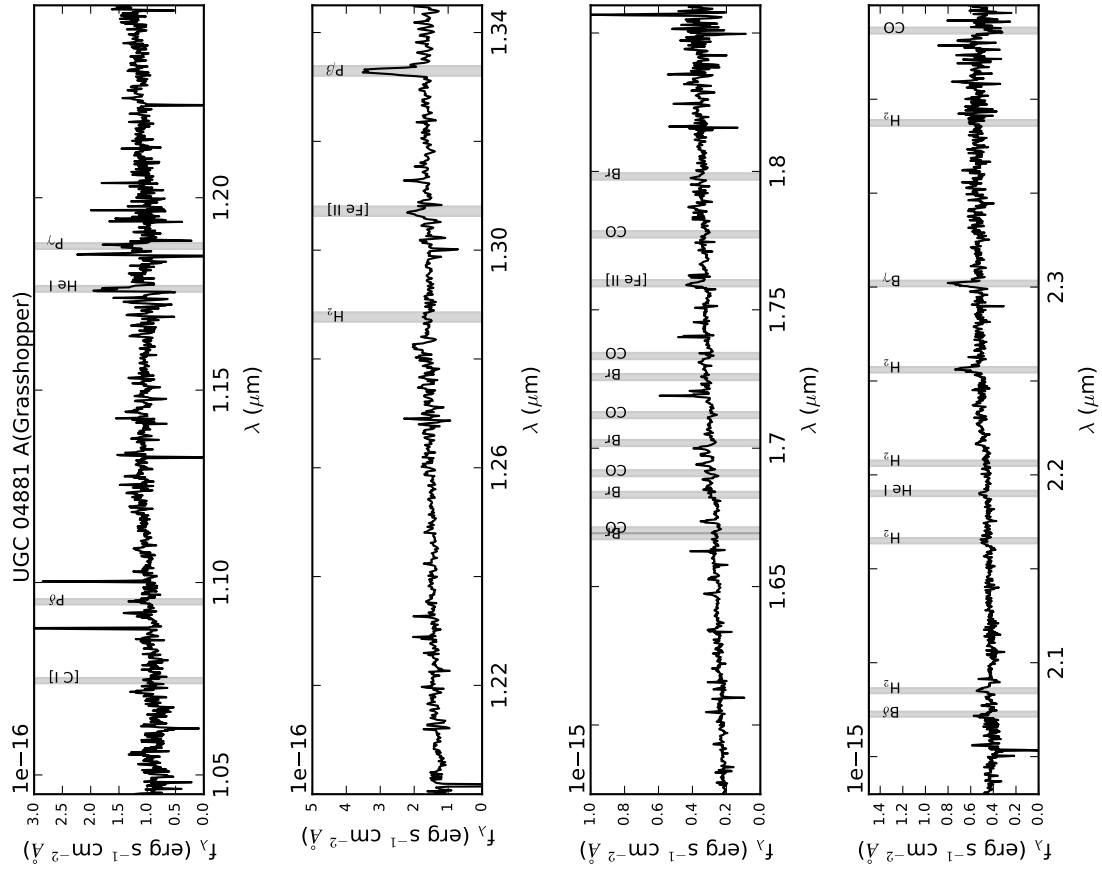
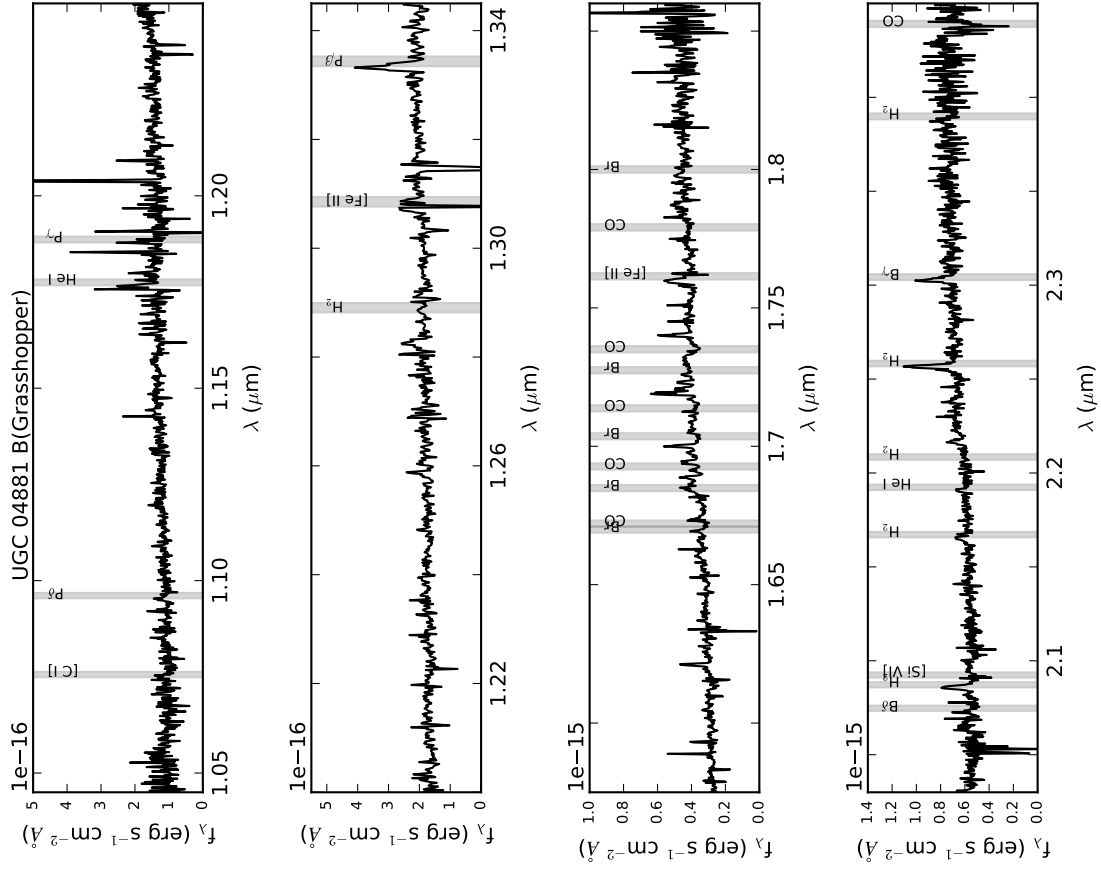


Fig. 2.2.—







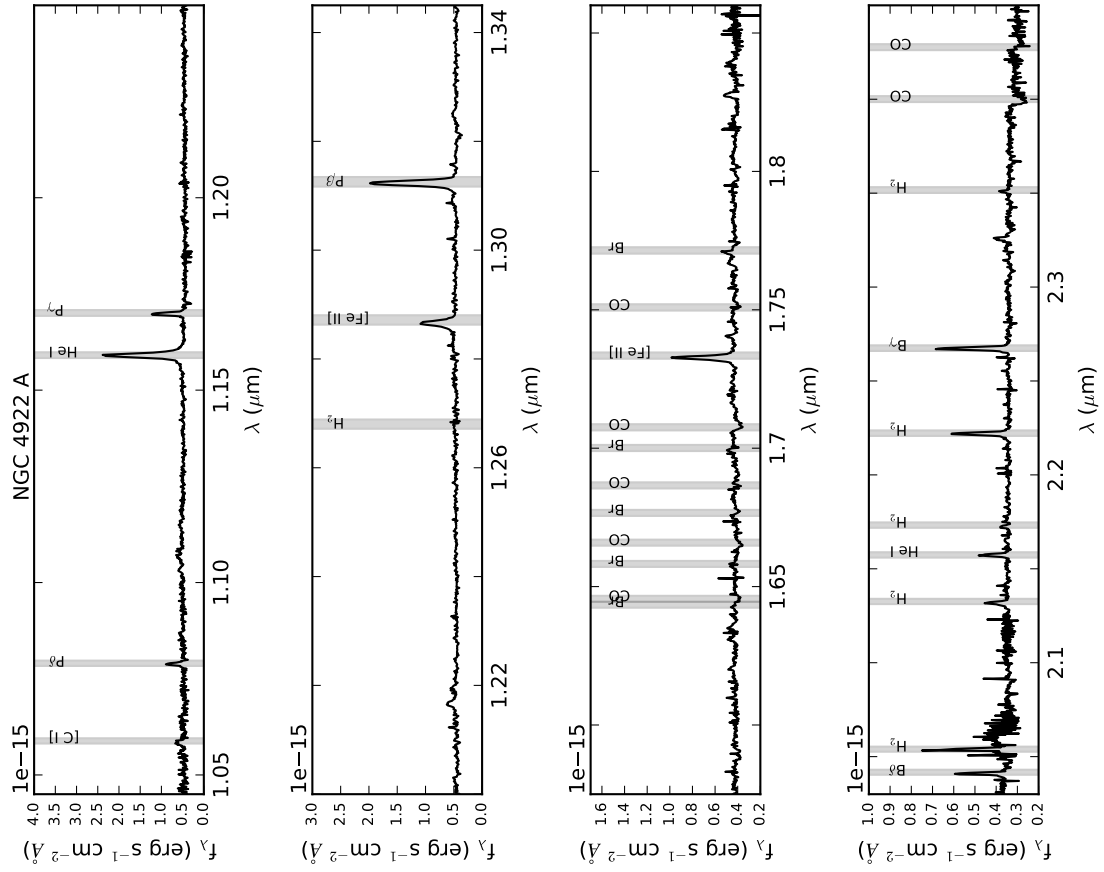


Fig. 2.2.—

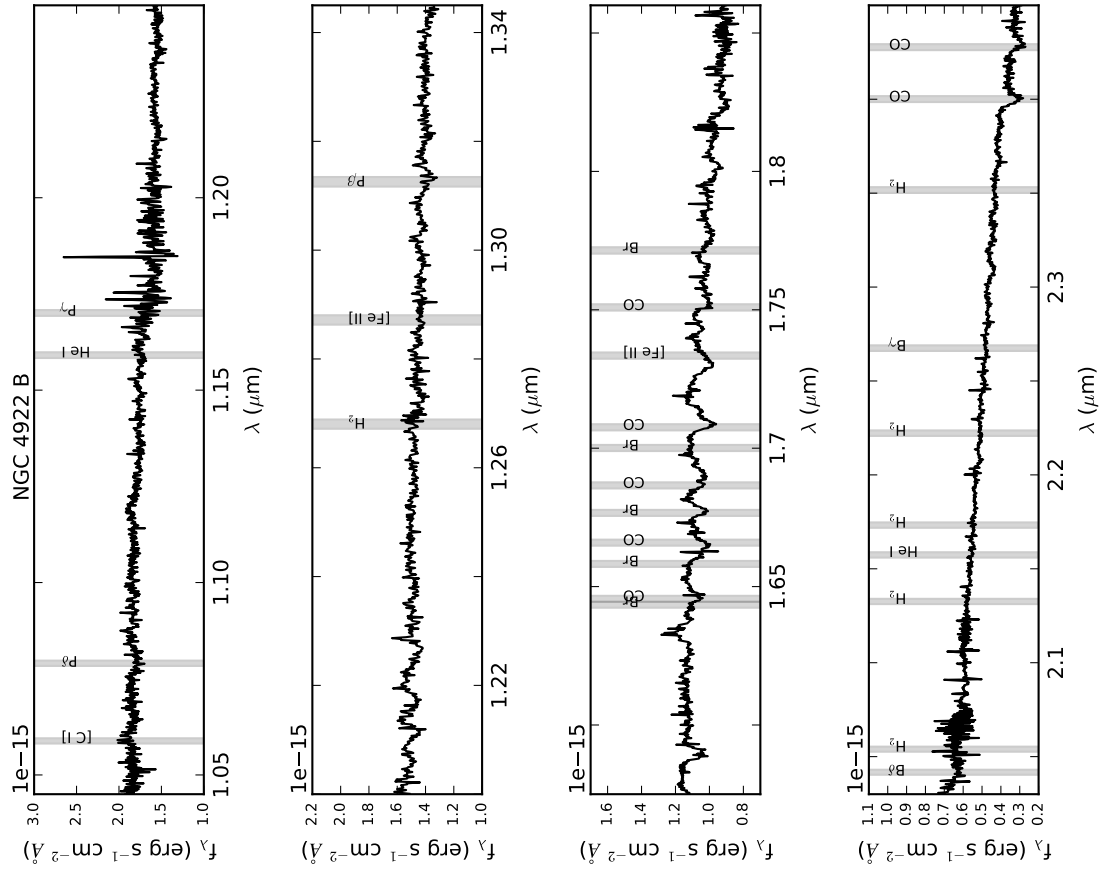


Fig. 2.2.—



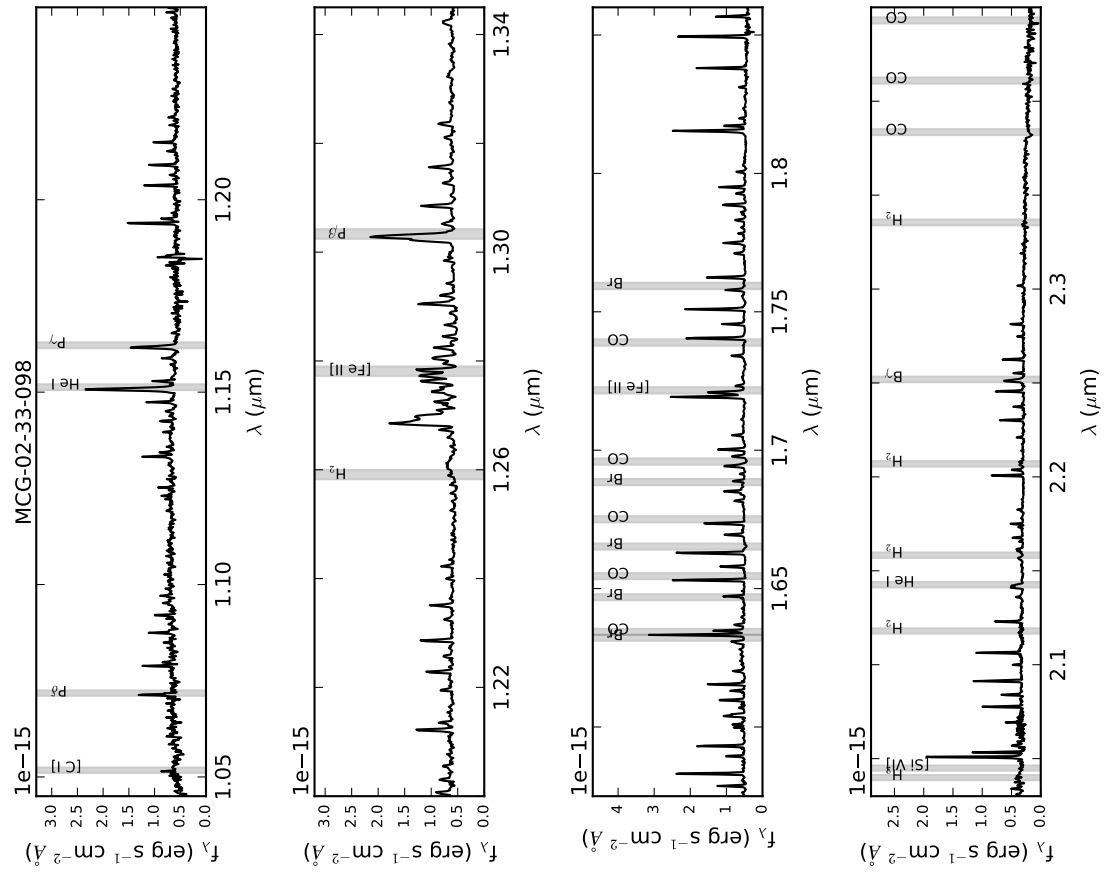


Fig. 2.-1.—

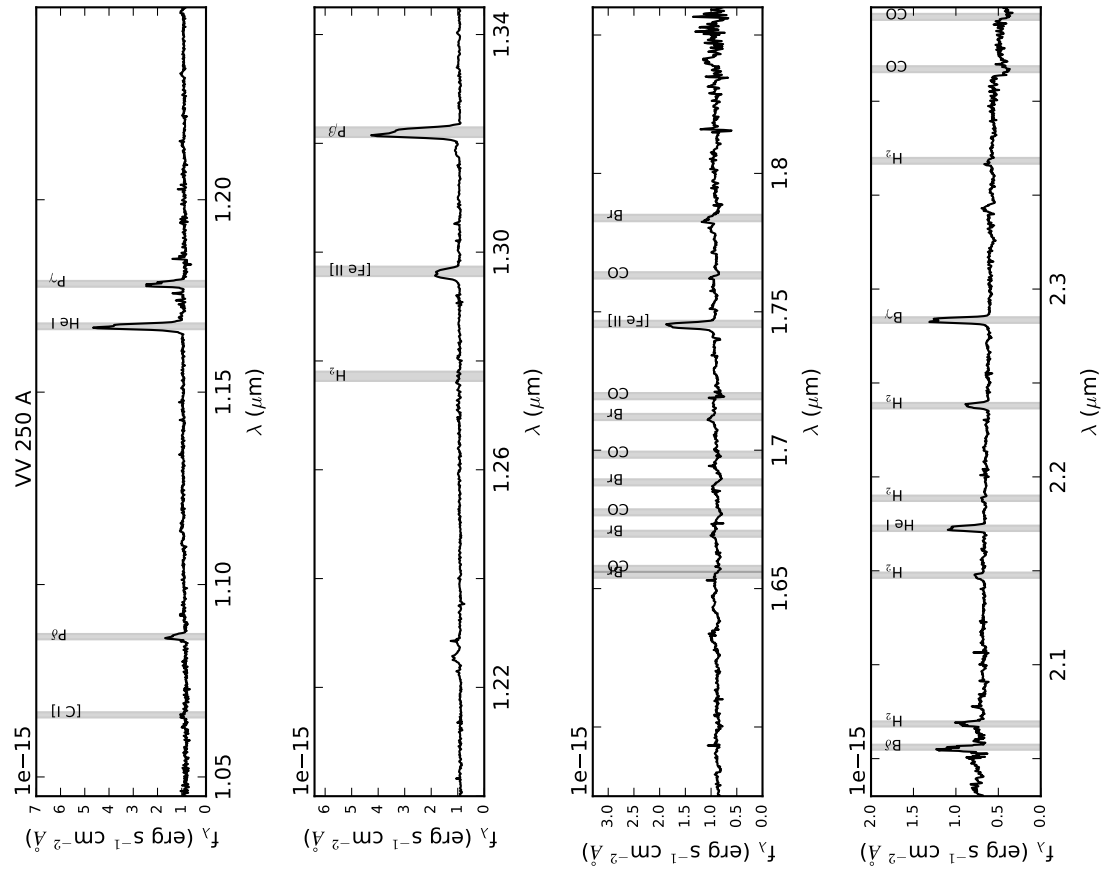


Fig. 2.-1.—

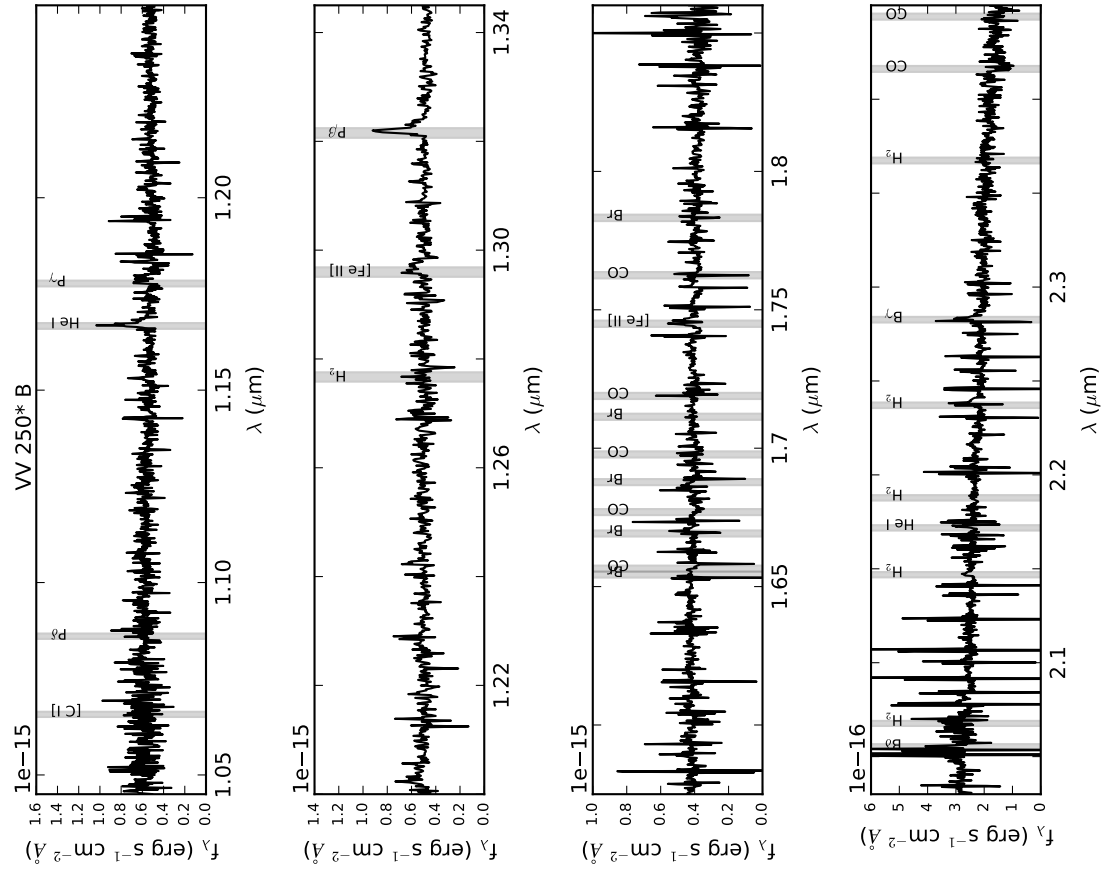


Fig. 2.-1.—

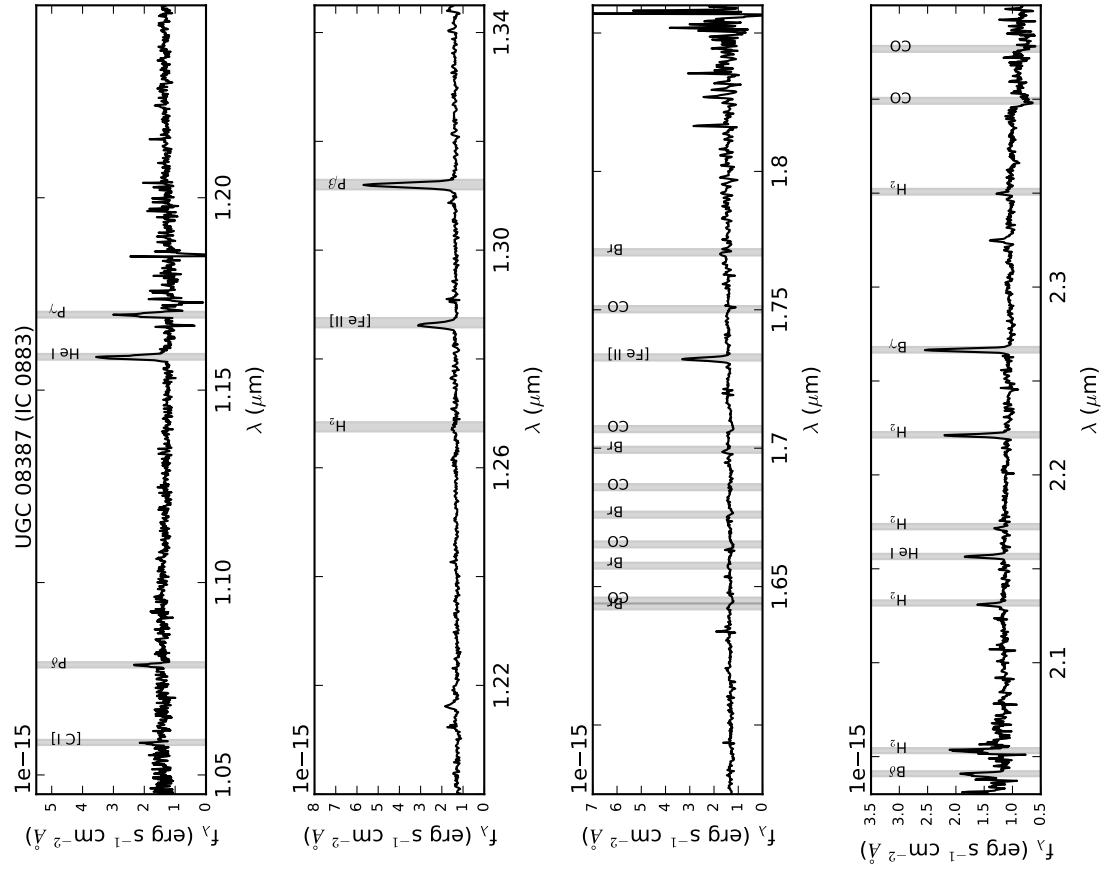


Fig. 2.-1.—

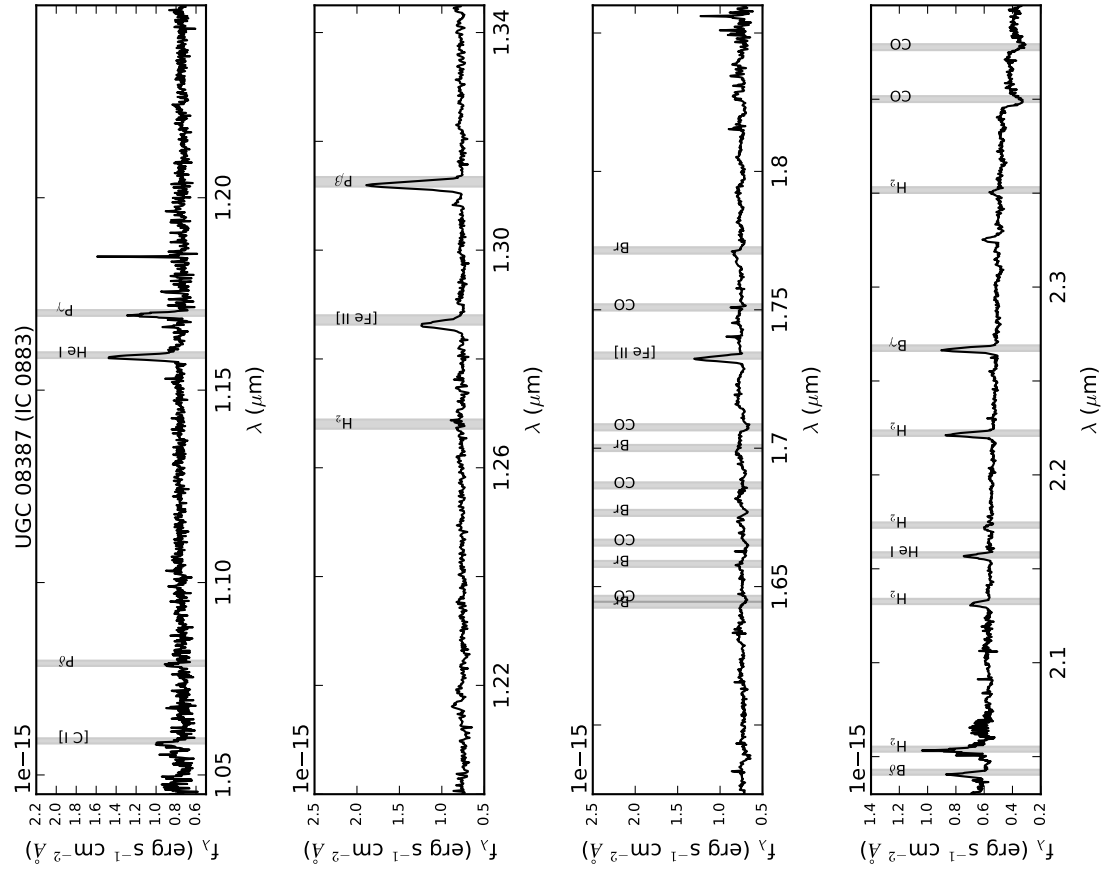


Fig. 2.-1.—



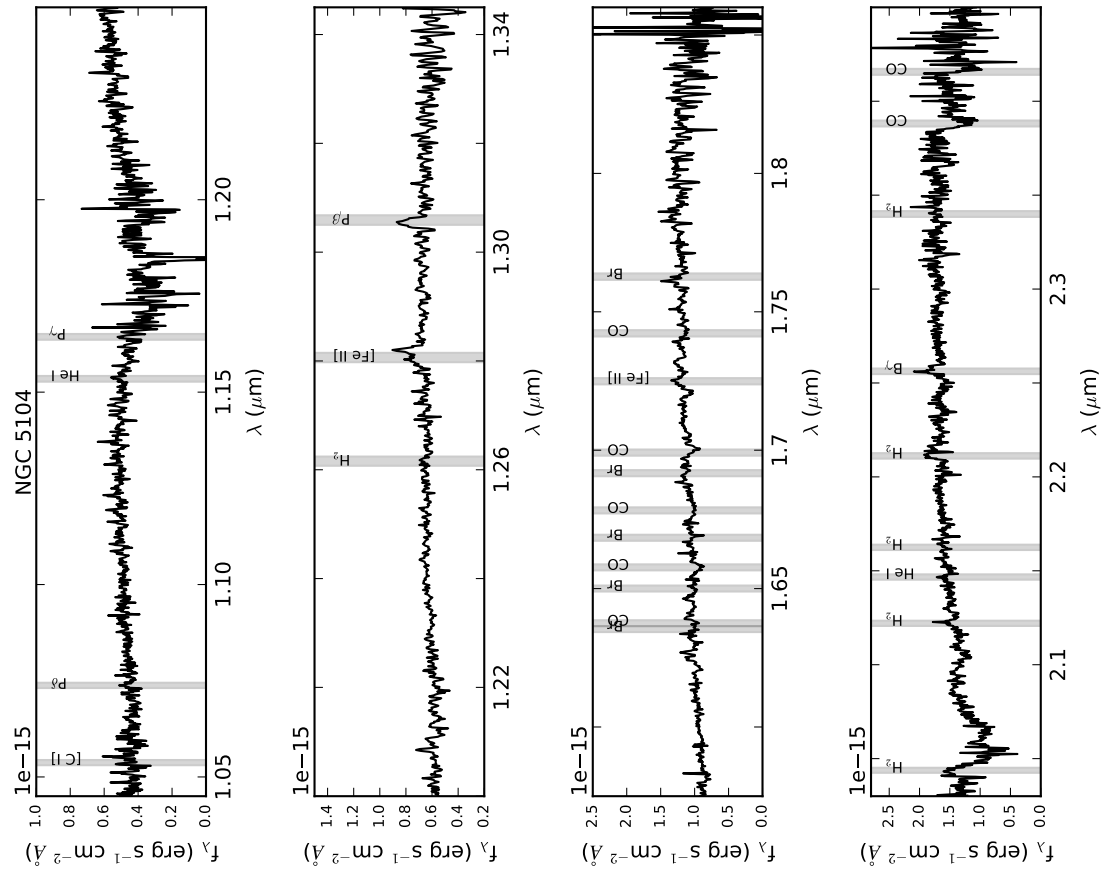


Fig. 2.-1.—

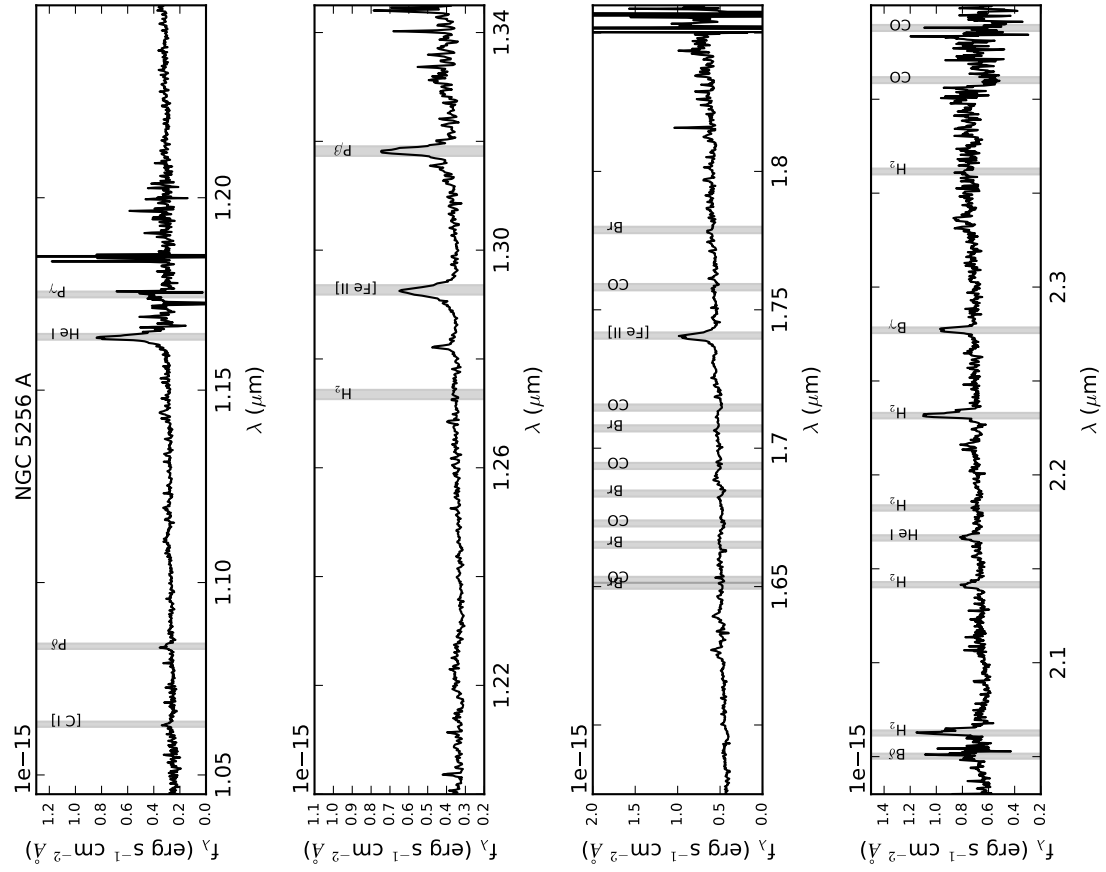


Fig. 2.-1.—



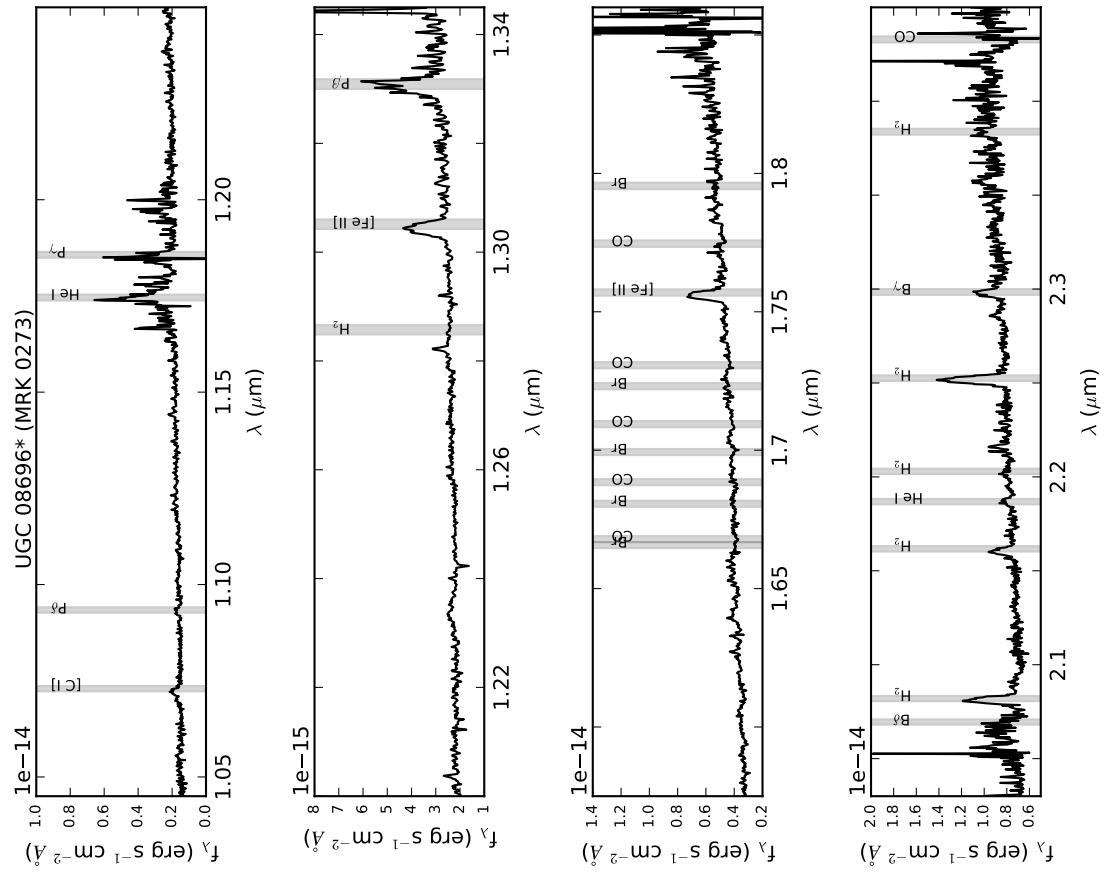


Fig. 2.-1.—

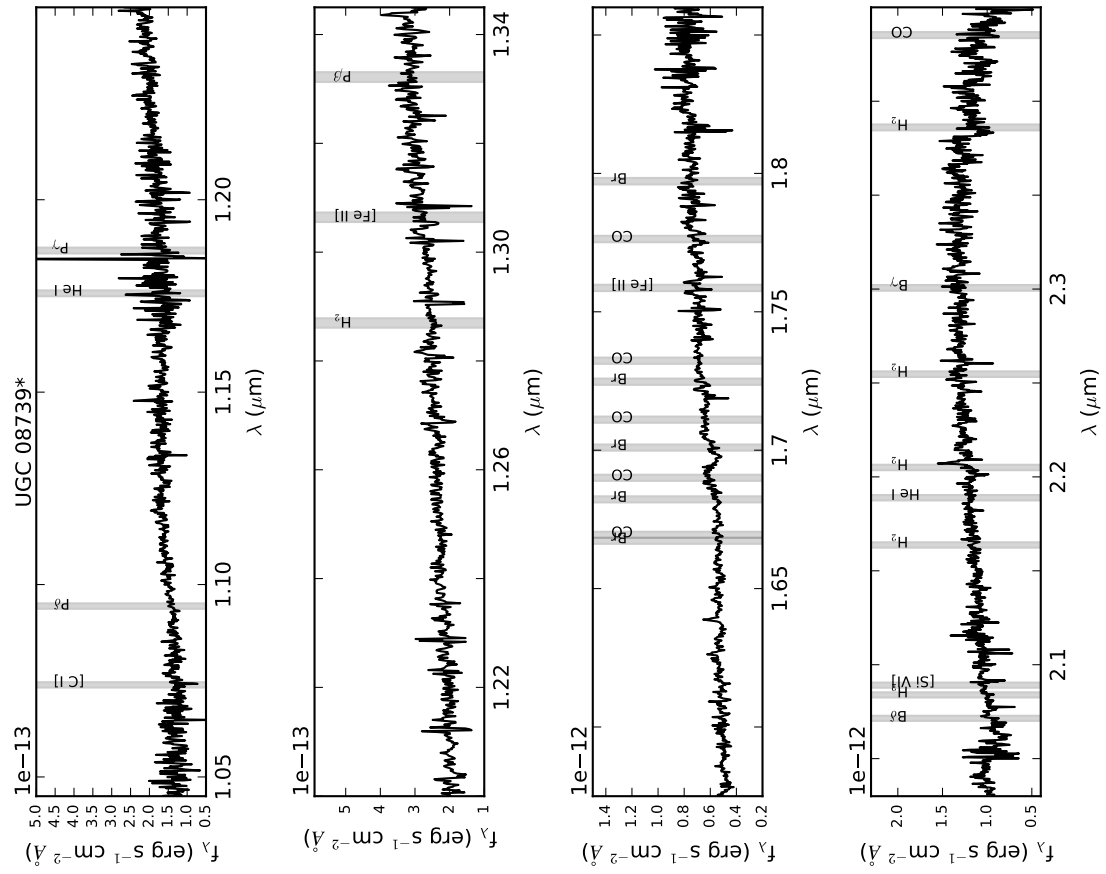


Fig. 2.-1.—

Fig. 2.-1.—

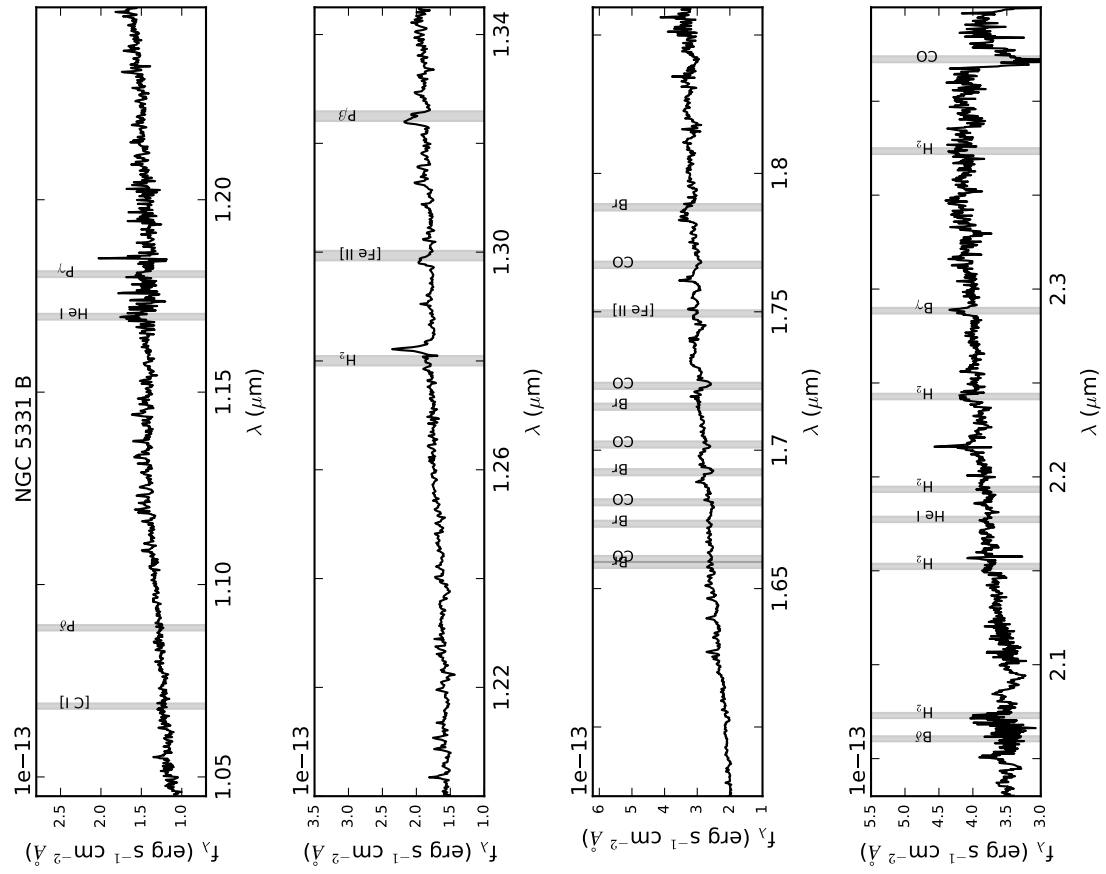


Fig. 2.-1.—

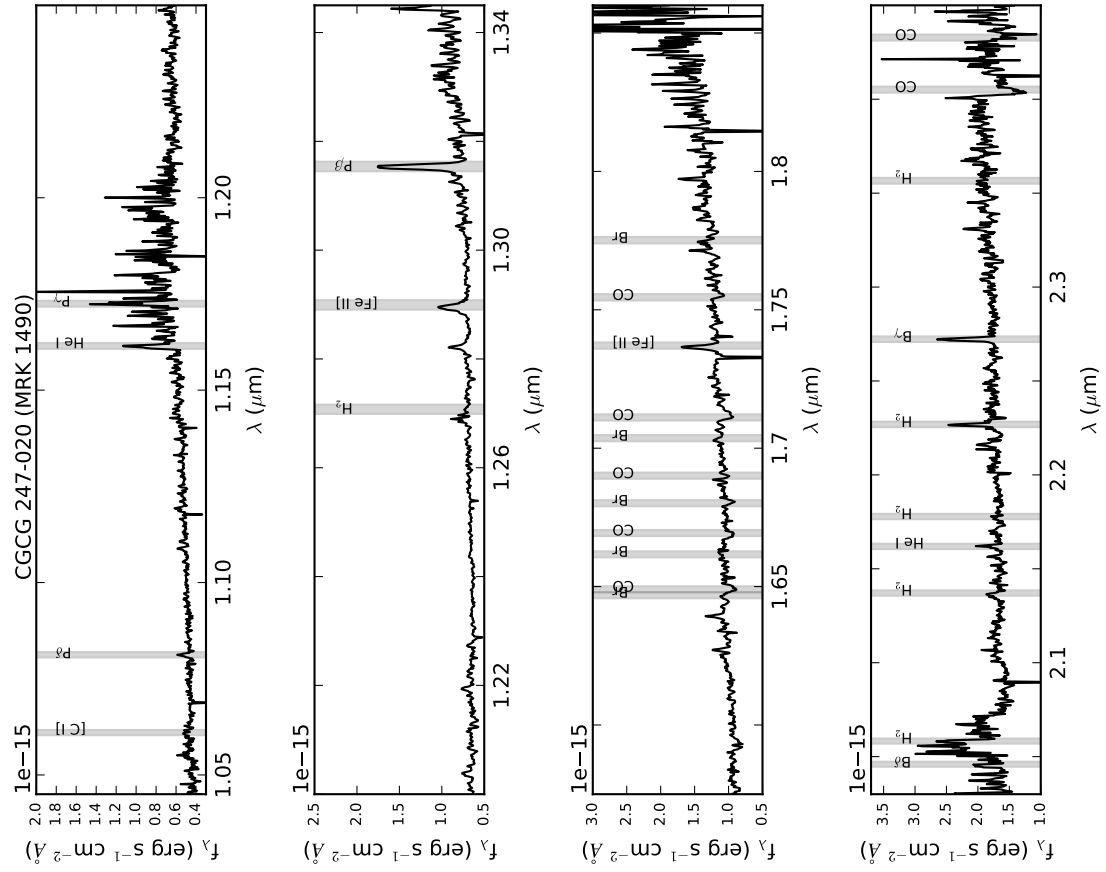


Fig. 2.-1.—



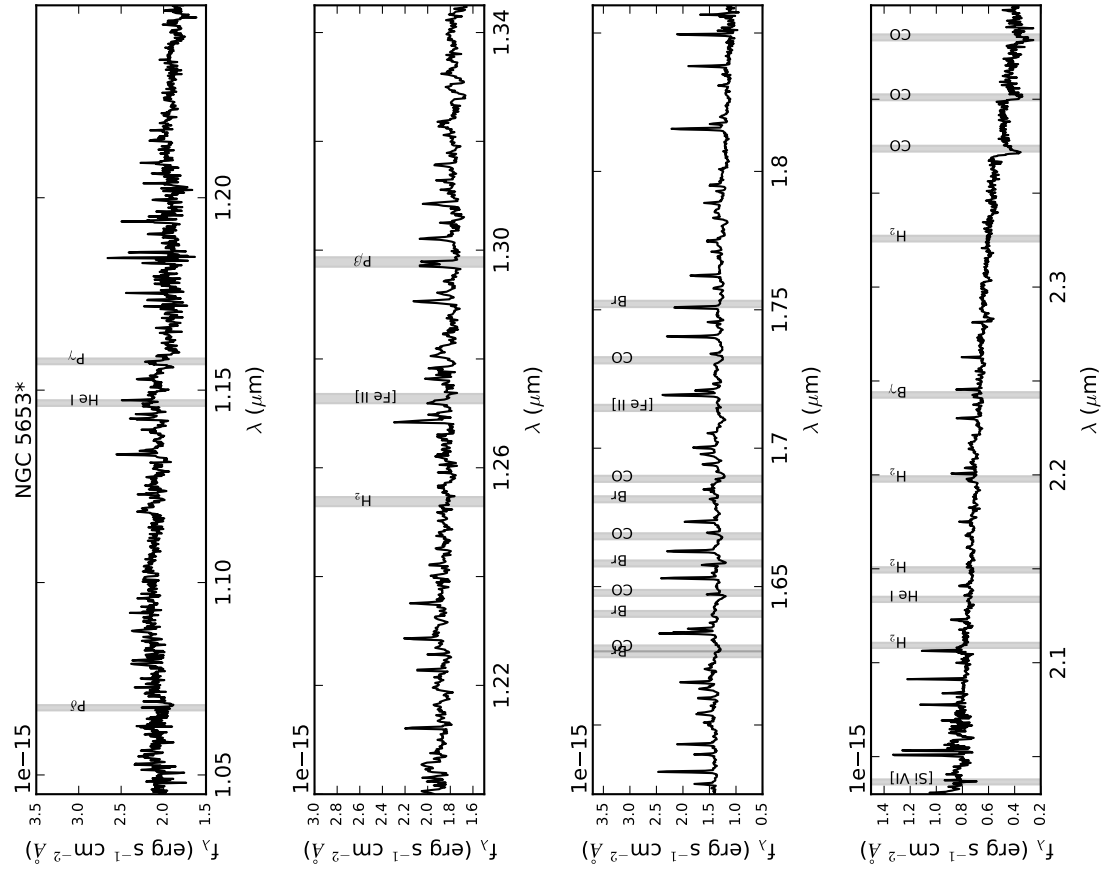


Fig. 2.-1.—

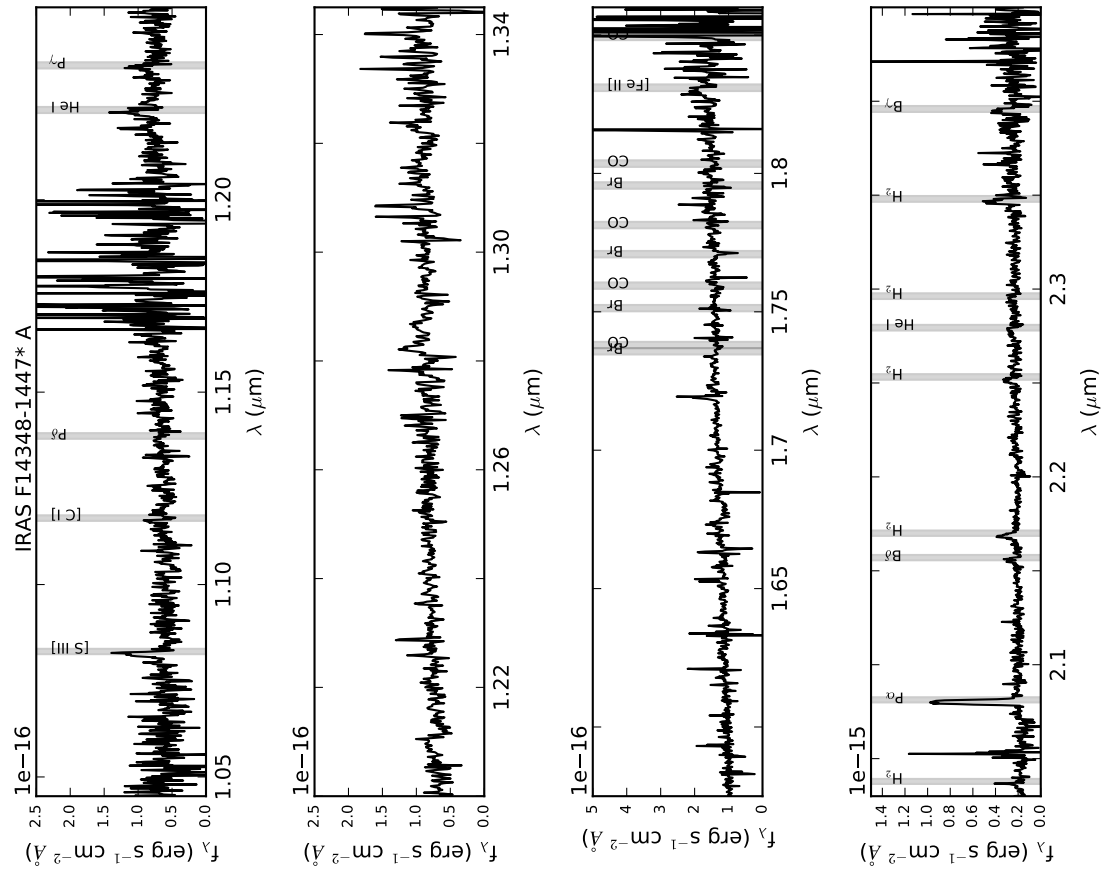


Fig. 2.-1.—

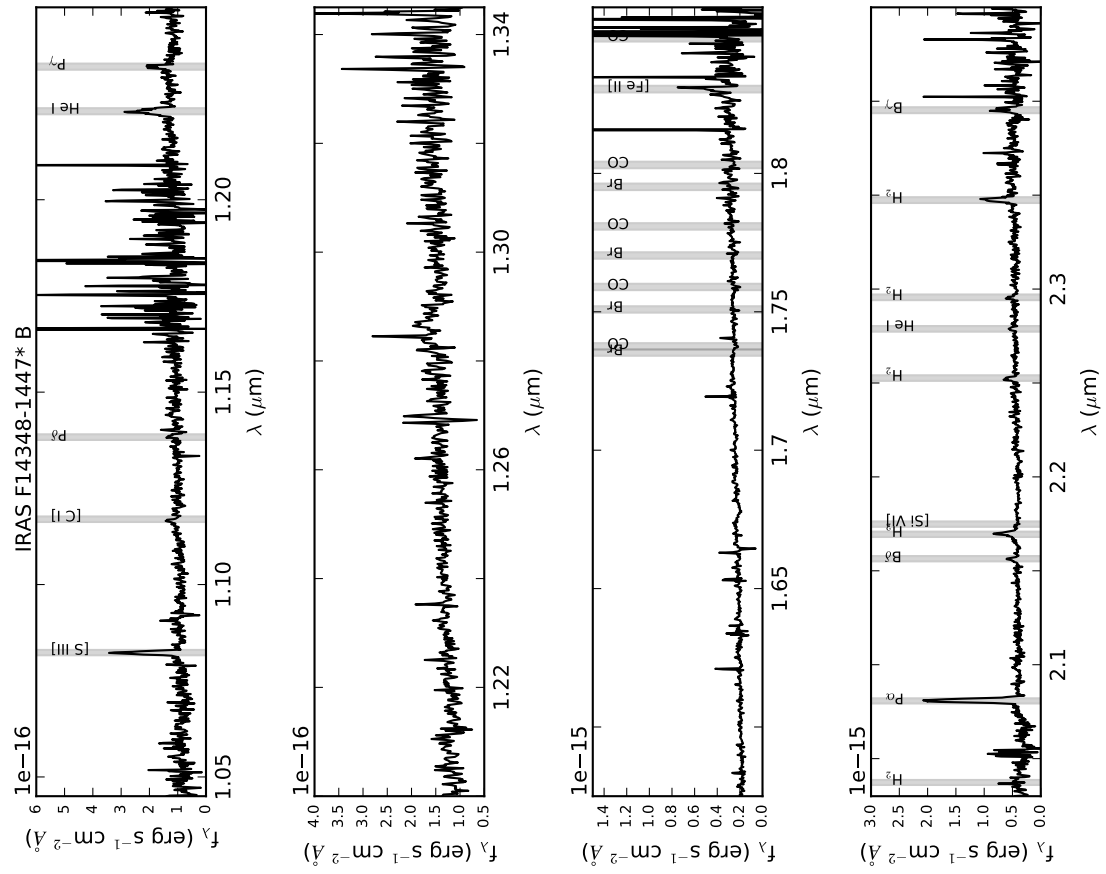


Fig. 2.-1.—

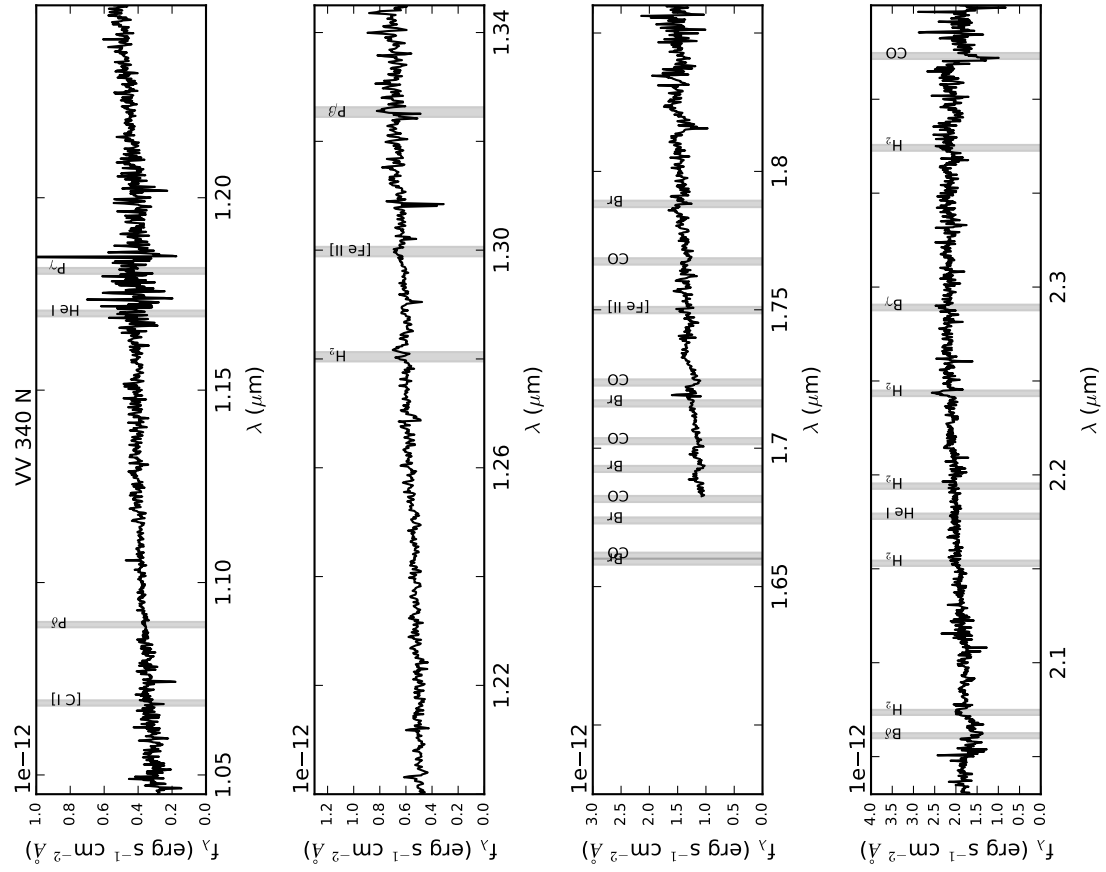


Fig. 2.-1.—

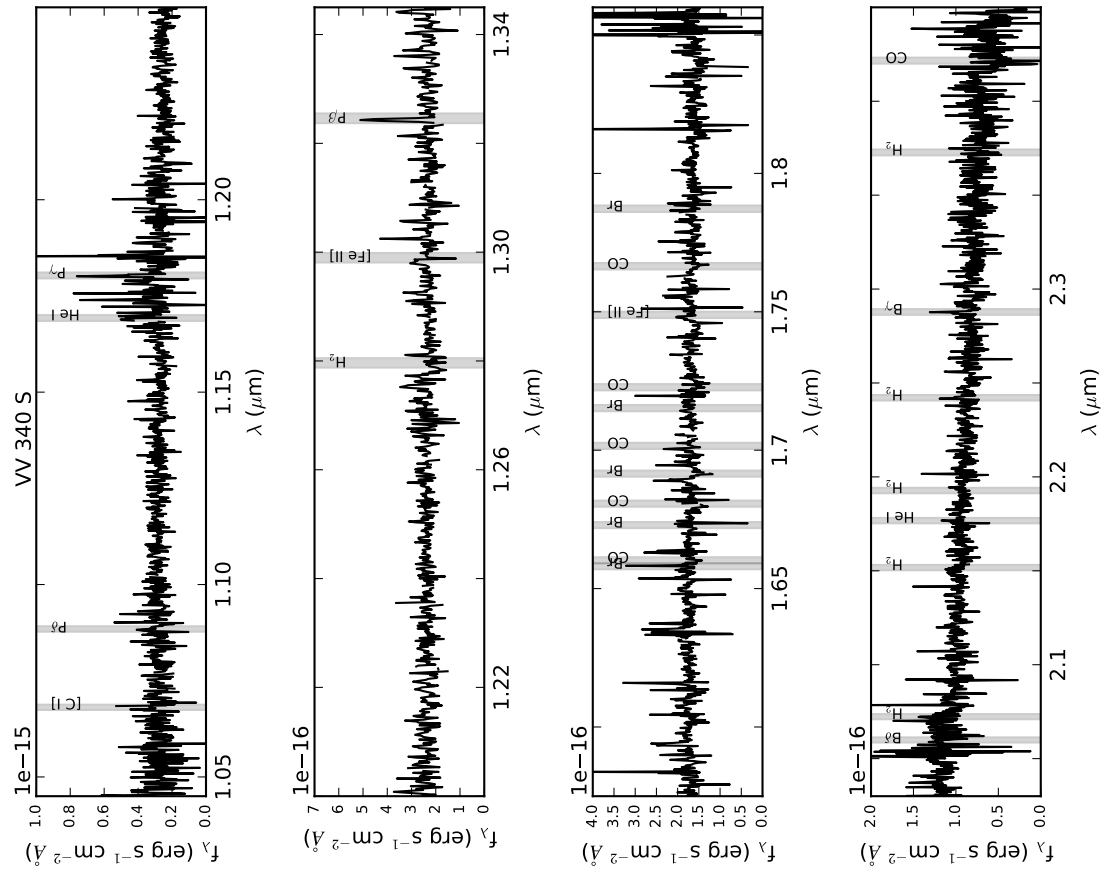


Fig. 2.-1.—

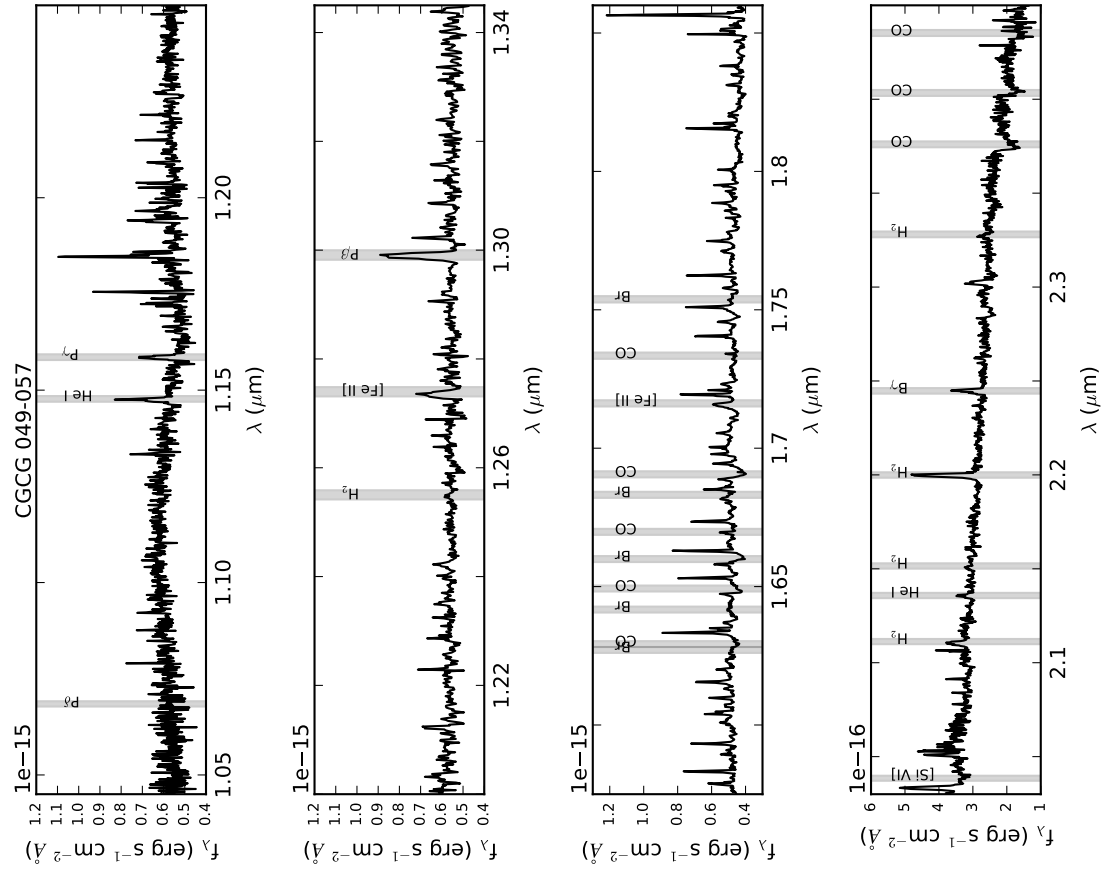


Fig. 2.-1.—

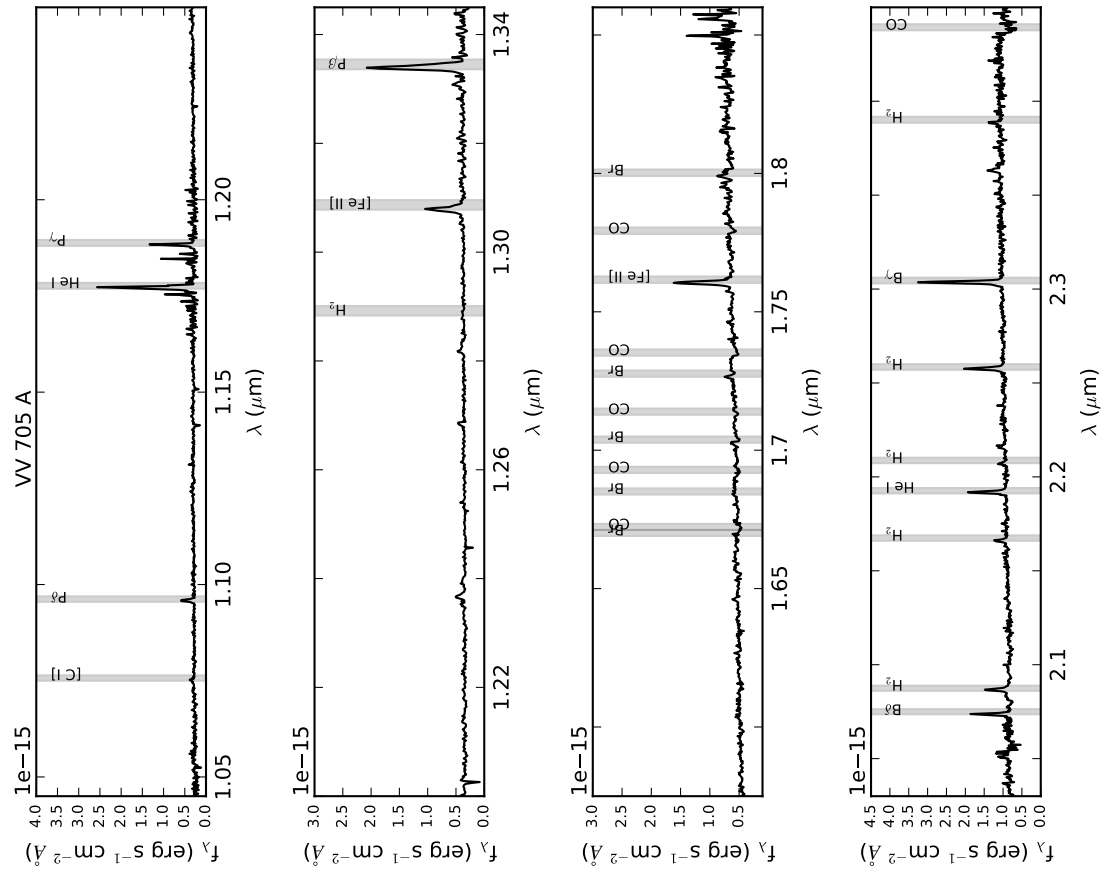


Fig. 2.-1.—

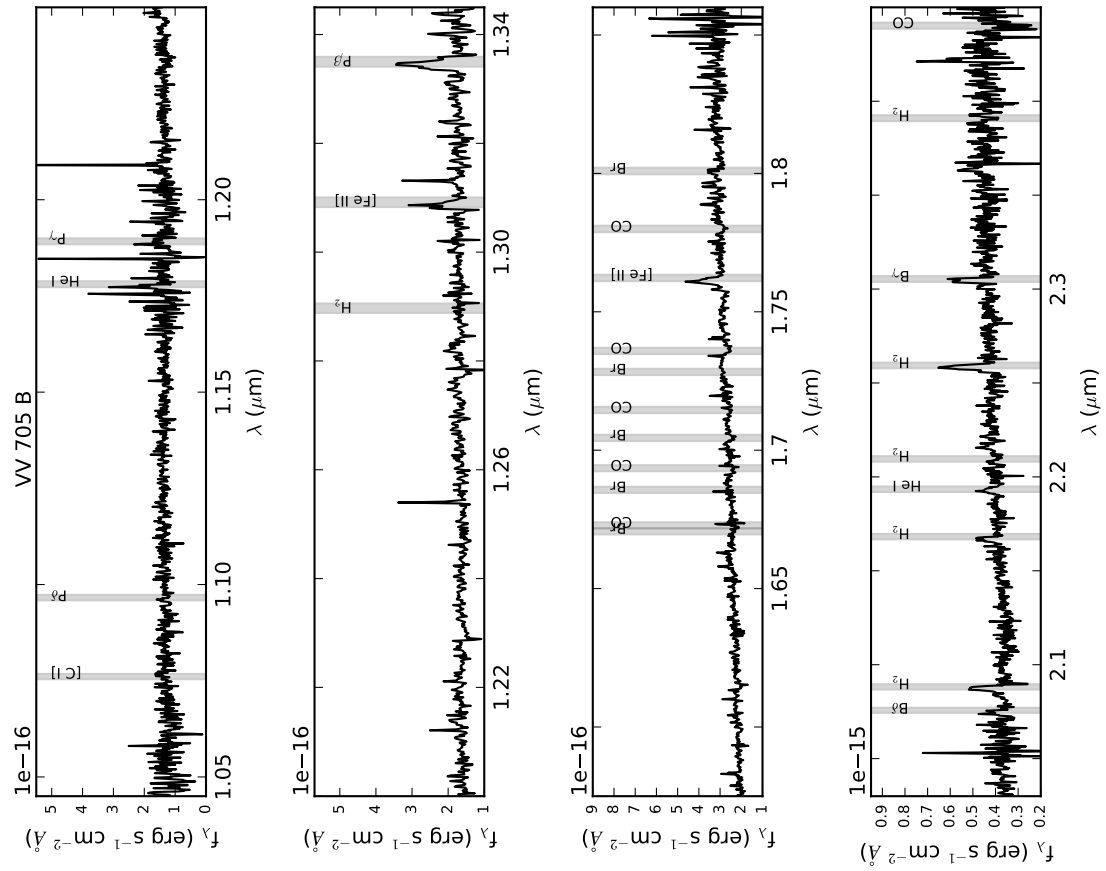


Fig. 2.-1.—



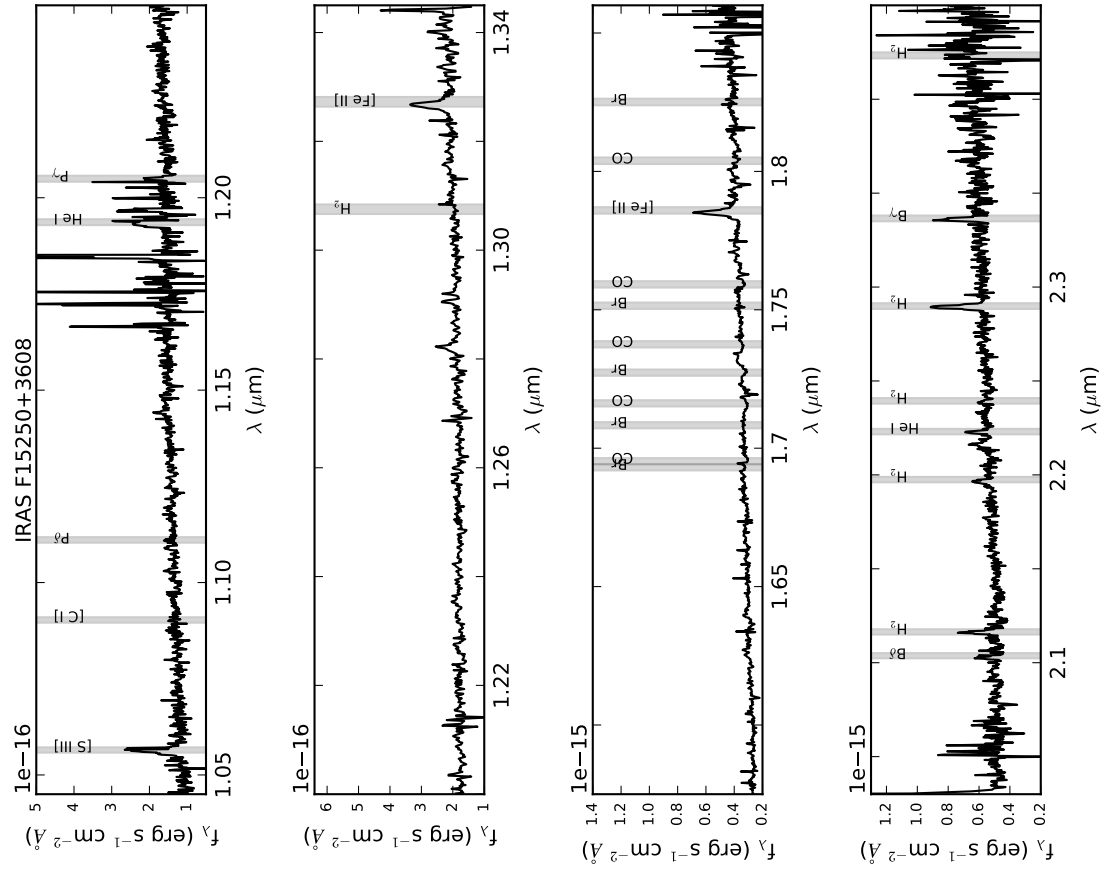


Fig. 2.-1.—

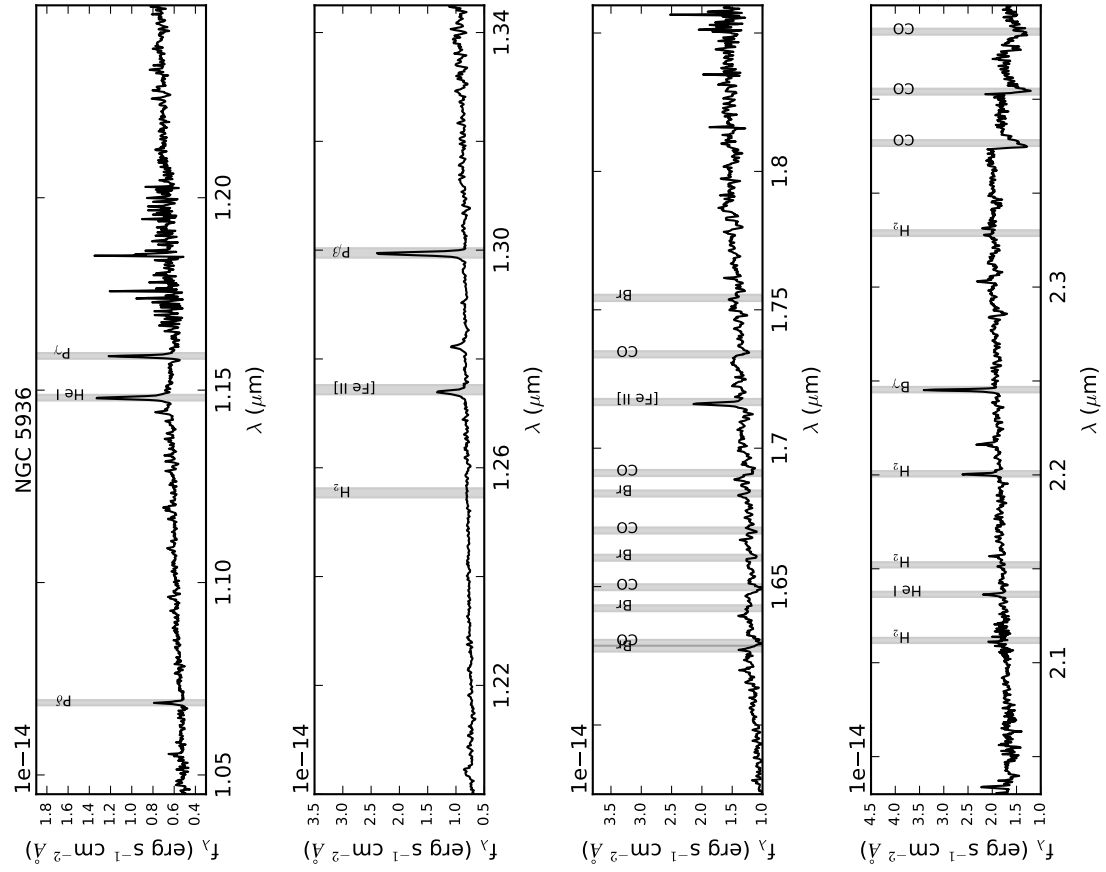


Fig. 2.-1.—

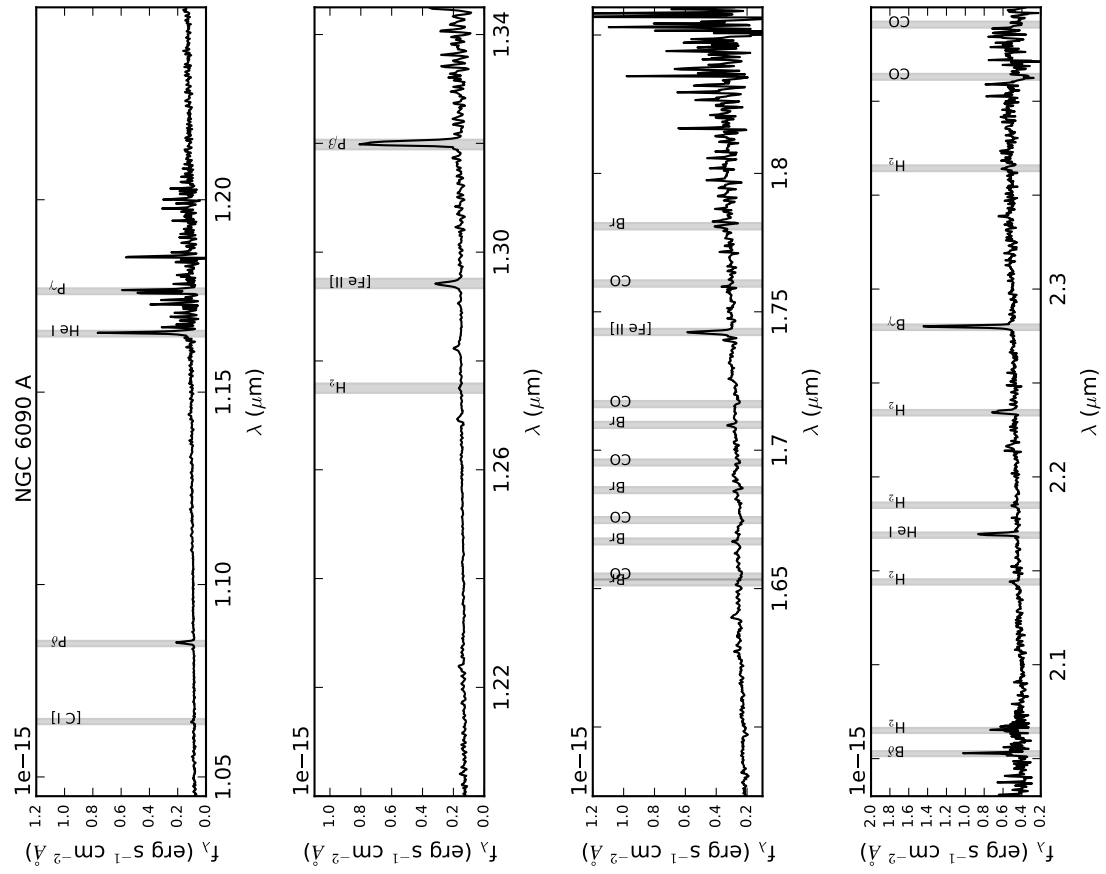


Fig. 2.-1.—

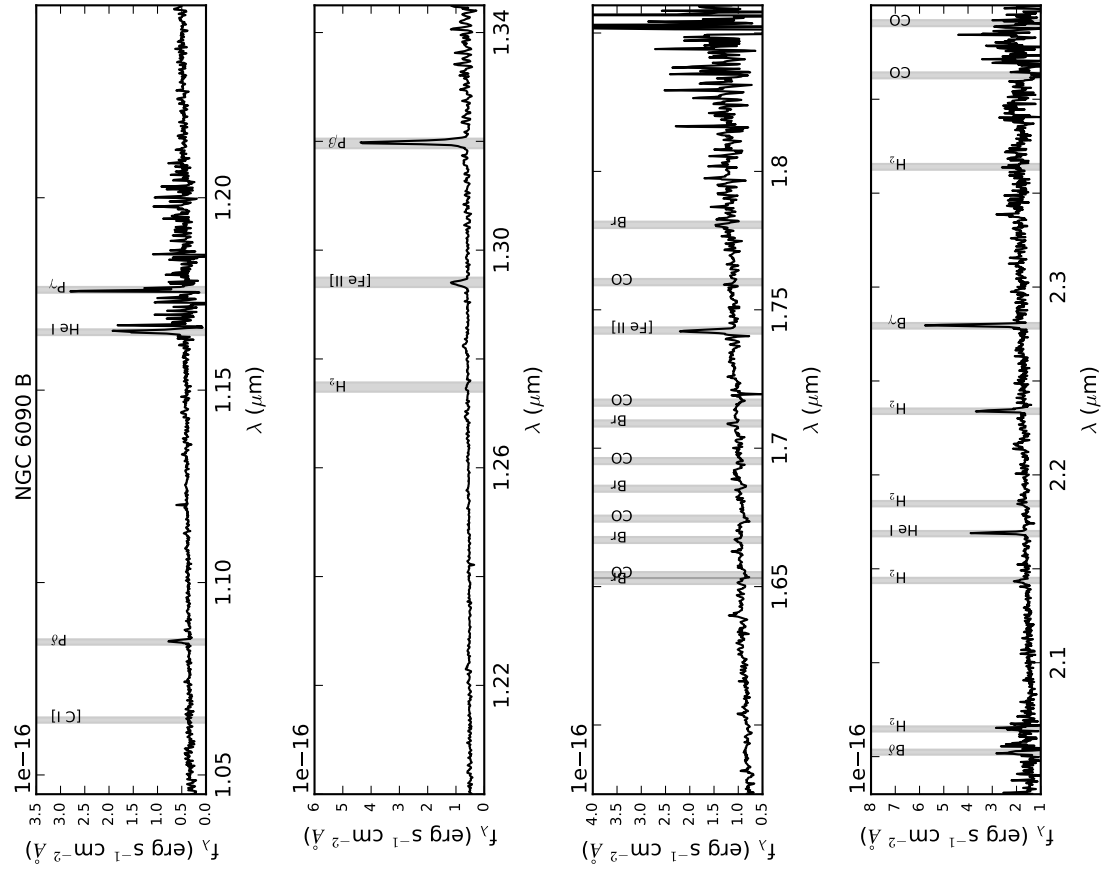


Fig. 2.-1.—

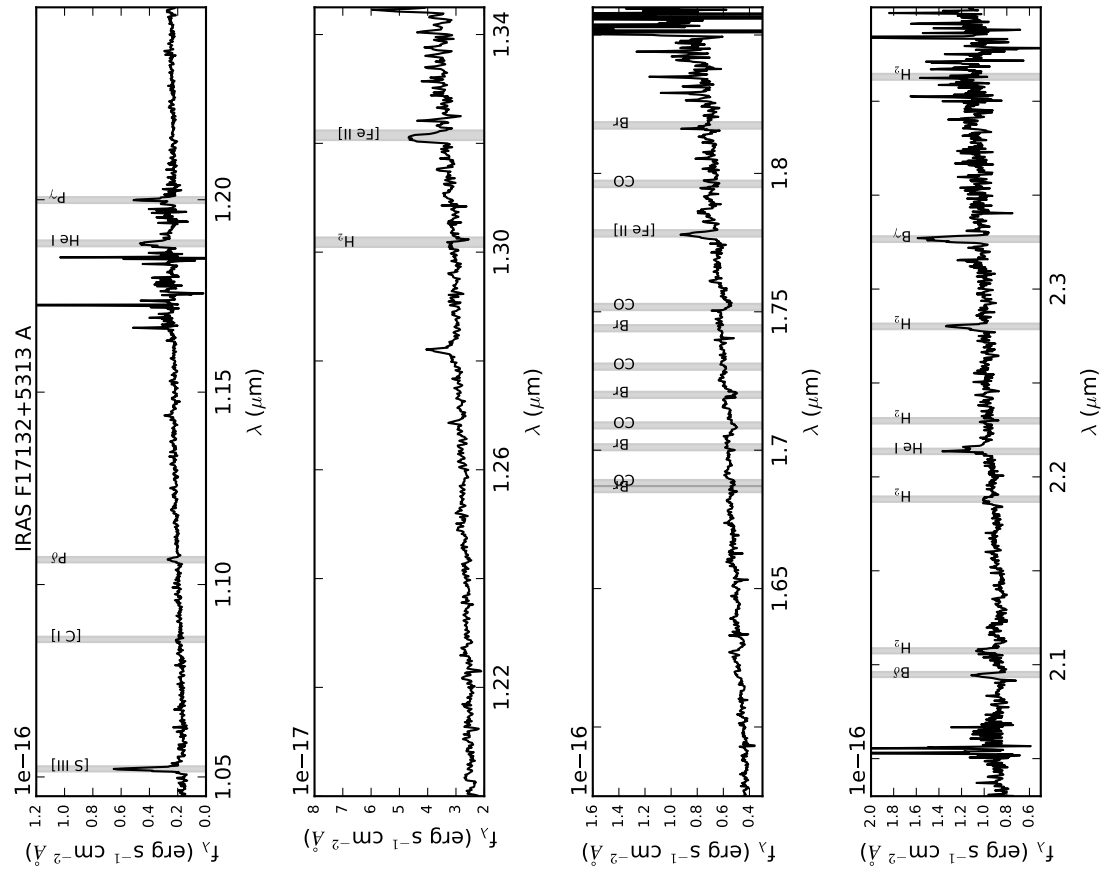


Fig. 2.-1.—

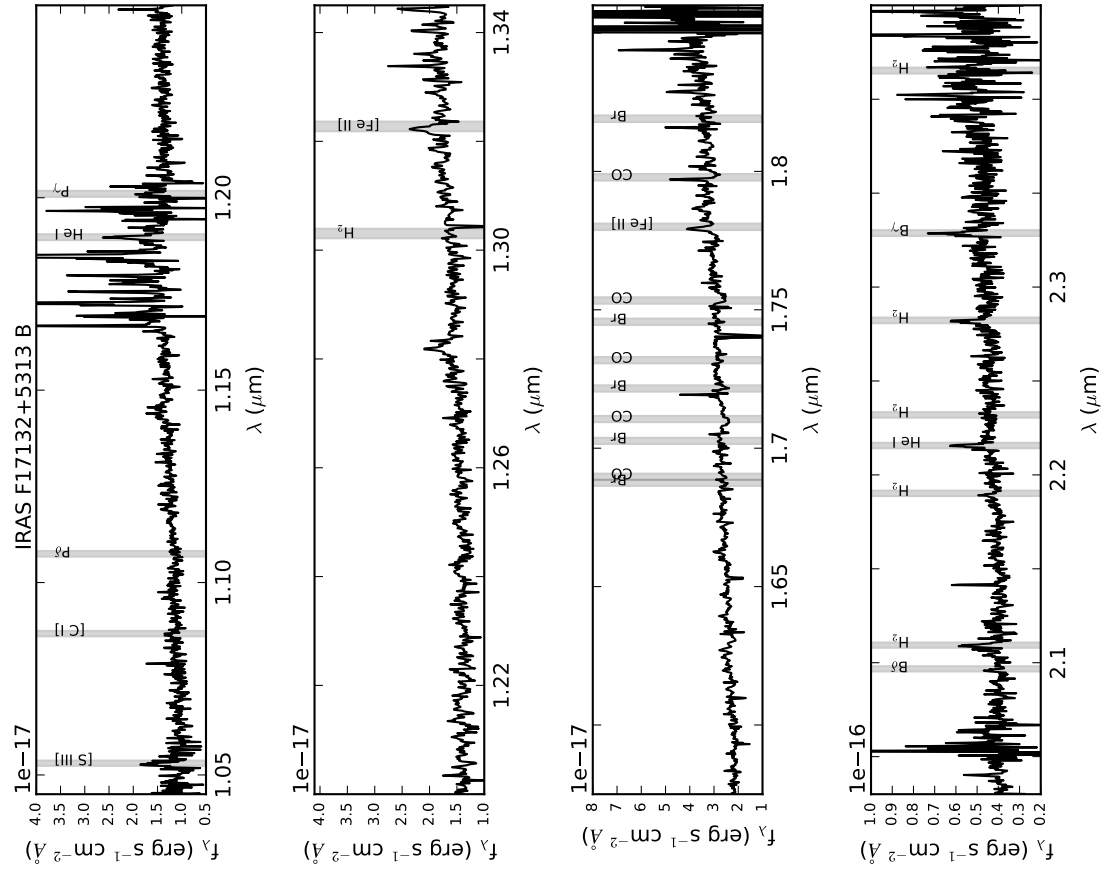


Fig. 2.-1.—









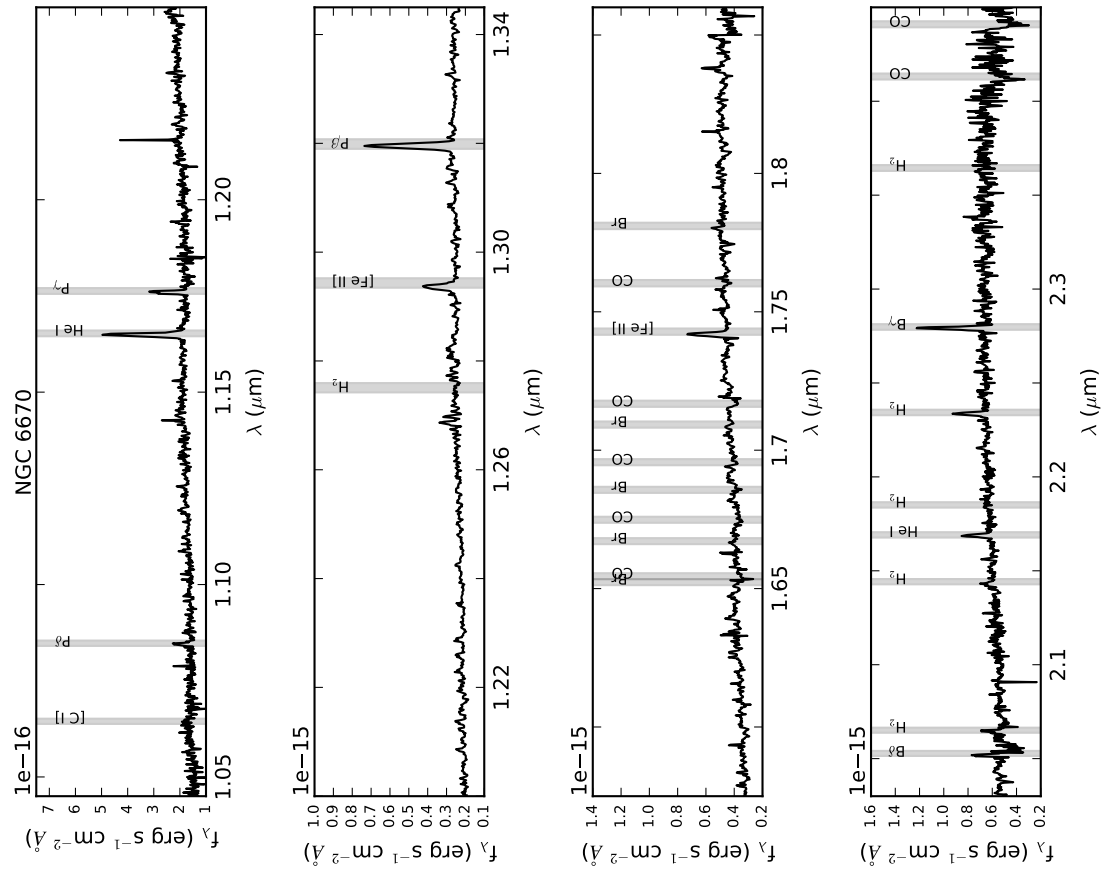


Fig. 2.-1.—

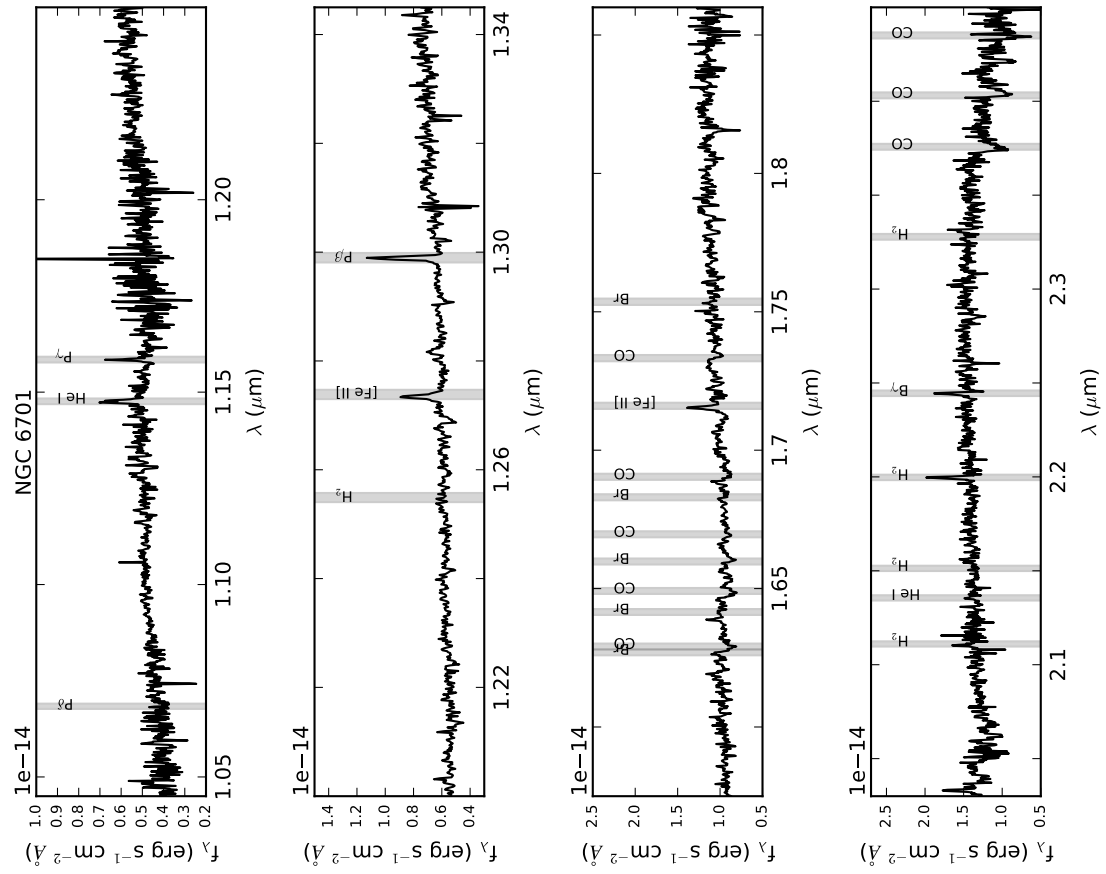


Fig. 2.-1.—



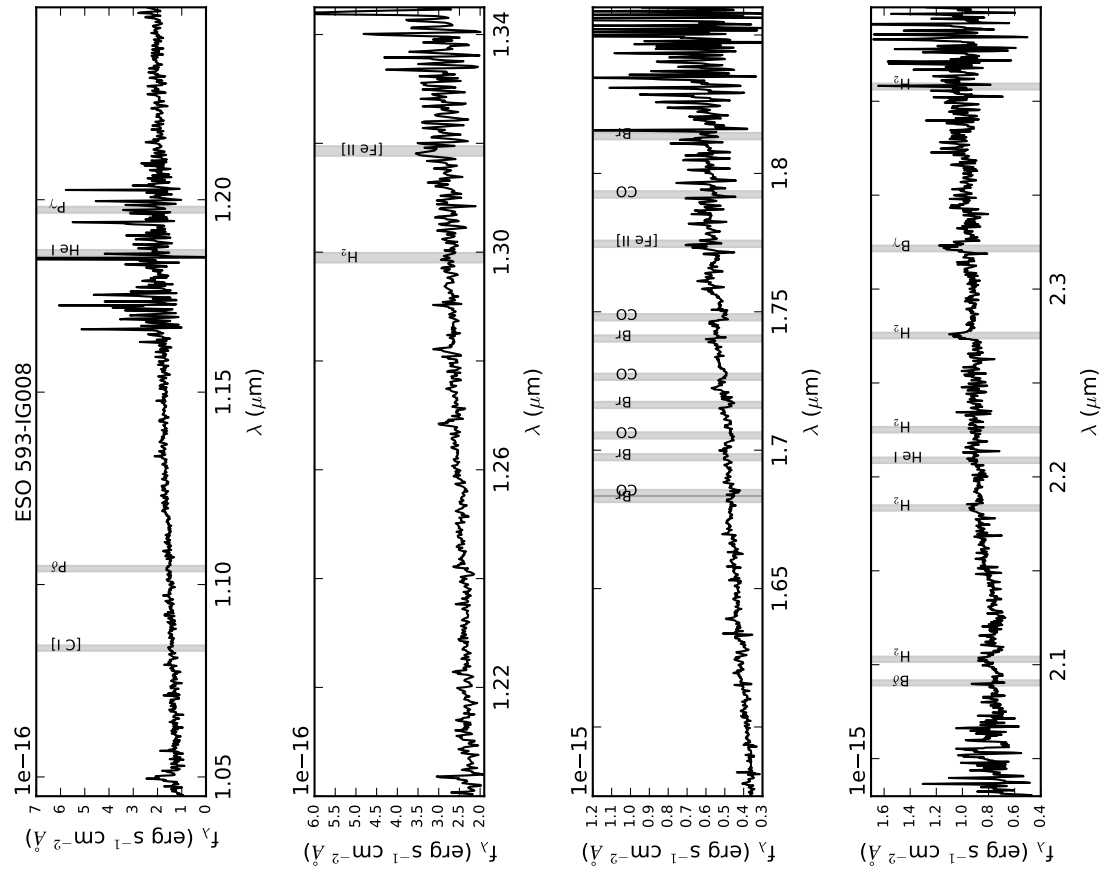


Fig. 2.-1.—

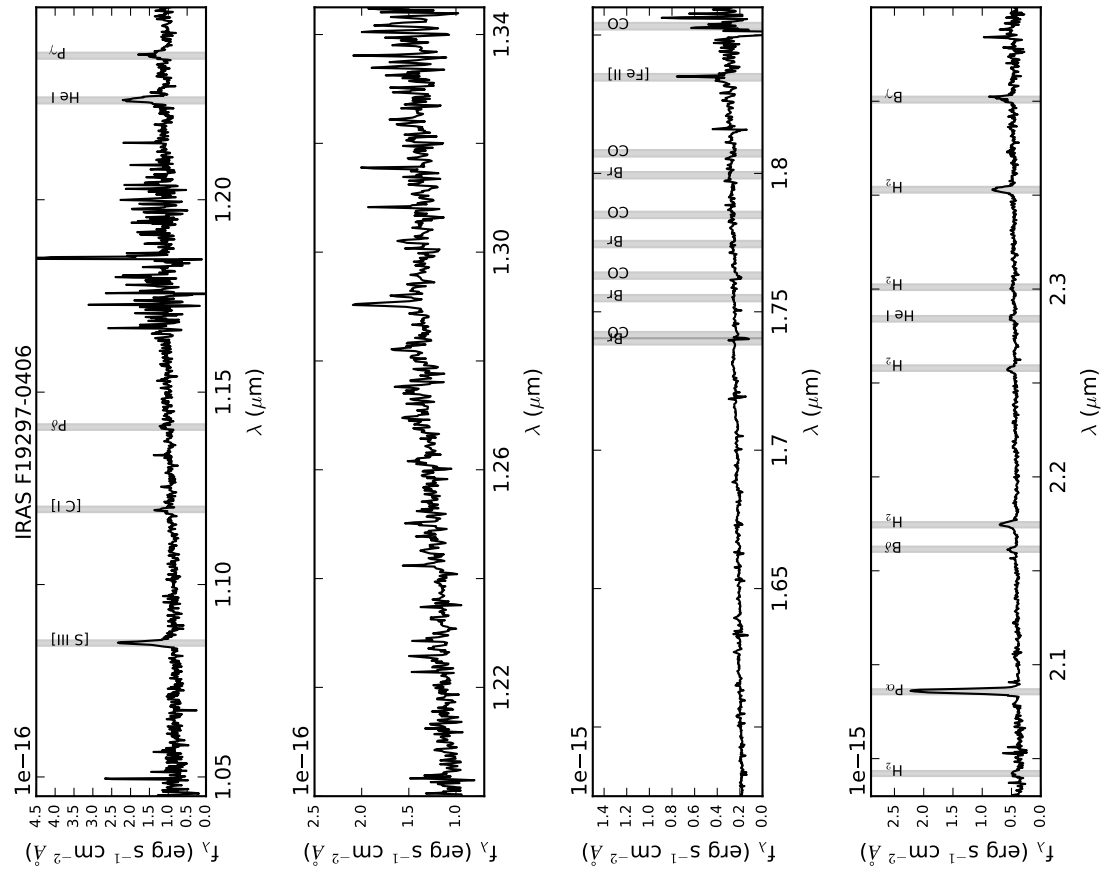


Fig. 2.-1.—

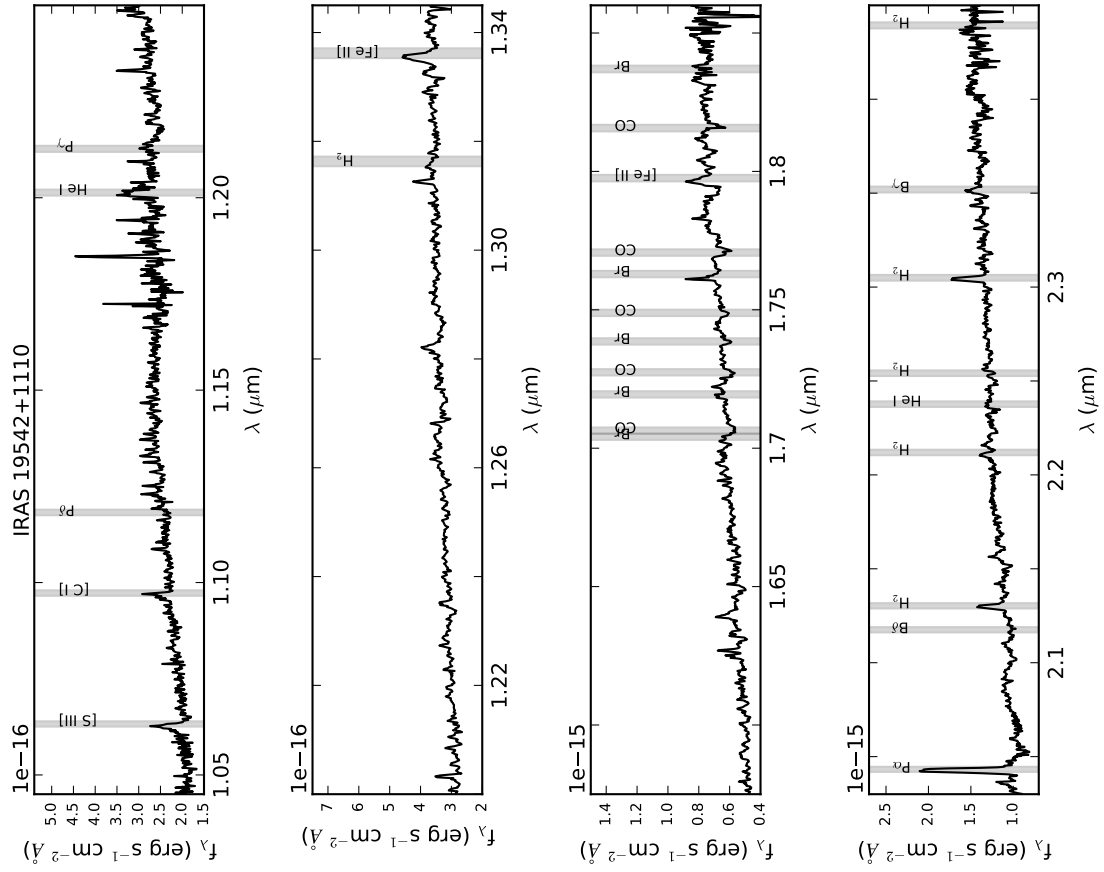


Fig. 2.-1.—





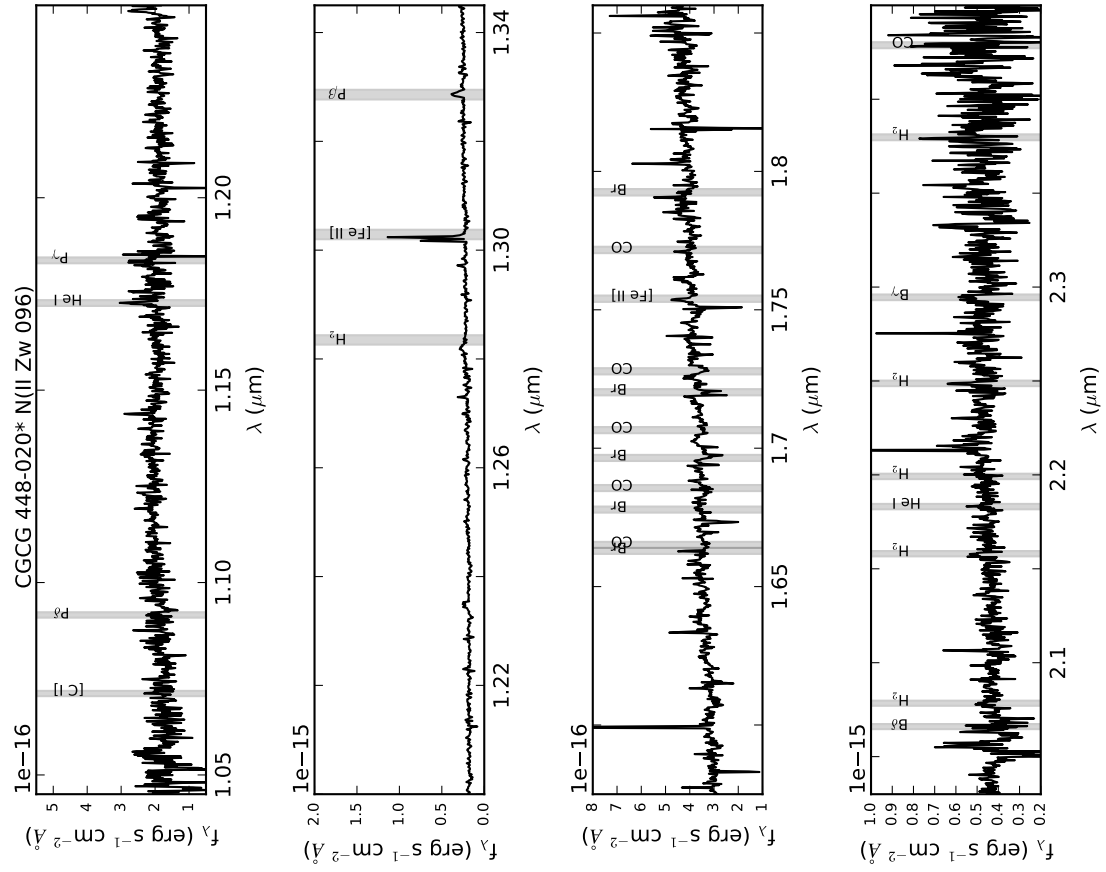


Fig. 2.-1.—

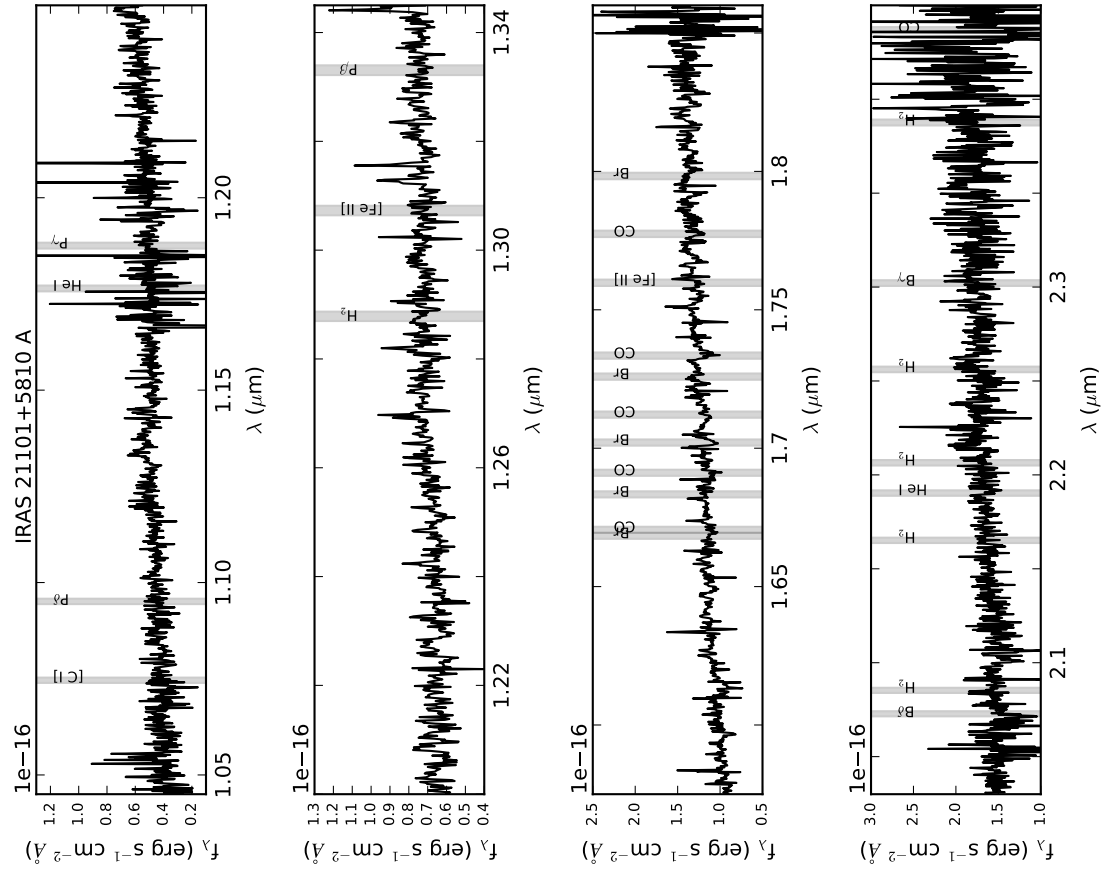


Fig. 2.-1.—

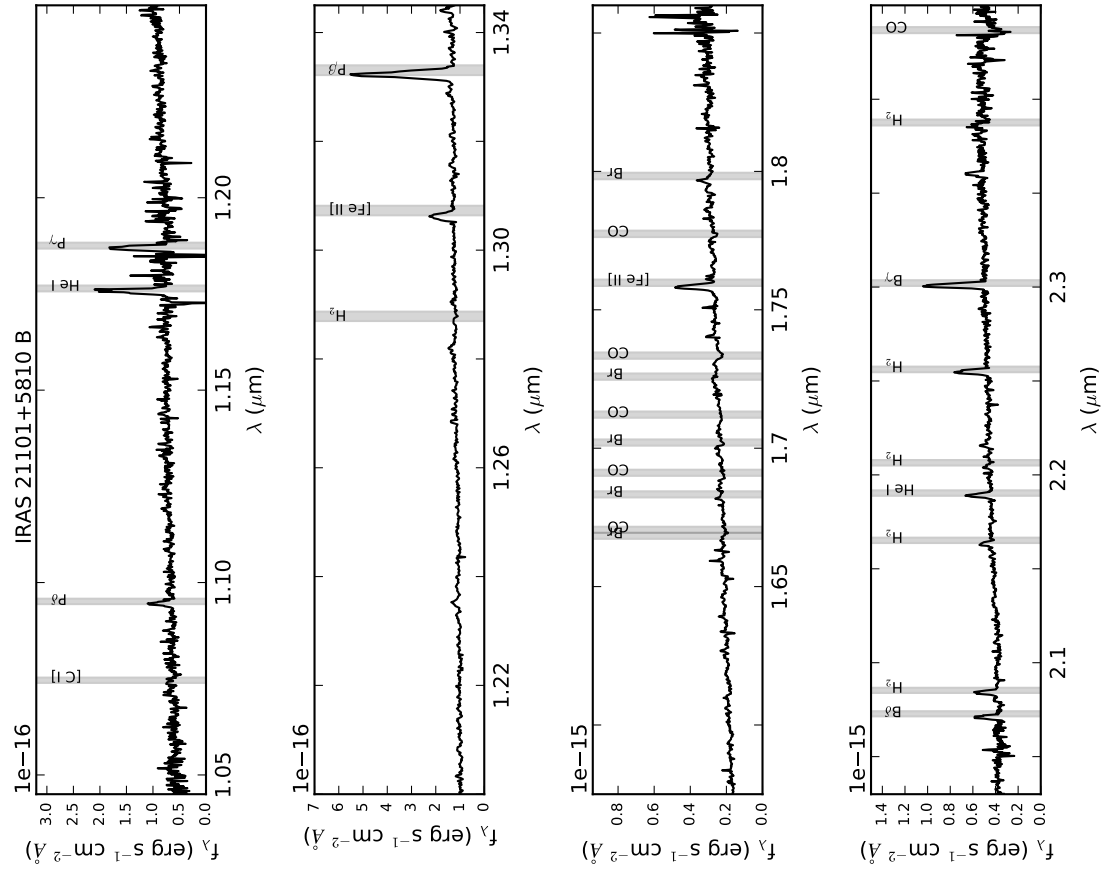


Fig. 2.-1.—

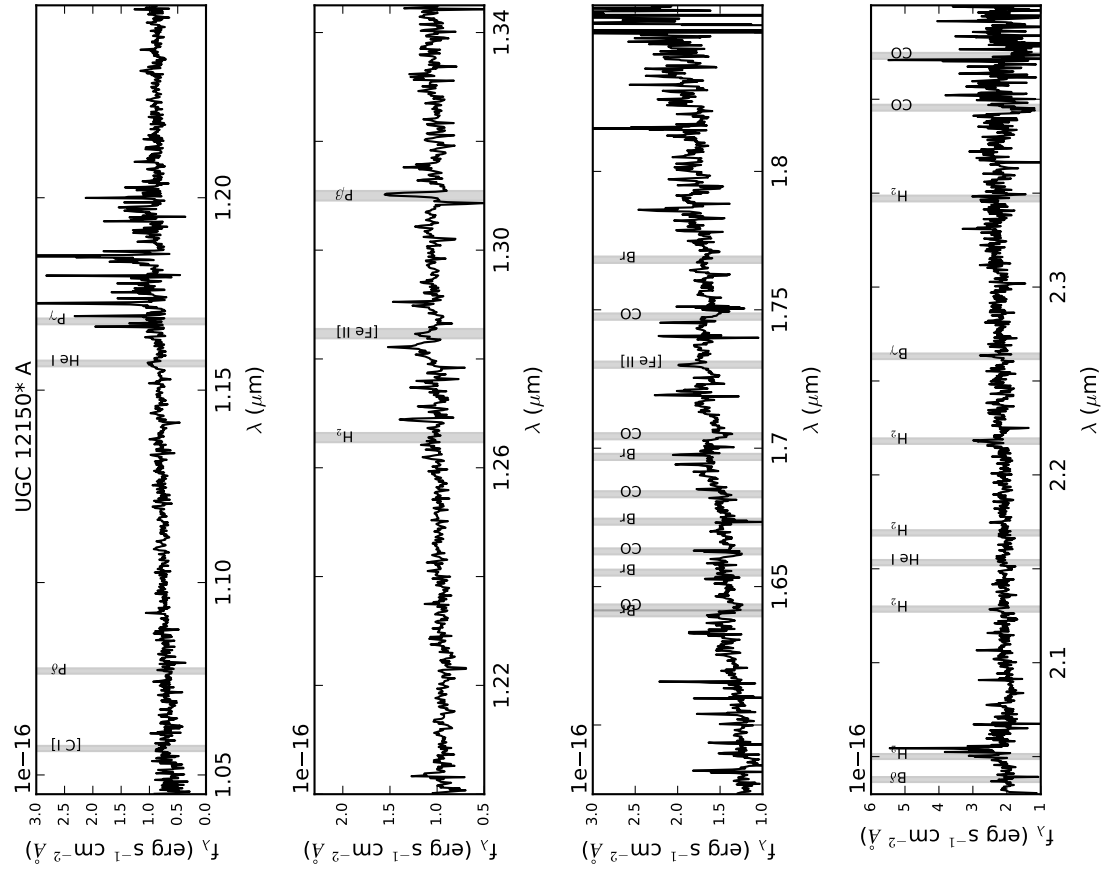


Fig. 2.-1.—

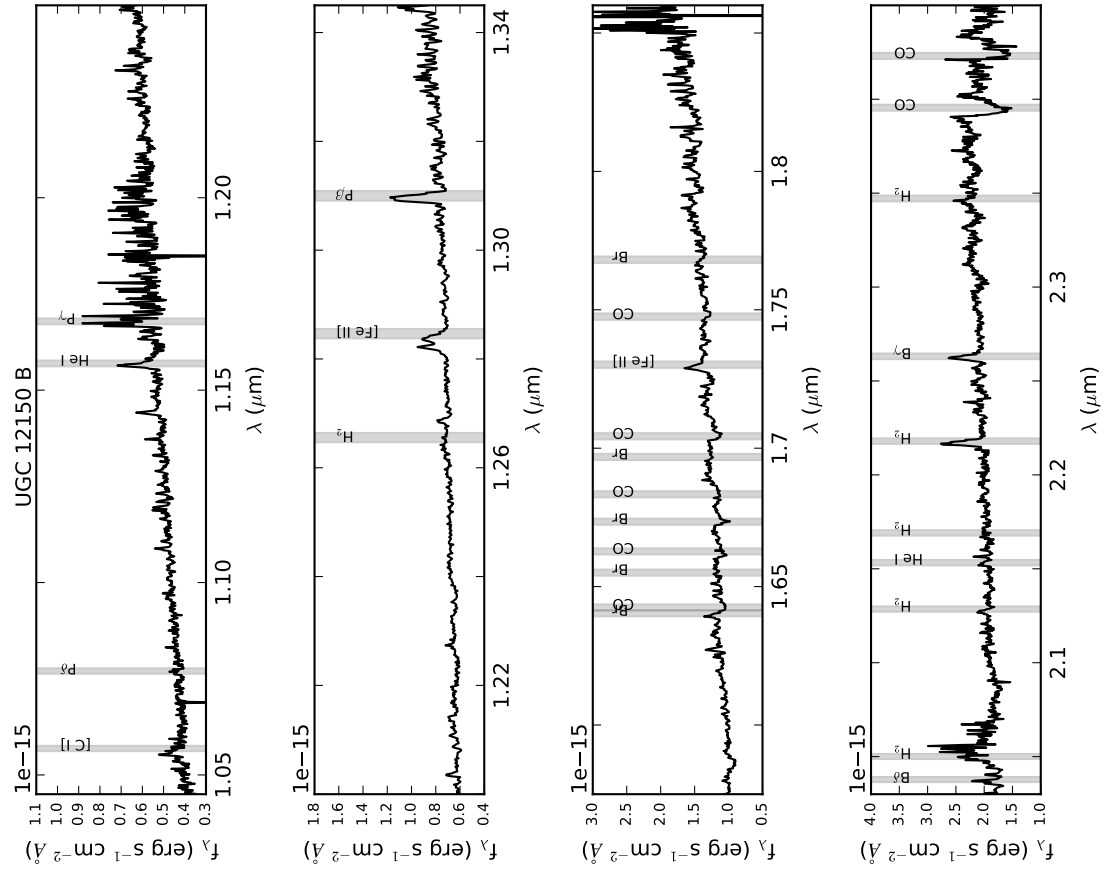


Fig. 2.-1.—

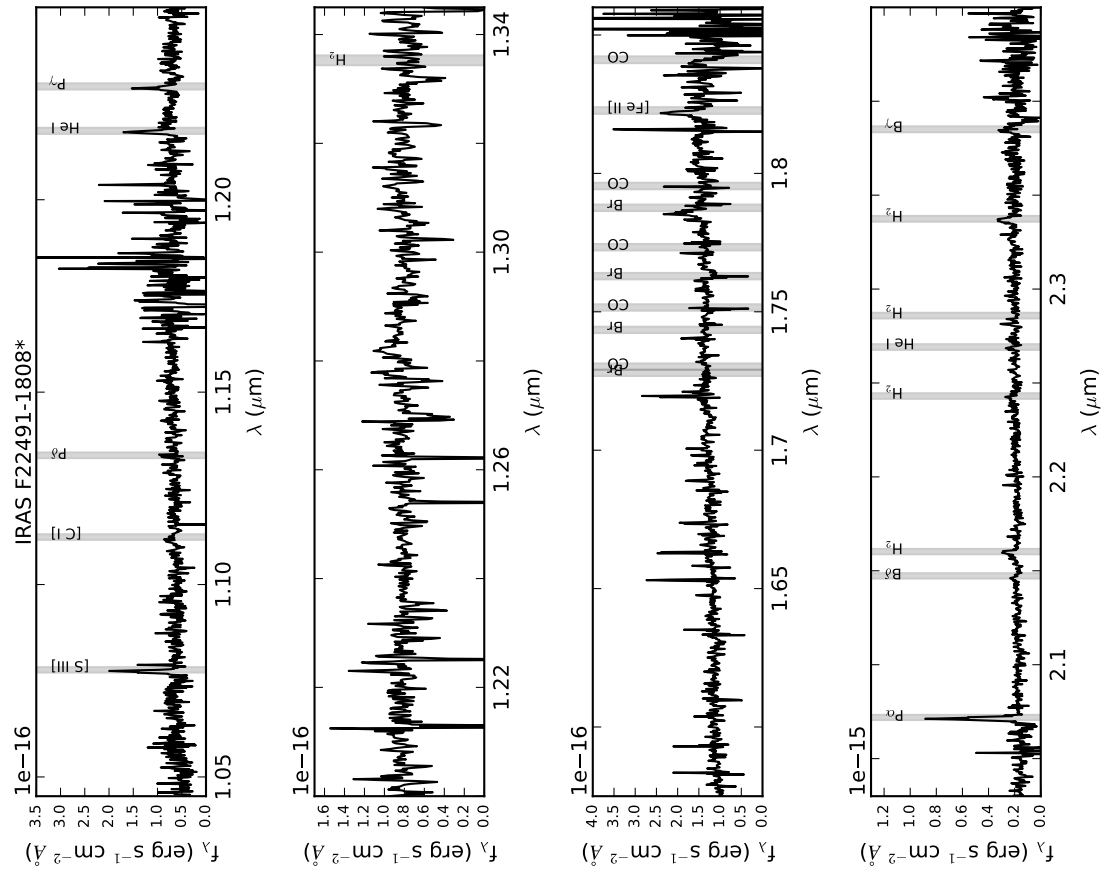


Fig. 2.-1.—

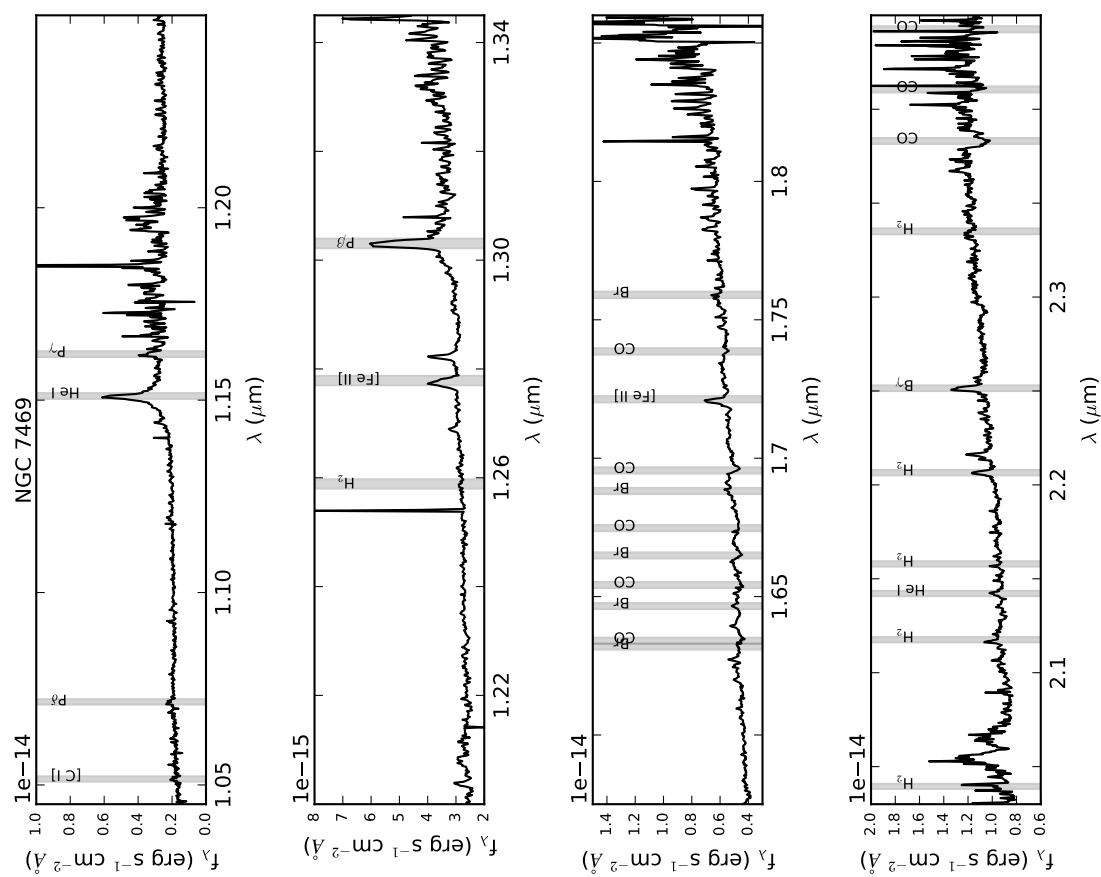


Fig. 2.-1.—

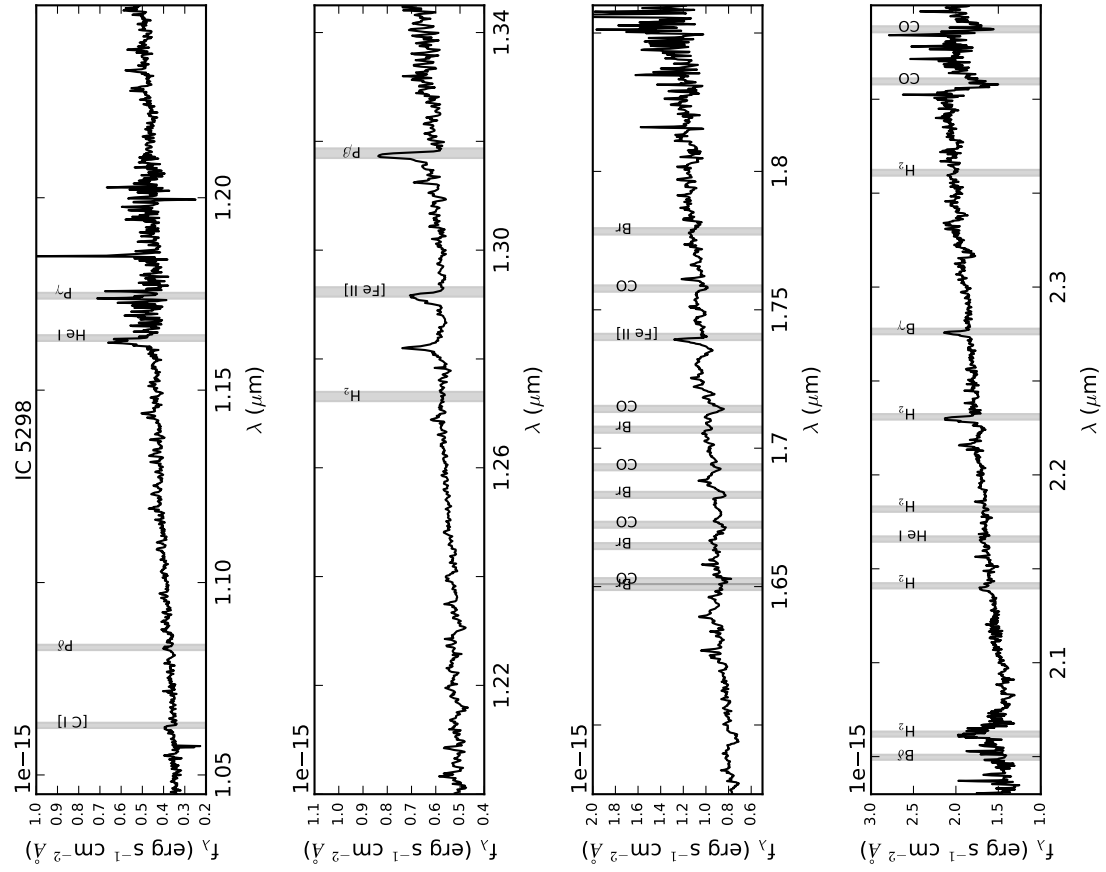


Fig. 2.-1.—



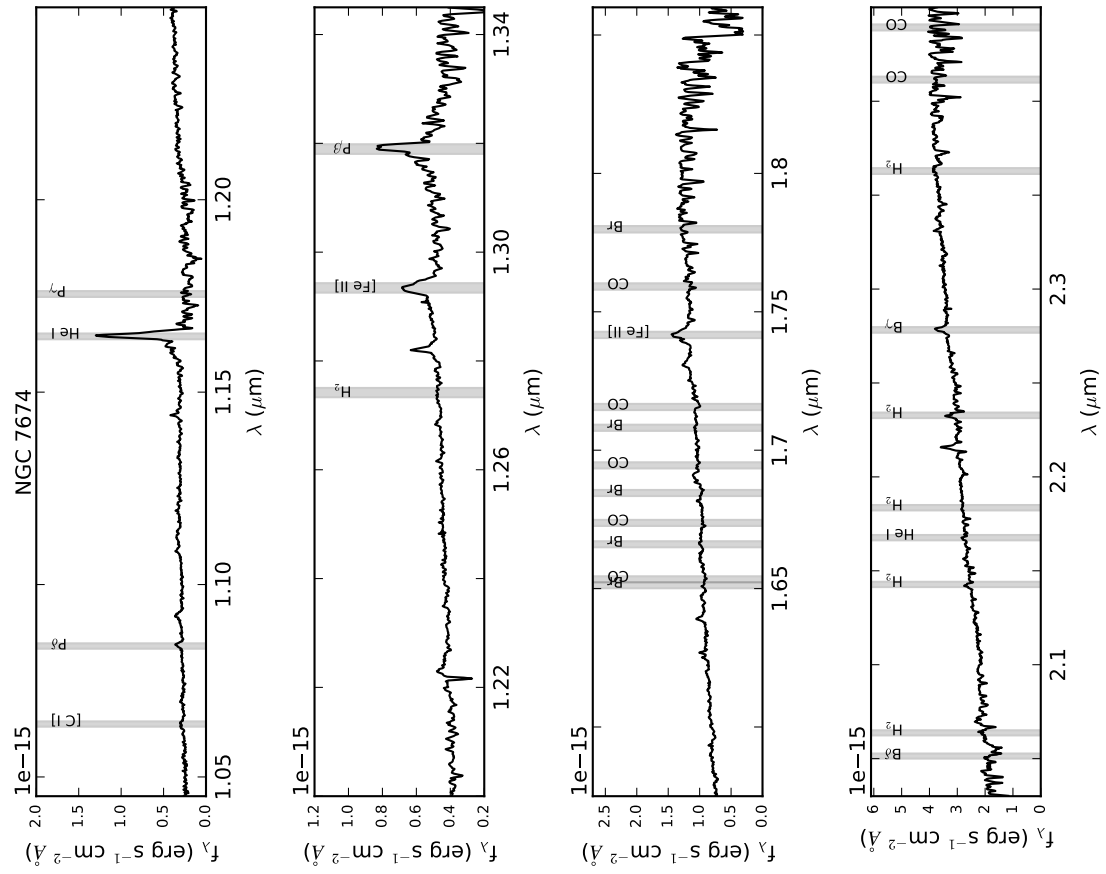


Fig. 2.-1.—

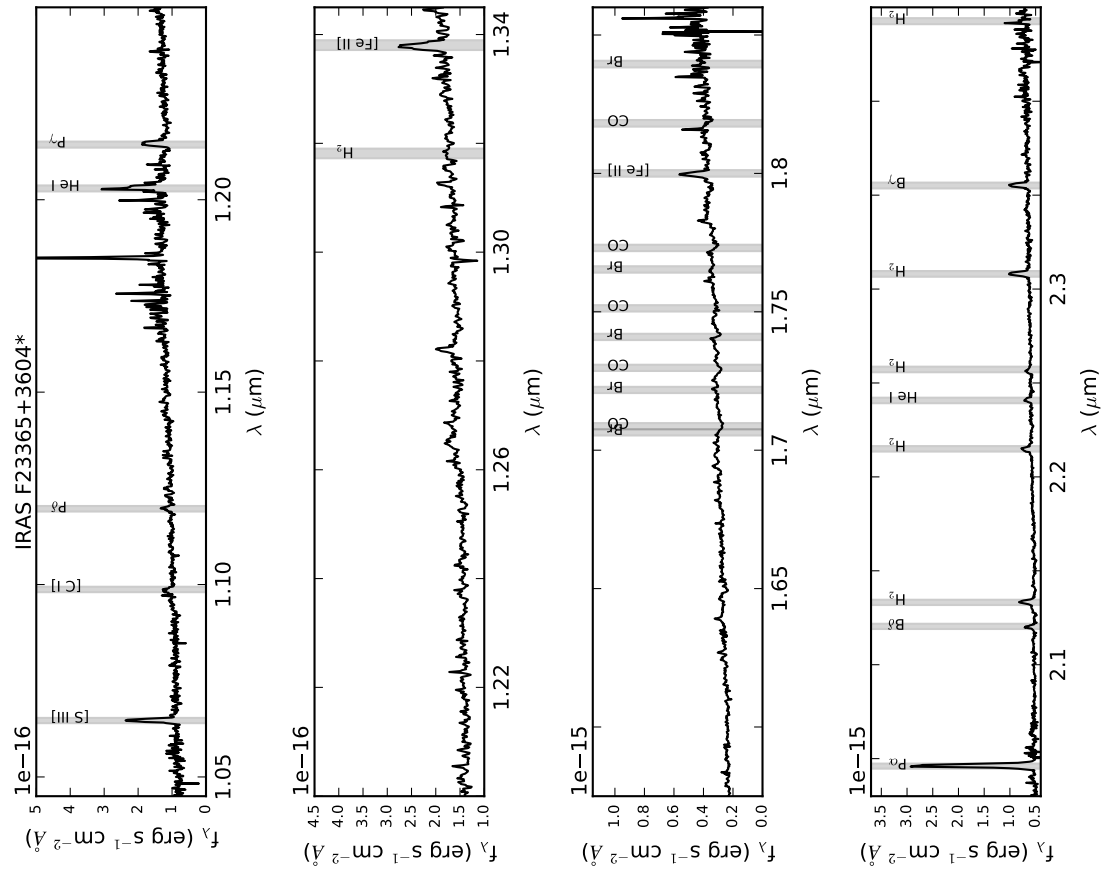


Fig. 2.-1.—

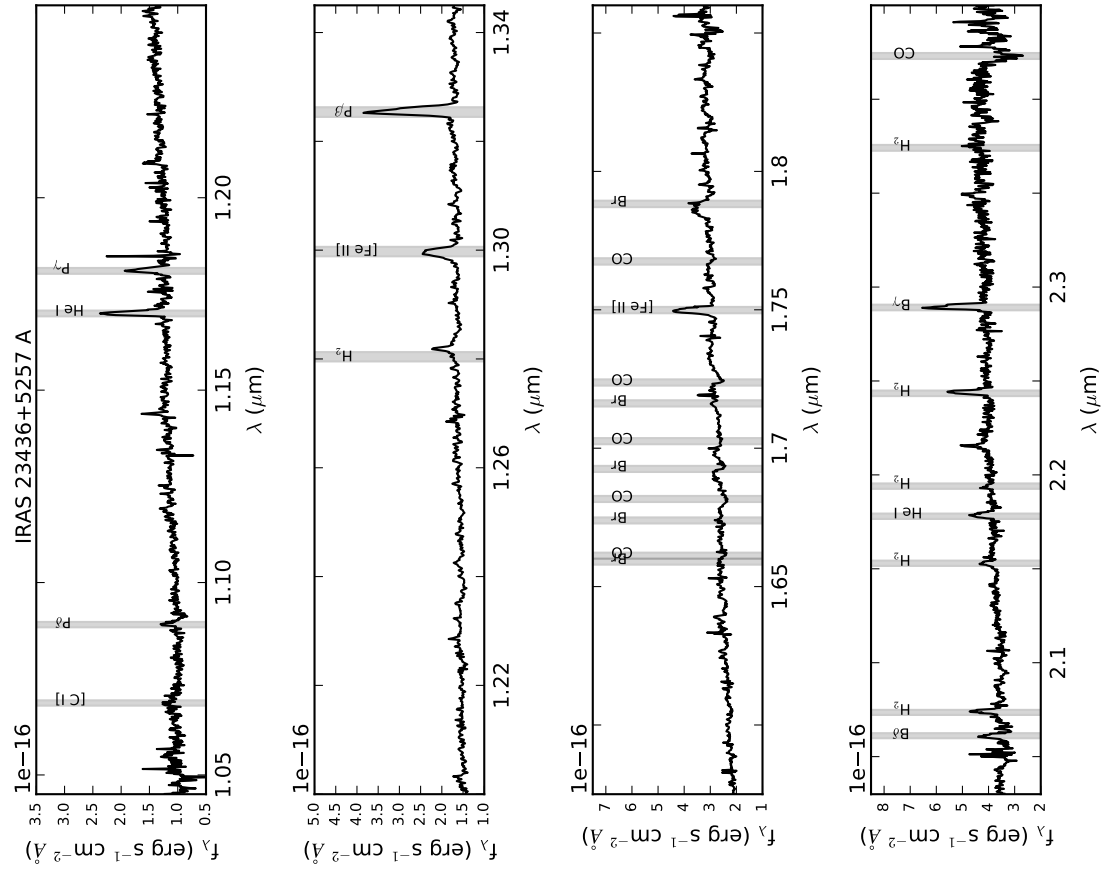


Fig. 2.-1.—



Table 2.4. Unidentified Lines

Source Name	Source Redshift <sup>a</sup>	Observed $\lambda$	Rest $\lambda$
IRAS 21101+5810	0.04	1.282	1.233
II Zw 096	0.0365	1.282	1.237
IRAS 20351+2521	0.0345	1.2683	1.226
	0.0345	1.686	1.630
	0.0345	2.245	2.170
IRAS 19542+1110	0.063	1.3125	1.235
	0.063	1.2816	1.206
	0.063	1.711	1.610
	0.063	1.589	1.495
	0.063	2.105	1.980
ESO 593-IG008	0.049	1.2683	1.209
	0.049	1.282	1.222
NGC 6786	0.025	1.282	1.251
	0.025	2.206	2.152
IRAS 18090+0130 B	0.0292	1.282	1.245
	0.0292	1.2684	1.232
IRAS 18090+0130 A	0.0291	1.312	1.275
	0.0291	1.2905	1.254
IRAS 17132+5313 A	0.0513	1.282	1.219
NGC6090 A	0.02963	1.282	1.245
	0.02963	1.269	1.232
	0.02963	2.165	2.103
NGC 5936	0.0138	1.282	1.265
	0.0138	2.165	2.136
	0.0138	2.253	2.222
IRAS 15250+3608	0.0559	1.282	1.214
VV 705 B	0.0415	2.372	2.277

Table 2.4—Continued

Source Name	Source Redshift <sup>a</sup>	Observed $\lambda$	Rest $\lambda$
	0.04112	1.2817	1.231
	0.04112	1.2683	1.218
CGCG 049-057	0.0135	2.252	2.222
IRAS 14348-1447 A	0.0833	1.323	1.221
NGC 5653	0.0125	1.281	1.265
	0.0125	1.069	1.056
CGCG 247-020	0.0262	1.282	1.249
	0.0262	1.764	1.719
	0.0262	1.321	1.287
NGC 5331 B	0.0337	1.282	1.240
NGC 5331 A	0.034	1.282	1.239
	0.034	2.297	2.221
Mrk 273	0.0383	1.282	1.235
	0.0383	2.306	2.220
NGC 5256 B	0.0285	1.282	1.247
NGC 5256 A	0.0284	1.282	1.247
IC 883 (January)	0.0236	1.216	1.188
	0.0236	2.275	2.223
IC883 (February)	0.024	1.216	1.188
	0.024	2.275	2.222
VV 250 A	0.0314	1.225	1.188
	0.0314	1.733	1.680
	0.0314	2.293	2.223
MCG -02-33-098	0.0168	1.269	1.248
CGCG 043-099	0.038	2.305	2.221
UGC 05101	0.039	2.31	2.223
UGC 04881 B	0.041	2.166	2.080

Table 2.4—Continued

Source Name	Source Redshift <sup>a</sup>	Observed $\lambda$	Rest $\lambda$
UGC 04881 A	0.041	1.282	1.231
	0.0399	1.282	1.233
	0.0399	2.166	2.083
NGC 1275	0.0176	2.263	2.223
UGC 02369 B	0.0317	1.282	1.242
	0.0317	1.226	1.188
	0.0317	1.735	1.682
UGC 02369 A	0.0317	2.293	2.223
	0.0317	2.293	2.223
	0.0317	1.735	1.682
	0.0317	1.282	1.243
	0.0271	1.282	1.248
MCG -02-01-051	0.0271	1.22	1.188
	0.0271	1.726	1.680
	0.0271	2.283	2.223

<sup>a</sup>Measured from the wavelengths of the stellar CO band-heads.

Upon plotting the locations of all lines on a single axis, we see that there are several clusters of features that may represent real lines. The locations are plotted in observed wavelength in Figure 2.0 and rest frame wavelength in Figure 2.1. In observed wavelength there appear to be true features that repeatedly occur around  $1.27\ \mu\text{m}$ ,  $1.28\ \mu\text{m}$ , and  $2.16\ \mu\text{m}$ . These are likely absorption features in the spectrum of the standard star that was used for telluric correction. Due to the difference in redshift between each standard star and target, they do not occur at the same observed wavelength as the corresponding emission lines from the target galaxies. Therefore these absorption line residuals can be safely ignored in the measurement of the emission lines. The feature at  $1.28\ \mu\text{m}$  is  $\text{Pa}\beta$ , and the feature at  $2.16\ \mu\text{m}$  is  $\text{Br}\gamma$ . There exist at least two features at  $1.27\ \mu\text{m}$  having to do with  $\text{O}_2$  or  $\text{O}_3$ , likely arising here from residual absorption due to the atmosphere of the Earth. There additionally exists an Ne I line at  $1.269\ \mu\text{m}$ . In the rest frame there appears to be a real emission feature arising in several sources at  $2.22\ \mu\text{m}$ . This is the molecular hydrogen  $\text{S}(0)\ 1-0$  line.

In addition to the unidentified lines which appear frequently, there are unidentified features that occur in two sources which merit additional consideration due to their strength. The rest frame wavelengths of these features are  $1.275\ \mu\text{m}$  in IRAS 18090+0130A and  $1.248\ \mu\text{m}$  in MCG -02-33-098. The line in MCG -02-33-098 was observed at a wavelength that is possibly associated with the aforementioned  $1.27\ \mu\text{m}$  telluric absorption feature. However, this features are of such strength that its origin as solely an artifact of the reduction seems implausible. The feature in IRAS 18090+0130 A seems to have a very similarly shaped profile to the detected  $\text{Pa}\beta$  line in the same spectrum. Assuming there are two unresolved nuclei within this source, with very similar excitation conditions leading to twin emission lines, these



observed line wavelengths would imply the two nuclei are moving relative to one another with a radial component of velocity  $\sim 1500 \text{ km s}^{-1}$ . These unidentified lines in IRAS 18090+0130A and MCG -02-33-098 remain mysterious, and we invite opinions explaining their origins. The other features listed in Table 2.4 are not strong enough and do not recur often enough to merit further consideration.

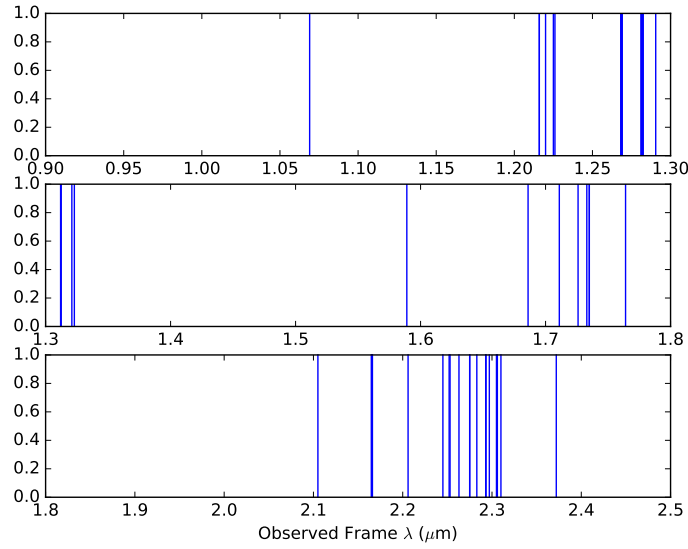


Fig. 2.0.— The observed wavelengths of all unidentified emission lines. Several lines cluster around  $1.27\mu\text{m}$ ,  $1.28\mu\text{m}$ , and  $2.16\mu\text{m}$ . We interpret these as artifacts created by absorption features in the standard star used for telluric correction.

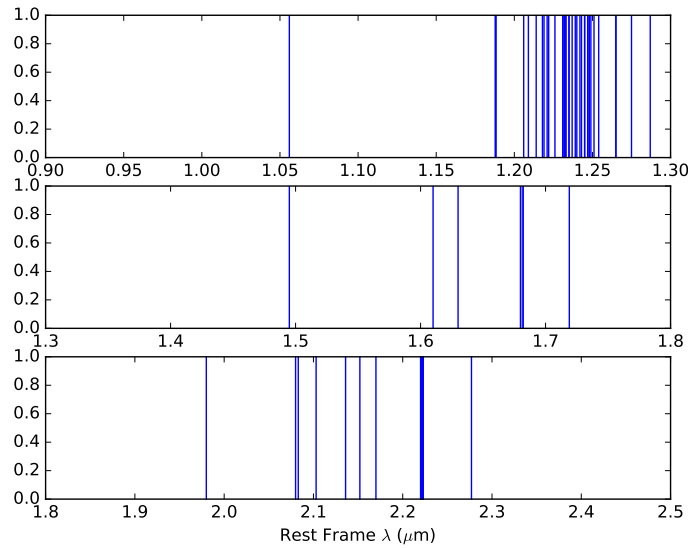


Fig. 2.1.— The rest frame wavelengths of all unidentified lines. There is clustering around  $2.22\mu\text{m}$ . This is likely the  $\text{H}_2$  S(0) 1-0 line.

Table 2.5. Strengths and Velocities of Strong Emission Lines

Name	S III ( $\lambda 0.9532$ )			C I ( $\lambda 0.9852$ )			Pa $\delta$ ( $\lambda 1.0049$ )		
	F <sup>a</sup>	$\delta f$	FWHM <sup>b</sup>	F <sup>a</sup>	$\delta f$	FWHM <sup>b</sup>	F <sup>a</sup>	$\delta f$	FWHM <sup>b</sup>
MCG-02-01-051	8.80e-15	2.00e-16	265	1.00e-16	<1e-16	85	1.00e-15	<1e-16	209
UGC 02369 B	7.40e-15	1.00e-16	220	3.00e-16	<1e-16	255	7.00e-16	<1e-16	208
UGC 02369 A	3.30e-15	1.00e-16	176	1.00e-16	<1e-16	85	5.00e-16	<1e-16	167
NGC 1275*	9.80e-14	2.30e-15	952	1.37e-14	4.00e-16	656	2.50e-15	3.00e-16	470
UGC 04881 A	1.00e-15	1.00e-16	174	1.00e-16	<1e-16	127	1.00e-16	1.00e-16	41
UGC 04881 B	...	<1e-16	...	2.00e-16	1.00e-16	253	2.00e-16	1.00e-16	124
UGC 05101	2.37e-14	1.10e-15	620	5.40e-15	4.00e-16	470	2.00e-16	2.00e-16	42
NGC 3221	3.00e-16	1.00e-16	87	...	<1e-16	...	...	<1e-16	...
NGC 4922 B	...	<1e-16	...	6.00e-16	2.00e-16	87	...	<1e-16	...
NGC 4922 A	3.96e-14	1.00e-15	270	2.20e-15	3.00e-16	304	3.20e-15	2.00e-16	170
CGCG 043-099	3.80e-15	3.00e-16	310	1.70e-15	2.00e-16	385	3.00e-16	1.00e-16	84
MCG -02-33-098	2.00e-16	2.00e-16	45	3.00e-15	5.00e-16	1048	2.50e-15	2.00e-16	43
VV 250* B	8.30e-15	1.20e-15	402	...	<1e-16	...	...	<1e-16	...
VV 250 A	8.60e-14	9.00e-16	358	2.30e-15	3.00e-16	388	8.90e-15	3.00e-16	295
UGC 08387 obs2	1.36e-14	1.10e-15	315	2.80e-15	4.00e-16	304	1.10e-15	2.00e-16	212
UGC 08387	3.25e-14	1.90e-15	180	3.50e-15	5.00e-16	174	6.20e-15	5.00e-16	170
NGC 5104	4.00e-16	1.00e-16	86	3.00e-16	1.00e-16	127	...	<1e-16	...
NGC 5256 A	1.19e-14	4.00e-16	309	7.00e-16	1.00e-16	256	8.00e-16	1.00e-16	293
NGC 5256 B	7.20e-15	4.00e-16	485	5.00e-16	1.00e-16	213	8.00e-16	1.00e-16	335
UGC 08696*	5.60e-14	2.60e-15	481	1.38e-14	7.00e-16	931	3.30e-15	4.00e-16	414
UGC 08739*	...	<1e-16	...	...	<1e-16	...	...	<1e-16	...
NGC 5331 B	2.20e-13	4.70e-14	263	...	<1e-16	...	...	<1e-16	...
NGC 5331 A	3.75e-13	5.32e-14	439	...	<1e-16	...	...	<1e-16	...
CGCG 247-020	7.70e-15	5.00e-16	265	1.00e-15	2.00e-16	428	7.00e-16	1.00e-16	168
NGC 5653*	...	<1e-16	...	5.00e-16	3.00e-16	88	...	<1e-16	...
IRAS F14348-1447* A	1.00e-15	1.00e-16	419	...	<1e-16	...	...	<1e-16	...
IRAS F14348-1447* B	2.20e-15	1.00e-16	209	6.00e-16	1.00e-16	1298	2.00e-16	<1e-16	159
CGCG 049-057	...	<1e-16	...	...	<1e-16	...	...	<1e-16	...
VV 705 A	1.91e-14	6.00e-16	218	1.00e-15	1.00e-16	337	1.90e-15	1.00e-16	165

Table 2.5—Continued

Name	S III ( $\lambda 0.9532$ )		C I ( $\lambda 0.9852$ )		Pa $\delta$ ( $\lambda 1.0049$ )	
	F <sup>a</sup>	$\delta f$	F <sup>a</sup>	$\delta f$	F <sup>a</sup>	$\delta f$
VV 705 B	1.60e-15	2.00e-16	2.00e-16	1.00e-16	...	<1e-16
IRAS F15250+3608	1.90e-15	1.00e-16	1.00e-16	<1e-16	...	<1e-16
NGC 5936	6.20e-15	1.40e-15	1.29e-14	7.00e-16	...	...
NGC 6090 A	5.90e-15	1.00e-16	1.00e-16	<1e-16	7.00e-16	<1e-16
NGC 6090 B	2.20e-15	1.00e-16	<1e-16	<1e-16	3.00e-16	<1e-16
IRAS F17132+5313 A	5.00e-16	<1e-16	<1e-16	<1e-16	1.00e-16	<1e-16
IRAS F17132+5313 B	1.00e-16	<1e-16	<1e-16	<1e-16	...	...
IRAS 18090+0130 A	2.00e-16	1.00e-16	...	<1e-16	1.00e-16	<1e-16
IRAS 18090+0130 B	1.40e-15	3.00e-16	4.00e-16	1.00e-16	2.00e-16	1.00e-16
IRAS 18090+0130 C	...	<1e-16	...	<1e-16	...	...
NGC 6670	3.90e-15	3.00e-16	2.00e-16	1.00e-16	5.00e-16	<1e-16
NGC 6701	9.40e-15	1.60e-15	...	<1e-16	...	167
ESO 593-IG008	1.30e-15	1.00e-16	1.00e-16	<1e-16	1.00e-16	<1e-16
NGC 6786	2.00e-16	<1e-16	<1e-16	<1e-16	<1e-16	164
IRAS F19297-0406	1.70e-15	1.00e-16	3.00e-16	<1e-16	<1e-16	126
IRAS 19542+1110	1.00e-15	1.00e-16	6.00e-16	<1e-16	2.00e-16	<1e-16
IRAS 20351+2521	1.97e-14	1.46e-14	...	<1e-16	...	...
II Zw 096	1.10e-15	2.00e-16	2.00e-16	1.00e-16	4.10e-15	6.00e-16
IRAS 21101+5810	1.10e-15	1.00e-16	<1e-16	<1e-16	...	83
IRAS 21101+5810 A	1.00e-16	<1e-16	...	<1e-16	<1e-16	<1e-16
IRAS 21101+5810 B	2.80e-15	1.00e-16	<1e-16	<1e-16	2.00e-16	<1e-16
UGC 12150 B	2.80e-15	2.00e-16	...	<1e-16	<1e-16	41
UGC 12150* A	4.00e-16	2.00e-16	1.70e-15	1.00e-16	4.00e-16	<1e-16
IRAS F22491-1808*	8.00e-16	1.00e-16	3.00e-16	1.00e-16	2.00e-16	1.00e-16
NGC 7469	2.70e-15	5.00e-16	4.30e-15	1.00e-16	<1e-16	<1e-16
IC 5298	3.50e-15	2.00e-16	6.00e-16	5.00e-16	1.00e-16	<1e-16
NGC 7674	2.53e-14	3.00e-16	7.00e-16	1.00e-16	2.00e-16	<1e-16
IRAS F23365+3604*	1.40e-15	1.00e-16	5.00e-16	<1e-16	2.00e-16	<1e-16
IRAS 23436+5257 A	3.00e-15	1.00e-16	3.00e-16	<1e-16	3.00e-16	<1e-16

Table 2.5—Continued

Name	S III ( $\lambda 0.9532$ )		C I ( $\lambda 0.9852$ )		Pa $\delta$ ( $\lambda 1.0049$ )	
	F <sup>a</sup>	$\delta f$	FWHM <sup>b</sup>	F <sup>a</sup>	FWHM <sup>b</sup>	$\delta f$
IRAS 23436+5257 B	2.80e-15	1.00e-16	219	4.00e-16	<1e-16	297
					4.00e-16	<1e-16
						125

<sup>a</sup>erg s<sup>-1</sup> cm<sup>-2</sup> - Not corrected for extinction.  
<sup>b</sup>km/s

Table 2.6. Strengths and Velocities of Strong Emission Lines

Name	He I ( $\lambda$ 1.0831)			Pa $\gamma$ ( $\lambda$ 1.0938)			[Fe II] ( $\lambda$ 1.2570)		
	F <sup>a</sup>	$\delta f$	FWHM <sup>b</sup>	F <sup>a</sup>	$\delta f$	FWHM <sup>b</sup>	F <sup>a</sup>	$\delta f$	FWHM <sup>b</sup>
MCG-02-01-051	4.90e-15	3.00e-16	233	3.10e-15	5.00e-16	308	3.60e-15	1.00e-16	241
UGC 02369 B	5.00e-15	2.00e-16	271	1.90e-15	3.00e-16	192	2.70e-15	1.00e-16	240
UGC 02369 A	2.10e-15	2.00e-16	155	1.20e-15	2.00e-16	153	1.10e-15	<1e-16	160
NGC 1275*	2.37e-13	8.00e-16	1416	...	<1e-16	...	3.59e-14	5.00e-16	488
UGC 04881 A	7.00e-16	1.00e-16	192	5.00e-16	2.00e-16	304	7.00e-16	1.00e-16	238
UGC 04881 B	...	<1e-16	...	...	<1e-16	...	1.00e-16	1.00e-16	40
UGC 05101	2.26e-14	1.20e-15	1722	...	<1e-16	...	1.07e-14	4.00e-16	557
NGC 3221	1.00e-16	2.00e-16	39	...	<1e-16	...	1.00e-16	2.00e-16	81
NGC 4922 B	...	<1e-16	...	3.00e-16	2.00e-16	39	...	<1e-16	...
NGC 4922 A	2.63e-14	1.20e-15	312	5.10e-15	1.20e-15	154	9.00e-15	3.00e-16	364
CGCG 043-099	3.50e-15	6.00e-16	308	2.00e-15	3.00e-16	304	3.50e-15	1.00e-16	438
MCG -02-33-098	1.15e-14	6.00e-16	158	4.90e-15	9.00e-16	117	5.40e-15	1.20e-15	490
VV 250* B	4.10e-15	3.00e-16	310	1.00e-15	3.00e-16	498	2.30e-15	4.00e-16	521
VV 250 A	5.12e-14	1.70e-15	349	1.55e-14	2.80e-15	306	1.65e-14	3.00e-16	401
UGC 08387 obs2	9.40e-15	6.00e-16	313	4.80e-15	6.00e-16	232	7.50e-15	2.00e-16	324
UGC 08387	2.49e-14	1.70e-15	234	1.36e-14	1.80e-15	193	1.76e-14	6.00e-16	202
NGC 5104	6.00e-16	1.00e-16	196	7.00e-16	2.00e-16	155	4.10e-15	3.00e-16	810
NGC 5256 A	1.02e-14	7.00e-16	349	9.00e-16	1.30e-15	346	6.40e-15	2.00e-16	441
NGC 5256 B	5.30e-15	9.00e-16	504	1.70e-15	1.50e-15	192	3.00e-15	2.00e-16	482
UGC 08696*	5.54e-14	6.70e-15	423	1.44e-14	2.70e-15	190	3.85e-14	1.20e-15	437
UGC 08739*	2.10e-13	5.81e-14	236	...	<1e-16	...	4.78e-14	5.70e-14	41
NGC 5331 B	2.35e-13	3.85e-14	309	1.34e-13	4.90e-14	344	2.33e-13	2.16e-14	240
NGC 5331 A	3.11e-13	2.49e-14	348	...	...	...	3.54e-13	2.46e-14	280
CGCG 247-020	3.30e-15	5.00e-16	156	4.10e-15	7.00e-16	193	4.10e-15	2.00e-16	241
NGC 5653*	1.20e-15	3.00e-16	752	1.30e-15	3.00e-16	156	...	<1e-16	...
IRAS F14348-1447* A	4.00e-16	1.00e-16	258	3.00e-16	1.00e-16	256	...	<1e-16	...
IRAS F14348-1447* B	1.70e-15	1.00e-16	369	6.00e-16	1.00e-16	219	...	<1e-16	...
CGCG 049-057	1.50e-15	2.00e-16	198	1.50e-15	2.00e-16	156	1.40e-15	1.00e-16	164
VV 705 A	1.37e-14	7.00e-16	153	4.00e-15	9.00e-16	76	6.20e-15	2.00e-16	159

Table 2.6—Continued

Name	He I ( $\lambda$ 1.0831)		Pa $\gamma$ ( $\lambda$ 1.0938)		[Fe II] ( $\lambda$ 1.2570)	
	F <sup>a</sup>	$\delta f$	FWHM <sup>b</sup>	F <sup>a</sup>	$\delta f$	FWHM <sup>b</sup>
VV 705 B	...	<1e-16	...	6.00e-16	2.00e-16	152
IRAS F15250+3608	...	<1e-16	...	2.00e-16	1.00e-16	112
NGC 5936	5.79e-14	4.40e-15	118	3.04e-14	4.30e-15	117
NGC 6090 A	3.00e-15	4.00e-16	78	2.40e-15	4.00e-16	269
NGC 6090 B	1.10e-15	2.00e-16	194	1.10e-15	5.00e-16	230
IRAS F17132+5313 A	2.00e-16	1.00e-16	266	2.00e-16	<1e-16	113
IRAS F17132+5313 B	<1e-16	1.00e-16	38	<1e-16	<1e-16	75
IRAS 18090+0130 A	3.00e-16	1.00e-16	116	3.00e-16	2.00e-16	1918
IRAS 18090+0130 B	1.20e-15	3.00e-16	271	...	<1e-16	...
IRAS 18090+0130 C	6.00e-16	1.00e-16	426	...	<1e-16	...
NGC 6670	2.90e-15	1.00e-16	233	9.00e-16	2.00e-16	154
NGC 6701	1.92e-14	1.70e-15	197	8.60e-15	1.80e-15	117
ESO 593-IG008	...	<1e-16	...	5.00e-16	2.00e-16	75
NGC 6786	2.00e-16	<1e-16	156	1.00e-16	<1e-16	154
IRAS F19297-0406	1.30e-15	1.00e-16	331	5.00e-16	1.00e-16	291
IRAS 19542+1110	1.00e-15	1.00e-16	375	1.00e-16	<1e-16	111
IRAS 20351+2521	2.06e-14	1.70e-15	270	8.90e-15	2.10e-15	153
II Zw 096	5.00e-16	1.00e-16	116	...	...	...
IRAS 21101+5810	3.20e-15	3.00e-16	38	...	<1e-16	...
IRAS 21101+5810 A	<1e-16	1.00e-16	77	<1e-16	1.00e-16	1178
IRAS 21101+5810 B	1.40e-15	3.00e-16	269	1.20e-15	2.00e-16	266
UGC 12150 B	1.60e-15	3.00e-16	234	2.30e-15	3.00e-16	271
UGC 12150* A	2.00e-16	1.00e-16	273	...	<1e-16	...
IRAS F22491-1808*	6.00e-16	1.00e-16	148	4.00e-16	1.00e-16	110
NGC 7469	7.96e-14	2.80e-15	393	4.80e-15	2.80e-15	156
IC 5298	2.90e-15	3.00e-16	388	8.00e-16	2.00e-16	77
NGC 7674	2.21e-14	5.00e-16	737	...	<1e-16	...
IRAS F23365+3604*	1.70e-15	1.00e-16	337	6.00e-16	1.00e-16	223
IRAS 23436+5257 A	1.30e-15	1.00e-16	270	7.00e-16	1.00e-16	268
				9.00e-16	1.00e-16	159
				1.00e-15	1.00e-16	274
				4.47e-14	3.20e-15	163
				1.30e-15	1.00e-16	160
				5.00e-16	<1e-16	160
				2.00e-16	<1e-16	275
				1.00e-16	<1e-16	196
				4.00e+00	1.00e+00	281
				2.10e-15	2.00e-16	441
				...	<1e-16	...
				1.90e-15	1.00e-16	200
				2.63e-14	2.00e-15	163
				8.00e-16	1.00e-16	236
				1.00e-16	<1e-16	161
				...	<1e-16	...
				1.20e-15	1.00e-16	233
				1.19e-14	6.00e-16	279
				3.80e-15	1.00e-16	159
				6.00e-16	1.00e-16	278
				...	<1e-16	...
				1.20e-15	<1e-16	238
				5.00e-15	1.00e-16	768
				1.00e-16	1.00e-16	121
				3.00e-15	9.70e-15	77
				1.28e-14	1.10e-15	284
				1.70e-15	2.00e-16	361
				4.90e-15	3.00e-16	481
				9.00e-16	2.00e-16	233
				1.40e-15	<1e-16	359

Table 2.6—Continued

Name	He I ( $\lambda$ 1.0831)		Pa $\gamma$ ( $\lambda$ 1.0938)		[Fe II] ( $\lambda$ 1.2570)				
	F <sup>a</sup>	$\delta f$	F <sup>a</sup>	$\delta f$	F <sup>a</sup>	$\delta f$			
		FWHM <sup>b</sup>		FWHM <sup>b</sup>		FWHM <sup>b</sup>			
IRAS 23436+5257 B	2.10e-15	1.00e-16	270	1.10e-15	2.00e-16	153	2.10e-15	1.00e-16	200

<sup>a</sup>erg s<sup>-1</sup> cm<sup>-2</sup> - Not corrected for extinction.  
<sup>b</sup>km/s



Table 2.7. Strengths and Velocities of Strong Emission Lines

Name	Pa $\beta$ ( $\lambda$ 1.2818)			[Fe II] ( $\lambda$ 1.6440)			Pa $\alpha$ ( $\lambda$ 1.8751)		
	F <sup>a</sup>	$\delta f$	FWHM <sup>b</sup>	F <sup>a</sup>	$\delta f$	FWHM <sup>b</sup>	F <sup>a</sup>	$\delta f$	FWHM <sup>b</sup>
MCG-02-01-051	1.12e-14	2.00e-16	236	9.40e-15	2.00e-16	230	...	1.00e-16	...
UGC 02369 B	7.90e-15	1.00e-16	275	5.80e-15	1.00e-16	267	8.81e-14	1.10e-14	223
UGC 02369 A	4.80e-15	<1e-16	118	2.50e-15	1.00e-16	153	7.83e-14	5.20e-15	178
NGC 1275*	2.43e-14	4.00e-16	1076	3.78e-14	5.00e-16	503	...	...	...
UGC 04881 A	2.30e-15	1.00e-16	233	1.50e-15	2.00e-16	227	3.32e-14	1.10e-15	221
UGC 04881 B	1.80e-15	1.00e-16	156	2.30e-15	2.00e-16	265	3.46e-14	1.70e-15	266
UGC 05101	9.20e-15	5.00e-16	311	8.20e-15	1.10e-15	529	6.52e-14	1.07e-14	446
NGC 3221	...	...	...	...	<1e-16	...	...	5.00e-16	...
NGC 4922 B	...	...	...	...	<1e-16	...	...	<1e-16	...
NGC 4922 A	1.65e-14	3.00e-16	198	8.30e-15	2.00e-16	231	3.05e-14	5.00e-15	226
CGCG 043-099	8.10e-15	2.00e-16	429	4.10e-15	2.00e-16	454	5.34e-14	3.50e-15	402
MCG -02-33-098	1.47e-14	7.00e-16	200	1.98e-14	5.00e-16	155	...	<1e-16	...
VV 250* B	5.10e-15	2.00e-16	236	...	<1e-16	...	1.49e-14	2.30e-15	90
VV 250 A	5.42e-14	4.00e-16	353	2.14e-14	4.00e-16	381	2.11e-13	3.90e-15	360
UGC 08387 obs2	1.55e-14	2.00e-16	277	9.20e-15	2.00e-16	307	1.16e-13	1.20e-14	226
UGC 08387	4.22e-14	5.00e-16	158	2.37e-14	4.00e-16	192	4.40e-13	7.33e-13	317
NGC 5104	2.60e-15	2.00e-16	278	2.70e-15	4.00e-16	348	...	<1e-16	...
NGC 5256 A	7.40e-15	2.00e-16	354	1.08e-14	2.00e-16	383	...	<1e-16	...
NGC 5256 B	7.80e-15	2.00e-16	433	5.20e-15	2.00e-16	460	...	<1e-16	...
UGC 08696*	6.43e-14	2.40e-15	585	7.88e-14	2.10e-15	570	4.00e-13	4.72e-13	89
UGC 08739*	3.37e-13	1.43e-13	199	4.99e-13	1.12e-13	77	4.66e-11	5.86e-11	2352
NGC 5331 B	4.25e-13	2.99e-14	274	...	<1e-16	...	6.12e-12	8.24e-13	312
NGC 5331 A	9.45e-13	2.87e-14	274	...	...	...	1.88e-11	1.74e-12	267
CGCG 247-020	1.16e-14	6.00e-16	197	7.50e-15	1.60e-15	192	...	8.00e-16	...
NGC 5653*	2.00e-15	3.00e-16	161	...	<1e-16	...	...	...	...
IRAS F14348-1447* A	...	...	...	...	<1e-16	...	...	...	...
IRAS F14348-1447* B	...	...	...	...	<1e-16	...	1.93e-14	5.00e-16	298
CGCG 049-057	3.30e-15	2.00e-16	160	...	<1e-16	...	3.93e-14	1.00e-15	298
VV 705 A	1.43e-14	3.00e-16	156	1.20e-15	3.00e-16	194	...	...	...
				1.29e-14	3.00e-16	189	2.16e-13	2.10e-15	177

Table 2.7—Continued

Name	Pa $\beta$ ( $\lambda$ 1.2818)			[Fe II] ( $\lambda$ 1.6440)			Pa $\alpha$ ( $\lambda$ 1.8751)		
	F <sup>a</sup>	$\delta f$	FWHM <sup>b</sup>	F <sup>a</sup>	$\delta f$	FWHM <sup>b</sup>	F <sup>a</sup>	$\delta f$	FWHM <sup>b</sup>
VV 705 B	2.20e-15	2.00e-16	272	2.60e-15	1.00e-16	303	2.84e-14	8.00e-16	265
IRAS F15250+3608	4.03e-14	1.79e-14	38	5.90e-15	3.00e-16	336	3.09e-14	1.60e-15	218
NGC 5936	1.15e-13	1.60e-15	160	8.20e-14	4.50e-15	156	1.44e-12	1.43e-13	45
NGC 6090 A	6.00e-15	1.00e-16	157	3.10e-15	1.00e-16	153	...	1.00e-16	...
NGC 6090 B	2.60e-15	1.00e-16	118	1.20e-15	<1e-16	153	...	...	...
IRAS F17132+5313 A	...	...	...	4.00e-16	<1e-16	262	9.00e-15	2.00e-16	263
IRAS F17132+5313 B	...	...	...	1.00e-16	<1e-16	150	2.70e-15	2.00e-16	219
IRAS 18090+0130 A	7.00e-16	1.00e-16	393	9.00e-16	1.00e-16	268	...	<1e-16	...
IRAS 18090+0130 B	4.80e-15	1.00e-16	432	4.20e-15	2.00e-16	421	...	...	...
IRAS 18090+0130 C	...	...	...	4.00e-16	1.00e-16	77	9.05e-14	2.20e-13	2060
NGC 6670	4.50e-15	1.00e-16	157	3.40e-15	1.00e-16	153	4.09e-14	1.70e-15	134
NGC 6701	3.16e-14	2.20e-15	120	3.59e-14	3.30e-15	156	...	1.00e-16	...
ESO 593-IG008	...	...	...	1.30e-15	2.00e-16	263	3.19e-14	3.10e-15	263
NGC 6786	4.00e-16	<1e-16	158	2.00e-16	<1e-16	154	7.60e-15	3.70e-15	674
IRAS F19297-0406	...	...	...	5.50e-15	9.00e-16	545	4.44e-14	4.00e-16	297
IRAS 19542+1110	...	...	...	2.20e-15	3.00e-16	260	2.94e-14	9.00e-16	347
IRAS 20351+2521	3.24e-14	8.00e-16	235	2.06e-14	1.90e-15	191	3.38e-13	1.07e-14	178
II Zw 096	1.00e-15	1.00e-16	156	...	...	...	2.31e-14	2.90e-15	267
IRAS 21101+5810	3.40e-15	2.00e-16	234	3.00e-15	2.00e-16	303	7.30e-14	1.18e-13	44
IRAS 21101+5810 A	...	<1e-16	...	...	<1e-16	...	...	<1e-16	...
IRAS 21101+5810 B	4.90e-15	1.00e-16	234	3.50e-15	1.00e-16	228	6.88e-14	1.02e-14	222
UGC 12150 B	5.20e-15	2.00e-16	238	6.20e-15	5.00e-16	347	3.91e-14	1.35e-14	50
UGC 12150* A	3.00e-16	<1e-16	79	3.00e-16	1.00e-16	116	...	<1e-16	...
IRAS F22491-1808*	8.00e-15	2.80e-15	75	1.40e-15	3.00e-16	219	1.04e-14	6.00e-16	214
NGC 7469	6.11e-14	2.40e-15	279	2.72e-14	1.10e-15	271	...	<1e-16	...
IC 5298	3.20e-15	2.00e-16	315	...	<1e-16	...	...	4.00e-15	...
NGC 7674	1.05e-14	4.00e-16	551	9.20e-15	4.00e-16	498	2.80e-15	1.31e-14	134
IRAS F23365+3604*	1.00e-14	3.36e-14	114	2.60e-15	2.00e-16	185	4.45e-14	6.00e-16	216
IRAS 23436+5257 A	3.00e-15	1.00e-16	274	2.90e-15	1.00e-16	343	1.46e-14	5.96e-14	178

Table 2.7—Continued

Name	Pa $\beta$ ( $\lambda$ 1.2818)		[Fe II] ( $\lambda$ 1.6440)		Pa $\alpha$ ( $\lambda$ 1.8751)				
	F <sup>a</sup>	$\delta f$	FWHM <sup>b</sup>	F <sup>a</sup>	$\delta f$	FWHM <sup>b</sup>			
IRAS 23436+5257 B	4.40e-15	1.00e-16	235	3.60e-15	1.00e-16	152	3.31e-14	4.90e-15	178

<sup>a</sup>erg s<sup>-1</sup> cm<sup>-2</sup> - Not corrected for extinction.

<sup>b</sup>km/s

Table 2.8. Strengths and Velocities of Strong Emission Lines

Name	Br $\delta$ ( $\lambda$ 1.9450)			He I ( $\lambda$ 2.0580)			H <sub>2</sub> S(1)-0 ( $\lambda$ 2.1213)			Br $\gamma$ ( $\lambda$ 2.1655)		
	F <sup>a</sup>	$\delta f$	FWHM <sup>b</sup>	F <sup>a</sup>	$\delta f$	FWHM <sup>b</sup>	F <sup>a</sup>	$\delta f$	FWHM <sup>b</sup>	F <sup>a</sup>	$\delta f$	FWHM <sup>b</sup>
MCG-02-01-051	7.20e-15	1.10e-15	86	1.07e-14	4.00e-16	163	8.10e-15	6.00e-16	238	2.61e-14	6.00e-16	233
UGC 02369 B	3.60e-15	6.00e-16	172	4.70e-15	2.00e-16	203	1.03e-14	2.00e-16	197	1.51e-14	3.00e-16	193
UGC 02369 A	2.80e-15	3.00e-16	86	3.20e-15	1.00e-16	122	...	...	...	9.70e-15	2.00e-16	155
NGC 1275*	...	<1e-16	...	1.40e-15	3.00e-16	165	2.70e-14	2.00e-16	320	4.00e-15	2.00e-16	744
UGC 04881 A	2.00e-15	5.00e-16	256	1.40e-15	2.00e-16	202	5.00e-15	4.00e-16	235	5.00e-15	3.00e-16	268
UGC 04881 B	...	<1e-16	...	...	<1e-16	...	9.60e-15	5.00e-16	274	5.90e-15	5.00e-16	268
UGC 05101	...	<1e-16	...	1.50e-15	3.00e-16	404	1.68e-14	6.00e-16	430	6.80e-15	5.00e-16	574
NGC 3221	...	<1e-16	...	...	<1e-16	...	...	...	...	1.10e-15	4.00e-16	39
NGC 4922 B	...	<1e-16	...	...	<1e-16	...	...	...	...	<1e-16	<1e-16	39
NGC 4922 A	2.40e-15	4.00e-16	131	1.80e-15	1.00e-16	164	4.70e-15	1.00e-16	159	5.90e-15	1.00e-16	156
CGCG 043-099	1.80e-15	4.00e-16	301	1.30e-15	1.00e-16	365	4.30e-15	1.00e-16	431	4.80e-15	1.00e-16	498
MCG -02-33-098	4.00e-15	5.00e-16	88	2.80e-15	4.00e-16	207	...	...	...	3.50e-15	6.00e-16	118
VV 250* B	1.20e-15	1.10e-15	216	5.00e-16	2.00e-16	82	...	...	...	2.20e-15	5.00e-16	193
VV 250 A	1.00e-14	7.00e-16	303	1.16e-14	2.00e-16	326	6.80e-15	1.00e-16	355	2.13e-14	2.00e-16	386
UGC 08357 obs2	4.00e-15	7.00e-16	218	3.80e-15	1.00e-16	288	8.30e-15	1.00e-16	318	9.80e-15	1.00e-16	311
UGC 08387	1.09e-14	1.90e-15	218	1.11e-14	5.00e-16	164	1.86e-14	4.00e-16	199	2.78e-14	6.00e-16	195
NGC 5104	4.50e-15	1.60e-15	2441	1.80e-15	5.00e-16	82	5.80e-15	8.00e-16	280	8.60e-15	8.00e-16	548
NGC 5256 A	3.90e-15	1.00e-15	216	3.50e-15	2.00e-16	367	1.22e-14	4.00e-16	356	8.10e-15	4.00e-16	349
NGC 5256 B	5.10e-15	1.00e-15	129	5.00e-15	4.00e-16	448	7.00e-15	7.00e-16	435	1.40e-14	5.00e-16	504
UGC 08696*	...	<1e-16	...	2.17e-14	2.80e-15	364	2.25e-13	3.90e-15	471	8.69e-14	5.90e-15	499
UGC 08739*	1.09e-12	5.09e-13	175	6.75e-13	2.66e-13	83	4.01e-12	4.89e-13	200	1.99e-12	5.63e-13	118
NGC 5331 B	...	<1e-16	...	5.76e-14	3.72e-14	41	7.37e-13	7.82e-14	394	7.59e-13	6.60e-14	424
NGC 5331 A	7.17e-13	1.92e-13	215	4.71e-13	7.03e-14	203	2.65e-12	1.22e-13	355	2.41e-12	9.65e-14	309
CGCG 247-020	1.50e-15	1.70e-15	87	4.00e-15	5.00e-16	123	1.15e-14	1.00e-15	159	1.47e-14	5.00e-16	155
NGC 5653*	...	<1e-16	...	...	<1e-16	...	7.00e-16	2.00e-16	201	6.00e-16	2.00e-16	158
IRAS F14348-1447* A	6.00e-16	2.00e-16	369	1.90e-15	3.00e-16	485	5.00e-15	4.00e-16	226	3.90e-15	7.00e-16	258
IRAS F14348-1447* B	2.20e-15	5.00e-16	164	1.50e-15	3.00e-16	155	1.07e-14	6.00e-16	263	5.70e-15	1.50e-15	331
CGCG 049-057	...	<1e-16	...	4.00e-16	1.00e-16	166	3.70e-15	1.00e-16	201	1.50e-15	1.00e-16	197
VV 705 A	...	<1e-16	...	1.31e-14	4.00e-16	161	1.47e-14	4.00e-16	156	3.11e-14	4.00e-16	153
VV 705 B	...	<1e-16	...	1.60e-15	2.00e-16	282	5.80e-15	3.00e-16	313	...	...	...
IRAS F15250+3608	1.30e-15	3.00e-16	341	1.80e-15	2.00e-16	159	7.30e-15	3.00e-16	231	4.80e-15	4.00e-16	189
NGC 5936	1.50e-15	3.00e-16	168	4.19e-14	4.90e-15	124	8.53e-14	6.90e-15	120	1.78e-13	6.40e-15	79
NGC 6090 A	4.30e-15	5.00e-16	86	5.40e-15	1.00e-16	122	3.60e-15	2.00e-16	198	1.24e-14	2.00e-16	116
NGC 6090 B	1.20e-15	2.00e-16	129	2.10e-15	1.00e-16	122	2.20e-15	1.00e-16	119	4.50e-15	1.00e-16	116
IRAS F17132+5313 A	4.00e-16	<1e-16	211	1.00e-15	<1e-16	519	7.00e-16	<1e-16	271	1.30e-15	1.00e-16	379
IRAS F17132+5313 B	...	<1e-16	...	3.00e-16	<1e-16	199	4.00e-16	<1e-16	193	3.00e-16	<1e-16	190
IRAS 18090+0130 A	...	<1e-16	...	1.00e-15	1.00e-16	285	2.60e-15	2.00e-16	316	2.20e-15	1.00e-16	232
IRAS 18090+0130 B	7.00e-16	4.00e-16	43	3.20e-15	4.00e-16	285	1.04e-14	5.00e-16	396	1.31e-14	4.00e-16	504
IRAS 18090+0130 C	...	<1e-16	...	...	<1e-16	...	...	...	...	2.00e-16	1.00e-16	39
NGC 6670	2.80e-15	4.00e-16	129	3.60e-15	2.00e-16	204	4.30e-15	3.00e-16	158	8.80e-15	3.00e-16	155

Table 2.8—Continued

Name	Br $\delta$ ( $\lambda$ 1.9450)			He I ( $\lambda$ 2.0580)			H $\alpha$ S(1)1-0 ( $\lambda$ 2.1213)			Br $\gamma$ ( $\lambda$ 2.1655)		
	F <sup>a</sup>	$\delta f$	FWHM <sup>b</sup>	F <sup>a</sup>	$\delta f$	FWHM <sup>b</sup>	F <sup>a</sup>	$\delta f$	FWHM <sup>b</sup>	F <sup>a</sup>	$\delta f$	FWHM <sup>b</sup>
NGC 6701	...	<1e-16	...	1.22e-14	5.20e-15	124	7.19e-14	4.80e-15	121	4.88e-14	5.20e-15	79
ESO 593-IG008	1.30e-15	4.00e-16	42	1.30e-15	4.00e-16	480	4.90e-15	5.00e-16	466	6.40e-15	6.00e-16	380
NGC 6786	3.00e-16	1.00e-16	173	2.00e-16	<1e-16	123	3.00e-16	<1e-16	159	6.00e-16	<1e-16	156
IRAS F19297-0406	2.10e-15	5.00e-16	205	1.90e-15	2.00e-16	309	9.80e-15	4.00e-16	338	7.60e-15	5.00e-16	367
IRAS 19542+1110	...	<1e-16	...	1.10e-15	4.00e-16	276	8.80e-15	4.00e-16	230	3.80e-15	4.00e-16	263
IRAS 20351+2521	...	<1e-16	...	1.89e-14	1.10e-15	203	3.25e-14	1.70e-15	236	6.09e-14	3.20e-15	231
II Zw 096	...	<1e-16	...	3.00e-16	2.00e-16	81	1.80e-15	3.00e-16	79	2.20e-15	7.00e-16	308
IRAS 21101+5810 A	...	<1e-16	...	2.80e-15	3.00e-16	202	7.20e-15	5.00e-16	235	1.06e-14	6.00e-16	268
IRAS 21101+5810 B	...	<1e-16	...	...	<1e-16	...	3.00e-16	1.00e-16	1213	...	...	...
UGC 12150 B	...	<1e-16	...	4.10e-15	2.00e-16	202	6.60e-15	2.00e-16	274	1.26e-14	2.00e-16	269
UGC 12150* A	...	<1e-16	...	2.50e-15	5.00e-16	205	1.86e-14	7.00e-16	319	1.33e-14	7.00e-16	273
IRAS F22491-1808*	...	<1e-16	...	1.00e-16	1.00e-16	41	8.00e-16	1.00e-16	120	5.00e-16	1.00e-16	39
NGC 7469	...	<1e-16	...	6.00e-16	2.00e-16	117	3.00e-15	3.00e-16	264	1.40e-15	5.00e-16	296
IC 5298	...	<1e-16	...	1.55e-14	2.40e-15	206	3.19e-14	3.80e-15	240	1.06e-13	3.70e-15	470
NGC 7674	...	<1e-16	...	2.20e-15	4.00e-16	245	8.40e-15	6.00e-16	277	6.30e-15	3.00e-16	194
IRAS F23365+3604*	2.10e-15	4.00e-16	167	2.00e-15	4.00e-16	122	6.30e-15	1.20e-15	237	1.29e-14	6.00e-16	310
IRAS 23436+5257 A	1.50e-15	3.00e-16	215	2.10e-15	2.00e-16	197	8.50e-15	2.00e-16	229	7.40e-15	3.00e-16	225
IRAS 23436+5257 B	1.60e-15	4.00e-16	43	1.90e-15	1.00e-16	284	3.30e-15	1.00e-16	236	5.60e-15	2.00e-16	347
				1.90e-15	2.00e-16	122	8.20e-15	2.00e-16	197	7.60e-15	2.00e-16	193

<sup>a</sup> erg s<sup>-1</sup> cm<sup>-2</sup> - Not corrected for extinction.<sup>b</sup> km/s

A salient characteristic of these spectra is the presence of strong, mostly narrow line emission from the Paschen series ( $\text{Pa}\alpha$ ,  $\text{Pa}\beta$ ,  $\text{Pa}\gamma$ , and  $\text{Pa}\delta$ ) as well as the  $[\text{S III}]$  line at  $\lambda 9530$ . Many spectra lack good detections of  $\text{Pa}\alpha$  and  $\text{Pa}\gamma$  due to atmospheric water absorption in those wavelength regions. In addition to the strong Paschen emission, the spectra contain predominantly weaker emission from Brackett  $\gamma$  and  $\delta$ , warm  $\text{H}_2$ , and  $[\text{Fe II}]$  at  $\lambda 16440$  and  $\lambda 12570$ . Faint emission is occasionally detected from  $\text{C I } \lambda 9850$ . Some lines are observed which we have yet to identify (e.g.  $1.2475\mu\text{m}$  in NGC 5256). The warm  $\text{H}_2$   $\text{S}(1)1-0$  line at  $\lambda 21213$  emission is the strongest of the molecular hydrogen lines. The flux from this line tends to be comparable to or slightly stronger than that of  $\text{Br}\gamma$ . The coronal  $[\text{Si VI}] \lambda 1.962 \mu\text{m}$  emission line, a detection of which would be a signature of photoionization by the hard ionizing continuum of an AGN, is not detected in any of the spectra presented here. Further discussion of the search for  $[\text{Si VI}]$  emission is presented in §2.4.1.

Strong stellar absorption from the Brackett series and  $\Delta\nu = 3$  CO bands is sometimes observed in the  $H$ -band. The Brackett series absorption feature at  $1.64 \mu\text{m}$  frequently overlaps with the  $[\text{Fe II}]$  emission feature at this wavelength, rendering the strength of that line an uncertain diagnostic marker for comparisons between galaxies with differing star formation histories. In §2.4, we focus on the  $[\text{Fe II}]$  feature at  $1.257 \mu\text{m}$ , in part, to avoid this ambiguity. Stellar absorption features arising in the atmospheres of cool giant or supergiant stars from the  $\Delta\nu = 2$  transitions of CO are also commonly present in the  $K$ -band. In some galaxies, strong stellar absorption features and no emission lines are observed (e.g. NGC 4922, aperture 2).

## 2.4 DISCUSSION

The high quality of the spectra provide many opportunities for detailed analysis. As stated in §1, the focus for the remainder of this paper will be on the ionization processes occurring in these galaxies as traced by near-infrared emission lines. Detailed line kinematics will be addressed in Chapter 3.

First we focus on a search for broad line regions, with the prior assumption that perhaps in such dusty systems, evidence of a broad line region which is masked at visible wavelengths may be revealed in observations in the near-infrared, where light suffers far less extinction due to dust. Similarly we search for evidence of AGN stimulated coronal emission lines, chiefly the [Si VI] feature at  $1.962\ \mu\text{m}$ . We also construct the near-infrared diagnostic diagram of  $\text{H}_2\ 2.121\ \mu\text{m}/\text{Brackett } \gamma$  vs. [Fe II]  $1.257\ \mu\text{m}/\text{Paschen } \beta$  as proposed in the context of LINERs by Larkin et al. (1998) and given further consideration regarding luminous AGN by Rodríguez-Ardila et al. (2004, 2005). Following Riffel et al. (2013) we compare our points on this diagram to a sample of low luminosity galaxies from the literature. We also investigate the distribution of the various optical classes within our sample on the near-infrared diagnostic diagram. In a related exercise, we construct a similar diagram using [S III]  $0.9853\ \mu\text{m}/\text{Paschen } \delta$  in place of  $\text{H}_2\ 2.121\ \mu\text{m}/\text{Brackett } \gamma$ . We compare our data points' locations of this diagram with predictions from the computational models of stellar photoionization and fast radiative shocks from the Mappings III code (Allen et al. 2008; Levesque et al. 2010).

### 2.4.1 AGN

Following Veilleux et al. (1997, 1999), we examine the spectra for the presence of broad ( $\text{FWHM} > 1000\ \text{km s}^{-1}$ ) hydrogen recombination lines and emission from

the high ionization [Si VI] line which are both indicative of AGN. In addition to detecting signatures of AGN in galaxies previously known to have optical evidence of AGN, the TripleSpec data allow the opportunity to detect AGN obscured by up to 10 magnitudes of visual extinction (e.g., Veilleux et al. 1997, 1999). A histogram of measured Br $\gamma$  line widths is shown in Figure 2.3. Most detections of this line have widths (FWHM),  $\Delta v_{\text{FWHM}} < 500$  km/s. The largest value of  $\Delta v_{\text{FWHM}}$  is 744 km s $^{-1}$  in NGC 1275. The observed values of FWHM in Br $\gamma$  do not represent line widths consistent with Doppler broadening in an AGN broad-line region, therefore we conclude there is no obvious evidence of AGN in the FWHMs of the detected Brackett $\gamma$  emission lines.

Figure 2.4 shows the FWHM distribution for the H $\alpha$  lines for most of the same LIRGs (all but NGC 1275, NGC 5331, IRAS 18090+0130, NGC 6786, IRAS 19542+1110, IRAS 20351+2521, IRAS 21101+5810, and IRAS 23436+5257) from Kim et al. (1995). The distribution of optical FWHMs roughly matches the distribution of near-IR FWHMs, with a peak at a few hundred km s $^{-1}$  and a tail of larger velocities truncating at about 800 km s $^{-1}$ . The low FWHM cut-off in Figure 2.4 can be explained by noting that the spectrograph used by Kim et al. (1995) had a resolution limit of  $\sim 400$  km s $^{-1}$ . Of the 45 LIRG nuclei represented in both diagrams, 38 (84%) are found to have Br $\gamma$  FWHM less than the 400 km s $^{-1}$  resolution limit of the spectrograph used by Kim et al. (1995).

Trends between the line width and the *IRAS* 25-to-60 $\mu$ m flux density ratio were also examined. A comparison is shown in Figure 2.5. This IR ratio is known to correlate with the presence or absence of an AGN, with values of the ratio above 0.2 being indicative of an AGN due to strong dust heating contributions from the accretion disk around 25 $\mu$ m (e.g., see Sanders et al. 1988). There is no trend connecting line width



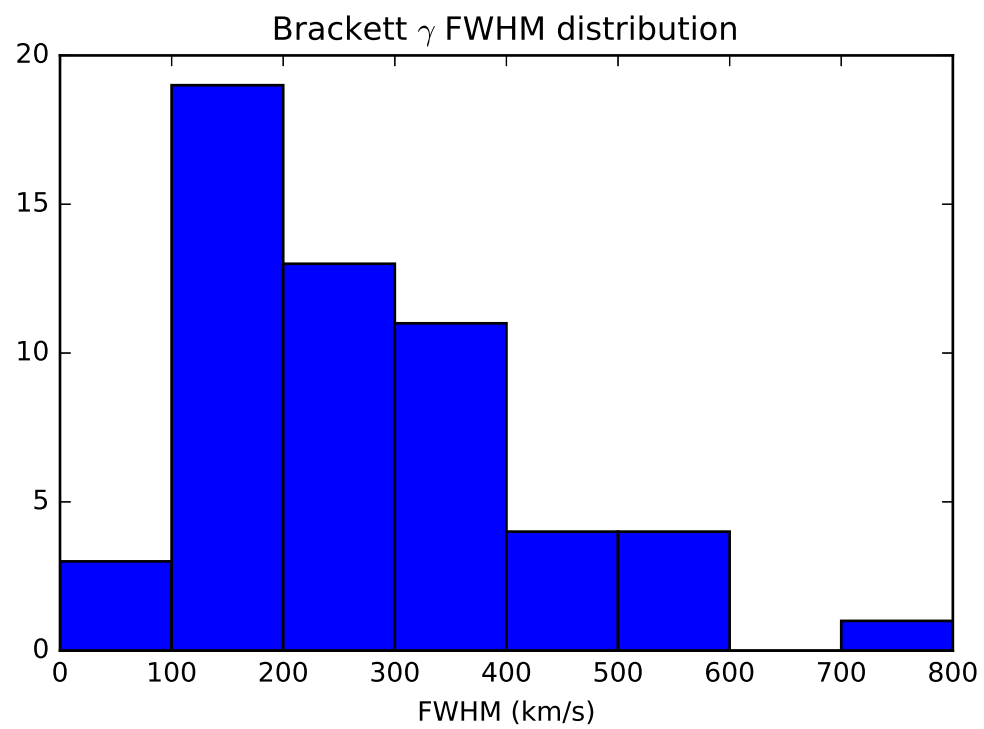


Fig. 2.3.— Histogram of all Brackett  $\gamma$   $\lambda 2.16 \mu\text{m}$  line widths measured from line fits described in Chapter 4.

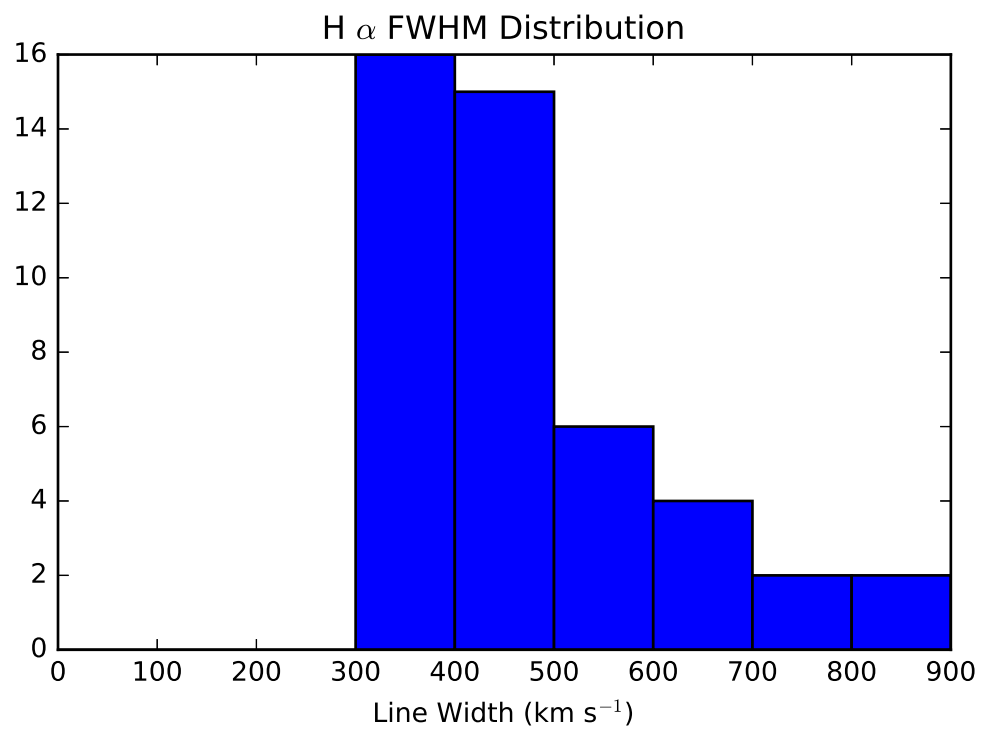


Fig. 2.4.— Histogram of all  $H\alpha$   $\lambda 0.5653\ \mu\text{m}$  line widths of a comparable sample from Kim et al. (1995)

and IRAS photometry, however NGC 1275, which has an outlying value of  $\Delta v_{\text{FWHM}} = 744 \text{ km s}^{-1}$  is a warm LIRG.

In addition to the *IRAS* 25-to-  $60\mu\text{m}$  flux density ratio, we also inspected our data in the context of the sources' mid infrared AGN markers. Ten of the 42 systems presented here have previous detections of  $[\text{Ne V}] \lambda 14.3 \mu\text{m}$  emission (ionization potential = 96 eV Petric et al. 2011), indicating excitation by an AGN. Within the mid-infrared band, equivalent widths of PAH emission lines are often cited as inverse gauges of AGN activity. This is due to the AGN both destroying PAHs and driving up the continuum contribution of warm dust. Nine of these 42 systems have a  $6.2\mu\text{m}$  PAH equivalent width lower than  $0.25 \mu\text{m}$  (Stierwalt et al. 2013). Each object which possesses at least one of these two AGN signatures is also classified by optical emission line ratios as either a Seyfert galaxy or a LINER. In concert, twelve of the 42 LIRGs presented here are detected in  $[\text{Ne V}]$  and/or have a  $6.2\mu\text{m}$  PAH equivalent width lower than  $0.25$ . Although none of the Brackett  $\gamma$  line FWHMs are broad enough ( $> 1000 \text{ km s}^{-1}$ ) to suggest the presence of a broad-line region, NGC 1275, NGC 7469, and NGC 7674 contain weak yet broad components within their near-IR recombination lines, constituting kinematic evidence for the presence of a broad line region. These components are shown in chapter 3. Therefore eight of the 42 LIRGs studied in this work present mid-IR markers for AGN activity, but only three of those eight present kinematic evidence for AGN activity within the TripleSpec bandpass.

In searching for the coronal  $[\text{Si VI}] \lambda 1.962 \mu\text{m}$  emission line (ionization potential = 167 eV), which indicates the hard ionizing continuum of an AGN accretion disk, previous studies such as Veilleux et al. (1997b, 1999b) were limited by the spectral resolution of their instruments. In contrast, our data achieves the requisite resolution to distinguish the  $[\text{Si VI}] \lambda 1.962 \mu\text{m}$  from the nearby line  $\text{H}_2 \lambda 1.958 \mu\text{m}$ .

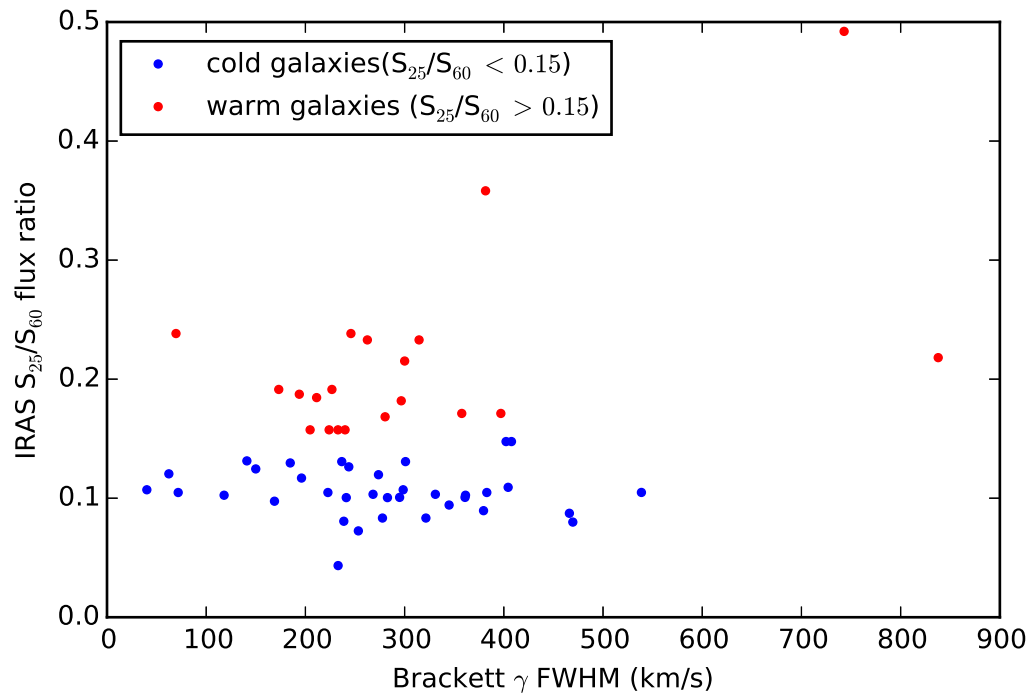


Fig. 2.5.—  $IRAS f_{\nu}(25 \mu\text{m})/f_{\nu}(60 \mu\text{m})$  plotted as a function of  $\Delta v_{\text{FWHM}}$  for the detections of Brackett  $\gamma$ . In the case of ULIRGs, objects with  $f_{\nu}(25 \mu\text{m})/f_{\nu}(60 \mu\text{m}) > 0.2$ , the so-called “warm” ULIRGs, show a tendency toward later merger stages and AGN activity (Sanders et al. 1988; Veilleux et al. 2002).

Despite documented cases of [Si VI]  $\lambda 1.962 \mu\text{m}$  emission in three of the galaxies observed here (Müller-Sánchez et al. 2011; Rodríguez-Ardila et al. 2011; U et al. 2013, in NGC 7469, NGC 7674, and Mrk 273 respectively), no [Si VI] emission is detected in any of our spectra. ([Si XI]  $\lambda 1.9196$  in NGC 1275 is claimed by Edge et al. (2002), however Rodríguez-Ardila et al. (2011) give an upper limit.) A likely explanation for this is the comparatively large aperture used for the present study (out to 12 kpc in some cases). It is possible that detections of the faint [Si VI] line requires an extraction of the central nuclear region of LIRGs hosting AGN.

Regarding the broader issue that most optical Seyfert U/LIRGs included in this study lack detections of [Si VI] here or elsewhere, it is possible that near-IR coronal lines in U/LIRGs are a less common occurrence than in low-luminosity Seyfert Galaxies, due to the prevalence of thick dust screens in U/LIRGs (For example, compare Murphy et al. (2001) to near-IR searches in low-luminosity Seyferts.)

## 2.4.2 The Near-IR Diagnostic Diagram: [Fe II], H<sub>2</sub>, Shocks v. Photoionization

The technique of classifying galaxies according to their relative emission line ratios dates back at least to Baldwin et al. (1981). Veilleux & Osterbrock (1987) determined optical classifications (e.g., HII Region-like, Seyfert, and LINER) based on the [O III]  $\lambda 5007 / \text{H}\beta$ , [N II]  $\lambda 6583 / \text{H}\alpha$ , [S II] ( $\lambda 6716 + \lambda 6731$ )/ $\text{H}\alpha$ , and [O I]  $\lambda 6300 / \text{H}\alpha$  line ratios. For a full discussion of the origins and utility of these line ratios, we refer the reader to the excellent discussion in Veilleux & Osterbrock (1987). In this scheme, AGN galaxies (Seyferts and LINERs) are distinguished from H II region-like galaxies, because in AGN a significant fraction of ionizing radiation is manifested as X-rays.

This harder ionizing spectrum can penetrate more deeply into the neutral regions of nebulae, creating an extended partially ionized zone, thereby enhancing emission from species such as  $S^+$ ,  $O^0$ , and  $N^+$ . Emission from  $O^{++}$  arises due to photoionization by UV photons in the ionized zone, and thereby is used to gauge the overall strength of the ionizing source, be it AGN or Star Formation.

Kewley et al. (2001) showed that supernova induced shocks resulting from a starburst can plausibly place star formation dominated galaxies into the LINER and Seyfert region of the plot determined by Veilleux & Osterbrock (1987). As a response, the authors introduced a new classification system including a composite region between the H II like space and the Seyfert/LINER spaces. It is possible that galaxies within this composite region have their line emission driven by AGN continuum excitation, SN shock excitation, or a combination of both. Although galaxies lying in the composite region can be driven by a combination of star formation and AGN induced ionization, Rich et al. (2014) showed that for massive gas-rich mergers such as U/LIRGs in the composite region, it is likely that the primary drivers of ionization are star formation induced shocks. The above mentioned mechanism whereby shocks or hard ionizing continua create extended partially ionized zones leading to enhanced emission from metal lines applies to the production of radiation in the infrared [Fe II] lines as well, however shocks are important in enhancing the emission due to release of Fe into the gas phase from grains. There is a similar mechanism for the enhancement of  $H_2$  rovibrational emission, but only due to shocks, not X-Rays. According to Wolfire & Konigl (1991), shocks enhance the  $H_2$  emission via collisional excitation in gas which has been heated by a shock.

In the case of both [Fe II] and  $H_2$  lines (and in emission from all forbidden lines), collisional excitation in the partially ionized zone created by the shock is an important

process in raising the ratio of the line to that of the recombination lines, which are primarily driven by photoionization.

Although Simpson et al. (1996) show that for some Seyferts and starbursts, the  $[\text{Fe II}]/\text{Pa}\beta$  value is consistent with photoionization of normally abundant interstellar material, Mouri et al. (2000) show that the strength of  $[\text{Fe II}]$  emission is primarily correlated with extensive partially ionized zones created *either* via shocks *or* X-rays. It is important to note that X-rays (not merely UV photons) are required to maintain partially ionized zones which are suitably extended to produce strong  $[\text{Fe II}]$  (Simpson et al. 1996; Dors et al. 2012). Dors et al. (2012) present models that demonstrate that X-ray heating is capable of producing the trend observed in the  $[\text{Fe II}]/\text{Pa}\beta$  vs.  $\text{H}_2/\text{Br}\gamma$  diagram for Seyferts by Knop et al. (2001); Reunanen et al. (2002); Rodríguez-Ardila et al. (2004); and Riffel et al. (2006).

Larkin et al. (1998) proposed a near-infrared emission-line diagnostic diagram which compares the ratio of  $[\text{Fe II}] \lambda 12570/\text{Pa}\beta$  with  $\text{H}_2 \text{ 1-0 S(1)} \lambda 21218/\text{Br}\gamma$  to diagnose the dominant energy source in the near-infrared from observations of LINER nuclei. Active and star-forming galaxies were also examined in the context of this diagram in Rodríguez-Ardila et al. (2004, 2005) and Riffel et al. (2013). These studies found that higher values of both ratios correspond roughly to AGN or shock-dominated activity, while lower values correspond roughly to excitation dominated by star-formation photoionization.

Figure 2.6 is a plot of  $[\text{Fe II}] \lambda 12570/\text{Pa}\beta$  versus  $\text{H}_2 \text{ 1-0 S(1)} \lambda 21218/\text{Br}\gamma$  for our sample. For comparison, normal star-forming galaxies, low luminosity LINERs and a supernova remnant are plotted. These latter two classes are systems in which strong shocks, and thus stronger  $[\text{FeII}]$  and  $\text{H}_2$  ro-vibrational line emission may be present. Two features are evident from the figure. First, the majority of the LIRGs

lie between  $[\text{Fe II}] \lambda 12570/\text{Pa}\beta \sim 0.2\text{--}1.0$ , with three LIRGs having ratios greater than 10 and one system clearly having a ratio less than 0.1. Second, there is a strong overlap between the normal star-forming galaxies and half of the LIRGs in the sample, which is suggestive that stellar photoionization is the dominant process producing the measured near-infrared line ratios.

We attempted to correlate positions on the near-IR diagnostic diagram with PAH equivalent widths from Stierwalt et al. (2014). No particular relationship was observed. The comparison is shown in figure 2.7.

Additional clarity is revealed in the near-infrared diagnostic diagram by plotting the LIRGs as a function of optical emission line classification. Figure 2.8 shows our data on the  $[\text{Fe II}]/\text{Pa}\beta$  vs.  $\text{H}_2/\text{Br}\gamma$  diagram, with symbol colors denoting the classifications from Yuan et al. (2010) in the classification scheme of Veilleux & Osterbrock (1987). (Only the objects in our sample which have also been classified by Yuan et al. (2010) in the Veilleux and Osterbrock scheme appear here. Notably absent are II Zw 096 and NGC 1275). The optical classifications are correlated with the  $[\text{Fe II}]/\text{Pa}\beta$  ratio, but independent of  $\text{H}_2/\text{Br}\gamma$ , with LINERS occupying  $[\text{Fe II}]/\text{Pa}\beta \geq 0.4$  and H II-like systems in the regions where  $[\text{Fe II}]/\text{Pa}\beta \leq 0.4$ . Seyfert galaxies are located where  $[\text{Fe II}]/\text{Pa}\beta \approx 0.4$ . A notable exception to this trend is NGC 7469, optically classified as a Seyfert 1. In addition to the active nucleus, NGC 7469 contains a ring of star-formation within its central 1 kpc (Izumi et al. 2015). This ring of star formation possibly places NGC 7469 among the H II like galaxies rather than in line with the other Seyferts. Figure 2.8 also includes the near-infrared observations of the nucleus of M82 from Lester et al. (1990). These measurements are included as an example of a local universe shocked starburst. Somewhat counterintuitively M82 lies on the low end of the distribution of H II-like galaxies. A possible explanation is that the higher



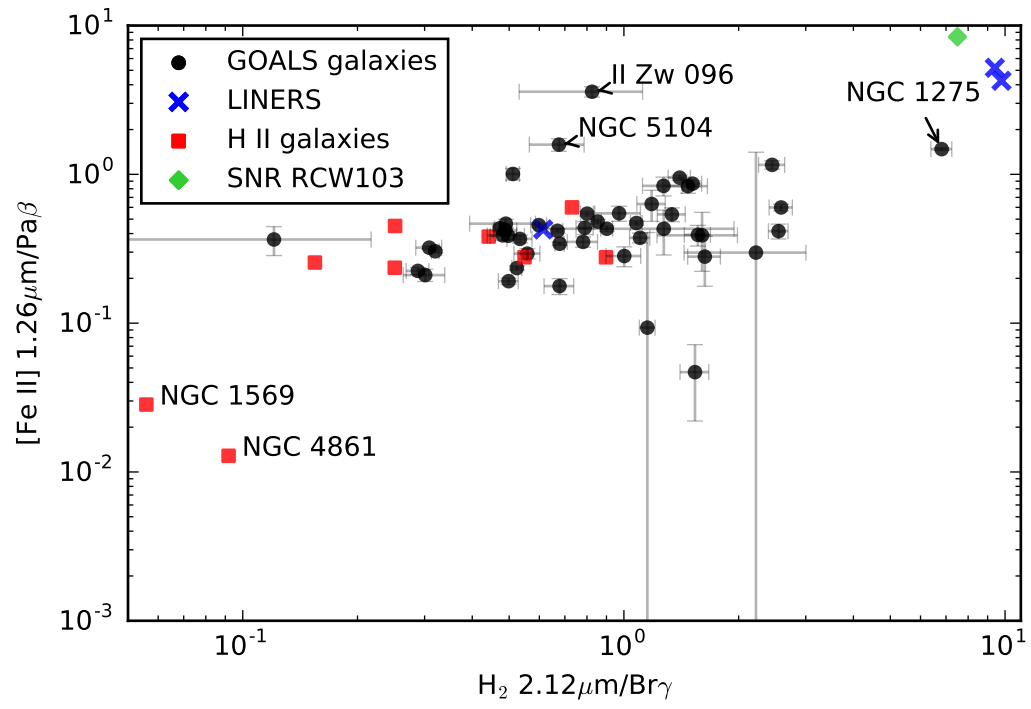


Fig. 2.6.— The canonical near-infrared line diagnostic diagram ( $[\text{Fe II}] \ \lambda 12570/\text{Pa}\beta$  versus  $\text{H}_2 \ 1-0 \ \text{S}(1) \ \lambda 21218/\text{Br}\gamma$ ) for our sample.

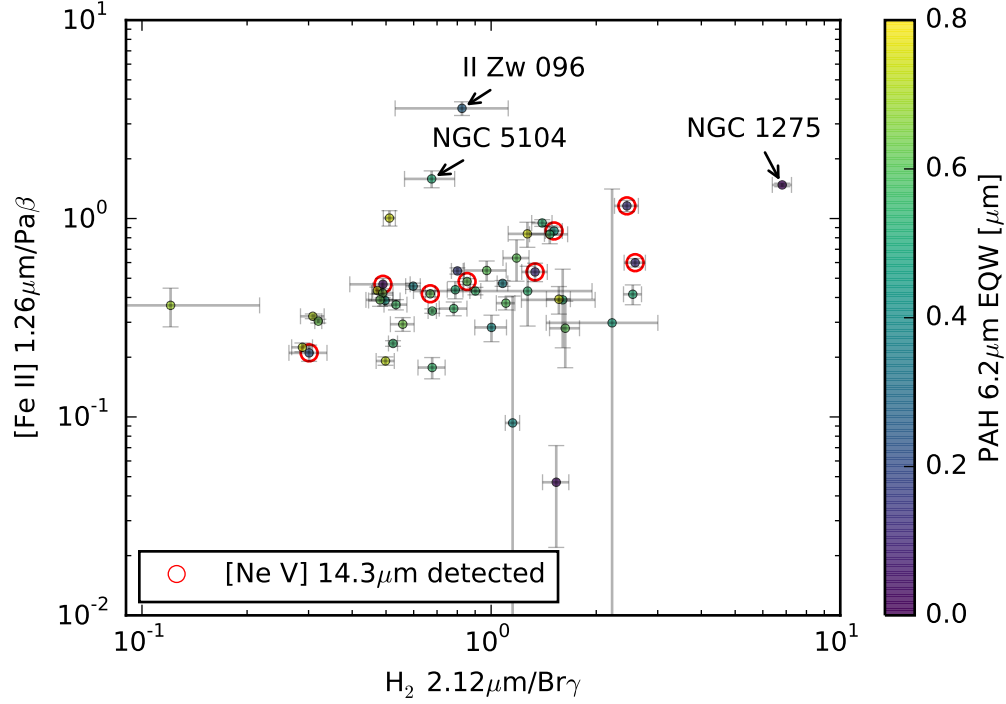


Fig. 2.7.— Our sample plotted on the near-infrared line diagnostic diagram ( $[\text{Fe II}] \lambda 12570 / \text{Pa}\beta$  versus  $\text{H}_2$  1-0 S(1)  $\lambda 21218 / \text{Br}\gamma$ ) compared with prominent mid-infrared markers of AGN activity. Data points are color coded according to their source's value of  $6.2 \mu\text{m}$  PAH equivalent width. Each source with a *Spitzer* detection of  $[\text{Ne V}] \lambda 14.5 \mu\text{m}$  is circled in red. There is no trend between the position on the diagram and the PAH equivalent width, however objects with detections of  $[\text{Ne V}]$  possess noticeably lower values of PAH equivalent width.

redshift LINERs in our sample may be understood to encapsulate a more intense starburst resulting in a more extended area of shock excitation. Quantitatively, this explanation is supported by a comparison of the global star formation rates for M82 and a typical LIRG; M82’s star formation rate is  $\sim 10 \text{ M}_{\odot} \text{ yr}^{-1}$  (Förster Schreiber et al. 2003) while LIRGs typically form stars at a rate nearly an order of magnitude larger.

LINERS are either low-luminosity Seyfert nuclei or predominantly star-forming systems distinguished by the presence of strong shocks. Larkin et al. (1998) identifies two continuous populations of LINERS based on their  $[\text{Fe II}]/\text{Pa}\beta$  ratios. Systems with intermediate values of this ratio are termed “weak”  $[\text{Fe II}]$  LINERS, while the higher valued systems are called “strong”  $[\text{Fe II}]$  LINERS. Strong  $[\text{Fe II}]$  LINERS tend to show auxiliary evidence for recent star formation and thus the high values of  $[\text{Fe II}]/\text{Pa}\beta$  are thought to arise from strong shocks driven by SNRs induced by the star formation. Weak  $[\text{Fe II}]$  LINERS are found to be more consistent with AGN activity based on detection of X-ray sources and broad optical recombination lines. These conclusions are supported by our finding that Seyfert galaxies lie on the low end of the LINER  $[\text{Fe II}]/\text{Pa}\beta$  spectrum.

As noted above, the optical classifications show no trend with  $\text{H}_2/\text{Br}\gamma$ . This suggests that the  $[\text{Fe II}]/\text{Pa}\beta$  is a more sensitive indicator of activity in the near-IR. This is reasonable, since iron is typically under-abundant in the gas phase except when grains have been dissociated by relatively fast shocks ( $v \sim 100 \text{ km s}^{-1}$ ) (Forbes & Ward 1993).

As an additional comparison, the LIRGs are plotted in Figure 2.9 as a function the optical emission line classification scheme derived from SDSS analysis utilizing the  $[\text{O III}] \lambda 5007 / \text{H}\beta$ ,  $[\text{N II}] \lambda 6583 / \text{H}\alpha$ ,  $[\text{S II}] (\lambda 6716 + \lambda 6731) / \text{H}\alpha$ , and  $[\text{O I}]$

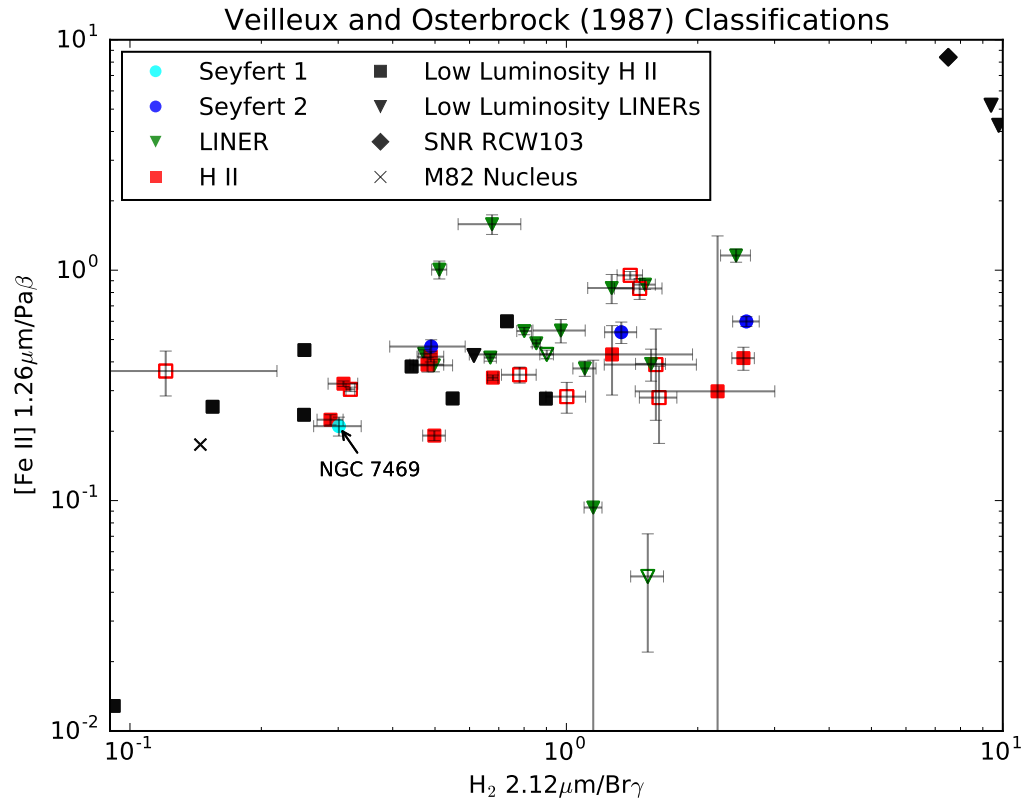


Fig. 2.8.— Open symbols indicate the optical classification does not agree in all three optical diagrams. This indicates that the data quality for that object was marginal, or the object represents a transitional object.

$\lambda 6300/\text{H}\alpha$  line ratios (see Kewley et al. 2006; Yuan et al. (2010)). In this scheme, a starburst+AGN “composite” region exists between the pure star-forming sequence (Kauffmann et al. 2003) and the maximum theoretical starburst line derived by Kewley et al. (2001). Our data is shown, color coded via its optical classification in the scheme from Yuan et al. (2010), on the  $[\text{Fe II}]/\text{Pa}\beta$  vs.  $\text{H}_2/\text{Br}\gamma$  diagram in Figure 2.9. LINER class disappears for our sample, having been replaced largely by composites. Additionally a few galaxies which were classified by Veilleux & Osterbrock (1987) as LINERs become Seyferts here, and a few which were classified as H II-like become composites as well. In Figure 2.9, there is a separation between the Seyferts and HII region-like galaxies as a function of  $[\text{Fe II}]/\text{Pa}\beta$ , however, the composites span the full range in  $[\text{Fe II}]/\text{Pa}\beta$ .

The obvious question is whether the position of a composite in Figure 2.9 is due to the level to which AGN or starbursts are driving the observed activity. To address this, we plot in Figure 2.10  $[\text{Fe II}]/\text{Pa}\beta$  as a function of the distance from the star-forming sequence in the  $[\text{O I}]/\text{H}\alpha$  vs.  $[\text{O III}]/\text{H}\beta$  diagram as given by Yuan et al. (2010). We observe no correlation between these parameters. We therefore conclude that the extent to which composite class objects are excited by AGN versus starburst activity has little bearing on their value of  $[\text{Fe II}]/\text{Pa}\beta$ .

Lastly, we find a scaling between the near-infrared  $[\text{Fe II}]/\text{Pa}\beta$  index and  $[\text{N II}]/\text{H}\alpha$ ,  $[\text{O I}]/\text{H}\alpha$ , and  $[\text{S II}]/\text{H}\alpha$  (Figures 2.11 - 2.13). These optical line ratios increase with increasingly extended shock regions within galaxies ??, so evidence of increasing  $[\text{Fe II}]/\text{Pa}\beta$  as a function of these optical ratios is consistent with the infrared ratio being a useful tool for assessing the relative strength of shocks within these extreme galaxies.

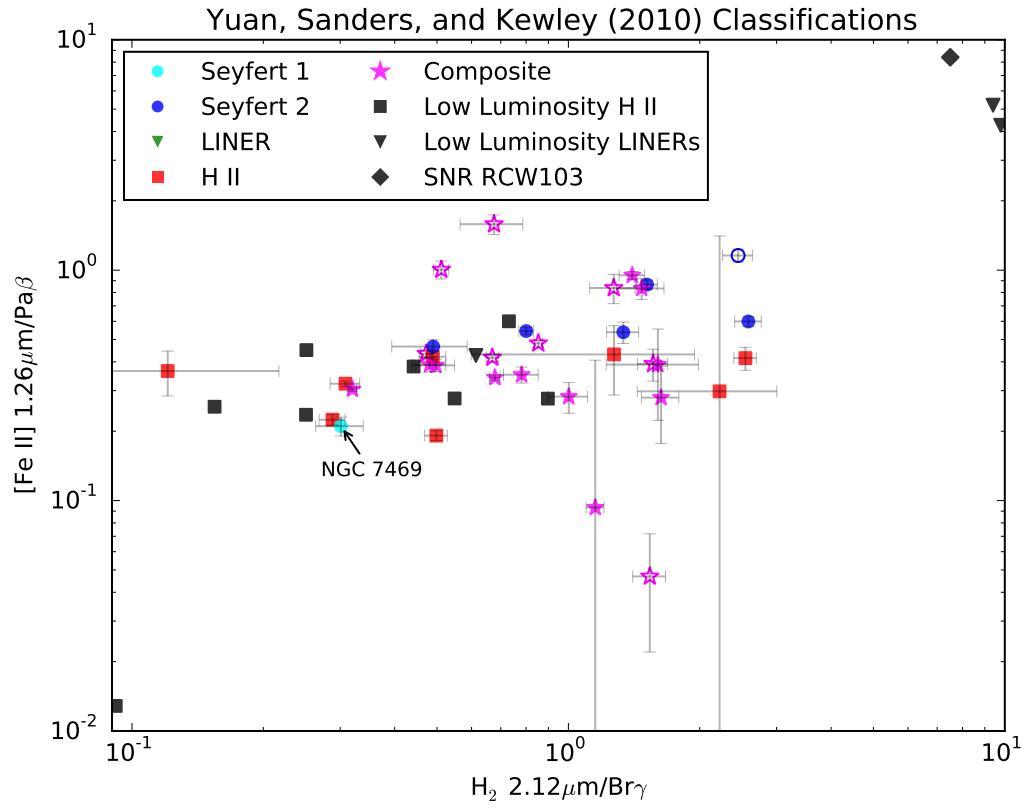


Fig. 2.9.— Open symbols indicate the optical classification does not agree in all three optical diagrams. This indicates that the data quality for that object was marginal, or the object represents a transitional object.

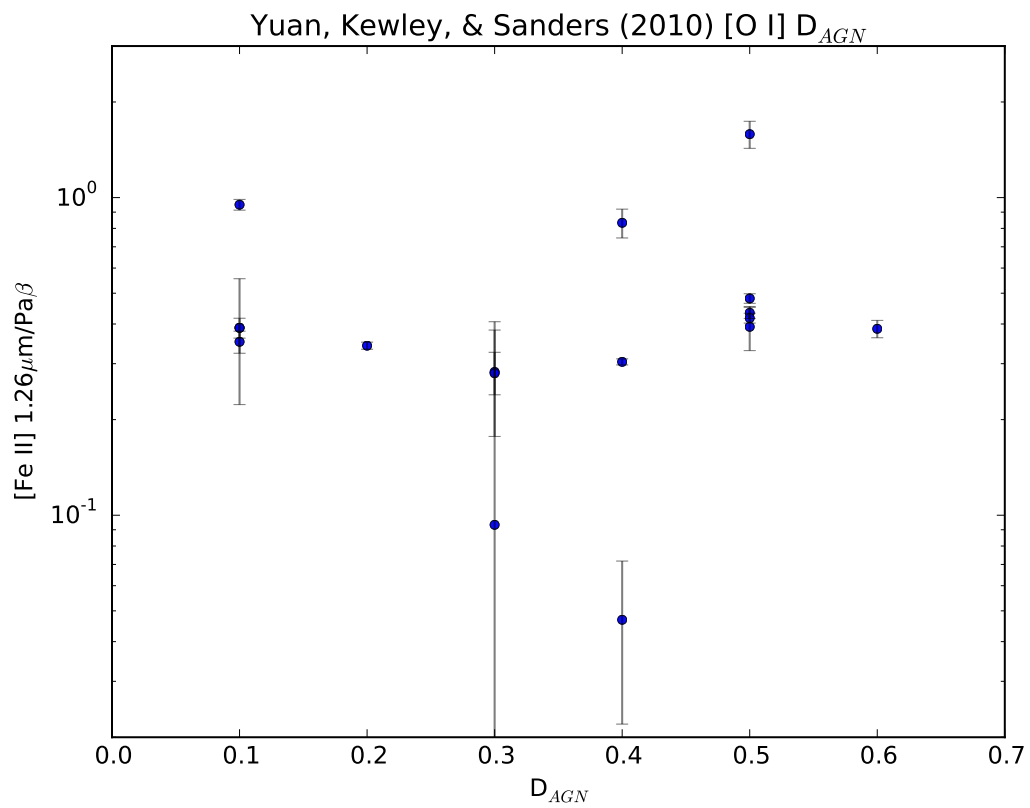


Fig. 2.10.—  $[\text{Fe II}]/\text{Paschen } \beta$  plotted as a function of distance from the star forming sequence of the BPT diagram.

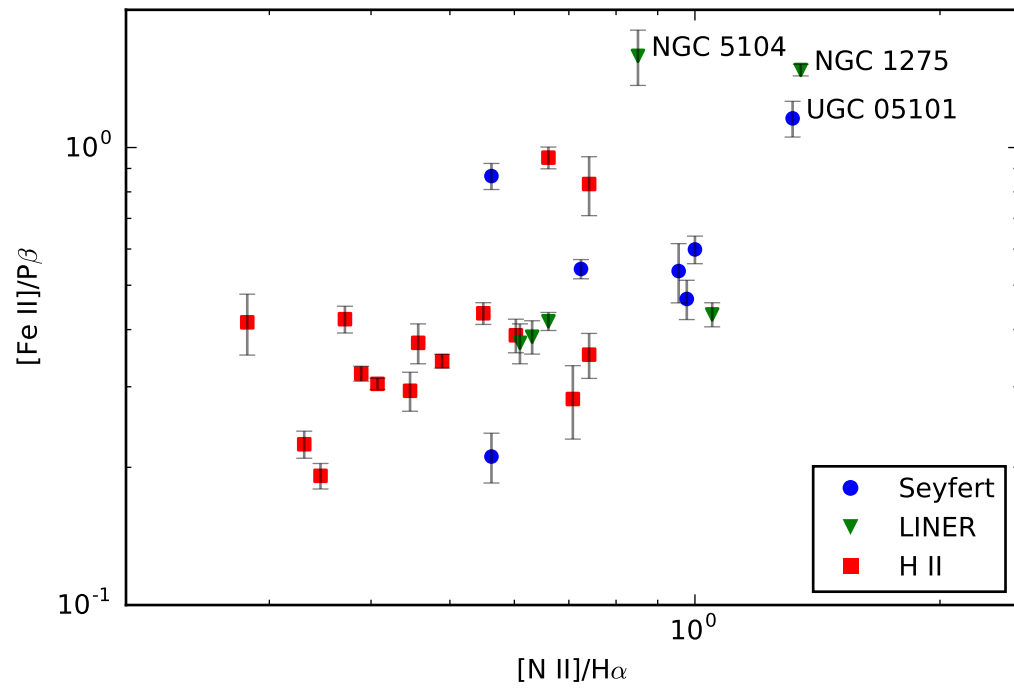


Fig. 2.11.—  $[\text{Fe II}]/\text{Paschen } \beta$  plotted as a function of  $[\text{N II}]/H\alpha$ .



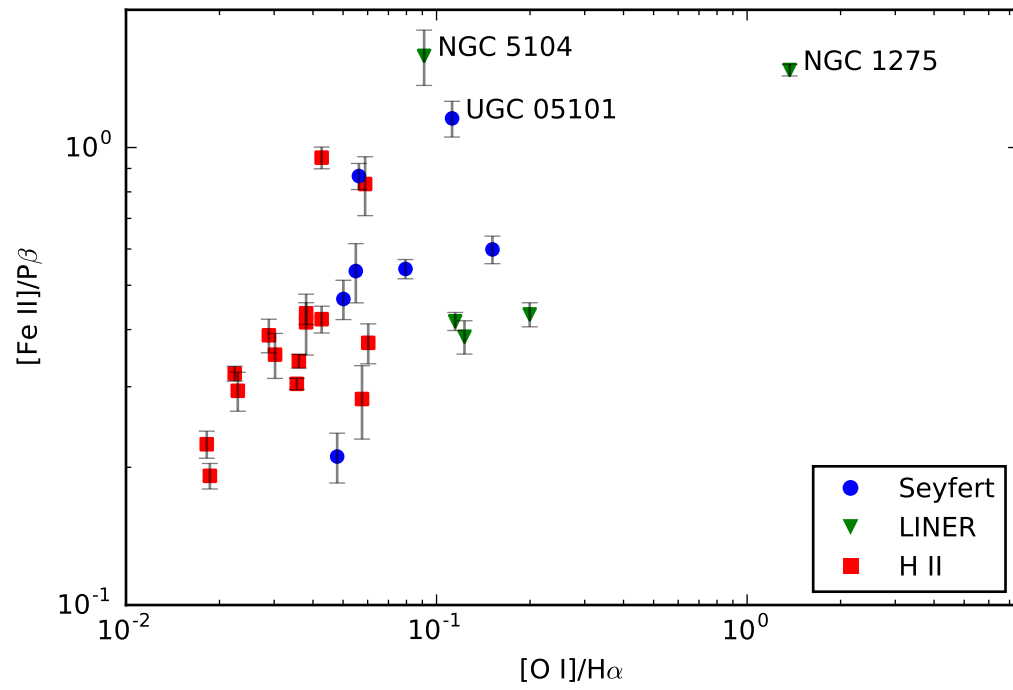


Fig. 2.12.—  $[Fe\ II]/\text{Paschen } \beta$  plotted as a function of  $[O\ I]/H\alpha$ .

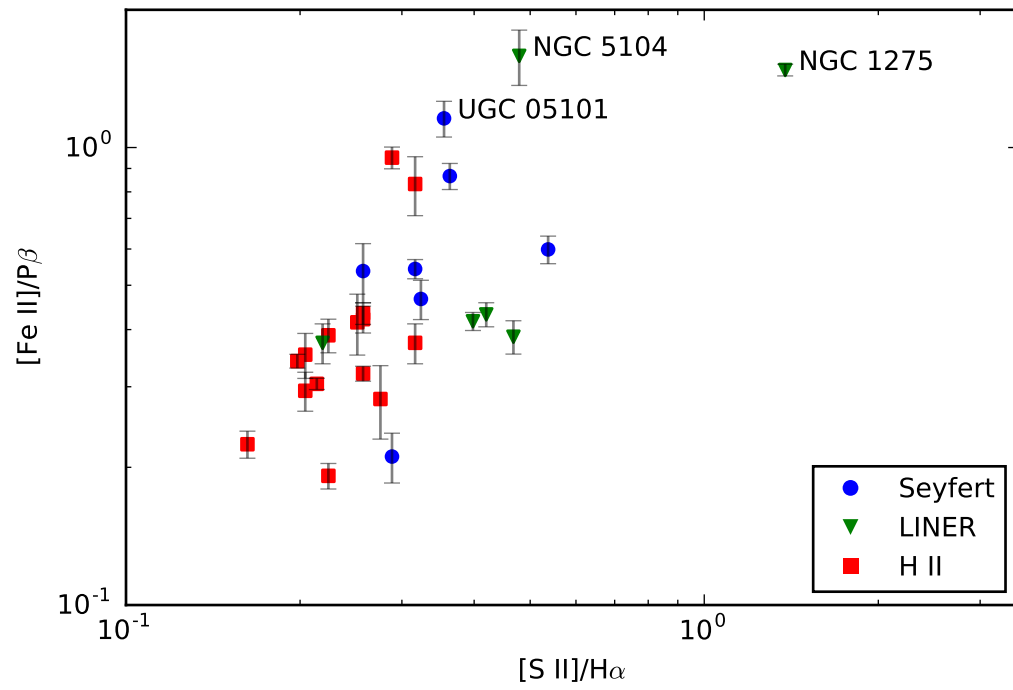


Fig. 2.13.—  $[Fe II]/\text{Paschen } \beta$  plotted as a function of  $[S II]/H\alpha$ .

### 2.4.3 Comparison to Computational Models

In addition to the empirical comparisons of the TripleSpec dataset with lower luminosity galaxies and SNR, we also made use of the latest shock and photoionization models to assess the processes driving the observed line emission.

Allen et al. (2008) computed fast ( $v > 100 \text{ km s}^{-1}$ ) radiative shock models with Mappings III. These models determined line emission for atomic species in the ionized shock precursor as well as atomic line emission within the shock itself. Because any shocks within our observations are unresolved, we compare our data to the combined shock+precursor emission. A major improvement of Mappings III over Mappings II is added stability to the method of choosing time steps, allowing simulation of faster shocks. These models do not include dust, and therefore operate under the assumption that shocks within the represented velocity range would easily destroy any dust grains in their path. (Draine & Salpeter 1979, Dwek et al. 1996, Jones et al. 1994,1996, Pineau des Fôrets & Flower 1997, and Perna & Lazzati 2002). Details of the calculations are discussed in Allen et al. (2008). At each time step, the ionization balance and cooling rate are computed using empirical models of all abundant atoms. Further details of these computations are given in Sutherland et al. (1993).

Examples of the results from the shock model comparison are provided as a function of near-infrared line ratios in Figures 2.14 and 2.15. Data from the LIRG sample are plotted alongside fast shock models grids from Allen et al. (2008, their “T” set of models). These models assume a density  $n = 0.01 \text{ cm}^{-3}$  and Solar elemental abundances. The shock velocity, running in increments of  $100 \text{ km s}^{-1}$  from  $100 \text{ km s}^{-1}$  to  $1000 \text{ km s}^{-1}$ , is traced by blue lines. The magnetic parameter,  $B/n^{1/2}$  or the transverse magnetic field strength divided by the square root of the density (a parametrization of the Alfvén velocity, the strength of which serves to limit compres-

sion behind the shock) is traced by orange/yellow lines. This model parameter is given values of  $10^{-4}$ , 0.5, 1.0, 2.0, 3.23, 4.0, 5.0, and  $10.0 \mu\text{G cm}^{3/2}$ . There is overlap between the data and the models in Figure 2.14, but no overlap in Figure 2.15. The likely explanations are that the LIRGs have lower velocity shocks than accounted for by the models ( $v < 100 \text{ km s}^{-1}$ ) and most importantly that Fe abundances in the models deviate from the actual abundances in LIRGs.

Levesque et al. (2010) used Starburst99 in conjunction with Mappings III to create stellar photoionization models of galaxy spectra. Starburst99 is a stellar evolutionary synthesis code that computes a FUV ionizing continuum which is in turn used by Mappings III to model gas excitation and an output spectrum. In the computation these models, the authors employed both the “standard” and “high” mass loss evolutionary tracks included in Starburst99. We compare to emission models computed using the “high” mass loss rates, as these better approximate the physical situation in which rotation leads to an earlier start to the Wolf-Rayet phase in massive stars. The authors model scenarios of a short burst of star formation and a continuous star formation rate over the past 5 Myr.

The photoionization models, which assume a continuous star formation rate and a density  $n = 0.01 \text{ cm}^{-3}$ , are plotted in Figure 2.16. The metallicity, running over 0.05, 0.2, 0.4, 1, and 2 times  $Z_{\odot}$  is traced in blue. The ionization parameter  $q$ , running over  $1 \times 10^7$ ,  $2 \times 10^7$ ,  $4 \times 10^7$ ,  $8 \times 10^7$ ,  $1 \times 10^8$ ,  $2 \times 10^8$ , and  $4 \times 10^8 \text{ cm s}^{-1}$  is traced in orange/yellow. The models do not overlap the data – in this case, the lack of overlap is likely due to iron abundances in the photoionization models which are too low.

Because Mappings III does not model emission from molecules, we have chosen strong atomic line emission detected in this sample.

Correctly representing the Fe abundance in cases of gas excitation such as those

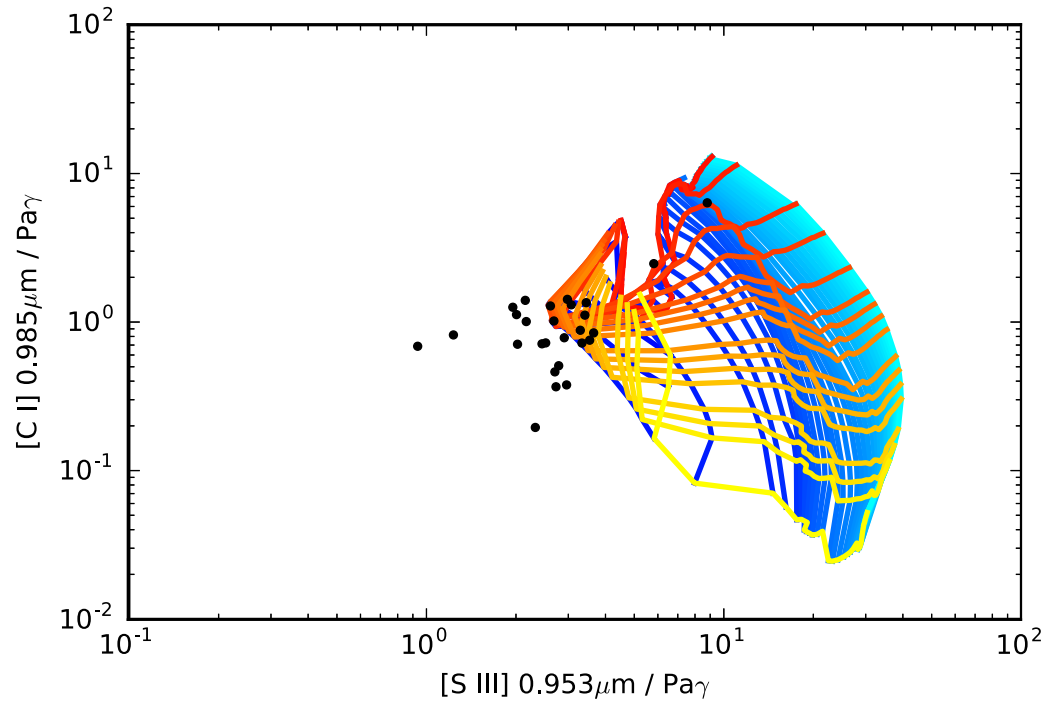


Fig. 2.14.— Comparison to shock models (Solar elemental abundance,  $n = 0.01 \text{ cm}^{-1}$ ) computed with Mappings III. Velocity is traced by blue lines. Magnetic field strength is traced by orange/yellow lines.

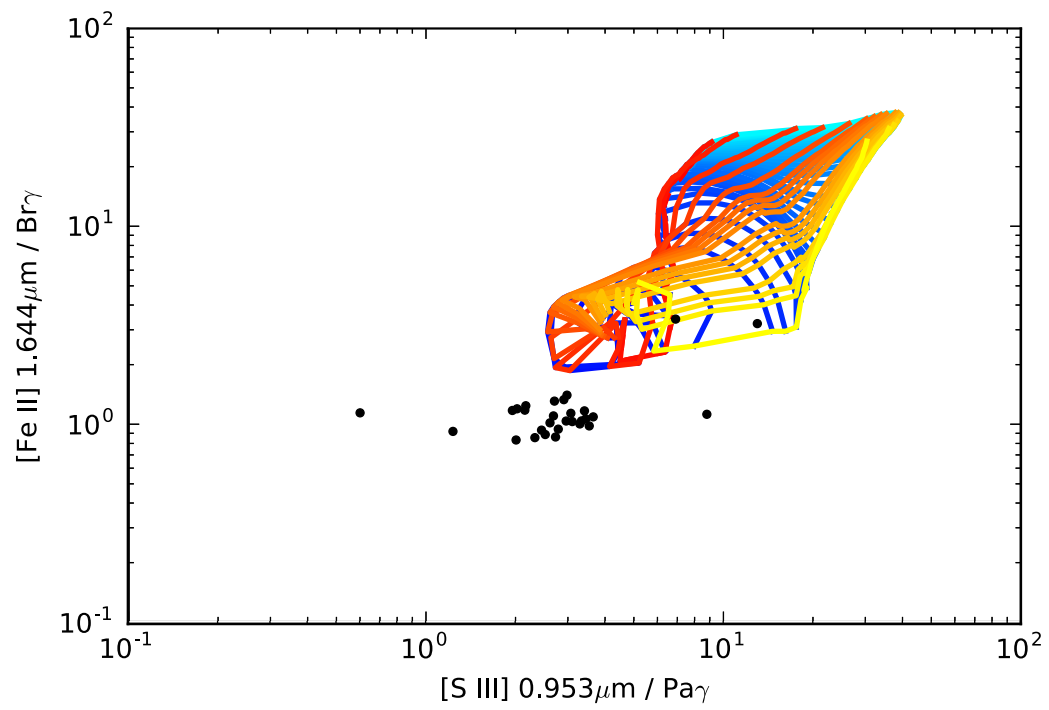


Fig. 2.15.— Same as 2.14

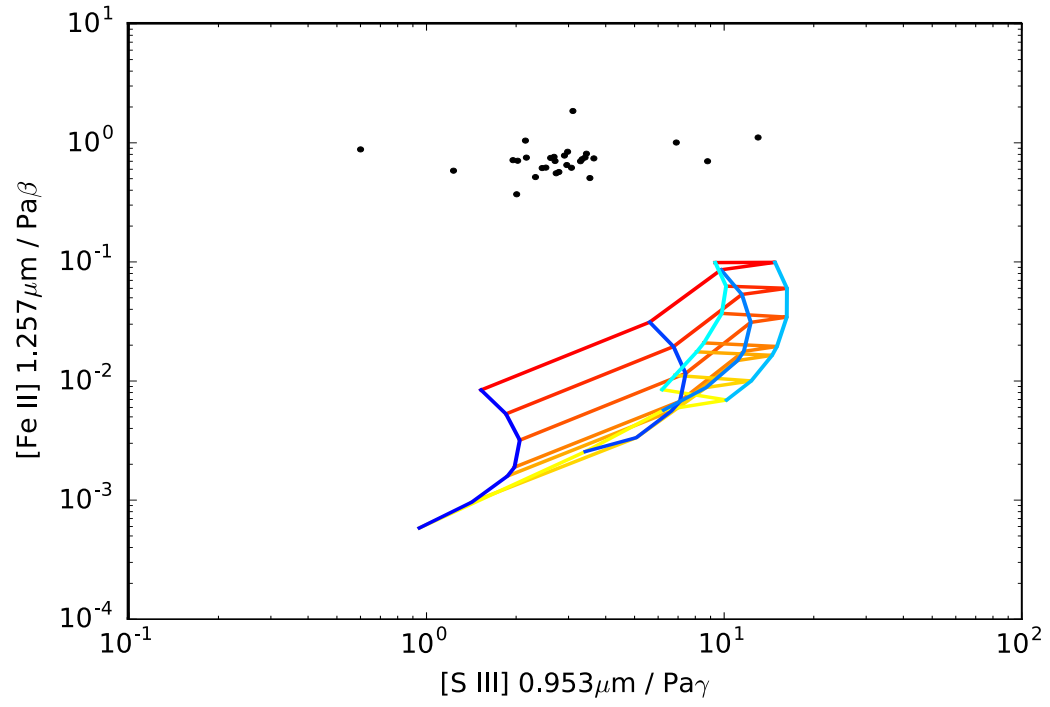


Fig. 2.16.— Comparison to photoionization models (instantaneous star formation burst,  $n = 0.01 \text{ cm}^{-3}$ ) computed with Mappings III. Metallicity is traced in blue, ionization parameter is traced in orange/yellow.

found in LIRGs is a well known problem in computational modeling. A simple reason for this is the high likelihood that a significant fraction of the Fe that has been nucleosynthesized resides in the solid phase on grain surfaces. Some Fe is bound to be released into gas by the destruction of grains, especially in the case of shocks. However in the situation of an unresolved source, it is unsurprising that correctly representing the average gas phase Fe abundance is a challenge.

## 2.5 CONCLUSIONS

We observed the nuclei of 52 GOALS galaxies with the TripleSpec near-infrared spectrograph. The following conclusions are reached:

- Strong emission from hydrogen recombination lines, forbidden lines and warm  $\text{H}_2$  from these galaxies are observed. In addition, strong CO absorption features are observed in the majority of the LIRGs.
- No evidence of previously unidentified optical AGN are observed in the sample. The total absence of [Si VI] ( $1.962 \mu\text{m}$ ) and broad recombination line emission in LIRGs not already known to host AGN indicate that AGN are either absent or too deeply embedded to be observed at near-IR wavelengths.
- Empirical comparisons of the  $[\text{Fe II}]/\text{Pa}\beta$  vs.  $\text{H}_2/\text{B}\gamma$  ratios of the LIRG sample with normal star-forming galaxies show a significant overlap between the two samples. In addition, we show the optical classifications (HII, LINER, Seyfert) for the sample are segregated by their near-IR  $[\text{Fe II}]/\text{Pa}\beta$  ratios, with LINERs and Seyferts having  $[\text{Fe II}]/\text{Pa}\beta \geq 0.4$  and HII region-like LIRGs having  $[\text{Fe II}]/\text{Pa}\beta \leq 0.4$ . This is likely due to the prevalence of shocks in LINERs increasing the fraction of gas-phase Fe. Finally, we find that the  $[\text{Fe II}]$  ratio



scales with  $[\text{N II}]/\text{H}\alpha$ ,  $[\text{O I}]/\text{H}\alpha$ , and  $[\text{S II}]/\text{H}\alpha$ . This is consistent with the idea that large values of  $[\text{Fe II}]/\text{P}\beta$  are indicative of strong, extended shocks within galaxies.

- Models of shock excitation provide better agreement with the observed near-IR line ratios than photoionization models. However, photoionization models also do not overlap significantly with normal star-forming galaxies, likely an indication that the iron abundances in the photoionization models are too low.

## Chapter 3

# Near-Infrared Spectroscopy of the GOALS Sample: Emission Line Fits and Kinematic Analysis

### 3.1 INTRODUCTION

Nuclear outflows may be a natural consequence of starburst activity. Chevalier & Clegg (1985) showed that large scale winds can be driven mainly by starburst activity via the thermalization of energy from supernovae. Since Luminous Infrared Galaxies are often powered predominantly by powerful starburst activity (Petric et al. 2011), we expect that gas outflows may be present in many of our sources. However, AGN may also occupy the role of dominant energy source in LIRGs. *Herschel* observations of the ULIRG Quasar Mrk 231 have shown the presence of molecular outflows (Fischer et al. 2010) with velocities in excess of  $1000 \text{ km s}^{-1}$ . This indication that extremely strong outflows capable of removing star-forming fuel from the system may be driven by energetically dominant AGN led Veilleux et al. (2013) to show that the molecular

outflow velocity traced by observations of the OH 119  $\mu\text{m}$  line is correlated with AGN luminosity,  $L_{\text{AGN}}$ .

In this chapter, we present fits to recombination (Paschen  $\beta$  and Brackett  $\gamma$ ) and molecular ( $\text{H}_2$  S(1) 1-0) emission line profiles. We find that each profile is well fit either by a single Gaussian component or two blended Gaussian components. We take the central velocity of the most blue-shifted component in each profile to represent a plausible outflow velocity and compare it to the AGN luminosity and starburst luminosity of each source in comparison with a similar analysis performed by Veilleux et al. (2013).

The reader is directed to Chapter 2 for a description of the observations and data reduction of the sample.

## 3.2 RESULTS

Here we use the non-linear least squares fitting package LMFIT in Python to compute Gaussian fits to the strong emission lines in the sample of spectra presented in Chapter 2. The instrumental line-spread function was not taken into account when determining any of the parameters of the fits as the typical FWHM of the fits are several times the width of the instrumental line-spread function. To ensure accurate measurements of velocities with respect to the systemic velocity in each observed galaxy, redshifts were measured directly from the ensemble of near-infrared stellar absorption lines detected in our TripleSpec spectra. Specifically, the source redshifts were measured from the observed wavelengths of the CO  $\Delta\nu = 2$  transitions in the  $K$  band ( $\lambda 2.294$ ,  $\lambda 2.323$ ,  $\lambda 2.354$ , and  $\lambda 2.383$ ), the CO  $\Delta\nu = 3$  transitions in the  $H$  band ( $\lambda 1.558$ ,  $\lambda 1.578$ ,  $\lambda 1.598$ ,  $\lambda 1.619$ ,  $\lambda 1.640$ , and  $\lambda 1.661$ ), and the  $n > 7$  Brackett series transitions in the  $H$  band ( $\lambda 1.556$ ,  $\lambda 1.571$ ,  $\lambda 1.589$ ,  $\lambda 1.611$ ,  $\lambda 1.641$ ,  $\lambda 1.681$ ). To

calibrate our TripleSpec measured  $2\ \mu\text{m}$  CO bandhead redshifts, we made use of redshifts measured from the centroid of the millimeter-wave rotational emission lines of our galaxies published in Herrero-Illana (2014); Sanders et al. (1991); Solomon et al. (1997); Yao et al. (2003). In the 33 cases where millimeter-wave CO redshifts were available from the literature, we find that they agree with our measured our TripleSpec measured  $2\ \mu\text{m}$  CO bandhead absorption line redshifts to within 0.4%. We thus make use of the CO band heads to estimate systemic redshifts for the LIRG sample. In the case of VV 340, stellar absorption line redshifts could not be used because no stellar absorption lines were detected. Therefore we directly adopted the millimeter-wave CO 1-0 redshift for the systemic velocity in VV 340. Table 3.1 gives our measurements of each source redshift and shows the agreement with redshifts from the literature where available.

Table 3.1. Target Redshifts from Stellar Absorption Features

IRAS	Name	$z_{NIR}$	$z_{CO}$	Reference
F00163-1039	MCG-02-01-051	$0.0271 \pm 0.0006$	0.02711	1
F02512+1446	UGC 02369 A	$0.0325 \pm 0.0003$	.	...
F02512+1446	UGC 02369 B	$0.0317 \pm 0.0007$	.	...
F03164+4119	NGC 1275	$0.017559 \pm 0.00006$	.	...
F09126+4432	UGC 04881 A	$0.0399 \pm 0.0009$	0.039885	2
F09126+4432	UGC 04881 B	$0.041 \pm 0.0023$	0.039885	2
F09320+6134	UGC 05101	$0.03931 \pm 0.0009$	0.03930	3
F10196+2149	NGC 3221	$0.014 \pm 0.0009$	.	...
F12590+2934	NGC 4922 A	$0.024 \pm 0.001$	0.02359	4
F12590+2934	NGC 4922 B	$0.024 \pm 0.0011$	0.02359	4
F12592+0436	CGCG 043-099	$0.038 \pm 0.0012$	.	...
F12596-1529	MCG -02-33-098	$0.0168 \pm 0.001$	.	...
F13136+6223	VV 250 A	$0.0315 \pm 0.0011$	0.031008	2
F13136+6223	VV 250 B	$0.0314 \pm 0.0009$	.	...
F13188+0036	NGC 5104	$0.0188 \pm 0.0006$	0.01861	4
F13497+0220	NGC 5331 A	$0.034 \pm 0.0015$	0.03308	1
F13497+0220	NGC 5331 B	$0.0337 \pm 0.0013$	0.03308	1
F13182+3424	UGC 08387 obs1	$0.0236 \pm 0.0011$	0.02335	4
F13182+3424	UGC 08387 obs2	$0.024 \pm 0.0013$	0.02335	4
F13362+4831	NGC 5256 B	$0.0285 \pm 0.0012$	0.02786	4
F13428+5608	UGC 08696	$0.0383 \pm 0.0008$	0.0377	3
F13428+5608	UGC 08696	$0.0383 \pm 0.008$	0.037133	
F13470+3530	UGC 08739	$0.0169 \pm 0.0005$	0.01679	4
F14179+4927	CGCG 247-020	$0.0262 \pm 0.0010$	0.02557	4
F14280+3126	NGC 5653	$0.0125 \pm 0.0014$	0.01188	4
F14348-1447	IRAS F14348-1447 A	$0.0833 \pm 0.0018$	0.08247	2
F14348-1447	IRAS F14348-1447 B	$0.083 \pm 0.0015$	0.08247	2
F14547+2449	VV 340 N	.	0.03302	4
F14547+2449	VV 340 S	.	0.03302	4
F15107+0724	CGCG 049-057	$0.0135 \pm 0.0010$	0.01300	4
F15163+4255	VV 705 A	$0.04112 \pm 0.04$	0.00016	4
F15163+4255	VV 705 B	$0.04112 \pm 0.00132$	0.04016	4
F15250+3608	IRAS F15250+3608	$0.0559 \pm 0.0015$	0.05538	4

Table 3.1—Continued

IRAS	Name	$z_{NIR}$	$z_{CO}$	Reference
F15276+1309	NGC 5936	$0.0138 \pm 0.0005$	0.01336	4
F16104+5235	NGC 6090 A	$\dots \pm 0.0287$	$\dots$	
F16104+5235	NGC 6090 B	$0.0295 \pm 0.0008$	0.02946	2
F16104+5235	NGC 6090 B	$0.0295 \pm 0.0008$	0.02946	2
F17132+5313	IRAS F17132+5313 A	$\dots \pm 0.0503$	$\dots$	
F17132+5313	IRAS F17132+5313 B	$0.0523 \pm 0.0013$	0.050742	2
18090+0130	IRAS 18090+0130 A	$0.0291 \pm 0.0008$	0.02886	1
18090+0130	IRAS 18090+0130 B	$0.0292 \pm 0.0009$	0.02886	1
18090+0130	IRAS 18090+0130 C	$0.02889 \pm 0.00089$	0.02886	1
F18239+5950	NGC 6670	$0.0297 \pm 0.0011$	.	$\dots$
F18425+6036	NGC 6701	$0.0134 \pm 0.0006$	0.01315	1
F19115-2124	ESO 593-IG008	$0.049 \pm 0.001$	0.04881	1
F19120+7320	NGC 6786	$0.025128 \pm 0.000628$	0.02510	1
F19297-0406	IRAS F19297-0406	$0.08571 \pm 0.00071$	0.08573	3
19542+1110	IRAS 19542+1110	$0.0289 \pm 0.0072$	.	$\dots$
20351+2521	IRAS 20351+2521	$0.0345 \pm 0.0011$	.	$\dots$
F20550+1655	II Zw 096	$0.0365 \pm 0.0012$	.	$\dots$
21101+5810	IRAS 21101+5810	$0.04 \pm 0.002$	0.03920	1
21101+5810	IRAS 21101+5810 A	$0.04 \pm 0.0018$	0.03920	1
21101+5810	IRAS 21101+5810 B	$0.04 \pm 0.0013$	0.03920	1
F22389+3359	UGC 12150 A	$0.022 \pm 0.001$	0.02151	1
F22389+3359	UGC 12150 B	$0.022 \pm 0.0015$	0.02151	1
F22491-1808	IRAS F22491-1808	$0.07728 \pm 0.00228$	0.07729	2
F23007+0836	NGC 7469	$0.0166 \pm 0.0008$	0.01655	2
F23135+2517	IC 5298	$0.0281 \pm 0.0016$	0.02749	2
F23254+0830	NGC 7674	$0.02898 \pm 0.00048$	0.03225	2
F23365+3604	IRAS F23365+3604	$0.064478 \pm 0.001478$	0.06448	3
23436+5257	IRAS 23436+5257 A	$0.034 \pm 0.0005$	.	$\dots$
23436+5257	IRAS 23436+5257 B	$0.03414 \pm 0.00084$	.	$\dots$

Note. — Reference for millimeter-wave CO redshifts: (1) Herrero-Illana (2014); (2) Sanders et al. (1991); (3) Solomon et al. (1997); (4) Yao et al. (2003)

For all line profile fits, a local linear background was fit at a range of 2000-3000  $km\ s^{-1}$  away from the line peak and subtracted before the Gaussian fits were performed. In a first pass through the data, all lines were fit with a single Gaussian component. Upon visual inspection of these fits, some features were identified as requiring two Gaussian emission components. Frequently, the [Fe II] line at 1.644  $\mu m$  required an additional fit to a Gaussian absorption feature, i.e., to a line of the Brackett series in the atmosphere of the evolved stellar population. Despite the determination of the necessity of multiple Gaussian components being by eye, the double Gaussian fits can be demonstrated to be a better description of the data distribution. Table 3.2 gives the values of reduced  $\chi^2$  for a single Gaussian fit and the adopted double Gaussian fit for each feature that was determined to be better fit by a double Gaussian. Table 3.2 additionally lists the change in reduced  $\chi^2$  and the signal-to-noise ratio (S/N) for each feature. Generally the features with lesser values of S/N seem to have undergone a trivial reduction in the reduced  $\chi^2$  ( $\lesssim 0.5$ ) upon switching from single to double Gaussian fitting. However the features with greater values of S/N have undergone substantial reduction in the reduced  $\chi^2$ , implying that the second Gaussian is a certainly a necessary component of the fit.

The atomic emission line profiles with the highest signal to noise ratio are Paschen  $\beta$  and Brackett  $\gamma$ . The parameters of the fits to these ionized features are shown in Table 3.3. In many sources the corresponding parameters of the fits to Pa $\beta$  and Br $\gamma$  don't match with one another. This is especially apparent in the velocity offset of the line centroid. One possible explanation for the discrepancy is the difference in line-of-sight extinction between the Pa $\beta$  and Br $\gamma$  wavelengths. (Br $\gamma$  is much less extincted.)

Table 3.2. Reduced  $\chi^2$  for single and double Gaussian fits

Name	$\lambda$ ( $\mu\text{m}$ )	$\chi^2$ single	$\chi^2$ double	$\Delta_{\chi^2}$	S/N
NGC 1275	1.2818	1.686	0.609	1.077	60.75
UGC 04881 A	2.1655	1.738	1.736	0.002	16.7
UGC 04881 B	1.2818	0.723	0.657	0.066	18
UGC 04881 B	2.1655	1.031	0.989	0.042	11.8
UGC 05101	1.2818	1.154	1.138	0.017	18.4
UGC 05101	2.1655	0.770	0.711	0.059	13.6
CGCG 043-099	1.2818	1.976	0.955	1.021	40.5
CGCG 043-099	2.1655	1.946	0.832	1.114	48.0
VV 250* B	1.2818	0.961	0.735	0.226	25.5
VV 250* B	2.1655	0.632	0.625	0.007	4.4
VV 250 A	1.2818	19.022	2.722	16.300	135.5
VV 250 A	2.1655	6.902	1.417	5.485	106.5
UGC 08387 obs2	1.2818	1.768	1.612	0.156	77.5
UGC 08387 obs1	1.2818	1.229	1.156	0.073	84.4
NGC 5104	1.2818	1.427	1.391	0.036	13.0
NGC 5104	2.1655	0.955	0.832	0.124	10.8
NGC 5256 A	1.2818	1.186	0.890	0.296	37.0
NGC 5256 B	1.2818	1.798	1.319	0.478	39.0
NGC 5256 B	2.1655	1.213	0.752	0.462	28.0
UGC 08696*	1.2818	0.396	0.386	0.010	26.8
NGC 5331 B	1.2818	1.310	1.174	0.136	14.2
NGC 5331 B	2.1655	0.956	0.850	0.106	11.5
NGC 5331 A	2.1655	1.388	1.203	0.185	25.0
IRAS F14348-1447 B	2.1655	1.908	1.854	0.054	3.8
VV 705 B	1.2818	0.475	0.475	0.000	11.0
NGC 5936	2.1655	1.179	1.154	0.025	27.8
IRAS F17132+5313 A	2.1655	1.908	1.748	0.160	13.0
IRAS 18090+0130 A	1.2818	8.213	7.715	0.498	7.0
IRAS 18090+0130 B	1.2818	2.253	1.068	1.185	48.0
IRAS 18090+0130 B	2.1655	1.382	0.745	0.637	32.8
ESO 593-IG008	2.1655	0.885	0.830	0.055	10.7
IRAS F19297-0406	2.1655	1.016	0.874	0.142	15.2
IRAS 21101+5810	1.2818	0.686	0.643	0.042	17.0
UGC 12150 B	1.2818	1.323	1.184	0.139	26.0
UGC 12150 B	2.1655	1.003	0.975	0.028	19.0
NGC 7469	1.2818	3.750	2.028	1.722	25.5
NGC 7469	2.1655	2.093	1.236	0.857	28.6
IC 5298	1.2818	1.559	1.367	0.192	16.0
NGC 7674	1.2818	2.380	1.068	1.312	26.3
IRAS 23436+5257 A	1.2818	2.795	1.427	1.368	30.0
IRAS 23436+5257 A	2.1655	2.243	1.669	0.574	28.0



Table 3.3. Recombination Line Fits

Source	Component	Paschen $\beta$ 1.2818 $\mu\text{m}$			Brackett $\gamma$ 2.1655 $\mu\text{m}$		
		Amplitude ( $10^{-16} \text{ erg s}^{-1} \text{ cm}^{-2} \text{ \AA}$ )	$\sigma$ ( $\text{km s}^{-1}$ )	Offset <sup>a</sup> ( $\text{km s}^{-1}$ )	Amplitude ( $10^{-16} \text{ erg s}^{-1} \text{ cm}^{-2} \text{ \AA}$ )	$\sigma$ ( $\text{km s}^{-1}$ )	Offset ( $\text{km s}^{-1}$ )
MCG-02-01-051	single	8.98	117.54	-2.07	12.69	109.46	16.18
UGC 02369 B	single	6.63	103.75	50.90	7.98	101.34	13.31
UGC 02369 A	single	5.72	74.02	0.65	6.63	74.67	0.00
NGC 1275	red	3.13	205.20	254.34	0.76	351.08	348.47
	central	...	...	...	0.18	255.26	-741.91
UGC 04881 A	blue	2.48	647.59	-98.84	0.49	126.53	-1350.06
	red	...	...	...	2.29	51.51	88.74
UGC 04881 B	central	1.87	118.45	0.00	...	...	...
	blue	...	...	...	1.83	83.57	-65.69
UGC 05101	red	1.60	88.85	-18.81	1.95	159.37	7.61
	blue	0.20	349.05	-50.27	1.55	47.31	-75.59
NGC 3221	red	1.28	63.16	289.94	1.66	174.15	85.12
	blue	5.48	144.75	-32.08	1.48	75.67	-215.40
NGC 4922 B	single	...	...	...	0.84	32.80	0.00
NGC 4922 A	single	...	...	...	0.07	33.58	0.00
MCG -02-33-098	single	15.53	96.78	0.00	3.26	99.02	0.00
	single	13.85	95.92	6.80	3.13	65.15	-0.01
VV 250 B	red	1.13	125.19	214.26	0.32	71.10	300.84
VV 250 A	blue	4.28	80.21	-86.32	0.95	104.43	-52.18
	red	30.74	81.61	-65.20	6.28	87.97	129.01
	blue	23.44	97.95	154.28	6.84	89.21	-93.28

Table 3.3—Continued

Source	Component	Paschen $\beta$ 1.2818 $\mu\text{m}$			Brackett $\gamma$ 2.1655 $\mu\text{m}$		
		Amplitude ( $10^{-16} \text{ erg s}^{-1} \text{ cm}^{-2} \text{ \AA}$ )	$\sigma$ ( $\text{km s}^{-1}$ )	Offset <sup>a</sup> ( $\text{km s}^{-1}$ )	Amplitude ( $10^{-16} \text{ erg s}^{-1} \text{ cm}^{-2} \text{ \AA}$ )	$\sigma$ ( $\text{km s}^{-1}$ )	Offset ( $\text{km s}^{-1}$ )
UGC 08387 obs1	red	2.85	176.59	-47.01	...	...	...
	single	...	...	...	15.14	99.31	9.79
UGC 08387 obs2	blue	40.67	85.56	3.41	...	...	...
	red	1.29	45.96	191.74	...	...	...
	central	...	...	...	3.82	146.06	-0.01
NGC 5104	blue	11.05	125.31	-8.49	...	...	...
	red	2.07	111.13	11.90	1.55	106.95	176.26
	blue	0.72	28.96	-180.01	3.69	67.44	-123.54
NGC 5256 A	red	3.60	152.16	88.95	...	...	...
	central	...	...	...	2.78	162.44	19.70
	blue	0.74	150.31	-565.98	...	...	...
NGC 5256 B	red	2.79	28.77	192.48	4.16	81.27	141.76
	blue	4.01	163.36	-0.27	2.82	156.28	-101.56
	red	15.64	41.14	200.23	5.33	463.50	292.87
UGC 08696	central	...	...	...	20.78	137.73	-28.53
	blue	20.52	259.02	9.86	12.68	56.49	-300.00
	single	296.52	71.64	0.00	1715.61	47.92	0.00
UGC 08739	red	194.34	44.65	212.61	320.83	77.16	85.66
	blue	300.67	105.45	-61.84	217.31	69.53	-165.12

Table 3.3—Continued

Source	Component	Paschen $\beta$ 1.2818 $\mu\text{m}$ Amplitude ( $10^{-16} \text{ erg s}^{-1} \text{ cm}^{-2} \text{ \AA}$ )	$\sigma$ ( $\text{km s}^{-1}$ )	Offset <sup>a</sup> ( $\text{km s}^{-1}$ )	Brackett $\gamma$ 2.1655 $\mu\text{m}$ Amplitude ( $10^{-16} \text{ erg s}^{-1} \text{ cm}^{-2} \text{ \AA}$ )	$\sigma$ ( $\text{km s}^{-1}$ )	Offset ( $\text{km s}^{-1}$ )
NGC 5331 A	red	...	...	...	893.16	75.25	102.33
	central	646.48	138.83	0.00	...	...	...
	blue	...	...	...	973.67	66.96	-88.81
NGC 5653	single	2.35	94.00	4.34	0.40	92.67	13.78
IRAS F14348-1447 A	single	...	...	...	1.77	124.29	-1.24
IRAS F14348-1447 B	red	...	...	...	2.49	117.83	12.25
	single	1.87	23.45	0.00	...	...	...
	blue	...	...	...	1.04	29.33	-81.63
VV 340 N	...	...	...	...	...	...	...
VV 340 S	single	...	...	...	0.48	44.73	0.00
CGCG 049-057	single	3.40	96.68	0.00	0.77	106.17	0.01
VV 705 A	single	15.70	85.27	0.00	21.88	74.69	3.83
VV 705 B	red	0.48	41.36	20.01	...	...	...
	blue	1.28	134.62	-19.44	...	...	...
IRAS F15250+3608	single	187.87	18.86	41.33	2.83	97.50	-13.21
NGC 5936	red	...	...	...	17.07	14.40	267.16
	single	155.12	66.33	0.00	...	...	...
	blue	...	...	...	152.17	60.15	-27.31
NGC 6090 A	single	6.65	83.82	0.01	9.64	66.76	-2.67
NGC 6090 B	single	3.76	60.86	0.00	3.78	64.75	-0.01
IRAS F17132+5313 A	red	...	...	...	0.48	85.64	97.21

Table 3.3—Continued

Source	Component	Paschen $\beta$ 1.2818 $\mu\text{m}$			Brackett $\gamma$ 2.1655 $\mu\text{m}$		
		Amplitude ( $10^{-16} \text{ erg s}^{-1} \text{ cm}^{-2} \text{ \AA}$ )	$\sigma$ ( $\text{km s}^{-1}$ )	Offset <sup>a</sup> ( $\text{km s}^{-1}$ )	Amplitude ( $10^{-16} \text{ erg s}^{-1} \text{ cm}^{-2} \text{ \AA}$ )	$\sigma$ ( $\text{km s}^{-1}$ )	Offset ( $\text{km s}^{-1}$ )
IRAS F17132+5313 B	blue	...	...	...	0.40	92.81	-109.06
IRAS 18090+0130 A	single	...	...	...	0.22	102.89	0.00
	red	0.89	38.88	88.60	...	...	...
	central	...	...	...	1.16	115.12	3.96
IRAS 18090+0130 B	blue	0.42	87.77	-43.78	...	...	...
	red	2.98	50.44	141.65	4.05	70.87	148.41
IRAS 18090+0130 C	blue	2.05	148.34	-65.36	3.24	142.64	-94.86
NGC 6670	single	...	...	...	0.48	35.90	4.00
NGC 6701	single	4.73	88.49	11.52	5.80	82.46	6.99
ESO 593-IG008	single	48.33	58.45	0.00	44.66	61.60	0.00
	red	...	...	...	1.19	47.49	323.07
NGC 6786	blue	...	...	...	1.87	168.82	-59.76
IRAS F19297-0406	single	0.39	85.86	6.89	0.41	85.31	3.08
	red	...	...	...	2.46	26.50	92.58
IRAS 19542+1110	blue	...	...	...	2.20	165.39	-21.79
IRAS 20351+2521	single	...	...	...	1.64	124.81	-84.68
II Zw 096	single	27.57	109.40	6.74	28.69	116.26	1.07
IRAS 21101+5810 A	single	1.41	71.40	-8.78	0.62	127.85	-24.90
IRAS 21101+5810 B	...	...	...	...	...	...	...
UGC 12150 B	single	4.04	112.17	-3.52	5.73	127.93	-2.05
	red	3.95	103.34	21.84	1.31	219.95	97.47

Table 3.3—Continued

Source	Component	Paschen $\beta$ 1.2818 $\mu\text{m}$		Brackett $\gamma$ 2.1655 $\mu\text{m}$		Offset <sup>a</sup>	Amplitude	$\sigma$	Offset
		Amplitude	$\sigma$	Amplitude	$\sigma$	( $\text{km s}^{-1}$ )	( $10^{-16} \text{ erg s}^{-1} \text{ cm}^{-2} \text{ \AA}$ )	( $\text{km s}^{-1}$ )	( $\text{km s}^{-1}$ )
UGC 12150 A	blue	1.95	47.57	-120.60	4.61	-120.60	4.61	118.43	-58.64
	single	0.59	56.83	0.00	0.66	0.00	0.66	42.29	20.44
IRAS F22491-1808	absorption	-0.57	28.67	-364.01	...	-364.01	...	...	...
	single	25.57	111.42	-15.11	0.77	-15.11	0.77	119.17	41.28
NGC 7469	red	4.88	708.99	135.97	6.70	135.97	6.70	285.70	493.80
	blue	24.83	121.44	-30.86	27.28	-30.86	27.28	152.80	-192.76
IC 5298	red	2.35	91.38	129.07	...	129.07	...	...	...
	central	...	...	...	3.01	...	3.01	113.41	-0.50
NGC 7674	blue	0.44	232.88	-243.30	...	-243.30	...	...	...
	red	2.76	125.88	276.78	...	276.78	...	...	...
	central	...	...	...	4.62	...	4.62	183.09	243.42
	blue	1.13	874.85	79.57	...	79.57	...	...	...
IRAS F23365+3604	single	8.40	27.85	-7.35	3.71	-7.35	3.71	111.30	-4.37
IRAS 23436+5257 B	single	4.10	87.69	74.96	4.53	74.96	4.53	94.14	-18.27
IRAS 23436+5257 A	red	2.04	83.30	-17.10	1.47	-17.10	1.47	71.42	132.52
	blue	1.09	80.28	168.22	2.46	168.22	2.46	86.08	-80.77

<sup>a</sup>This is the difference in velocity between the centroid of the fit and the expected line center for a non moving emitter.

The profile fits to the recombination lines can be placed into three broad categories: a single Gaussian component, two Gaussian components which both have relatively narrow velocity dispersions, or two Gaussian components where one has a narrow dispersion and the other has a broad velocity dispersion. These are shown in Figures 3.1 – 3.3. The single component fits have a median velocity dispersion and standard deviation of  $217 \text{ km s}^{-1}$  and  $72 \text{ km s}^{-1}$  respectively. These line widths likely represents the dominant rotational velocities in these systems. We believe the emission lines display widths roughly equal to the dominant rotation velocities because the large extraction apertures used encompass enough of the source to fully sample the rotation velocities as well as the full extent of star formation, some of which is spread outside each nucleus. The symmetric blended narrow component fits appear to be two spatially unresolved versions of the single component scenario. Of the detected Paschen  $\beta$  lines, 27 of 49 are fit by a single Gaussian component, and 22 of 49 are fit by two blended Gaussian components. Of the detected Brackett  $\gamma$  lines, 36 of 55 are fit by a single Gaussian component, and 19 of 55 are fit by two blended Gaussian components.

The highest signal to noise molecular gas line is the  $\text{H}_2$  S(1) 1-0 line at wavelength  $\lambda 2.1213 \mu\text{m}$ . In fitting this line we find similar behavior to the fits of the atomic lines (single Gaussian or double Gaussian components), with the exception that the molecular gas is never found to have an emission component with dispersion  $\sigma \geq 250 \text{ km s}^{-1}$ . The parameters for the fits to the  $\text{H}_2$   $\lambda 2.1213$  line are shown in Table 3.4. An example of a single Gaussian fit is shown in Figure 3.4 (NGC 6786), while Figure 3.5 represents a double Gaussian fit. Figure 3.6 shows the fit to the  $\text{H}_2$   $\lambda 2.1213$  line for NGC 1275, an illustration that the broad components seen in some recombination lines of the sample are absent in the corresponding molecular profiles. Of the sources

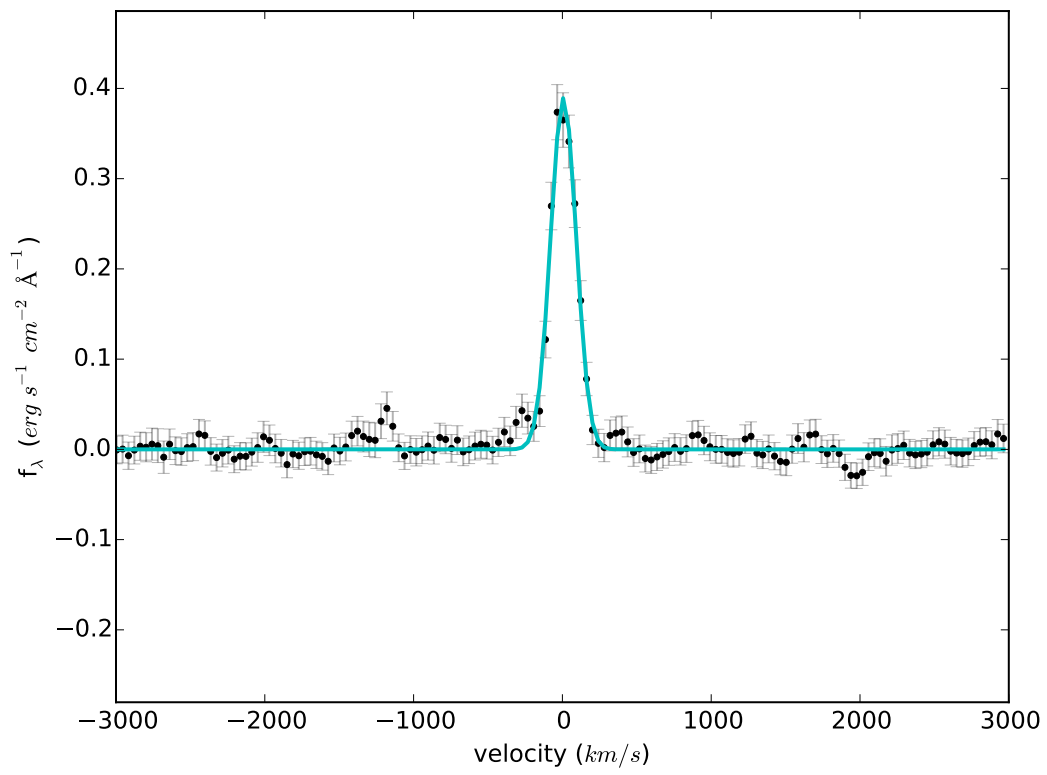


Fig. 3.1.—  $\text{Pa}\beta$  from NGC 6786, an example of a single Gaussian. Y-axis units are  $f_\lambda$  in  $10^{-16} \text{ erg s}^{-1} \text{ cm}^{-2} \text{ \AA}^{-1}$ . X-axis units are velocity in  $\text{km s}^{-1}$ .

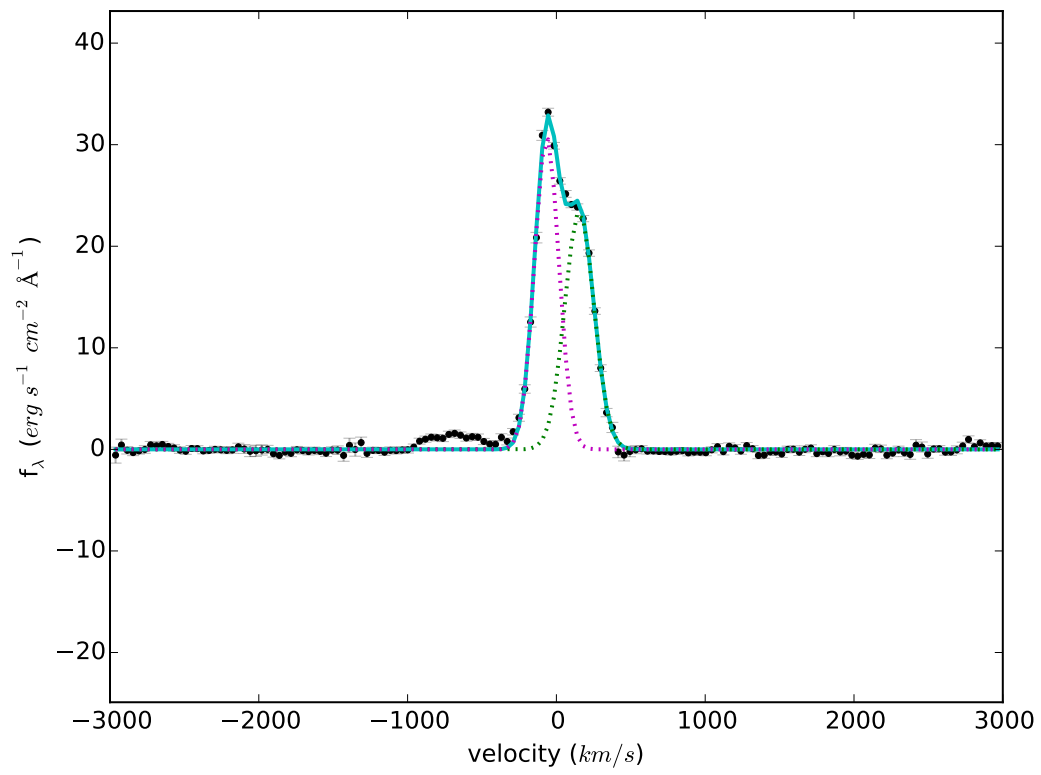


Fig. 3.2.—  $\text{Pa}\beta$  from VV 250a, an example of a double narrow Gaussian. Y-axis units are  $f_\lambda$  in  $10^{-16} \text{ erg s}^{-1} \text{ cm}^{-2} \text{ \AA}^{-1}$ . X-axis units are velocity in  $\text{km s}^{-1}$ .



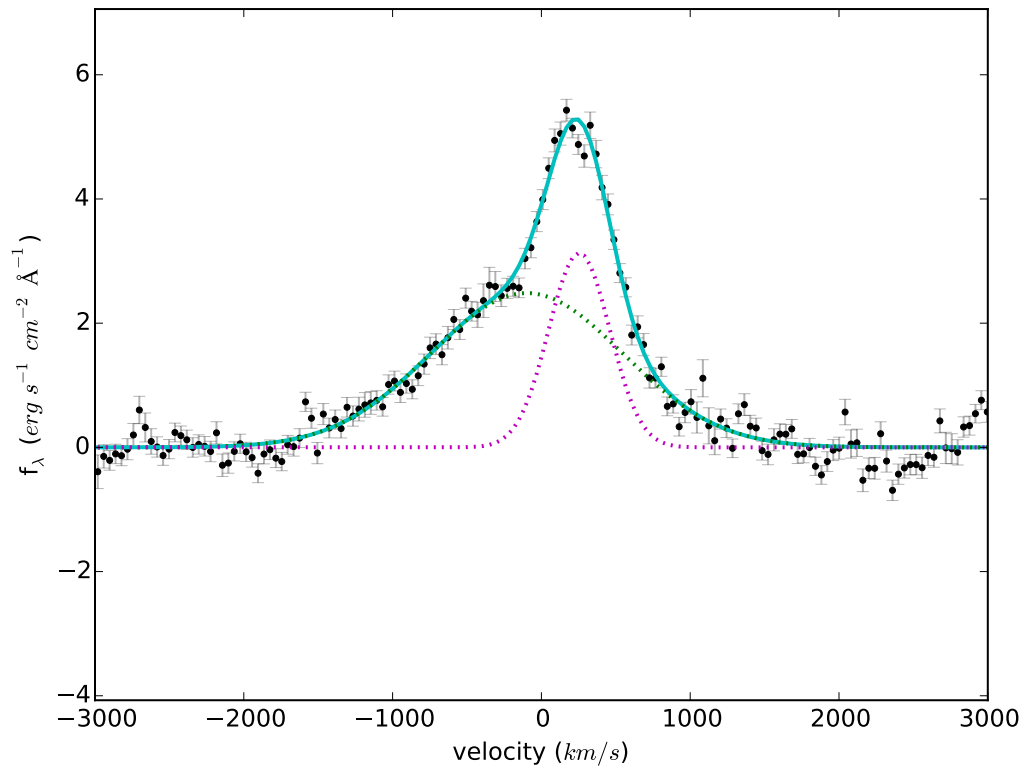


Fig. 3.3.—  $\text{Pa}\beta$  from NGC 1275, an example of a narrow plus broad Gaussian. Y-axis units are  $f_\lambda$  in  $10^{-16} \text{ erg s}^{-1} \text{ cm}^{-2} \text{ \AA}^{-1}$ . X-axis units are velocity in  $\text{km s}^{-1}$ .

with detected profiles of  $\text{H}_2$ , 41 of 55 are fit by a single Gaussian component, and 14 of 55 are fit by two blended Gaussian components. Six of these  $\text{H}_2$  profiles show some evidence for blue-shifted absorption. The absorption components are included in Table 3.4, but are not included in further analysis. As an illustration that the  $\text{H}_2$  and recombination lines behave similarly (with the exception of broad components) we have overplotted normalized versions of the fits to the  $\text{Pa}\beta$  and  $\text{H}_2$  S(1) 1-0 profiles from VV 250 A. This example is shown in Figure 3.7. We observe the components to be fairly closely aligned. The red side component in the neutral Hydrogen recombination profile is roughly 60% as strong as its counterpart in the molecular Hydrogen profile.

Table 3.4. Molecular Line Fits

Source	Component	H <sub>2</sub> 2.1213 $\mu\text{m}$		
		Amplitude ( $10^{-16} \text{ erg s}^{-1} \text{ cm}^{-2} \text{ \AA}$ )	$\sigma$ ( $\text{km s}^{-1}$ )	Offset ( $\text{km s}^{-1}$ )
MCG-02-01-051	single	3.91	110.45	82.67
UGC 02369 A	single	...	...	...
UGC 02369 B	single	5.90	92.84	68.67
NGC 1275	single	9.62	158.94	105.74
UGC 04881 A	red	1.23	161.33	40.24
	blue	0.90	64.11	74.22
UGC 04881 B	single	3.97	119.00	93.37
UGC 05101	red	1.58	285.81	90.94
	blue	3.08	161.76	74.65
NGC 3221	single	...	...	...
NGC 4922 B	single	...	...	...
NGC 4922 A	single	2.70	90.69	74.57
CGCG 043-099	red	1.21	96.06	83.52
	blue	1.13	94.03	305.37
MCG -02-33-098	single	...	...	...
VV 250 A	red	2.14	78.48	214.11
	blue	2.15	94.43	22.29
VV 250 B	single	...	...	...
UGC 08387 obs1	single	11.03	90.62	22.54
UGC 08387 obs2	single	3.26	143.97	74.77
NGC 5104	single	2.27	117.88	71.40
NGC 5256 B	red	2.77	200.23	269.99
	blue	0.78	88.72	-149.30
	absorption	-0.85	672.72	-149.34
NGC 5256 A	emission	3.98	168.38	261.02
	absorption	-0.41	495.17	-655.38
UGC 08696	single	57.47	223.09	29.66
UGC 08739	single	2595.86	72.81	70.78
NGC 5331 B	single	223.71	158.58	136.07
NGC 5331 A	red	1031.44	63.53	28.28
	blue	912.77	80.35	213.57

Table 3.4—Continued

Source	Component	H <sub>2</sub> 2.1213 $\mu\text{m}$		Offset ( $\text{km s}^{-1}$ )
		Amplitude ( $10^{-16} \text{ erg s}^{-1} \text{ cm}^{-2} \text{ \AA}$ )	$\sigma$ ( $\text{km s}^{-1}$ )	
CGCG 247-020	single	7.38	75.29	149.64
NGC 5653	emission	0.48	95.68	105.21
	absorption	-0.36	458.21	-604.98
IRAS F14348-1447 A	single	2.38	116.89	29.81
IRAS F14348-1447 B	single	5.35	114.05	166.07
VV 340 N	single	3957.27	98.46	220.77
VV 340 S	single	0.24	58.78	6.09
CGCG 049-057	single	1.96	102.33	126.49
VV 705 A	single	9.96	78.33	-136.57
VV 705 B	single	2.22	135.02	237.96
IRAS F15250+3608	single	3.47	119.32	145.60
NGC 5936	emission	78.88	62.15	83.69
	absorption	-8.22	1365.03	133.60
NGC 6090 A	single	2.28	84.16	67.77
NGC 6090 B	single	1.87	62.47	4.05
IRAS F17132+5313 A	red	0.12	69.82	-63.23
	blue	0.36	89.95	172.21
IRAS F17132+5313 B	red	0.14	64.11	117.15
	blue	0.05	248.95	-18.91
IRAS 18090+0130 A	red	1.22	59.48	200.16
	blue	1.08	65.40	24.69
IRAS 18090+0130 C	single	...	...	...
IRAS 18090+0130 B	red	3.00	48.18	224.27
	blue	3.66	115.13	-7.40
NGC 6670	single	2.70	90.58	116.23
NGC 6701	single	56.57	66.22	60.97
ESO 593-IG008	red	1.40	103.30	184.66
	blue	1.05	79.39	-47.46
NGC 6786	single	0.24	79.30	2.64
IRAS F19297-0406	single	3.54	153.16	-29.17
IRAS 19542+1110	single	0.50	-53.02	-100.98

Table 3.4—Continued

Source	Component	H <sub>2</sub> 2.1213 $\mu$ m		
		Amplitude ( $10^{-16}$ <i>erg s<sup>-1</sup> cm<sup>-2</sup> Å</i> )	$\sigma$ ( <i>km s<sup>-1</sup></i> )	Offset ( <i>km s<sup>-1</sup></i> )
IRAS 20351+2521	single	19.10	85.04	200.13
II Zw 096	single	1.83	54.76	106.29
IRAS 21101+5810 B	single	2.97	130.85	95.09
IRAS 21101+5810 A	single	...	...	...
UGC 12150 A	red	0.83	63.19	-82.92
	blue	0.46	65.60	-398.20
UGC 12150 B	red	5.24	139.95	62.44
	blue	3.63	54.74	-64.51
IRAS F22491-1808	single	1.35	133.30	179.01
NGC 7469	single	17.17	121.87	28.32
IC 5298	emission	3.64	127.78	20.51
	absorption	-0.89	250.99	-789.69
NGC 7674	emission	4.20	126.38	-48.61
	absorption	-1.52	894.51	-456.14
IRAS F23365+3604	single	4.02	116.93	10.82
IRAS 23436+5257 B	single	4.80	88.17	-10.05
IRAS 23436+5257 A	single	1.56	117.53	50.86

### 3.3 DISCUSSION

It is unsurprising that the recombination lines often trace multiple unresolved components, given the merger activity inherent in the majority of the GOALS sample as well as the property of LIRGs to be driven by compact nuclear activity, be it due to a starburst, an AGN or a combination of the two. It follows that the material which is most ionized should lie at the center of the activity (the nuclei), and it might well move in coherent flows at speeds on the order of the dynamical speed. Further we take the presence of each distinct broad emission component observed here, namely those found in NGC 1275, NGC 7469, and NGC 7674 to be associated with the Seyfert nuclei associated with these sources. The absence of these broad components in the molecular profiles provides further evidence for this relationship (since the material locked in outflows may be mostly ionized).

We note that the fits to Paschen  $\beta$  and Brackett  $\gamma$  profiles are distinct in many sources. The parameters of the fits and even the number of components required to fit each profile often varies between the two lines. As an illustration of this, Figures 3.8 and 3.9 show the fits to Pa $\beta$  and Br $\gamma$  respectively in UGC 12150 B. Both fits are double Gaussians, but the fit parameters are markedly different. The differences in the line profiles can be plausibly attributed to significantly more absorption of the shorter wavelength line by dust grains. This is supported by the extinction model of Rieke & Lebofsky (1985) which shows the near infrared J band is more than twice as extinguished as the near infrared K band ( $A_{1.28\mu m}/A_{2.16\mu m} = 2.5$ ).

To examine the relationship between outflows and their sources, we test for any correlation between the outflow velocities and the strength of each starburst or AGN as possible drivers for the acceleration of outflowing material. In Figure 3.10 we show starburst luminosity,  $L_{SB}$ , and AGN luminosity,  $L_{AGN}$ , for each system plotted

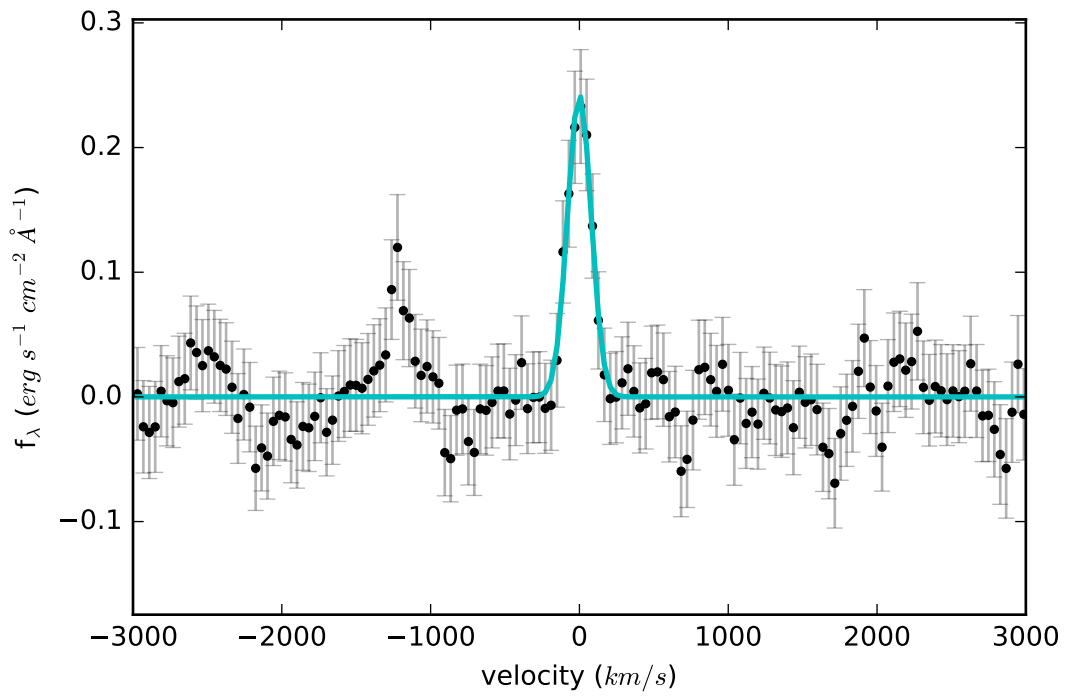


Fig. 3.4.—  $\text{H}_2$  S(1) 1-0 from NGC 6786. Y-axis units are  $f_\lambda$  in  $10^{-16} \text{ erg s}^{-1} \text{ cm}^{-2} \text{ \AA}^{-1}$ . X-axis units are velocity in  $\text{km s}^{-1}$ .

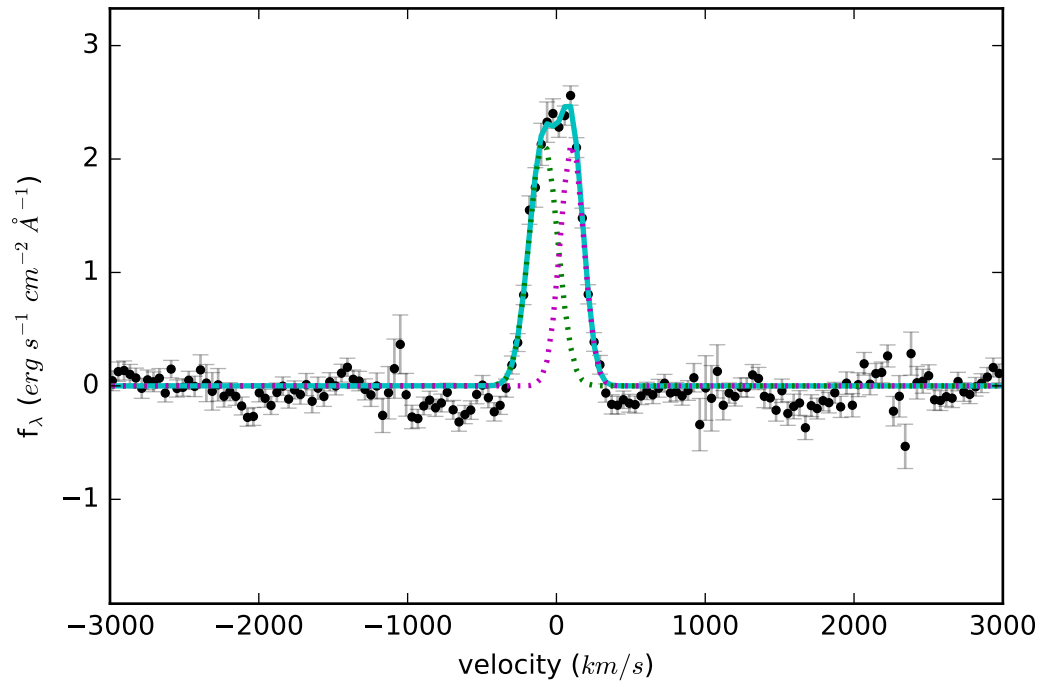


Fig. 3.5.—  $\text{H}_2$  S(1) 1-0 from VV 250a. Y-axis units are  $f_{\lambda}$  in  $10^{-16} \text{ erg s}^{-1} \text{ cm}^{-2} \text{ \AA}^{-1}$ . X-axis units are velocity in  $\text{km s}^{-1}$ .



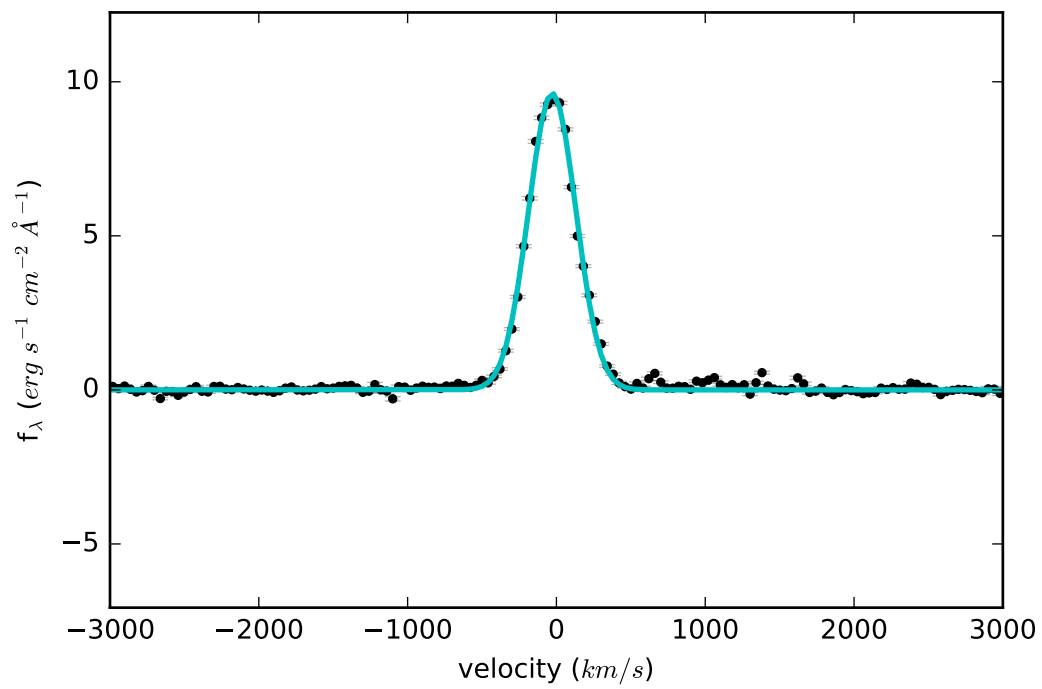


Fig. 3.6.— H<sub>2</sub> S(1) 1-0 from NGC 1275. Y-axis units are  $f_{\lambda}$  in  $10^{-16} \text{ erg s}^{-1} \text{ cm}^{-2} \text{ \AA}^{-1}$ . X-axis units are velocity in  $\text{km s}^{-1}$ .

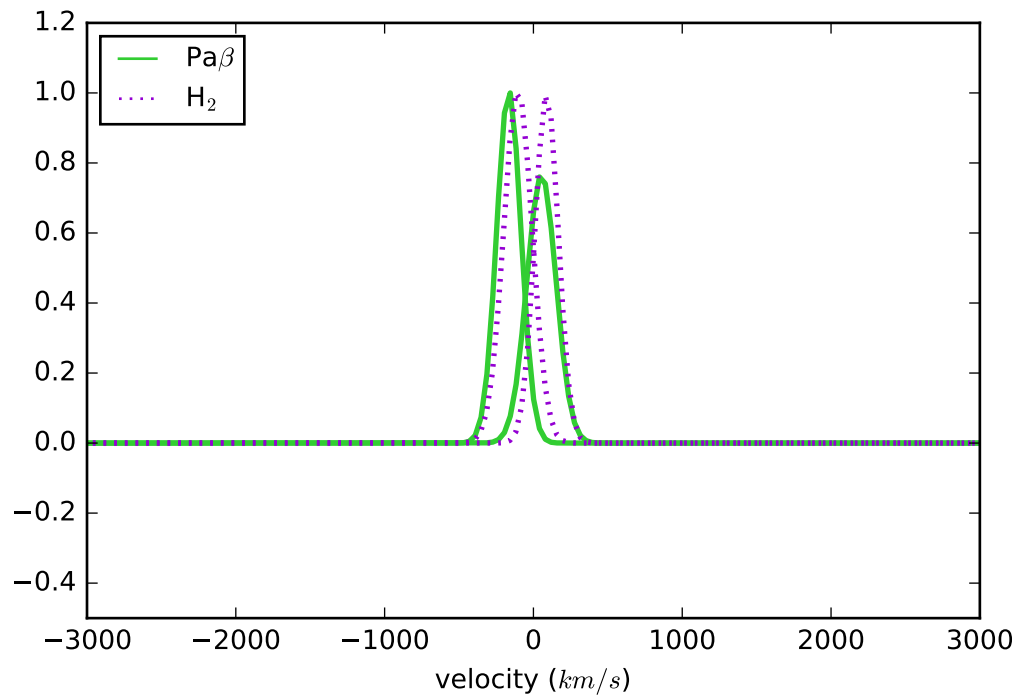


Fig. 3.7.— A direct comparison between the double Gaussian fits to the  $\text{Pa}\beta$  profile and the profile of  $\text{H}_2$  S(1) 1-0  $\lambda 2.1213 \mu\text{m}$ . For the purposes of this comparison each fit profile has been normalized by its overall height. Thus the y-axis is a unitless ratio. X-axis units are velocity in  $\text{km s}^{-1}$ .

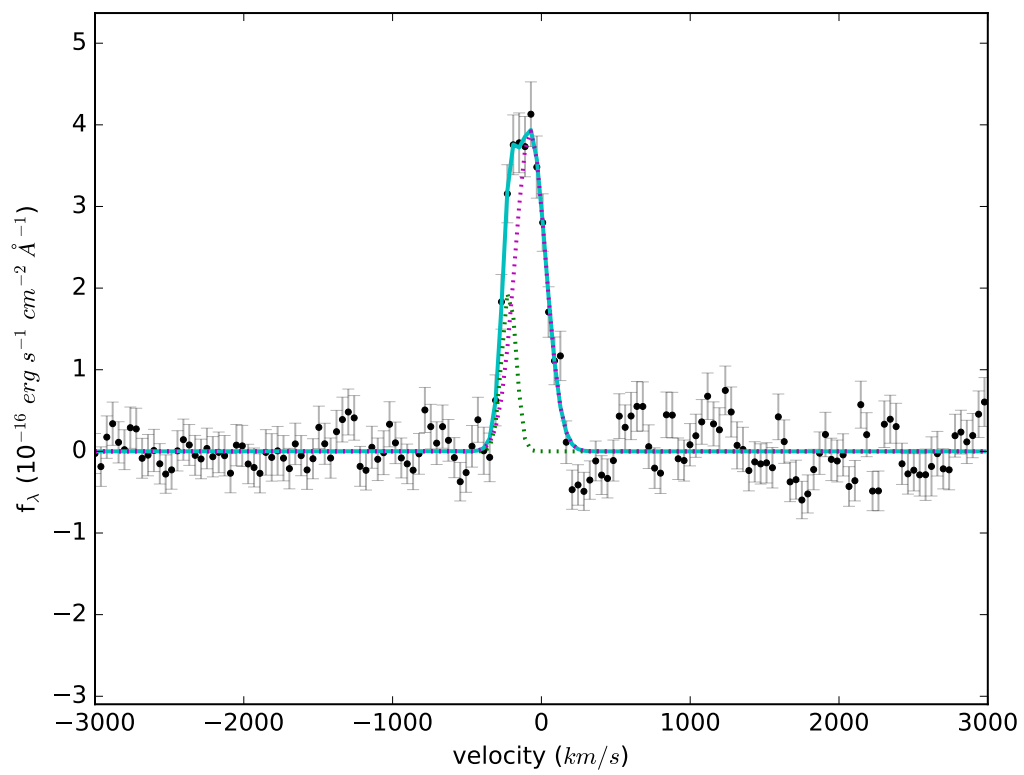


Fig. 3.8.— Paschen  $\beta$  profile fit from UGC 12150 B. Y-axis units are  $f_\lambda$  in  $10^{-16} \text{ erg s}^{-1} \text{ cm}^{-2} \text{ \AA}^{-1}$ . X-axis units are velocity in  $\text{km s}^{-1}$ .

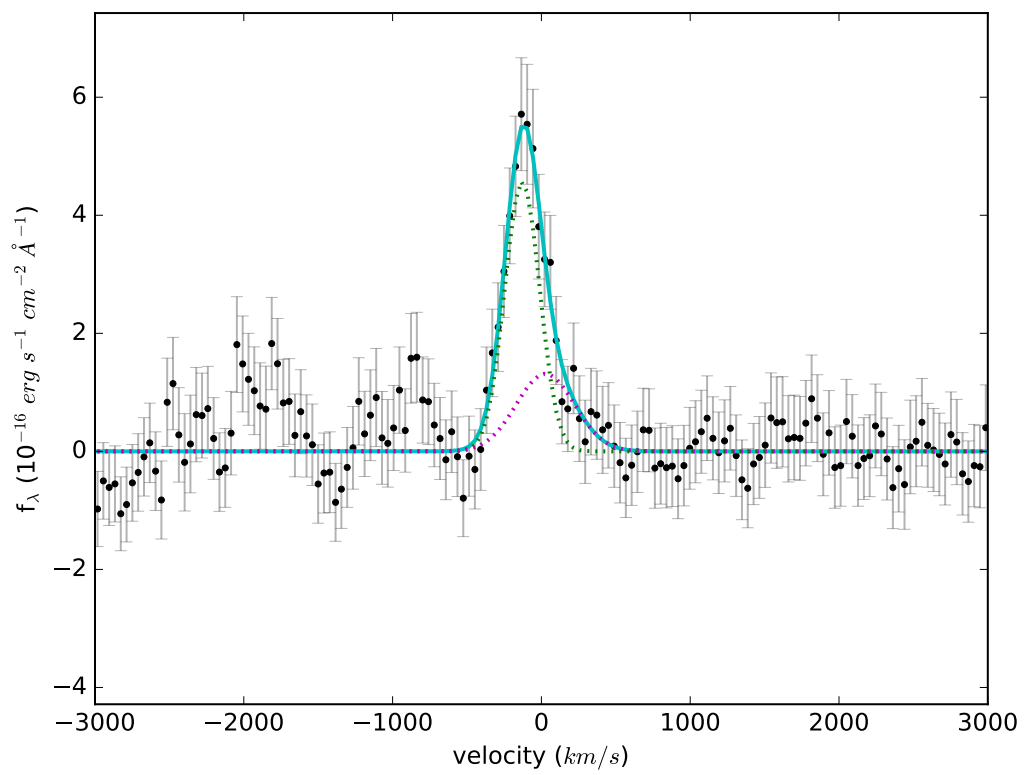


Fig. 3.9.— Brackett  $\gamma$  profile fit from UGC 12150 B. Y-axis units are  $f_{\lambda}$  in  $10^{-16} \text{ erg s}^{-1} \text{ cm}^{-2} \text{ \AA}^{-1}$ . X-axis units are velocity in  $\text{km s}^{-1}$ .

against the central velocity of the most blue-shifted emission component,  $v_{50}$ , for the fits to both Paschen  $\beta$  and  $H_2 \lambda 2.1213 \mu\text{m}$ .  $L_{SB}$  was computed with a simple linear mixing model (given in Armus et al. (2007); Petric et al. (2011)) in which the equivalent width of the  $6.2 \mu\text{m}$  PAH feature represents the contribution of the starburst to the bolometric luminosity,  $L_{bol} = 1.15 \times L_{IR}$  (following Veilleux et al. (2009)). The 100% starburst threshold is taken to be the average of the  $6.2 \mu\text{m}$  PAH equivalent width (0.53) in pure starburst galaxies (Bernard-Salas et al. 2009). Throughout the analysis we ignore the UV contribution to the SFR (Howell et al. (2010) shows the contribution is always relatively small).  $L_{AGN}$  is given by

$$L_{AGN} = L_{bol} - L_{SB} \quad (3.1)$$

The derived values of  $L_{SB}$  and  $L_{AGN}$  are given in Table 3.5 along with the values of  $6.2 \mu\text{m}$  PAH equivalent width.

Table 3.5. Derived Values of  $L_{SB}$  and  $L_{AGN}$ 

Source	$W_{6.2\mu m}$ ( $\mu m$ )	$\log(L_{SB})$	$\log(L_{AGN})$
MCG-02-01-051	0.72	11.47	...
UGC 02369 B	0.57	11.66	...
UGC 02369 A	0.57	11.66	...
NGC 1275	0.02	9.84	11.24
UGC 04881 A	0.4	11.63	11.14
UGC 04881 B	0.61	11.75	...
UGC 05101	0.51	11.99	10.59
NGC 4922 B	0.16	8.41	8.77
NGC 4922 A	0.16	10.86	11.22
CGCG 043-099	0.55	11.68	...
MCG -02-33-098	0.7	11.17	...
VV 250 A	0.13	11.19	11.68
UGC 08387 obs2	0.62	11.73	...
UGC 08387 obs1	0.62	11.73	...
NGC 5104	0.51	11.24	9.84
NGC 5256 A	0.44	11.47	10.78
NGC 5256 B	0.44	11.47	10.78
UGC 08696	0.12	11.56	12.09
UGC 08739	0.57	11.14	...
NGC 5331 B	0.61	11.65	...
NGC 5331 A	0.6	11.65	...
CGCG 247-020	0.76	11.38	...
NGC 5653	0.54	11.12	...
IRAS F14348-1447 A	0.25	12.03	12.08
IRAS F14348-1447 B	0.25	12.03	12.08
CGCG 049-057	0.51	11.31	9.91
VV 705 A	0.75	11.95	...
VV 705 B	0.75	11.95	...
IRAS F15250+3608	0.03	10.83	12.06
NGC 5936	0.62	11.13	...
NGC 6090 A	0.73	11.57	...
NGC 6090 B	0.73	11.57	...
IRAS 18090+0130 A	0.61	11.64	...
IRAS 18090+0130 B	0.52	11.63	9.92
IRAS 18090+0130 C	0.52	11.63	9.92
NGC 6670	0.62	11.66	...
NGC 6701	0.55	11.11	...
ESO 593-IG008	0.56	11.93	...
NGC 6786	0.64	11.49	...
IRAS F19297-0406	0.3	12.18	12.07
IRAS 19542+1110	0.29	11.84	11.76
IRAS 20351+2521	0.57	11.60	...

Table 3.5—Continued

Source	$W_{6.2\mu m}$ ( $\mu m$ )	$\log(L_{SB})$	$\log(L_{AGN})$
II Zw 096	0.27	11.64	11.62
IRAS 21101+5810 A	0.55	11.81	...
IRAS 21101+5810 B	0.55	11.81	...
UGC 12150 B	0.53	11.35	...
UGC 12150 A	0.53	11.35	...
IRAS F22491-1808	0.48	12.13	11.15
NGC 7469	0.23	11.29	11.40
IC 5298	0.12	10.96	11.49
NGC 7674	0.02	10.14	11.54
IRAS F23365+3604	0.41	12.08	11.55
IRAS 23436+5257 A	0.37	11.41	11.05
IRAS 23436+5257 B	0.37	11.41	11.05

In addition, we plot similar data derived from a sample of galaxies observed in the OH 119 line by Veilleux et al. (2013).

As can be seen in the Pa $\beta$  figure (top left of 3.10). The majority of our galaxies show no or moderate deviations from  $v_{50} = 0 \text{ km s}^{-1}$ . Only in the case of 5 galaxies are offsets from the system velocity larger than  $100 \text{ km s}^{-1}$  actually measured. Four out of the 5 of these sources have starburst luminosities  $> 10^{10.9} L_{\odot}$ , corresponding to star formation rates of  $> 10 M_{\odot} \text{ yr}^{-1}$ . Only one LIRG, NGC 5256, has a velocity offset comparable to the largest offsets measured in OH by Veilleux et al. (2013). The OH line is clearly tracing more extreme outflows than measured by the recombination lines. This result may be a function of obscuration - the OH 119  $\mu\text{m}$  line is able to trace gas much closer to the embedded energy sources than the Pa $\beta$  can. The acceleration of gas is likely to be strongest in close proximity to the obscured starburst and/or AGN.

As mentioned above, NGC 5256 A (the eastern nucleus) is a notable outlier to the relationship between  $L_{AGN}$  and  $v_{50}$  for the Paschen  $\beta$  profile. Although we compute an  $L_{AGN}$  of only  $10^{10.8} L_{\odot}$  for this source, it shows evidence for outflowing material at over  $500 \text{ km s}^{-1}$ . The fit to the NGC 5256 Pa $\beta$  line is shown in Figure 3.11. The other notable outlier in figure 3.10 is UGC 12150 A, which indicates a blueshifted component at  $\sim 400 \text{ km s}^{-1}$  in its H<sub>2</sub> 2.1213  $\mu\text{m}$  line. The fit to H<sub>2</sub> 2.1213  $\mu\text{m}$  in UGC 12150 A is shown in Figure 3.12.

It's important to note that in addition to outflows, blueshifted emission components may be caused by multiple, spatially unresolved nuclei. NGC 5256 is known to contain two nuclei moving with velocity relative to one another of  $\sim 280 \text{ km s}^{-1}$  (Mazzarella et al. 2012). These nuclei were spatially resolved in our observations and appear in this work as NGC 5256 A and NGC 5256 B, two spectra extracted



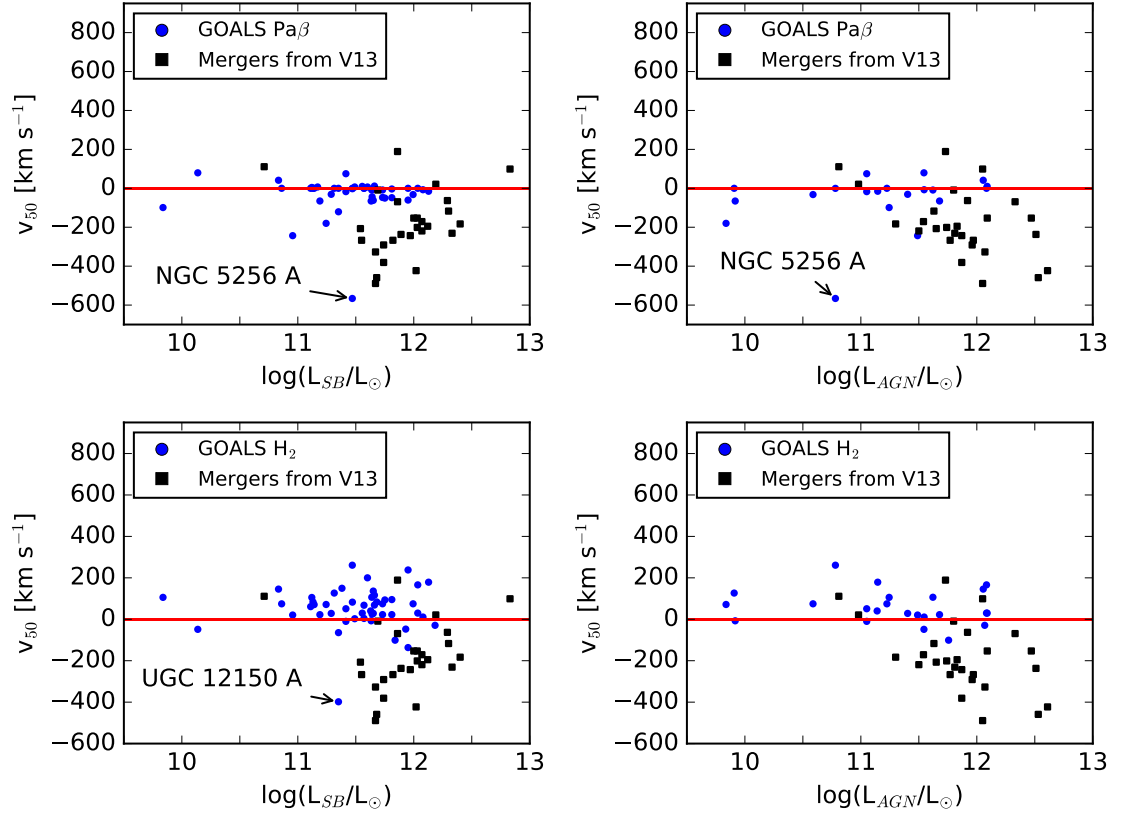


Fig. 3.10.— Velocity offsets from  $\text{Pa}\beta$  (top row) and  $\text{H}_2$  2.1213  $\mu\text{m}$  (bottom row) plotted against starburst luminosity,  $L_{SB}$ , and AGN luminosity,  $L_{AGN}$ . Blue circles are data from this thesis, while black squares are from Veilleux et al. (2013)

from a single pointing. Each spectrum was assigned a systemic velocity measured from its own near-infrared CO bandhead stellar absorption features. It is relative to this systemic velocity that the blueshifted component having  $v \sim 500 \text{ km s}^{-1}$  was measured. A visual inspection of NICMOS high spatial resolution imaging does not reveal any obvious signs of multiple nuclei that were spatially unresolved in our TripleSpec observations. However, this possibility cannot be fully ruled out without even higher spatial resolution imaging. UGC 12150 lacks coverage from the Hubble Space Telescope, thus we have been unable to investigate high resolution imaging in that source. Therefore the outflow in UGC 12150 implied in this work may be viewed with considerably more skepticism than that in NGC 5256 A.

### 3.4 CONCLUSIONS

We present multi-component Gaussian fits to the Paschen  $\beta$ , Brackett  $\gamma$ , and  $\text{H}_2$  2.1213  $\mu\text{m}$  profiles of the spectra presented in Chapter 2. We find

- Recombination line profiles ( $\text{Pa}\beta$  and  $\text{Br}\gamma$ ) tend to be well fit by single Gaussians of velocity dispersion  $\sim 30 - 200 \text{ km s}^{-1}$  or two blended Gaussians of similar widths. In the cases of known Seyfert Galaxies NGC 1275, NGC 7469, and NGC 7674, we see evidence for faint broad Gaussian components of width  $\sim 650 - 800 \text{ km s}^{-1}$ . The molecular line profiles ( $\text{H}_2$  2.1213  $\mu\text{m}$ ) also tend to be observed to be single or double Gaussians with similar velocity dispersions. Broad components are not observed in the molecular profiles, consistent with broad components associated with AGN broad line regions.
- Fits to the  $\text{Pa}\beta$  and  $\text{Br}\gamma$  profiles in a given source are often significantly different. This behavior may be attributed to intrinsic extinction by dust. A careful

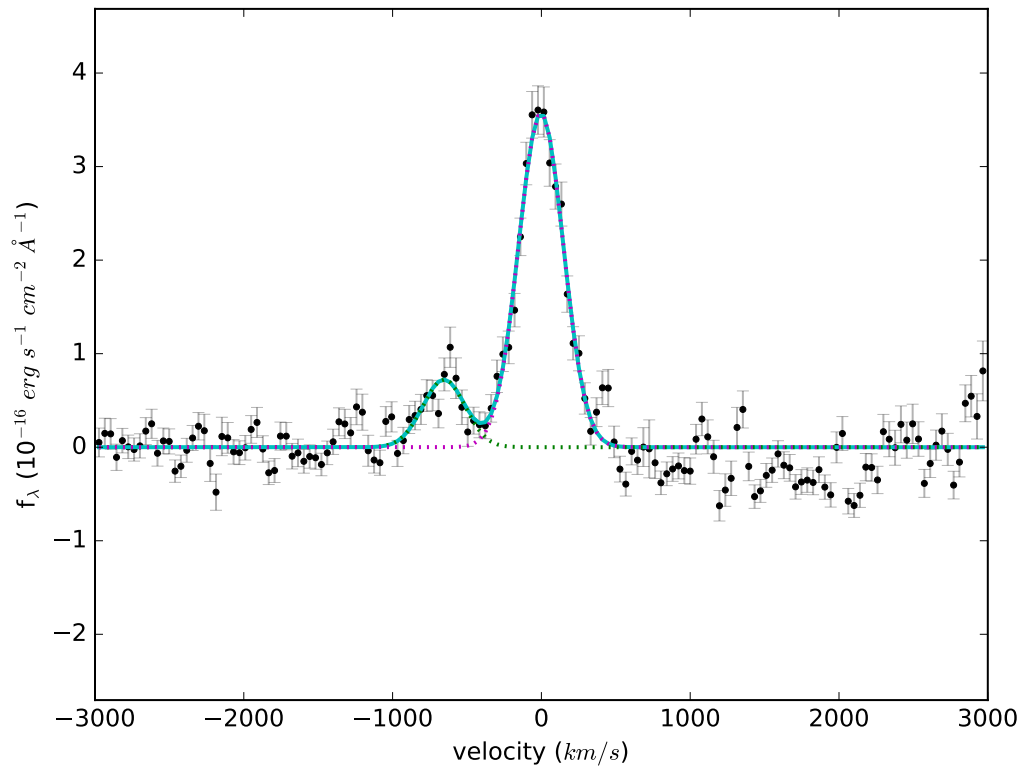


Fig. 3.11.—  $\text{Pa}\beta$  from NGC 5256 A. Note the highly blueshifted component of the line. Y-axis units are  $f_{\lambda}$  in  $10^{-16} \text{ erg s}^{-1} \text{ cm}^{-2} \text{ \AA}^{-1}$ . X-axis units are velocity in  $\text{km s}^{-1}$ .

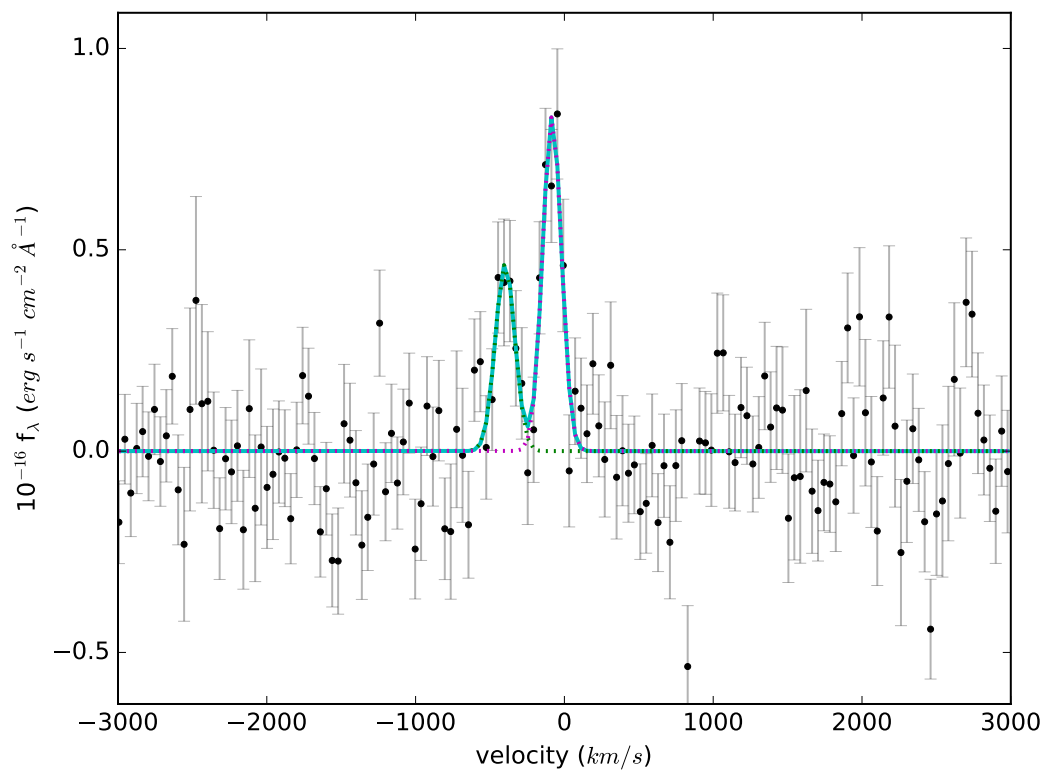


Fig. 3.12.—  $\text{H}_2$  S(1) 1-0 from NGC 5256 A. Note the highly blueshifted absorption component of the line. Y-axis units are  $f_{\lambda}$  in  $10^{-16} \text{ erg s}^{-1} \text{ cm}^{-2} \text{ \AA}^{-1}$ . X-axis units are velocity in  $\text{km s}^{-1}$ .

comparison of the difference between the  $\text{Pa}\beta$  and  $\text{Br}\gamma$  profiles for a given source may be used to estimate the relative extinction of each observed component.

- We find that five of the LIRGs in our sample show evidence for outflow velocities  $> 100 \text{ km s}^{-1}$ . Four of these five LIRGs have starburst luminosity  $L_{SB} > 10^{10.9} L_{\odot}$ . Only one source (NGC 5256) has an estimated outflow velocity comparable to the highest outflow velocities observed in OH  $119 \mu\text{m}$  by Veilleux et al. (2013). The relative lack of high velocity outflows observed in the  $\text{Pa}\beta$  lines as compared to that seen in OH may be an optical depth effect, i.e., the OH line is likely probing regions closer to the obscured starburst and/or AGN where the acceleration is plausibly the strongest.

## Chapter 4

# Evidence for High Velocity Ejecta in the Near Infrared Emission Lines of SN 2010jl

### 4.1 INTRODUCTION

Type IIn supernovae (SNe IIn) are characterized by narrow optical emission lines and a blue continuum (Schlegel 1990). The presence of a narrow line component at early times is taken to indicate a dense surrounding circumstellar medium that is heated and ionized by radiation from the explosion and the continuing interaction. The presence of wings on the narrow lines, as observed for the Type IIn SN 1998S (Leonard et al. 2000), can at least in some cases be explained by electron scattering in a mildly optically thick medium (Chugai 2001). The optical luminosity of a Type IIn event can also be explained by shock interaction with a dense circumstellar medium (Chugai & Danziger 1994). The velocity of the circumstellar mass loss can be deduced from the velocities indicated by P Cygni line profiles observed in the H Balmer lines;

the typical line velocities are  $100 - 1400 \text{ km s}^{-1}$  (Kiewe et al. 2012). The mass loss rates implied by the interaction luminosities are  $\sim 0.01 - 0.1 M_{\odot} \text{ yr}^{-1}$ . High mass loss rates were also derived from infrared emission attributed to circumstellar dust (Fox et al. 2011). Roughly  $6\% - 11\%$  of core collapse supernovae are of Type IIn (Smith et al. 2011a).

These rates of mass loss are much higher than those found in normal stars, and the place of Type IIn events in stellar evolution is unclear. The progenitor stars have been linked to luminous blue variables (LBVs) because these have the requisite mass loss density and outflow velocity during their eruptive phases (e.g., Smith et al. 2010; Fox et al. 2011; Kiewe et al. 2012). In addition, the progenitor of SN 2005gl is consistent with an LBV (Gal-Yam & Leonard 2009). A problem is that stars in this evolutionary phase are not expected to undergo supernova explosions (although see the rotating models of Groh et al. 2013). Suggestions for the proximity in time of mass loss and explosion include wave-driven mass loss (Quataert & Shiode 2012) and binary-driven mass loss (Chevalier 2012), but these studies are very speculative. Soker (2013) also attributes the dense circumstellar medium around SNe IIn to binary interaction.

The bright Type IIn supernova SN 2010jl was discovered on UT 2010 November 3.5 by Newton & Puckett (2010). It was subsequently confirmed at an unfiltered magnitude of 12.9. Pre-discovery images showed that the supernova was present on 2010 October 9.6 (Stoll et al. 2011), which we use as our zero point in time. The supernova is located at R.A. =  $9^{\text{h}}42^{\text{m}}53^{\text{s}}.33$ , Dec. =  $+9^{\circ}29'41''.8$  (equinox 2000.0). It lies  $2''.4$  east and  $7''.7$  north of the center of the host galaxy, UGC 5189A. We take the distance to the supernova to be 49 Mpc (Smith et al. 2011b) and the reddening to be  $E(B - V) = 0.058$  (Fransson et al. 2014). Smith et al. (2011b) used pre-explosion

HST imaging to identify a bright, blue point source coincident with the position of the supernova, which they took to imply that the progenitor of SN 2010jl had a mass above  $30 M_{\odot}$ . Andrews et al. (2011) observed the supernova in the *Spitzer* 3.6 and  $4.5 \mu\text{m}$  bands and the *JHK* bands during days 90 – 108, finding evidence for 7500 K and 750 K components. However, Fransson et al. (2014) have examined the IR data for this age and find the temperature of the cool component to be  $\sim 1800$  K; this temperature characterizes the cool component for 100’s of days. Fransson et al. (2014) presented one  $0.3 - 2.4 \mu\text{m}$  spectrum of SN 2010jl (on day 460), as well as extensive optical and ultraviolet observations and near infrared (NIR) photometry. *Spitzer* observations were also presented by Fox et al. (2013), who find evidence for circumstellar emission and a high mass loss rate. Maeda et al. (2013) presented a spectrum (optical through NIR) on day 563, finding evidence for dust formation in the supernova ejecta.

SN 2010jl has also been detected as an X-ray source (Immler et al. 2010; Chandra et al. 2012; Ofek et al. 2014). Observations on 2010 December 7 – 8 (day 58 since discovery of the supernova) showed a hot ( $kT > 8$  keV) thermal spectrum with an absorbing column  $\sim 10^{24} \text{ cm}^{-2}$ , assuming incomplete ionization of the circumstellar gas and a metallicity 0.3 of solar (Chandra et al. 2012). This column density corresponds to an electron scattering optical depth  $\sim 1$ . By 2011 October 17 – 18 (day 372), the absorbing column declined by a factor of 3, but the X-ray emission remained steady and hot ( $kT > 12$  keV). However, Ofek et al. (2014) re-examined the *Chandra* data and found them difficult to model. Hard X-ray observations with *NuSTAR* on 2012 October 6 yielded a temperature of  $\sim 18_{-4}^{+6}$  keV (Ofek et al. 2014), which corresponds to a shock velocity of  $\sim 4000 \text{ km s}^{-1}$ .

Here we present a set of 10 NIR spectra of SN 2010jl spanning 529 days (Section



2). The various components contributing to the line and continuous emission are described in Section 3. The physical picture implied by the observations is discussed in Section 4 and the conclusions are in Section 5.

## 4.2 OBSERVATIONS

Data presented here were obtained using TripleSpec, an  $0.9 - 2.4 \mu\text{m}$ ,  $R \sim 3000$  spectrograph, on the ARC 3.5 m telescope at Apache Point Observatory (Wilson et al. 2004; Herter et al. 2008). The supernova was observed 10 times between 2010 November 15 and 2012 April 26. Table 4.1 shows the details of each observation. Day numbers listed in Table 4.1 refer to time elapsed since the first detection of the supernova on 2010 Oct 9. Integration time refers to the total exposure time for each date. Individual exposures were 5 minutes in length and nodded in an ABBA pattern along the slit. We also observed the spectrophotometric standard HD 85377 for the telluric correction and photometric calibration. The airmass at the time of each observation is given in Table 4.1 for both SN 2010jl and HD 85377. Sky subtraction was achieved by differencing each pair of A and B exposures. Sky subtraction, spectral extraction, telluric correction, and photometric calibration were carried out using a modified version of the IDL utility *SpexTool* (Cushing et al. 2004).

Figures 4.1 – 4.3 show the spectra in the  $J$ ,  $H$ , and  $K$  bands, respectively. The spectra are normalized to have the same continuum intensity at  $1.55 \mu\text{m}$ . Identifications of the dominant lines are given.

Variations in seeing and cloud cover are problematic for photometric calibration of any long-slit spectrum. Therefore, the photometric calibrations produced by *SpexTool* are only roughly accurate. Much of the following discussion deals with descriptions of the line or continuum shapes, rendering a precise photometric calibration unim-

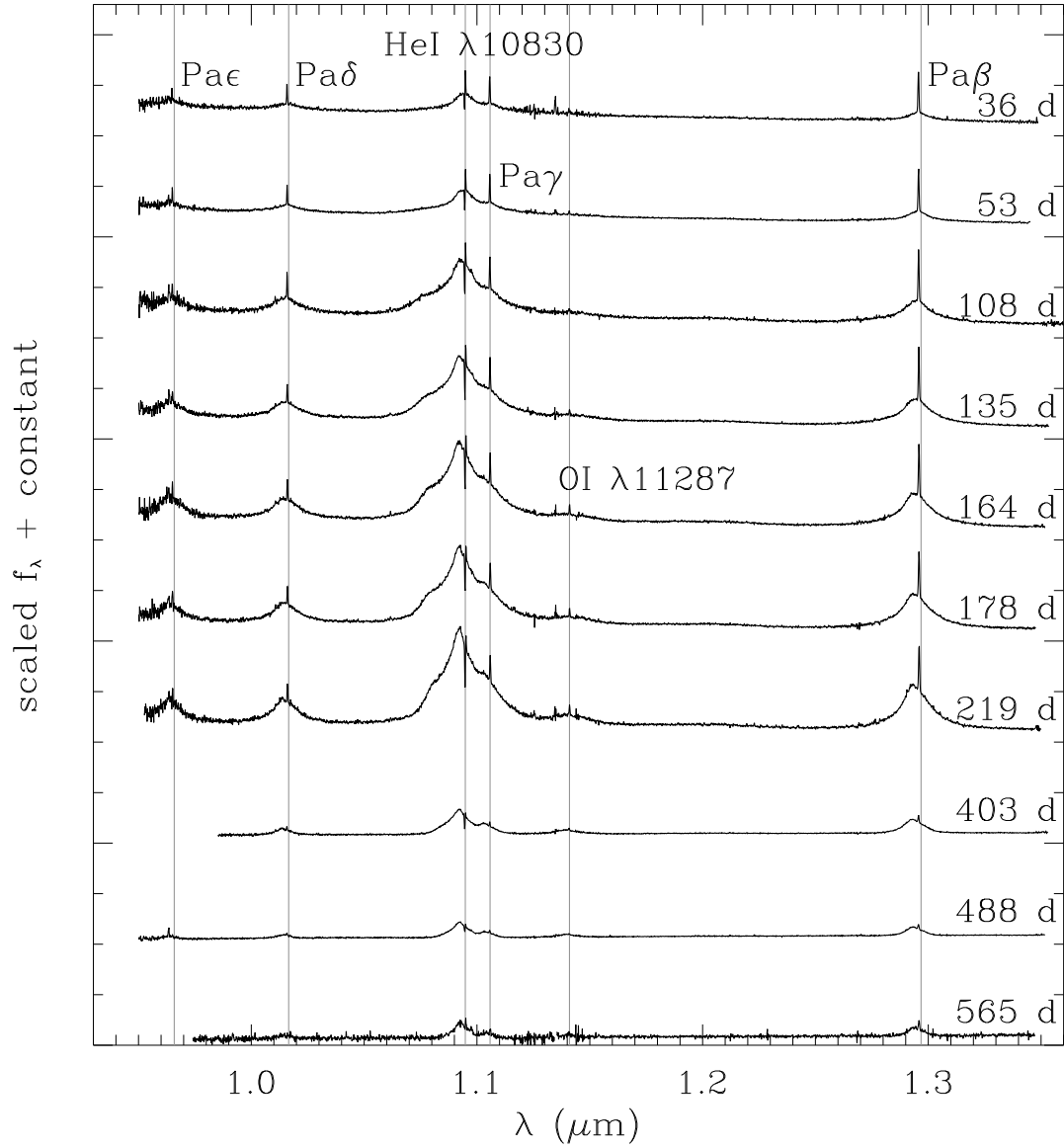


Fig. 4.1.— *J* band spectra of SN 2010jl taken at the ARC 3.5m Telescope. The data have not been corrected for redshift or reddening. The spectra have been scaled so that the continuum of each spectrum has the same strength at 1.55  $\mu\text{m}$  and then displaced vertically for clarity. The day numbers refer to the earliest observation, 2010 October 9. Figures 4.2 and 4.3 were prepared in the same way.

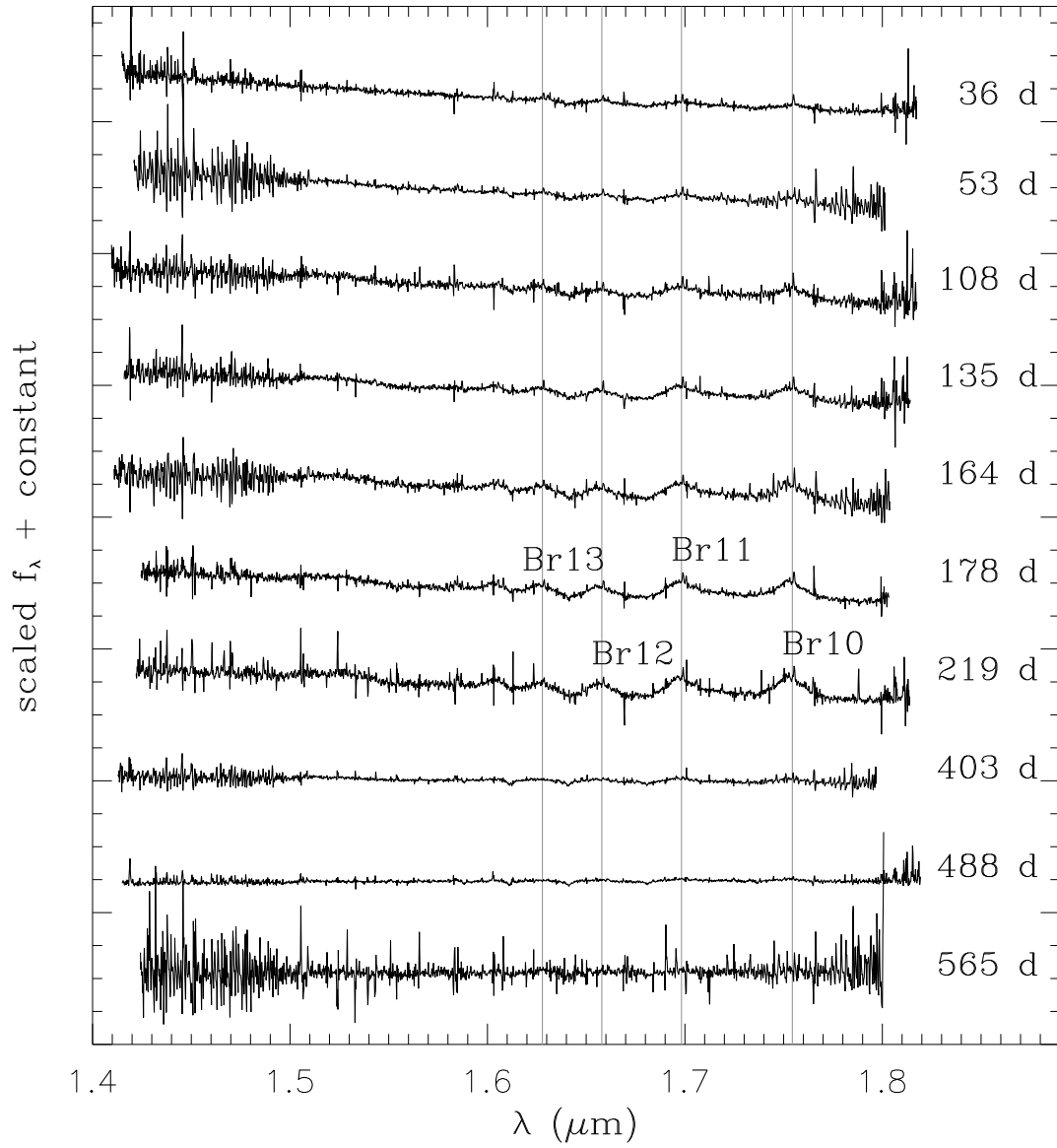


Fig. 4.2.—  $H$  band spectra of SN 2010jl taken at the ARC 3.5m Telescope.

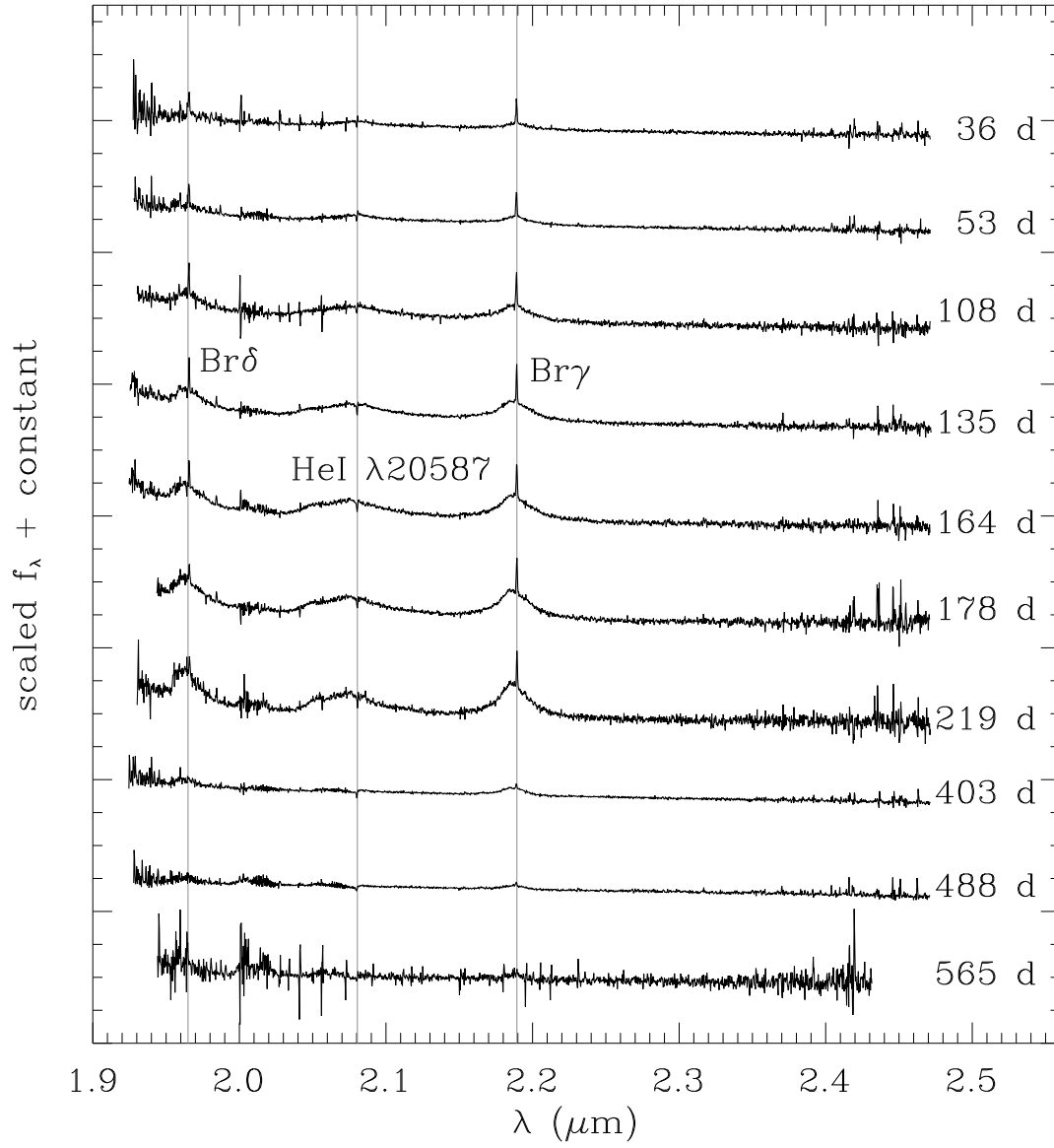


Fig. 4.3.—  $K$  band spectra of SN 2010jl taken at the ARC 3.5m Telescope.

portant. Figures 4.5, 4.9, 4.15, and 4.16 show the true flux density as revealed by photometric observations collected by Fransson et al. (2014). To estimate  $H$ -band magnitudes at the exact dates of our observations we fit separate  $2^{nd}$  degree polynomials to the early time (before 250 days) and late time (after 403 days)  $H$ -band light curves published by Fransson et al. (2014). Because Fransson et al. (2014) does not publish photometry nearby in time to day 403, we used cubic spline interpolation over the full light curve to estimate the magnitude at 403 days. As a result, the calibration to the photometry for day 403 is somewhat more uncertain than that at other dates. Nevertheless, the behavior of the flux density at day 403 seems to fall in line with the other observations. Once  $H$  magnitudes had been determined for each TripleSpec observation, we converted each magnitude to a flux density using

$$H = -2.5 \log(f_{1.63\mu m}) - 24.860, \quad (4.1)$$

where  $1.63 \mu m$  and  $-24.860$  are the effective wavelength and magnitude zero-point of the NIR  $H$ -band as given by Bessell et al. (1998). We then scaled the spectra output by *SpexTool* to the level of the calculated flux density at  $1.63 \mu m$ .

## 4.3 SPECTRAL COMPONENTS

### 4.3.1 Continuum Emission

At early times the continuum emission has a slope that is slightly flatter than Rayleigh-Jeans. The flatness of the continuum relative to the blackbody shape indicates the combination of warm and cool components. The reason for this can be seen in the decomposition of the continuum emission by Fransson et al. (2014), who model the optical through infrared spectrum and find that a relatively cool ( $1800 - 1900$  K)

component is present from early times as well as a warmer ( $\sim 7000$  K) component. Because the blackbody peak is in the optical range, temperatures determined from optical observations should be more reliable than those determined from the infrared through day 219. At times in excess of one year, the continuum emission has a local maximum within the wavelength range of our observations. On 2011 November 17 (403 days), the continuum peak is found at about  $1.5 \mu\text{m}$ . By 2012 February 9 (488 days), it has moved to about  $1.7 \mu\text{m}$ . Figure 4.4 presents the spectrum at 488 days overlaid with five blackbodies ranging in temperature from 1500 to 1900 K, showing that the observed continuum is flatter than a blackbody. Modifying the blackbody curve to account for the emissivities of various dust grains does not produce a shape which fits the continuum emission because the efficiency of dust emission drops with increasing wavelength.

Assuming a cooler component contributes to the emission at wavelengths longer than  $1.5 \mu\text{m}$ , we identified selected areas of continuum emission and fit to a blackbody using the IDL fitting package MPFIT (Markwardt 2009; Moré 1978) for each observation later than 1 year. The temperatures of these fits are  $\sim 2000$  K and are shown in Table 4.2. In Figure 4.4, the best fits to the continuum short of  $1.9 \mu\text{m}$  lie well within 100 K of 1800 K. We therefore cite an approximate uncertainty of  $\pm 75$  K for these temperatures. This is the uncertainty in the shortest wavelength emission observed in the NIR and does not take into account the evidence for cooler emission at wavelengths longer than  $1.9 \mu\text{m}$ . By fitting the shortest wavelength emission we estimate the temperature of the warmest dust. Although the shape of the continuum on days 488 and 565 does not fit a pure blackbody, a temperature of  $\sim 1900 - 2000$  K is consistent with emission from hot dust and with the observations of Fransson et al. (2014). Such emission has previously been observed in a number of Type IIIn

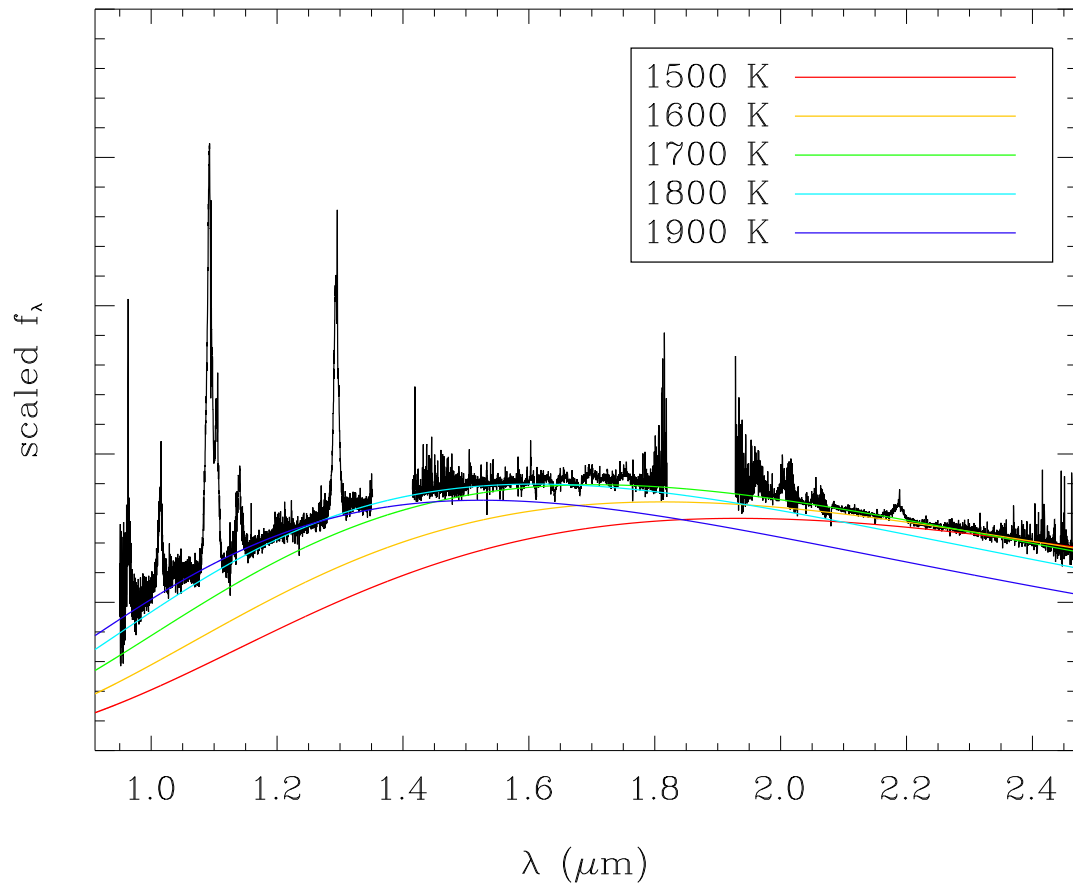


Fig. 4.4.— The spectrum at 488 days overlaid with blackbody curves. The blackbodies span the range in temperature for which the blackbody peak lies within the near-infrared.

supernovae (Fox et al. 2011).

### 4.3.2 Hydrogen Lines

As can be seen in Figures 4.1 – 4.3, many emission lines of the Paschen and Brackett series of H are detected. Each line shows 2 distinct components: a narrow component that is close to zero velocity in the host galaxy and a broad component. Although narrow lines could have their origin in the interstellar medium of the host galaxy, we attribute the emission primarily to the unshocked circumstellar medium. One reason is that the fluxes of narrow lines at later times ( $t \gtrsim 380$  day) decline to about 1/10 of the fluxes at earlier times, implying we can comfortably ignore the contribution of host galaxy emission lines at early times. Another reason is that interstellar emission lines would also be present in the Balmer series. Observations of the early  $H\alpha$  line show a narrow P Cygni feature (Smith et al. 2011b; Fransson et al. 2014), indicating that the circumstellar medium is optically thick in the H Balmer lines. The P Cygni features observed in the  $H\alpha$  line indicate an expansion velocity of  $100 \text{ km s}^{-1}$  (Fransson et al. 2014). The Paschen and Brackett series lines do not show absorption, suggesting they are optically thin. The narrow lines are plausibly formed in a region of circumstellar mass loss.

Broadened emission from hydrogen is visible in the data throughout the accessible lines of the Paschen and Brackett series. The best detected lines are Paschen  $\beta$ , Brackett  $\gamma$ , and Paschen  $\delta$ . The shape and evolution of the Paschen  $\beta$  line are shown in Figure 4.5. Paschen  $\gamma$  is also strong, but is heavily blended with the red side of the broad He I  $\lambda 10830$  line. Paschen  $\epsilon$  is sometimes observed, but it lies on the edge of an atmospheric absorption region, making the determination of its shape and strength strongly dependent on changing atmospheric conditions. Many of the



Table 4.1. Observing Details

Observation Date	Supernova Age (days)	Integration Time (minutes)	SN2010jl Airmass	HD85377 Airmass	Observers
2010 Nov 15	36	20	1.10	1.15	M. Drosback, O. Fox
2010 Dec 02	53	20	1.10	1.16	Y. Shen, O. Fox
2011 Jan 26	108	25	1.10	1.16	G. Privon, O. Fox
2011 Feb 22	135	20	1.10	1.18	Y. Shen, O. Fox
2011 Mar 23	164	20	1.32	1.47	S. Schmidt, O. Fox
2011 Apr 06	178	20	1.13	1.17	J. Borish, M. Skrutskie
2011 May 17	219	20	1.56	1.80	J. Borish, O. Fox
2011 Nov 17	403	40	1.59	1.50	J. Borish, B. Breslauer, A. Kingery
2012 Feb 09	488	40	1.14	1.24	J. Borish
2012 Apr 26	565	40	2.0	2.1	J. Borish

Table 4.2. Blackbody Fits to the Near Infrared

Observation Date	Supernova Age (days)	Blackbody Temperature (K)
2011 Nov 17	403	2090
2012 Feb 09	488	1890
2012 Apr 26	565	1910

Note. — Uncertainty in each temperature is approximately  $\pm 75$  K.

weaker Brackett series lines are identifiable in the data, and corroborate the common line shape of broad H emission.

At early times, the broad component is fairly symmetric about zero velocity. In other Type II supernovae, a Lorentzian profile gives a reasonable fit to broad Balmer lines (Leonard et al. 2000; Smith et al. 2010). Here, the broad Paschen  $\beta$  line is moderately well fit by a Lorentzian profile (see also Smith et al. 2011b, for  $H\alpha$ ). However, the broad line profile is presumably the result of the thermal particle velocities and scattering; this situation does not naturally produce a Lorentzian profile. The broad line profile is naturally produced by electron scattering (Chugai 2001; Fransson et al. 2014), without the need for Doppler effects due to bulk motion. The narrow line component is made up of photons that escape without scattering, so its strength relative to the broad component places constraints on the scattering optical depth to the line photon source. At early times, the broad component is symmetric, implying that the electron thermal velocities are much larger than systematic velocities. At late times, the broad lines are seen to become asymmetric with regard to zero velocity, although the  $H\alpha$  line remains fairly symmetric relative to the line peak (Fransson et al. 2014); the peak of the broad component shifts to the blue by  $\sim 700 \text{ km s}^{-1}$ , as also occurs in the optical lines. Figure 4.5 shows that the extended wings in the Paschen  $\beta$  line have diminished by day 400. We take this to indicate that the electron scattering optical depth is decreasing, which could occur because the shock wave overruns the scattering region or there is a change in the ionization of the gas.

In addition to finding that the emission lines shift to the blue with time, Fransson et al. (2014) found that the lines remain symmetric about a blueshifted wavelength during the shift. They used this property to argue that the line emission and scattering occur in a comoving slab of material. In Figure 4.6 we show the Paschen  $\beta$

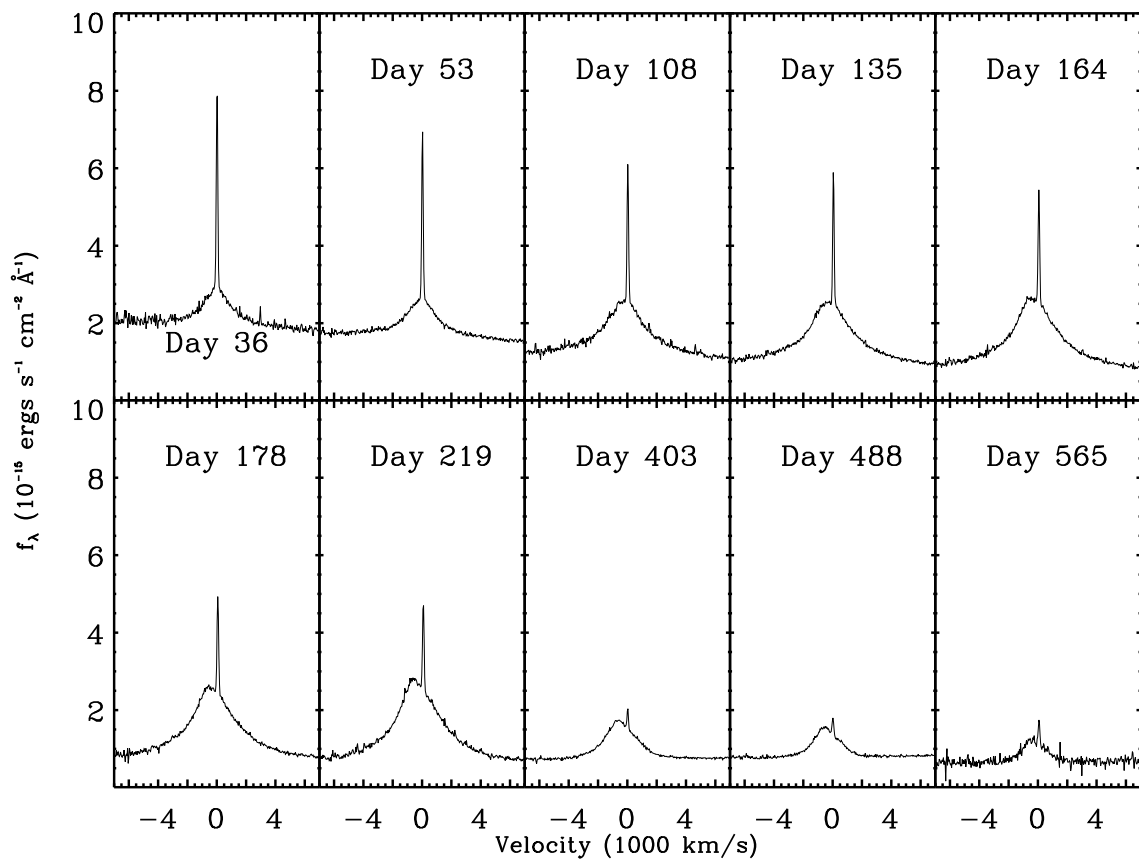


Fig. 4.5.— Time evolution of the Paschen  $\beta$  line.

line on day 219 as well as its reflection about a particular velocity, using a procedure essentially the same as that used by Fransson et al. (2014). The velocity of the shift is chosen so that the wings of the lines over  $1000 - 5000 \text{ km s}^{-1}$  match up. It can be seen that there is an asymmetry near the peak of the line. Although the asymmetry is small, it shows that the hypothesis of electron scattering in a comoving slab is not completely accurate. Fransson et al. (2014) presented NIR spectroscopy of the supernova on day 465, finding symmetry of the lines at that time. Our late time spectra also show that the degree of asymmetry becomes small.

Figure 4.7 compares the broad components of the Paschen  $\beta$ , Brackett  $\gamma$ , and Paschen  $\delta$  lines at one time, 164 days. It can be seen that the FWHM of the lines are similar. There are deviations in the line wings, but this aspect is sensitive to the continuum subtraction. We conclude that there is no strong evidence for differences between the lines. In the case of SN 1994W, Dessart et al. (2009) discussed differences between these lines caused by differences in optical depth. However, those authors were considering a case where the emission was from shocked, and thus very high density, gas. In our case, we believe the broad lines are formed in the unshocked circumstellar medium, where the densities are lower.

Figure 4.8 and Table 4.3 shows the evolution of the flux in the narrow component to that in the broad component of Paschen  $\beta$ , Paschen  $\delta$ , Brackett  $\gamma$ , and OI  $\lambda 11287$ .

Figure 4.8 and Table 4.4 show the evolution of the equivalent widths of the prominent lines. In order to measure both narrow component strength to broad component strength ratios and equivalent widths, a linear fit to the continuum in the vicinity of each emission line was found. The ratios of narrow component strength to broad component strength were measured by direct integration over each component after subtraction of the continuum fit. The quoted uncertainties were found by allowing

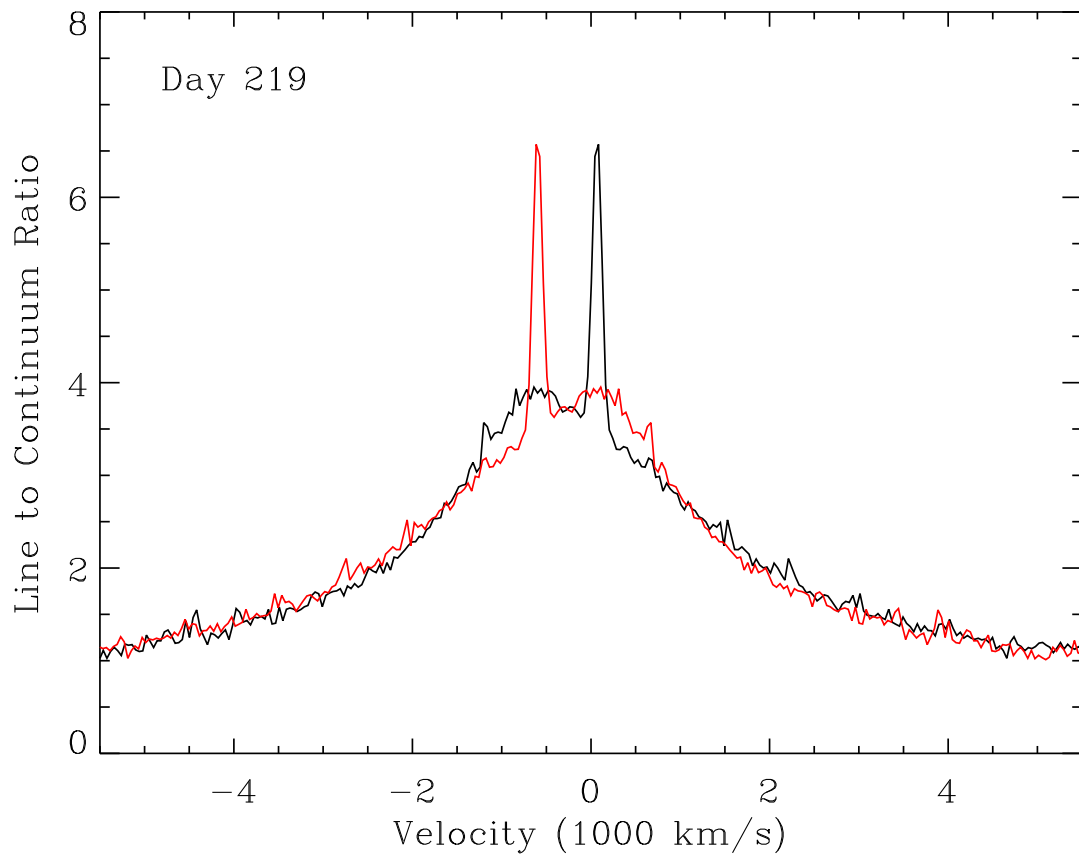


Fig. 4.6.— Mirroring the profile of Paschen  $\beta$  on day 219 about a velocity of  $265 \text{ km s}^{-1}$  reveals an asymmetry in the line core when the reflection of the wings is well matched.

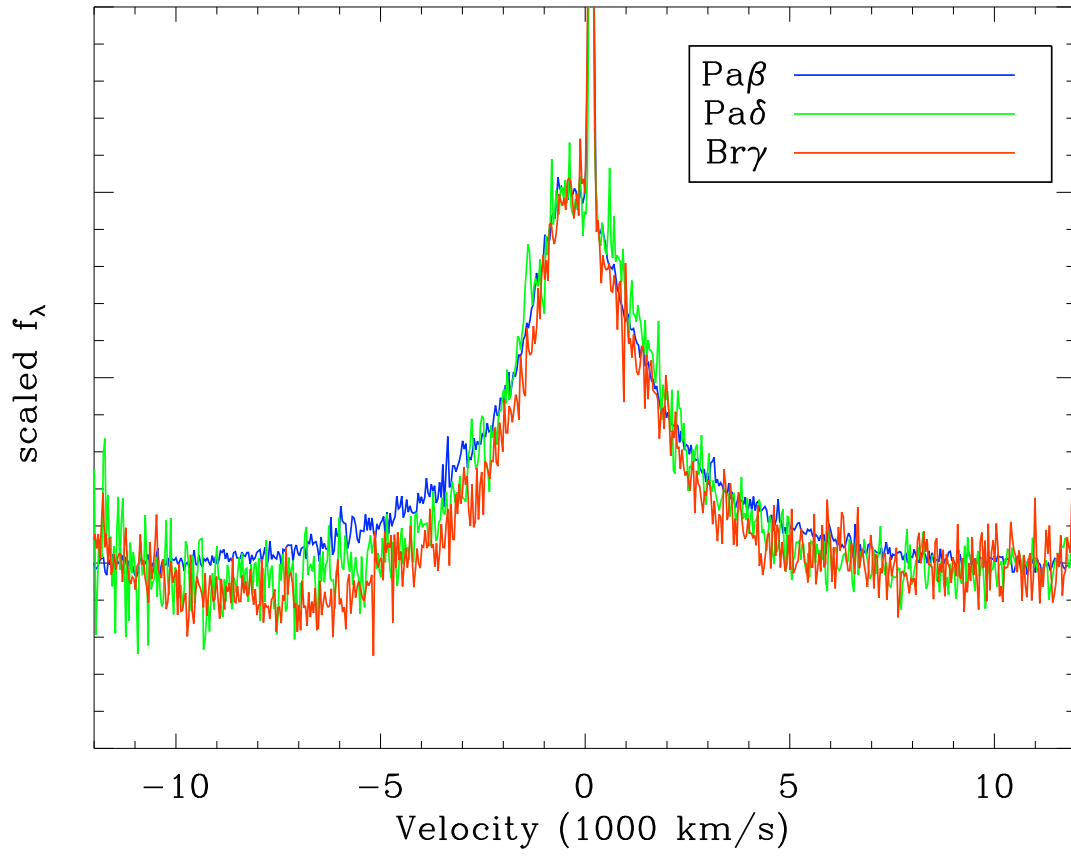


Fig. 4.7.— Comparison of the different H lines at day 164. After subtraction of a 4865 K blackbody, a linear background was fit between velocities of  $\pm 10,000 \text{ km s}^{-1}$  and  $\pm 12,000 \text{ km s}^{-1}$  and subtracted. Each line was then scaled to a height of 1.

the full width of the narrow component to vary by one pixel in each direction while also taking into account the noise in the continuum about the line. It can be seen that the ratio of narrow to broad line flux decreases with time. Equivalent widths were measured by directly integrating over the ratio of line to continuum. The quoted uncertainties were found by allowing the constant parameter in the linear continuum fit to vary by  $1\sigma$  in both directions. There is an initial approximately linear increase of the equivalent width with time, followed by a decline between days 220 and 400. Zhang et al. (2012) and Fransson et al. (2014) found a similar evolution for the  $H\alpha$  line.

### 4.3.3 He lines

Broad He emission features are detected at  $1.0830\mu\text{m}$  and  $2.0587\mu\text{m}$ . The evolution of the He lines, especially He I  $\lambda 10830$ , shows some similarities to the H lines, although there are significant differences (Figure 4.9). The broad component shows an increasing equivalent width, in the same way as the H lines (Figure 4.8).

A comparison of the He I  $\lambda 10830$  line with the Paschen  $\beta$  line on day 164 is shown in Figure 4.10. It can be seen that both lines show extended wings going out  $\sim 8000 - 9000 \text{ km s}^{-1}$ . On the red side of the He I  $\lambda 10830$  line, there is the superposition of the Paschen  $\gamma$  line, which has both broad and narrow emission components like the Paschen  $\beta$  line. Assuming the line profile of Paschen  $\gamma$  is identical to Paschen  $\beta$ , in Figure 4.10 we use Paschen  $\beta$  as a template to obtain a Paschen  $\gamma$  subtracted He profile. The shift and scale of the Paschen  $\beta$  template is chosen in order to best fit the template narrow peak to the narrow peak of Paschen  $\gamma$ . The peak of the broad component shows a shift to the blue by  $\sim 1000 \text{ km s}^{-1}$  in contrast to the  $\sim 700 \text{ km s}^{-1}$  shift in the peak of the H lines (Figure 4.10 inset). As described

Table 4.3. Narrow to Broad Line Ratio

Date	Day	Paschen $\beta$	Paschen $\delta$	Brackett $\gamma$
2010 Nov 15	36	0.20 $\pm$ 0.028	0.12 $\pm$ 0.021	0.16 $\pm$ 0.029
2010 Dec 02	53	0.15 $\pm$ 0.023	0.08 $\pm$ 0.019	0.17 $\pm$ 0.028
2011 Jan 26	108	0.07 $\pm$ 0.017	0.05 $\pm$ 0.017	0.08 $\pm$ 0.023
2011 Feb 22	135	0.05 $\pm$ 0.017	0.03 $\pm$ 0.016	0.06 $\pm$ 0.021
2011 Mar 23	164	0.05 $\pm$ 0.017	0.03 $\pm$ 0.016	0.05 $\pm$ 0.020
2011 Apr 06	178	0.04 $\pm$ 0.017	0.03 $\pm$ 0.017	0.05 $\pm$ 0.020
2011 May 17	219	0.03 $\pm$ 0.017	0.03 $\pm$ 0.016	0.04 $\pm$ 0.020
2011 Nov 17	403	0.02 $\pm$ 0.023	0.02 $\pm$ 0.026	0.03 $\pm$ 0.026
2012 Feb 09	488	0.04 $\pm$ 0.027	0.04 $\pm$ 0.033	0.06 $\pm$ 0.029
2012 Apr 26	565	0.11 $\pm$ 0.032	...	...

Table 4.4. Equivalent Widths (Angstroms)

Date	Day	Paschen $\beta$	Paschen $\delta$	Brackett $\gamma$
2010 Nov 15	36	84 $\pm$ 20	25 $\pm$ 8	50 $\pm$ 17
2010 Dec 02	53	114 $\pm$ 16	36 $\pm$ 7	59 $\pm$ 12
2011 Jan 26	108	291 $\pm$ 38	75 $\pm$ 18	119 $\pm$ 32
2011 Feb 22	135	371 $\pm$ 34	93 $\pm$ 17	160 $\pm$ 24
2011 Mar 23	164	441 $\pm$ 38	111 $\pm$ 20	207 $\pm$ 37
2011 Apr 06	178	480 $\pm$ 48	118 $\pm$ 22	219 $\pm$ 39
2011 May 17	219	573 $\pm$ 58	148 $\pm$ 26	261 $\pm$ 60
2011 Nov 17	403	156 $\pm$ 11	64 $\pm$ 20	29 $\pm$ 5
2012 Feb 09	488	93 $\pm$ 11	41 $\pm$ 15	12 $\pm$ 4
2012 Apr 26	565	71 $\pm$ 29	...	...

Note. — **Broad and narrow line fluxes are included**



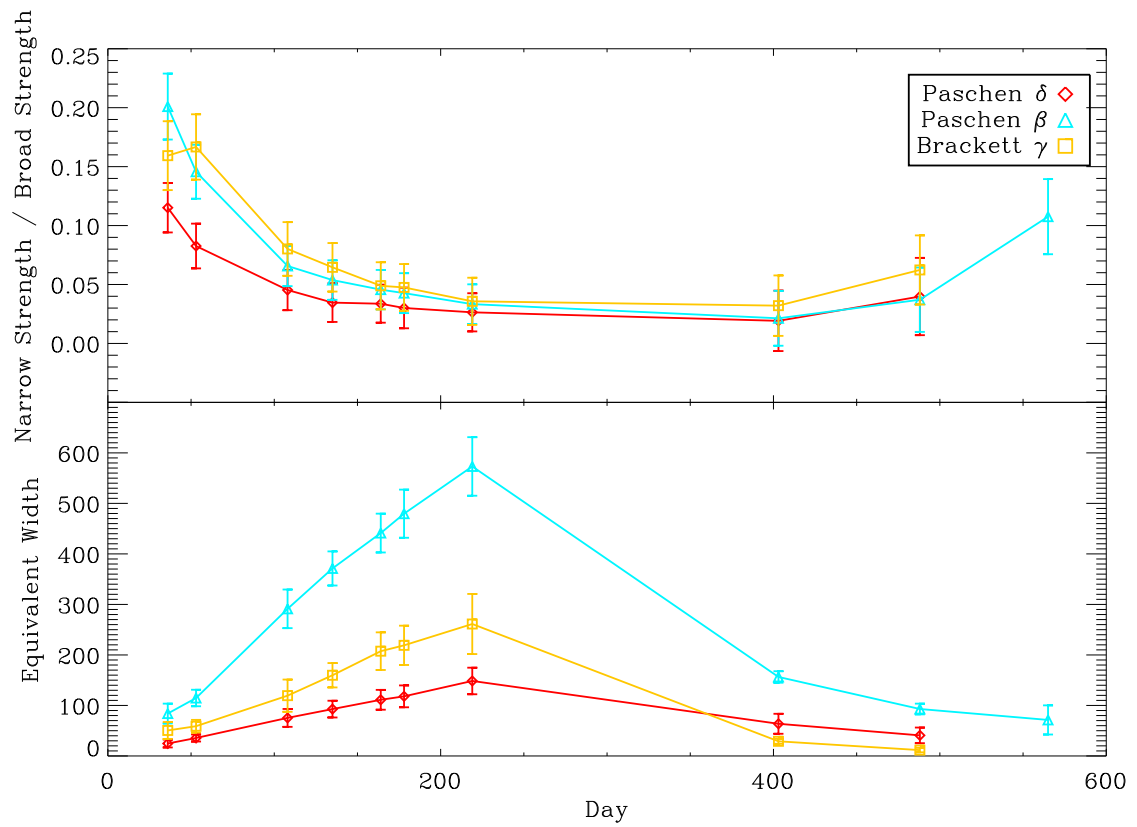


Fig. 4.8.— Evolution of the equivalent widths and narrow to broad line strengths of several prominent lines. **The equivalent widths plotted include both narrow and broad line flux.**

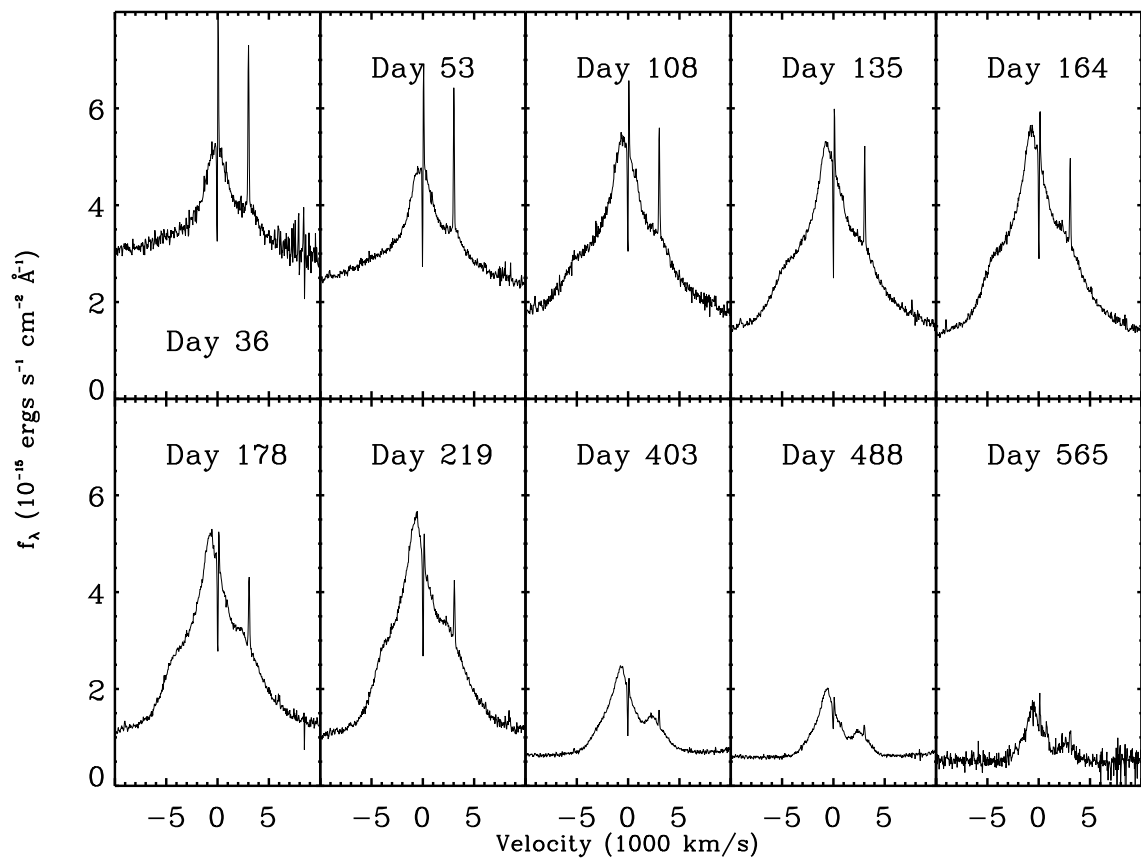


Fig. 4.9.— Time evolution of the He I  $\lambda 10830$  line. The Pa $\gamma$  line is superposed on the redshifted He I emission.

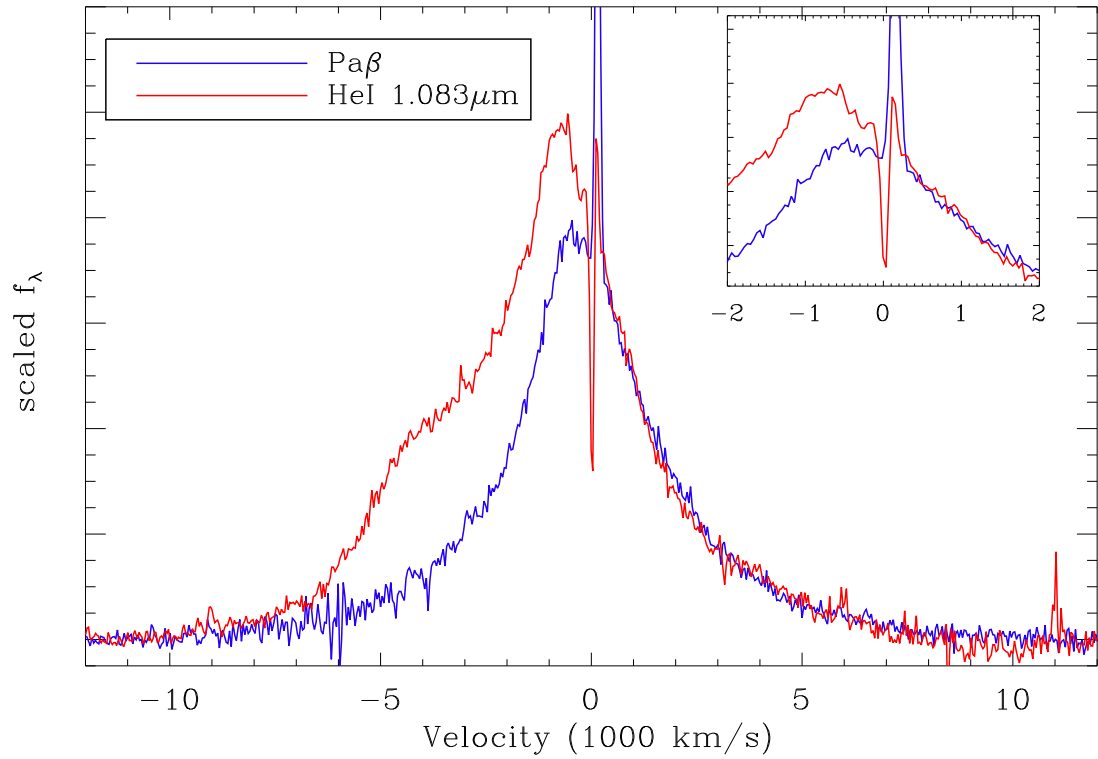


Fig. 4.10.— Comparison of the He  $\lambda 10830$  to the H Pa $\beta$  line at day 178. After subtraction of a 4865 K blackbody, the Paschen  $\beta$  profile was scaled to the strength of the Paschen  $\gamma$  and subtracted, as described in the text. The inset shows the difference in velocity between the peak of the helium profile and that of the hydrogen profile.

below, we attribute this difference to an additional component in the He line.

On the blue side on day 164, there is a shoulder feature in the He I line that is not present in the H line. In Figure 4.10, the Paschen  $\gamma$ -subtracted He I line is overplotted with the Paschen  $\beta$  line so that the line profiles match at positive velocities. We have used a similar procedure to search for excess emission on the other dates of observation. On days 36 and 53, the feature is not discernable; on days 402 and 488, there is not a well defined shoulder feature, but there is weak excess He emission that peaks at  $\sim -2500 \text{ km s}^{-1}$ . The feature grows and fades in relative strength roughly in the same way as the broad H lines. One possibility for the origin of this feature is that it is a separate line with only a broad component and no narrow component. However, a comparison of the He I  $\lambda 10830$  line to the He I  $\lambda 20587$  line (Figure 4.11) shows that the shoulder feature is present in both lines. The broad wings are likely due to electron scattering; components with different temperatures are possible, but this would not produce a shoulder structure on one side of the line profile. The implication is that the feature is due to material with systematic velocities up to  $\sim 5000 \text{ km s}^{-1}$  towards the observer. Figure 4.12 shows the excess blueshifted emission in the He I  $\lambda 10830$  line relative to the Paschen  $\beta$  line; the emission extends to at least  $-6000 \text{ km s}^{-1}$ . In addition, the shoulder feature of excess emission moves to the red with time (Figure 4.13), which is the opposite of the evolution of the H broad features. The deceleration of the break in the shoulder feature follows a velocity evolution  $t^{-0.39 \pm 0.08}$  (Figure 4.14). The error bars in the shoulder-break velocities shown in figure 4.14 are estimated by measuring the overlap of the  $1\sigma$  uncertainty regions for each linear fit component shown in figure 4.12.

In addition to the broad line feature, there is a narrow P Cygni feature in the He I  $\lambda 10830$  line. Figure 4.15 shows that initially (day 36) the emission component domi-

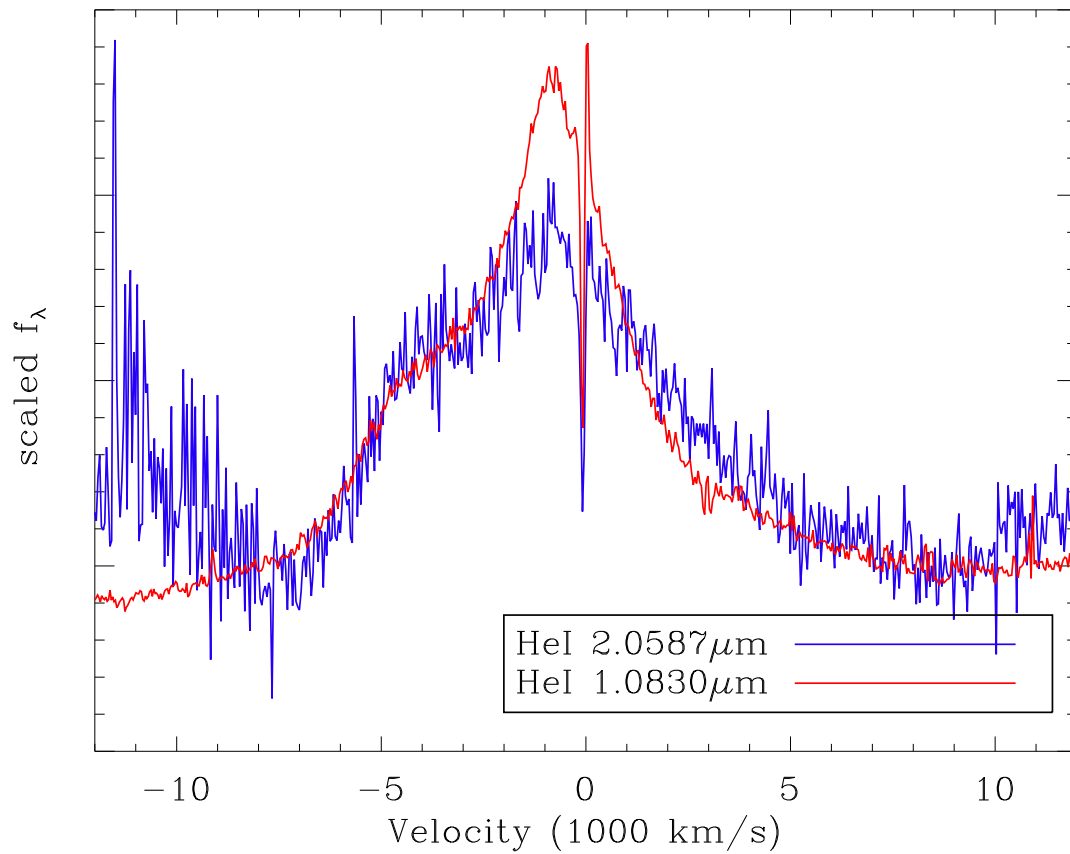


Fig. 4.11.— Comparison of the He I  $\lambda 10830$  line to the  $\lambda 20587$  line at day 164. After subtraction of a 4865 K blackbody, a linear background was fitted between velocities of  $\pm 7,000 \text{ km s}^{-1}$  and  $\pm 9,000 \text{ km s}^{-1}$  and subtracted. Each line was then scaled to a height of 1.

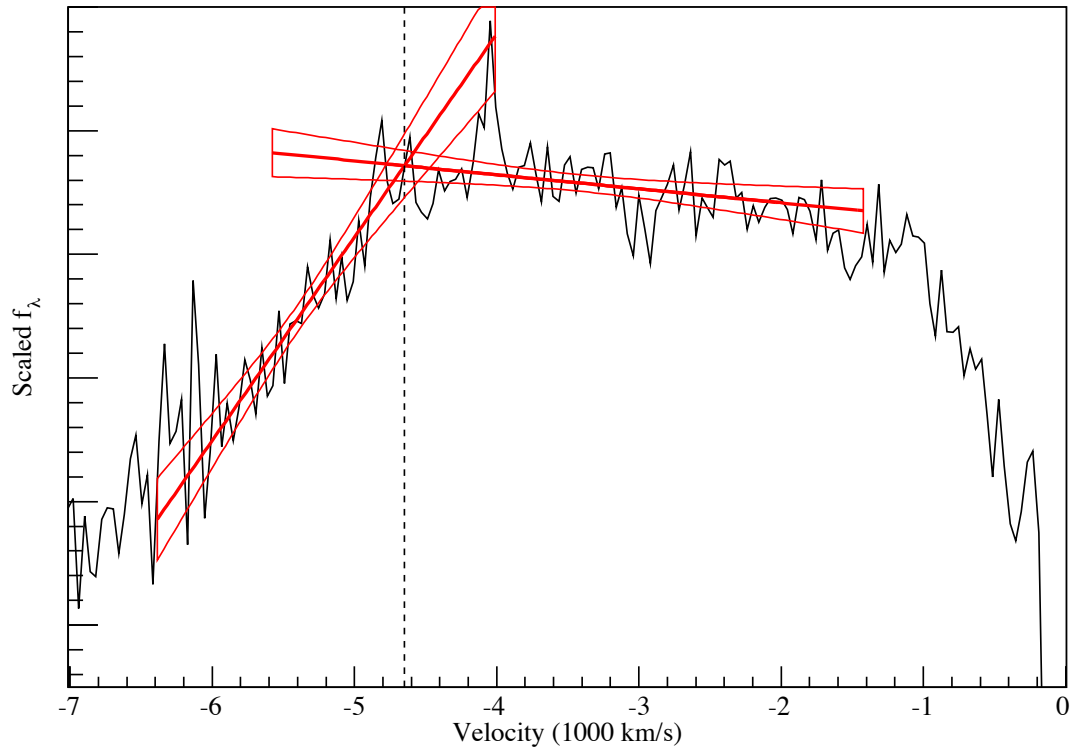


Fig. 4.12.— The residual of a subtraction of Paschen  $\beta$  from He  $\lambda 10830$  (Figure 4.10), showing the distribution of blueshifted excess He emission on day 178. We find the velocity of the inflection point in the emission (at  $\sim -5000 \text{ km s}^{-1}$ ) by fitting lines to each region adjacent to the inflection point. Also overplotted are regions of 95% confidence about the linear fits. The quoted uncertainty in the inflection point is given by the width of the overlap of the uncertainty regions of each fit.

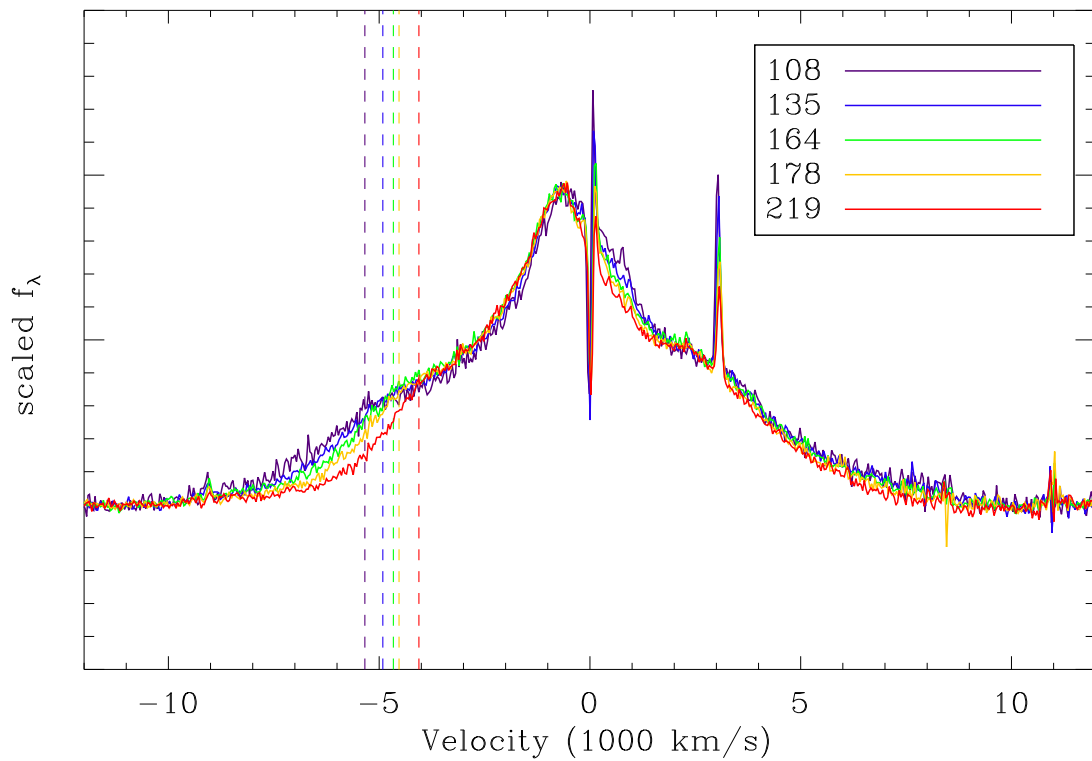


Fig. 4.13.— Plot of broad He I  $\lambda 10830$  emission from day 108–219 showing evolution of the broad shoulder. Dashed lines show the velocity of the break in the shoulder at each time.

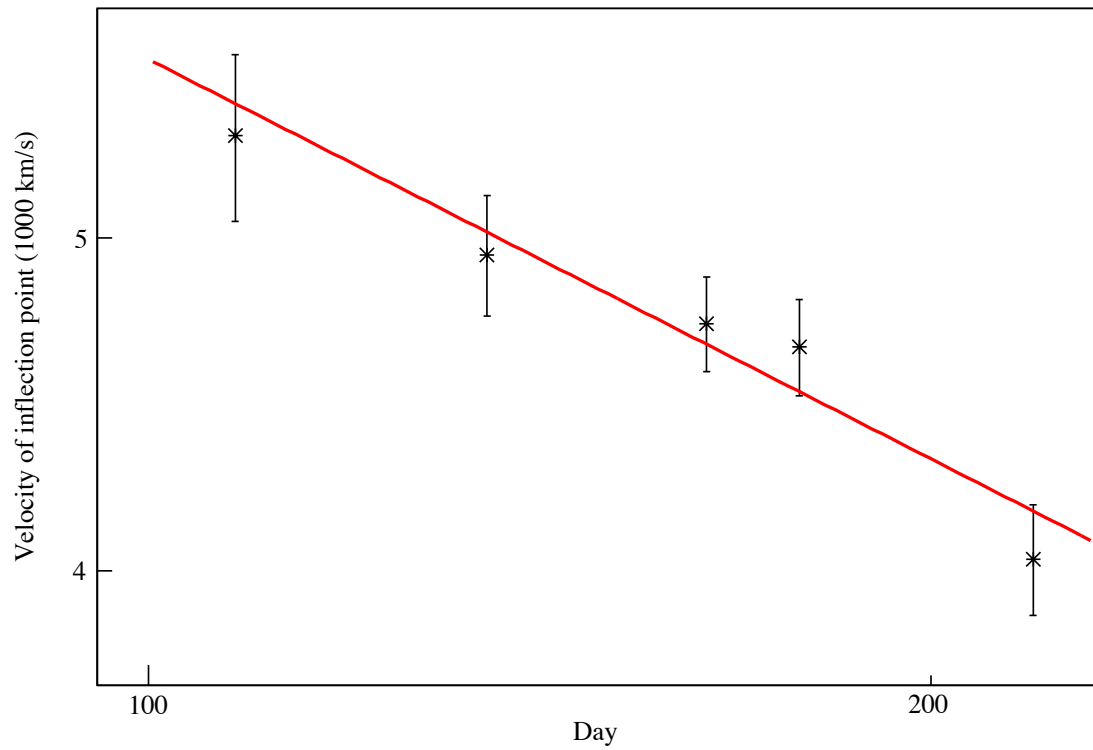


Fig. 4.14.— Evolution of the velocity of the inflection point in the broad He I  $\lambda 10830$  emission profile over days 108 – 219. This is a log – log plot and the line shows an evolution of velocity  $\propto t^{-0.39}$ . Error bars have been calculated based on the uncertainty shown in figure 4.12.



nates over the narrow absorption. By day 53, the 2 components are at nearly equal strength and at later times, the absorption component dominates. Since the resolution of the observations is about  $100 \text{ km s}^{-1}$ , we place an upper limit of  $100 \text{ km s}^{-1}$  on the wind velocity of the CSM. The width of the absorption line does not change with the time of our observations. The same is true for the  $\text{H}\alpha$  line (Fransson et al. 2014). This is indicative of the formation of the circumstellar medium in an approximately steady flow. If the material were launched in an eruptive event, the CSM velocity would increase roughly linearly with radius, and over time the observed emission-line widths should increase. This is not observed, at least within the spectral resolution. The narrow component in the He I  $\lambda 20587$  line is not as well defined as in the  $\lambda 10830$  line; it appears only in absorption.

#### 4.3.4 Other Lines

The O I line at  $1.129 \text{ }\mu\text{m}$  is in a noisy part of the spectrum where there is confusion with night sky features. In addition, it overlaps the red wing of the He I  $\lambda 10830$  line, but it is clearly present (Figure 4.16). The line shows a broad emission component with properties and an evolution that are comparable to those of the H lines. A narrow line may be detected but is uncertain because of the contamination by night sky lines. The observed emission is compatible with the view that the O I line is the result of pumping by the  $\text{Ly}\beta$  line (Fransson et al. 2014).

In addition, there is a line present at  $\sim 1.2 \text{ }\mu\text{m}$  (Figure 4.16). It has a broad, but no narrow, component. We tentatively identify it as Si I  $1.1991 - 1.2270 \text{ }\mu\text{m}$ . We also considered Mg I  $\lambda 11828$ , but it gave a poor fit to the line profile, under the assumption that the line profile is comparable to that of He I  $\lambda 10830$ . The line profile, when taken to be the Si I line, shows that there is emission associated with the blue

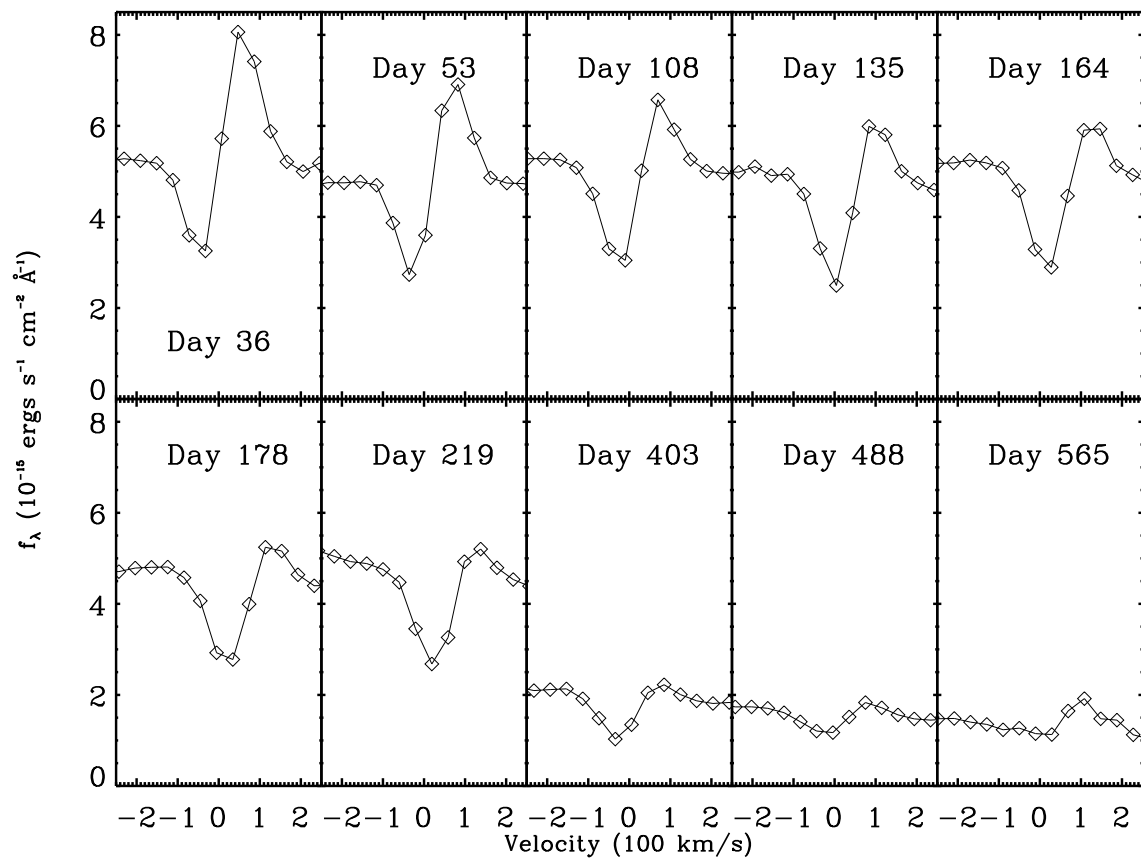


Fig. 4.15.— Time evolution of the narrow P-Cygni feature in the He I  $\lambda 10830$  line.

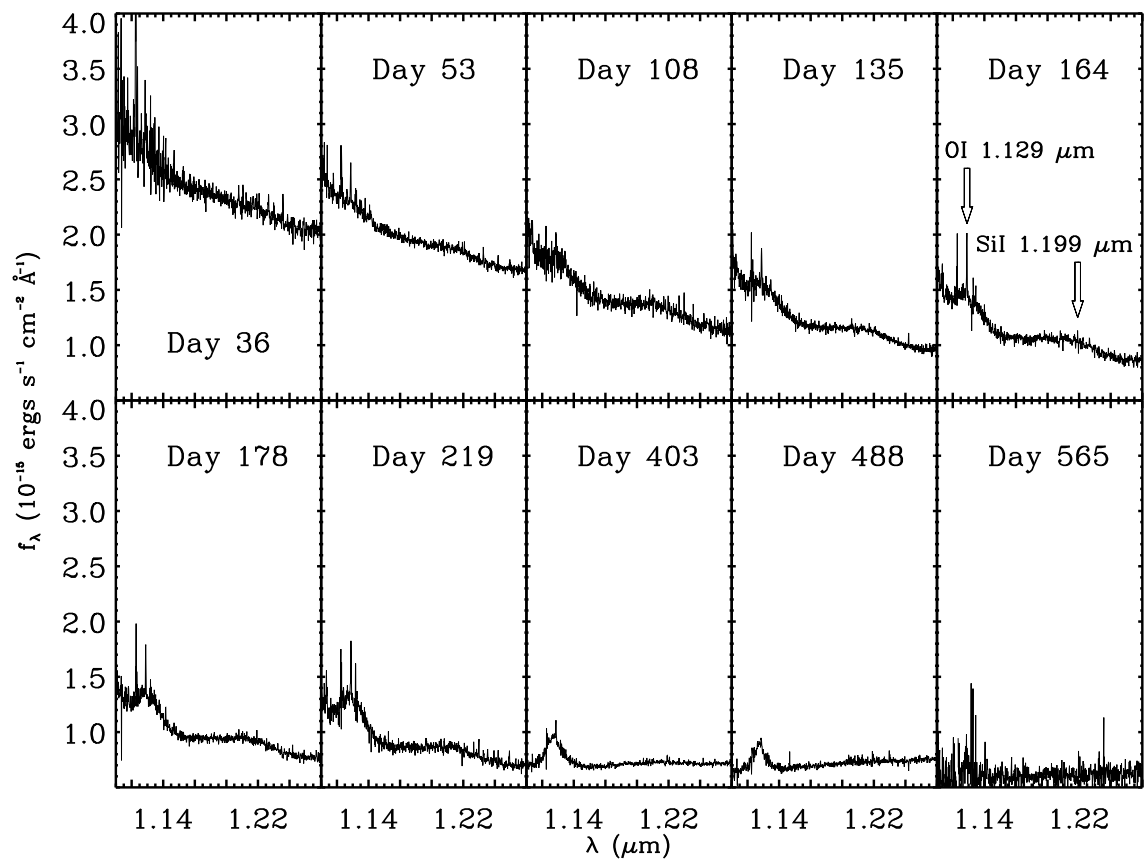


Fig. 4.16.— Time evolution of the O I  $\lambda 11287$  and Si I  $\lambda 11991$  features.

shoulder emission observed in the He lines (Figure 4.17).

## 4.4 PHYSICAL PICTURE

Our interpretation of the NIR spectra builds on previous discussions of Type IIIn supernovae (Chugai & Danziger 1994; Leonard et al. 2000; Fransson et al. 2002; Hoffman et al. 2008; Fransson et al. 2014). One component is the pre-supernova mass loss region with which the supernova is interacting. The mass loss has an outward velocity of  $100 \text{ km s}^{-1}$  and is fairly steady over the region of observation. The region is photoionized by X-ray radiation coming from the shock interactions.

In our first epoch of NIR spectra, the H line profiles show a narrow component due to the slow wind and a broad symmetric component that we attribute to electron scattering in the slow wind. The line width reflects a combination of the electron scattering optical depth,  $\tau_e$ , and the gas temperature (Chugai 2001; Huang 2016). We initially assume that the emitting gas is the same as the scattering gas, and both are associated with the slow wind which has a density profile  $n \propto r^{-2}$  over an extended region. The scattering process was modeled by a Monte Carlo code to follow the scattering and wavelength shifts of line photons. As in Fransson et al. (2014), the broad line component is well-reproduced by the electron scattering line profile (Figure 4.18).

The model assumed spherical symmetry, with an absorbing sphere for an inner boundary  $R_i$ . As shown in Huang (2016), the FWHM of the scattered line, which has an approximately exponential shape, depends on the optical depth to  $R_i$ ,  $\tau_e$ , and the temperature  $T$ . Provided that the ratio of outer radius to  $R_i$  is  $> 10$ , the results are not sensitive to the exact value of the ratio. The line width in velocity space is proportional to the thermal velocity and is thus  $\propto T^{1/2}$ . For the Paschen  $\beta$  line on

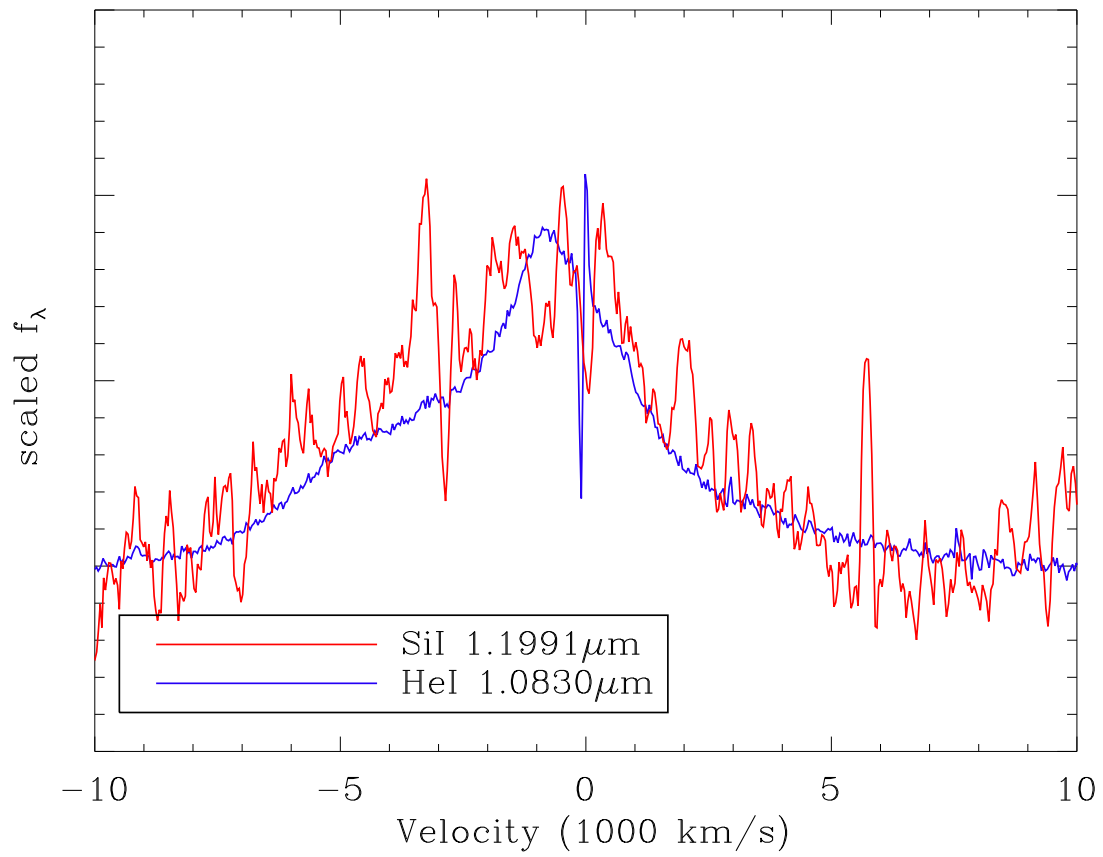


Fig. 4.17.— Si I  $\lambda 11991$  overlaid with He I  $\lambda 10830$  on day 135.

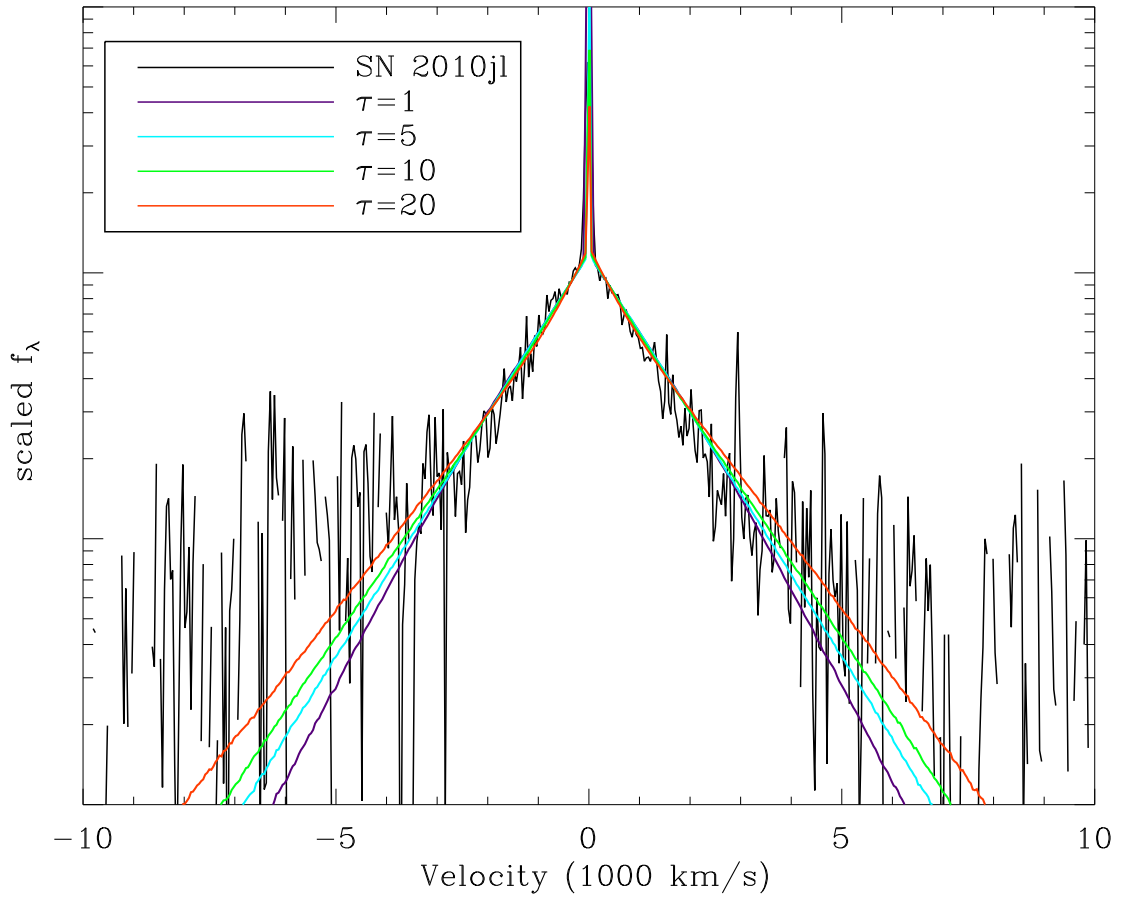


Fig. 4.18.— Electron scattering profiles overlaid on the broad component of the Paschen  $\beta$  line at an age of 36 days. In order to compare the line profile shapes, the model profiles have been scaled to approximately the same FWHM as the Paschen  $\beta$  line.

day 36 we find the observed FWHM to be  $\sim 2030 \text{ km s}^{-1}$ , which is consistent with the following pairs of values of  $(\tau_e, T)$ : (1, 58600 K), (5, 16400 K), (10, 7760 K), and (20, 3700 K).

After interpolating over the narrow component of the day 36 Paschen  $\beta$  line, we perform least squares fits of the electron scattering models to the broad component. We find the reduced  $\chi^2$  to lie in the range 1.39 – 1.55 for  $\tau_e$  ranging between 20 and 1 (Figures 4.18). The data is best fit to the  $\tau_e = 20$  profile, with a reduced  $\chi^2$  of 1.39. Such a high optical depth should be viewed with skepticism, especially in view of the small range of  $\chi^2$  when  $\tau_e$  varies between 1 and 20.

If the emitting and scattering gas are the same, another constraint on the emission comes from the ratio of the narrow line flux to the flux in the broad wings, which is found to be 0.17 on day 36 for the Paschen  $\beta$  line. Using the model results from Huang (2016), we find that the ratio observed for SN 2010jl corresponds to  $\tau_e \sim 4$ , which suggests a lower limit of the scattering gas optical depth by assuming there is no other source of narrow line emission. The observed temperature is then  $\sim 20,000$  K, which is reasonable for the ionized gas. Another measure of  $\tau_e$  is provided by the outer wings of the line. By adjusting the temperature, we can generate line profiles with the same FWHM at different  $\tau_e$ , the line wings become slightly stronger for higher values of  $\tau_e$ . However, our data for SN 2010jl do not have sufficient signal-to-noise in the wings to be able to use this method (Figure 4.18), as is indicated by the small range of reduced  $\chi^2$  over the range of  $\tau_e$  from 1 to 20.

Although a consistent picture for mixed emission and scattering can be developed for the earliest time, it has problems at later times, indicating that application of the model to the narrow line at early times may be misleading. Over 100's of days, the broad component in the lines shifts to the blue, as also observed in optical lines

(Fransson et al. 2014). One suggestion is that the shift is due to dust formation in the expanding medium (Smith et al. 2012; Maeda et al. 2013; Gall et al. 2014). In that picture, the redshifted photons emitted by material expanding away from the observer on the far side of the supernova are preferentially absorbed as they travel through a longer column of dust than their blueshifted near side counterparts. This would lead to a line profile that is less strong on the red side, an effect that would be more pronounced in the shorter wavelength lines as dust absorption within the ultraviolet/optical/near-infrared bands is more effective at shorter wavelengths. Smith et al. (2012) made this argument based on spectra at an age  $\sim 100$  days and Maeda et al. (2013) based on a spectrum at age 563 days. At the earlier times, our spectra show a shift in the Brackett  $\gamma$  line that is similar to that at shorter wavelengths (Figure 4.7), although there is some uncertainty in the continuum level. However, our observations cover a relatively small, long wavelength range and do not provide a good test of wavelength dependent line profiles.

Fransson et al. (2014) discussed a number of problems with the shift in the broad component being due to dust, and proposed a model in which there is radiative acceleration of the gas that gives rise to the broad component. Since the narrow component does not shift to the blue along with the broad component, the two components must originate in different places. The equivalent width in the narrow component of the H lines remains roughly constant over the first 200 days, so the ionized circumstellar medium appears to evolve slowly and the growth in the equivalent width of the H lines is primarily due to the growth of the broad component. Over the first 200 days, the NIR luminosity of SN 2010jl dropped by a factor of 3 (Fransson et al. 2014), so the narrow lines dropped by this factor and the flux in the broad components approximately doubled from our earliest observation to an age of 200 days. Formation



of the narrow and broad lines in the same place would imply that the optical depth increases with time because fewer photons escape without scattering at higher optical depth. This is unexpected, giving further evidence that the line components form in separate regions. The properties of the H emitting regions are distinct from those of the X-ray emitting region, where the shock front has a velocity  $\sim 4000 \text{ km s}^{-1}$  and a preshock  $\tau_e \sim 1$  on day 58 if there is incomplete ionization of the gas (Chandra et al. 2012; Ofek et al. 2014). The preshock column density subsequently declines. As discussed by Fransson et al. (2014), the fact that the broad component shows a systematic shift indicates that there is a large scale asymmetry in the object and that the optical emission is perhaps from a polar flow.

As discussed in Section 2.3, the NIR He lines show a difference with the H lines. In addition to the growth of a broad component shifted by  $-1000 \text{ km s}^{-1}$ , the He lines develop a shoulder out to  $-4000$  to  $-5500 \text{ km s}^{-1}$ . The velocity indicates that this component may be associated with the higher velocities inferred from the X-ray emission. The fact that this feature does not appear in the H lines indicates a difference in composition; the high velocity He feature may be associated with supernova ejecta in which H is underabundant.

A surprisingly similar situation has been observed in the Type IIn SN 1997eg (Hoffman et al. 2008). SN 1997eg had a maximum absolute  $V$  magnitude  $\sim 1.5$  magnitudes fainter than SN 2010jl, so a lower density interaction is indicated. Hoffman et al. (2008) find that the H lines do not have Lorentzian profiles, implying that electron scattering related to the thermal velocities of electrons is not important and consistent with a low density. In addition, SN 1997eg was detected as a radio source at an age of 7 months (Lacey et al. 1998). No detections of SN 2010jl have yet been reported, suggesting higher absorption in this case. Despite the apparent difference

in circumstellar density, there are interesting similarities in the H and He lines. In SN 1997eg, the H Balmer lines showed a shift in the peak of the line to the blue by  $\sim 700 - 800 \text{ km s}^{-1}$ . At the same time, the He I  $\lambda 7065$  and  $\lambda 5876$  lines showed a strong shoulder of emission to the blue by  $\sim 5000 \text{ km s}^{-1}$ . At later times, a peak like the one extending to the blue developed to the red in the H lines. Hoffman et al. (2008) interpret the line emission as coming from an asymmetric region with different geometries for the H and He dominated emission regions. The H lines are attributed to shocks driven into a dense circumstellar disk or torus, while the He emission is from H depleted gas that is expanding more rapidly into a lower density circumstellar medium. This view is supported by polarization observations of the supernova.

Our observations of H and He lines in SN 2010jl show similar shifts. The H lines show only a blueshifted component, without the redshifted side. We attribute the difference to the higher density and optical depths in the SN 2010jl case. There is also evidence for blueshifted He rich gas moving at  $5000 \text{ km s}^{-1}$ . However, the He emission is also strong in the lower velocity component, as opposed to the case of SN 1997eg.

Our spectral line observations indicate 3 kinds of emitting regions: a narrow line region of presupernova mass loss with velocities  $\sim 100 \text{ km s}^{-1}$ , an intermediate line region involving  $\sim 700 \text{ km s}^{-1}$  gas in an asymmetric structure, and a He dominant region of supernova ejecta with velocities  $\sim 5000 \text{ km s}^{-1}$ . The lines are affected by electron scattering in the early phases of evolution and electron scattering may be responsible for the extended line wings through day  $\sim 400$ . After day 400, the lines no longer show the characteristic electron scattering profiles and the line widths probably reflect gas velocities to  $\sim 2000 \text{ km s}^{-1}$ . However, the bulk of H rich material is moving at  $\sim 700 \text{ km s}^{-1}$ . The broad feature observed in the He lines could be produced by

a uniformly expanding shell of gas with velocity  $\sim 5000 \text{ km s}^{-1}$ ; the absence of the redshifted part of the shell may be due to the supernova being opaque. Similar regions have been observed in other Type IIn supernovae, although the high velocity ejecta region is sometimes observed to be O rich, e.g., SN 1986J (Milisavljevic et al. 2008) and SN 1995N (Fransson et al. 2002).

## 4.5 DISCUSSION AND CONCLUSIONS

Our study shows that NIR spectral observations of Type IIn supernovae can provide an interesting window on these events. For the H lines in SN 2010jl at early times, the NIR lines (Brackett and Paschen series) have broad components with profiles that are similar to the broad components of the optical Balmer lines (Zhang et al. 2012; Fransson et al. 2014). The line profiles are consistent with the lines being formed by electron scattering in the circumstellar medium. The narrow line components in the Balmer lines show absorption features, i.e. they are optically thick, while the Paschen and Brackett lines are not. The NIR narrow emission thus gives a measure of the flux of unscattered line photons emitted by the slow circumstellar medium.

In SN 2010jl, the optical He I lines are relatively weak so there is not much information on their profiles. However, the NIR  $\lambda 10830$  line is strong and the profile is well defined in our observations. We find a clear difference with the H lines in that there is a shoulder to the blue that implies gas approaching at  $4000 - 5500 \text{ km s}^{-1}$ . The emission can be interpreted as H poor supernova ejecta that are expanding into a region of relatively small circumstellar density. A similar situation is observed in SN 1997eg (Hoffman et al. 2008).

The NIR continuum can provide important information on the emission from warm dust, which appears to be frequently present around Type IIn supernovae (Fox

et al. 2011). However, at early times the hotter photospheric emission is present and optical observations are needed to separate out the photospheric emission from the dust emission (Fransson et al. 2014). At later times, when the photospheric emission has faded, the NIR observations can provide crucial information on dust emission.

# Chapter 5

## Summary

### 5.1 A Near-IR Spectroscopic Survey of the Embedded Nuclear Regions of Luminous Infrared Galaxies

The bulk of my dissertation research has focused on using near-infrared spectroscopy ( $1\mu\text{m} - 2.5\mu\text{m}$ ) to study the ionization mechanisms in a sample of 42 low-redshift LIRGS in the GOALS sample (Armus et al. 2009). LIRGs are important laboratories for the study of star formation and AGN processes in extreme environments. However, the active regions within LIRGs are dust-enshrouded, thus observations at wavelengths longward of optical are necessary to probe the physical phenomena energizing these galaxies. Our spectroscopy work allowed for a detailed study of the global properties of LIRG power sources by using a single aperture to capture the entire LIRG spectrum from 1 to  $2.5\mu\text{m}$ . These spectra show strong emission from hydrogen recombination lines, [Fe II] and warm  $\text{H}_2$ . The total absence of [Si VI] ( $1.962\mu\text{m}$ ) and broad recombination line emission in LIRGs not already known to host AGN

indicate that AGN are either absent or too deeply embedded to be observed at near-IR wavelengths. In comparing the measured near-IR line ratios with models of shocks and photoionization, I find that models of shock excitation provide better agreement with the observed near-IR line ratios than photoionization models. However, I find that the photoionization models do not overlap significantly with normal star-forming galaxies, likely an indication that the iron abundances in the photoionization models are too low. Indeed, empirical comparisons of the  $[\text{Fe II}]/\text{Pa}\beta$  vs.  $\text{H}_2/\text{B}\gamma$  ratios of the LIRG sample with normal star-forming galaxies show a significant overlap between the two samples. I find that the optical diagnostic classification (Veilleux & Osterbrock 1987) correlates with the value of the  $[\text{Fe II}]/\text{Pa}\beta$  ratio. This suggests that the optically revealed prevalence of shocks is mirrored in the near-IR by this ratio. I have additionally tabulated kinematic information via decompositions of observed line profiles into Gaussian components. Five of the 42 LIRGs surveyed show evidence of outflows in  $\text{Pa}\beta$  with velocities  $> 100 \text{ km s}^{-1}$ . The range in outflow velocities are significantly less than what is seen OH 119 micron - this difference may be a result of the ability of the far-infrared line to probe regions closer to the obscured starburst and/or AGN where the acceleration may be the strongest.

## 5.2 A Time Domain Study of the Type IIn SN 2010jl's NIR Spectrum

In addition to our work on extreme starburst galaxies, I led a near-IR spectroscopic investigation of the extragalactic type IIn supernova SN 2010jl in the galaxy UGC 5189A. This dataset is unique in that it follows the evolution of the supernova near-infrared spectrum with relatively high spectral resolution and very high time resolu-

tion. Over a period of 219 days, the supernova was observed once every 30 days on average. After this period, the rate of spectral evolution slowed dramatically, and I observed the Supernova roughly once every 4 months for 346 additional days. The He I  $\lambda 10830$  profile shows excess blue emission in the form of a shoulder with a velocity of  $v \approx -5000 \text{ km s}^{-1}$ . This feature is absent in the Hydrogen profile, suggesting that it originates in an He-rich ejecta flow. This high velocity component is consistent with a with a high velocity flow indicated by X-ray observations of this supernova. The broad H profiles are consistent with electron scattering in the circumstellar medium of the supernova, while the optically thin narrow H lines provide a constraint on the ratio between scattered and unscattered photons. We also show that a significant fraction of the continuum emission is due to a blackbody with temperature of  $T \approx 1900 \text{ K}$ , consistent with emission from warm dust observed in similar objects.

### **5.3 Future Research – Resolved Spectroscopy of Star Formation and Feedback in the Hearts of Galaxies**

Our slit spectroscopy campaign allowed for a detailed study of the global properties of LIRG power sources by using a single aperture to capture the entire LIRG spectrum from 1 to  $2.5 \mu\text{m}$ . However, the spatial resolution of TripleSpec only allows for the global emission line measurements of LIRGs to be captured. Indeed, much of the detailed processes and kinematics occurring on smaller scales are not accessible with TripleSpec. The next step in pursuing additional near-IR observations of star forming galaxies is to focus on datasets which spatially resolve the detailed physics occurring within their most active regions. The best option to create such a dataset is the use

of AO capabilities in conjunction with a near-infrared IFU (e.g. OSIRIS on Keck). With IFU data, I will be able to address the following goals:

**(1) I will construct diagnostic plots of the resolved nuclear regions within each galaxy to spatially map the dominant excitation processes.** By resolving the active regions at such fine spatial resolutions, I will determine how the embedded energy sources contribute to shock excitation and photoionization as a function of position within, or in proximity to, the nuclear regions.

**(2) I will make use of the line kinematics to measure rotation, and to identify outflows.** I will construct maps of both velocity dispersion (line width) and systemic velocity offset for each line observed. This information will be used to search for outflows, derive outflow rates, and to calculate the masses of supermassive black holes orbited by gas disks (e.g. U et al. 2013; Medling et al. 2015). These measurements are crucial for investigating the effects of nuclear feedback (from *either* star formation or AGN activity) on the surrounding host galaxy’s environment. I will correlate the kinematic measurements with the results from (1) to better understand the physics driving the kinematics.

**(3) I will characterize the uniformity of the obscuring dust** by measuring the amount of extinction implied by the ratio of Brackett  $\gamma$  to Brackett  $\delta$  across the active nuclear regions.

**(4) I will make use of the CO absorption bands to estimate the range of ages in each nuclear starburst.** In addition to information about the ISM, the near-infrared spectra of star-forming nuclei often contain prominent absorption from the stellar population. Of particular use are the CO absorption bands at wavelengths longer than  $2.3\mu\text{m}$ . They have been used in conjunction with both narrow-band imaging and spectroscopy (e.g., Doyon et al. 1994; Falc3n-Barroso et al. 2014) to



constrain starburst ages in LIRGs.

Such an IFU study will be well matched to the resolution of ALMA, allowing for a comparison between spatial extent of star-forming gas tracers (ALMA) and both recent, massive star formation (as traced via hydrogen recombination lines) and hot molecular gas (near-infrared IFU). In the future, JWST NIRSPEC (with IFU capability from  $1 - 5 \mu\text{m}$ ) will provide the tools to study high-redshift star-forming galaxies near the peak of the cosmic star formation history in the manner proposed here.

# References

- Abt, H. 2009, ApJS, 180, 117
- Allen, M. G., Groves, B. A., Dopita, M. A., Sutherland, R. S., & Kewley, L. J. 2008, ApJS, 178, 20
- Alonso-Herrero, A., Pereira-Santaella, M., Rieke, G. H., & Rigopoulou, D. 2012, ApJ, 744, 2
- Andrews, J. E., Clayton, G. C., Wesson, R., et al. 2011, AJ, 142, 45
- Armus, L., Charmandaris, V., Bernard-Salas, J., et al. 2007, ApJ, 656, 148
- Armus, L., Mazzarella, J. M., Evans, A. S., et al. 2009, PASP, 121, 559
- Baldwin, J. A., Phillips, M. M., & Terlevich, R. 1981, PASP, 93, 5
- Bernard-Salas, J., Spoon, H. W. W., Charmandaris, V., et al. 2009, ApJS, 184, 230
- Bessell, M. S., Castelli, F., & Plez, B. 1998, A&A, 333, 231
- Borish, H. J., Huang, C., Chevalier, R. A., et al. 2015, ApJ, 801, 7
- Chandra, P., Chevalier, R. A., Irwin, C. M., et al. 2012, ApJ, 750, 2
- Chevalier, R. A. 2012, ApJ, 752, 2

- Chevalier, R. A., & Clegg, A. W. 1985, *Nature*, 317, 44
- Chugai, N. N. 2001, MNRAS, 326, 1448
- Chugai, N. N., & Danziger, I. J. 1994, MNRAS, 268, 173
- Cushing, M. C., Vacca, W. D., & Rayner, J. T. 2004, PASP, 116, 362
- Dannerbauer, H., Rigopoulou, D., Lutz, D., et al. 2005, A&A, 441, 999
- Dessart, L., Hillier, D. J., Gezari, S., Basa, S., & Matheson, T. 2009, MNRAS, 394, 21
- Dors, O. L., Riffel, R. A., Cardaci, M. V., et al. 2012, MNRAS, 422, 252
- Downes, D., & Solomon, P. 1998, ApJ, 507, 615
- Edge, A. C., Wilman, R. J., Johnstone, R. M., et al. 2002, MNRAS, 337, 49
- Evans, A. S. 2008, in Astronomical Society of the Pacific Conference Series, Vol. 395, *Frontiers of Astrophysics: A Celebration of NRAO's 50th Anniversary*, ed. A. H. Bridle, J. J. Condon, & G. C. Hunt, 113
- Fischer, J., Sturm, E., González-Alfonso, E., et al. 2010, A&A, 518, L41
- Forbes, D. A., & Ward, M. J. 1993, ApJ, 416, 150
- Förster Schreiber, N. M., Genzel, R., Lutz, D., & Sternberg, A. 2003, ApJ, 599, 193
- Fox, O. D., Filippenko, A. V., Skrutskie, M. F., et al. 2013, AJ, 146, 2
- Fox, O. D., Chevalier, R. A., Skrutskie, M. F., et al. 2011, ApJ, 741, 7
- Fransson, C., Chevalier, R. A., Filippenko, A. V., et al. 2002, ApJ, 572, 350

- Fransson, C., Ergon, M., Challis, P. J., et al. 2014, *ApJ*, 797, 118
- Gal-Yam, A., & Leonard, D. C. 2009, *Nature*, 458, 865
- Gall, C., Hjorth, J., Watson, D., et al. 2014, *Nature*, 511, 326
- Goldader, J., Joseph, R. J., Doyon, R., & Sanders, D. B. 1995, *ApJ*, 444, 97
- Goldader, J. D., Joseph, R. D., Doyon, R., & Sanders, D. B. 1997a, *ApJ*, 474, 104
- Groh, J. H., Meynet, G., & Ekström, S. 2013, *A&A*, 550, L7
- Herrero-Ilana, R. 2014, D.P.M. Thesis
- Herter, T. L., Henderson, C. P., Wilson, J. C., et al. 2008, *Ground-based and Airborne Instrumentation for Astronomy II*. Edited by McLean, 7014, 30
- Hoffman, J. L., Leonard, D. C., Chornock, R., et al. 2008, *ApJ*, 688, 1186
- Howell, J., Armus, L., Mazzarella, J. M., et al. 2010, *ApJ*, 715, 572
- Huang, C. 2016, in preparation
- Immler, S., Milne, P., & Pooley, D. 2010, *The Astronomer's Telegram*, 3012, 1
- Iwasawa, K., Sanders, D. B., Teng, S. H., et al. 2011, *A&A*, 529, A106
- Izotov, Y. I., & Izotova, I. Y. 1989a, *Astrophysics*, 30, 18
- . 1989b, *Astrophysics*, 30, 188
- Izumi, T., Kohno, K., Aalto, S., et al. 2015, *ApJ*, 811, 39
- Kauffmann, G., Heckman, T., Tremonti, C., et al. 2003, *MNRAS*, 346, 1055

- Kewley, L. J., Dopita, M. A., Sutherland, R. S., Heisler, C. A., & Trevena, J. 2001, *ApJ*, 556, 121
- Kewley, L. J., Groves, B., Kauffmann, G., & Heckman, T. 2006, *MNRAS*, 372, 961
- Kiewe, M., Gal-Yam, A., Arcavi, I., et al. 2012, *ApJ*, 744, 10
- Kim, D.-C., Sanders, D., Veilleux, S., Mazzarella, J., & Soifer, B. 1995, *ApJS*, 98, 129
- Kim, D.-C., Veilleux, S., & Sanders, D. 1998, *ApJ*, 508, 627
- Knop, R., Armus, L., Matthews, K., Murphy, T., & Soifer, B. 2001, *AJ*, 122, 764
- Lacey, C. K., Weiler, K. W., Sramek, R. A., & van Dyk, S. D. 1998, *IAU circ.*, 7068, 2
- Lagache, G., Puget, J.-L., & Dole, H. 2005, *ARAA*, 43, 727
- Larkin, J., Armus, L., Knop, R., Soifer, B., & Matthews, K. 1998, *ApJS*, 114, 59
- Leonard, D. C., Filippenko, A. V., Barth, A. J., & Matheson, T. 2000, *ApJ*, 536, 239
- Lester, D. F., Gaffney, N., Carr, J. S., & Joy, M. 1990, *ApJ*, 352, 544
- Levesque, E., Kewley, L., & Larson, K. 2010, *AJ*, 139, 712
- Maeda, K., Nozawa, T., Sahu, D. K., et al. 2013, *ApJ*, 776, 5
- Marconi, A., Moorwood, A. F. M., Salvati, M., & Oliva, E. 1994, *A&A*, 291, 18
- Markwardt, C. B. 2009, *Astronomical Data Analysis Software and Systems XVIII*, 411, 251

- Matsuoka, Y., Yuan, F.-T., Takeuchi, Y., & Yanagisawa, K. 2012, PASJ, 64, arXiv:1111.4522
- Mazzarella, J. M., & Balzano, V. A. 1986, ApJS, 62, 751
- Mazzarella, J. M., Bothun, G. D., & Boroson, T. A. 1991, AJ, 101, 2034
- Mazzarella, J. M., Iwasawa, K., Vavilkin, T., et al. 2012, AJ, 144, 125
- Milisavljevic, D., Fesen, R. A., Leibundgut, B., & Kirshner, R. P. 2008, ApJ, 684, 1170
- Moré, J. 1978, Numerical Analysis, 630, 105
- Mouri, H., Kawara, K., & Taniguchi, Y. 2000, ApJ, 528, 186
- Müller-Sánchez, F., Prieto, M. A., Hicks, E. K. S., et al. 2011, ApJ, 739, 69
- Murphy, T. W., Soifer, B. T., Matthews, K., Armus, L., & Kiger, J. R. 2001, AJ, 121, 97
- Neugebauer, G., Soifer, B., Beichman, C., et al. 1984, *Science*, 224, 14
- Newton, J., & Puckett, T. 2010, CBET, 2532, 1
- Ofek, E. O., Zoglauer, A., Boggs, S. E., et al. 2014, ApJ, 781, 42
- Oja, T. 1991, A&AS, 89, 415
- Petric, A. O., Armus, L., Howell, J., et al. 2011, ApJ, 730, 28
- Privon, G. C., Barnes, J. E., Evans, A. S., et al. 2013, ApJ, 771, 120
- Quataert, E., & Shiode, J. 2012, MNRAS, 423, L92

- Reunanen, J., Kotilainen, J. K., & Prieto, M. A. 2002, MNRAS, 331, 154
- Rich, J. A., Kewley, L. J., & Doptia, M. A. 2014, ApJ, 781, 12
- Rieke, G. H., & Lebofsky, M. J. 1985, ApJ, 288, 618
- Riffel, R., Rodríguez-Ardila, A., Aleman, I., et al. 2013, MNRAS, 430, 2002
- Riffel, R., Rodríguez-Ardila, A., & Pastoriza, M. G. 2006, A&A, 457, 61
- Rodríguez-Ardila, A., Pastoriza, M. G., Viegas, S., Sigut, T. A. A., & Pradhan, A. K. 2004, A&A, 425, 457
- Rodríguez-Ardila, A., Prieto, M. A., Portilla, J. G., & Tejeiro, J. M. 2011, ApJ, 743, 100
- Rodríguez-Ardila, A., Riffel, R., & Pastoriza, M. G. 2005, MNRAS, 364, 1041
- Sanders, D. B., Mazzarella, J. M., Kim, D.-C., Surace, J. A., & Soifer, B. T. 2003, AJ, 126, 1607
- Sanders, D. B., & Mirabel, I. F. 1996, ARAA, 34, 749
- Sanders, D. B., Scoville, N. Z., & Soifer, B. T. 1991, ApJ, 370, 158
- Sanders, D. B., Soifer, B. T., Elias, J. H., Neugebauer, G., & Matthews, K. 1988, ApJ, 328, 35
- Schlegel, E. M. 1990, MNRAS, 244, 269
- Simpson, C., Forbes, D. A., Baker, A. C., & Ward, M. J. 1996, MNRAS, 283, 777
- Skrutskie, M. F., Cutri, R. M., Stiening, R., et al. 2006, AJ, 131, 1163

- Smith, N., Chornock, R., Silverman, J. M., Filippenko, A. V., & Foley, R. J. 2010, *ApJ*, 709, 856
- Smith, N., Li, W., Filippenko, A. V., & Chornock, R. 2011a, *MNRAS*, 412, 1522
- Smith, N., Li, W., Miller, A. A., et al. 2011b, *ApJ*, 732, 63
- Smith, N., Silverman, J. M., Filippenko, A. V., et al. 2012, *AJ*, 143, 17
- Soifer, B. T., Sanders, D. B., Madore, B. F., et al. 1987, *ApJ*, 320, 238
- Soker, N. 2013, preprint (arXiv:1302.5037)
- Solomon, P., Downes, D., Radford, S. J. E., & Barrett, J. W. 1997, *ApJ*, 478, 144
- Stierwalt, S., Armus, L., Surace, J. A., et al. 2013, *ApJS*, 206, 1
- Stierwalt, S., Armus, L., Charmandaris, V., et al. 2014, *ApJ*, 790, 124
- Stoll, R., Prieto, J. L., Stanek, K. Z., et al. 2011, *ApJ*, 730, 34
- Sturm, E., Lutz, D., Genzel, R., et al. 1996, *A&A*, 315, 133
- U, V., Medling, A., Sanders, D. B., et al. 2013, *ApJ*, 775, 115
- van Leeuwen, F. 2007, *A&A*, 474, 653
- Veilleux, S., Kim, D.-C., & Sanders, D. B. 1999a, *ApJ*, 522, 113
- . 2002, *ApJS*, 143, 315
- Veilleux, S., Kim, D.-C., Sanders, D. B., Mazzarella, J. M., & Soifer, B. T. 1995, *ApJS*, 98, 171
- Veilleux, S., Meléndez, M., Sturm, E., et al. 2013, *ApJ*, 776, 27



- Veilleux, S., & Osterbrock, D. 1987, *ApJS*, 63, 295
- Veilleux, S., Rupke, D. S. N., Kim, D.-C., et al. 2009, *ApJS*, 182, 628
- Veilleux, S., Sanders, D. B., & Kim, D.-C. 1997b, *ApJ*, 484, 92
- . 1999b, *ApJ*, 522, 139
- Wilson, J. C., Henderson, C. P., Herter, T. L., et al. 2004, in *Proc. SPIE*, Vol. 5492, Ground-based Instrumentation for Astronomy, ed. A. F. M. Moorwood & M. Iye, 1295
- Wolfire, M. G., & Konigl, A. 1991, *ApJ*, 383, 205
- Xu, C., & de Zotti, G. 1989, *A&A*, 225, 12
- Yao, L., Seaquist, E. R., Kuno, N., & Dunne, L. 2003, *ApJ*, 588, 771
- Yuan, T.-T., Kewley, L. J., & Sanders, D. B. 2010, *ApJ*, 709, 884
- Zhang, T., Wang, X., Wu, C., et al. 2012, *AJ*, 144, 131